DOE/SF/90506-1
(DE83014527)

1/4 MEGAWATT SOLAR RECEIVER

Final Report

23.2401

October 1979

Work Performed Under Contract No. AC03-77SF90506

Sanders Associates, Inc.
Energy Systems Center
Nashua, New Hampshire

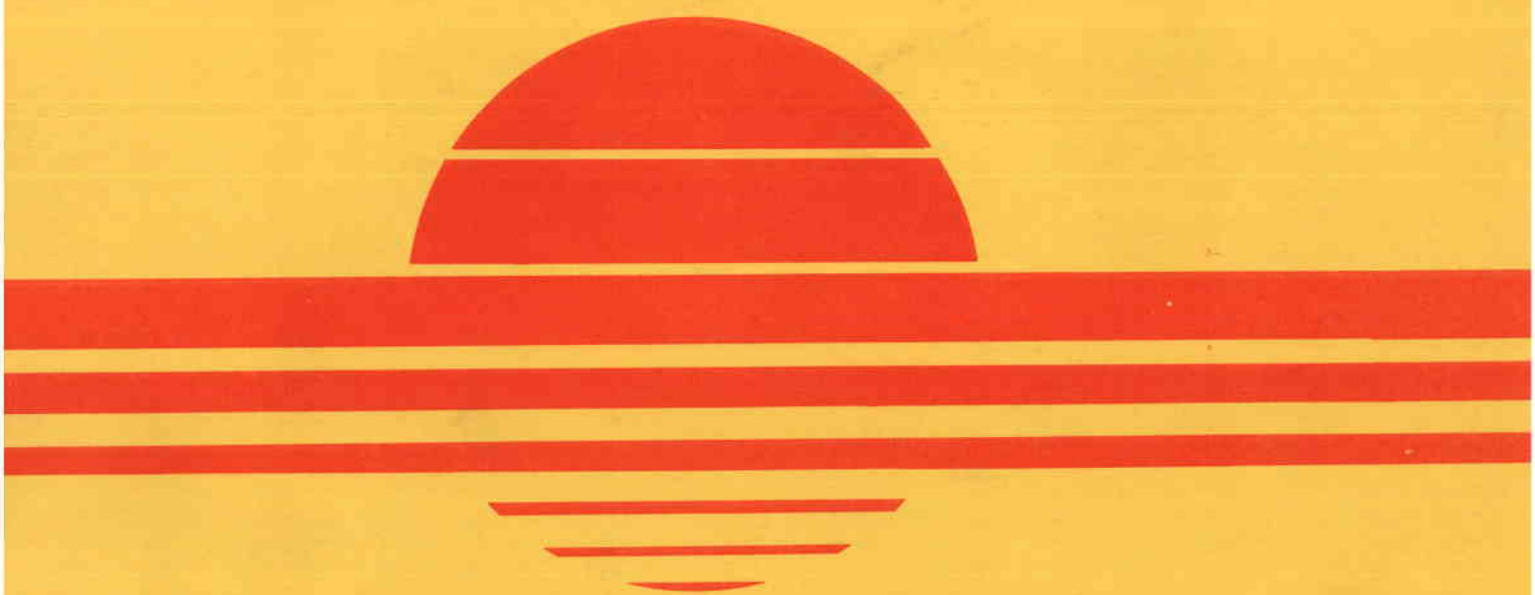

U.S. Department of Energy

Solar Energy

DISCLAIMER

Available from the National Technical Information Service, U. S. Department of Commerce, Springfield, Virginia 22161.

Price: Printed Copy A12
Microfiche A01

Codes are used for pricing all publications. The code is determined by the number of pages in the publication. Information pertaining to the pricing codes can be found in the current issues of the following publications, which are generally available in most libraries: *Energy Research Abstracts (ERA); Government Reports Announcements* and Index (*GRA* and I); *Scientific and Technical Abstract Reports (STAR);* and publication NTIS-PR-360 available from NTIS at the above address.

DOE/SF/90506-1
(DE83014527)
Distribution Category UC-62d

1/4 MEGAWATT SOLAR RECEIVER FINAL REPORT

OCTOBER 1979

WORK PERFORMED UNDER DOE CONTRACT

EG-77-C-03-1555

FOR

THE DEPARTMENT OF ENERGY
SAN FRANCISCO OPERATIONS OFFICE
1333 BROADWAY
OAKLAND, CA 94612

SANDERS ASSOCIATES, INC.
ENERGY SYSTEMS CENTER
95 CANAL STREET
NASHUA, NH 03061

TABLE OF CONTENTS

TABLE OF CONTENTS (Continued)

LIST OF ILLUSTRATIONS

LIST OF ILLUSTRATIONS (Continued)

LIST OF TABLES

SECTION 1
INTRODUCTION AND SUMMARY

1.1 INTRODUCTION

Sanders Associates, Inc., has completed the design and construction of a 1/4 MWt Air Cycle Solar Receiver and has successfully tested it at the Georgia Institute of Technology, Advanced Components Test Facility. The receiver was designed to deliver air at 1100°C (2000°F). The receiver operates at ambient pressure and does not require a window to seal the aperture. By using a novel ceramic matrix for solar energy absorption and heat transfer, the receiver can provide high efficiency solar energy collection with very low pressure drops. A terminal concentrator surrounding the receiver aperture is used to boost aperture concentration to about 2000. An additional feature is a compliant ceramic support system which minimizes the thermal stresses.

Before beginning the receiver tests, the flux distribution near the focal zone was mapped by GIT personnel. As part of the test series, additional measurements were made using both the GIT flux scanner and a flux scanner built by Sanders to map the flux distribution on the receiver surfaces. The flux scans indicated a mirror aiming and tracking error, σ = 11.8 mrad for the facility. Sigma has a large impact on the amount of energy which can be directed into a receiver. The Sanders receiver is designed for a field pointing dispersion of σ = 6.6 mrad. The receiver aperture diameter has been reduced to 50.8 cm (20 in) by using a terminal concentrator to redirect the outer rays into the aperture. The increase in σ from 6.6 mrad to 11.8 mrad results in a reduction in the solar energy, which can be directed into the receiver, from 316 kW to 190 kW.

Based on this evaluation of the facility, a limited test plan aimed at providing a shakedown of both the Sanders receiver and the GIT facility was followed. The objectives of this first test series have been successfully accomplished. They are:

- Output air temperatures of 815°C (1955°) were maintained with honeycomb temperatures of ∿1200°C (∿2200°F) for reduced flow with an average insolation of ∿900 W/m^2. No visible changes in the receiver interior were noticeable after thermal cycling.

- Output air temperatures of ∿830°C (∿1530°F) were obtained for design mass flow with approximately 100 KW delivered to the air. Insolation for this test was ∿805 W/m^2.

- Several hot convective loss runs were conducted using excess nitrogen as the trace gas and oxygen concentration as the measured variable. Maximum wind velocities of 2.4 m/sec (8 ft/sec) produced heat loss determinations, that confirmed the Wolfeboro Railroad test; i.e., ∿1/2% of design thermal input.

1.1.1 Sanders' Concept

Sanders' solar thermal electric power conversion concept calls for two separate operating cycles. The collection cycle stores solar energy as sensible heat in ceramic material. The fully charged storage unit is subsequently switched to the power extraction cycle where the energy is converted to electric power by the recuperated, open cycle Brayton driven generator. This allows each subsystem to be optimized independently to effect a more efficient solar electric generating plant. The concept schematic is presented in Figure 1-1.

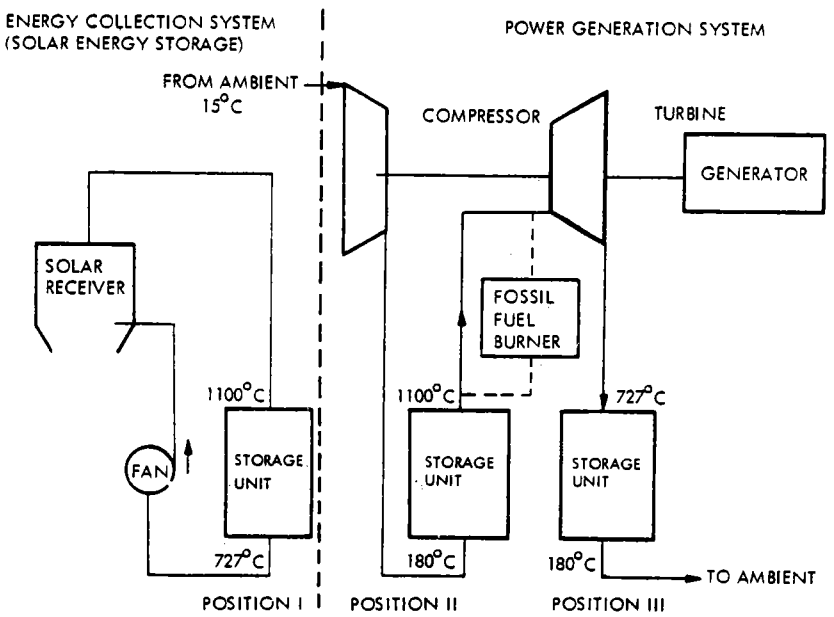

Figure 1-1. Sanders' Concept

In August 1977, Sanders was awarded Contract EG-77-C-03-155 by ERDA, now the Department of Energy. Under terms of that contract, Sanders was to design and test a 1/4 MWt (megawatt thermal) solar receiver to validate the receiver portion of the solar thermal electric power plant concept.

1.1.2 SOW Requirements

The Statement of Work prescribed the seven following tasks to be accomplished by the contractor:

- Task 1 - Design of the 1/4 MWt Receiver
- Task 2 - Convective Heat Loss Experiment
- Task 3 - Systems Analyses
- Task 4 - Construction of the 1/4 MWt Heat Receiver
- Task 5 - Testing of the 1/4 MWt Heat Receiver
- Task 6 - Liaison with Georgia Institute of Technology
- Task 7 - Review

A change of scope was negotiated to add the following subtasks to the original contract:

- Task 1 - Amended to include optical analysis, and preparation of an optical flux mapping code
- Task 5 - Amended to include design compatibility with single GIT aim point, and to provide a flux scanner to map solar flux at the receiver ceiling and cylindrical wall.

The complete Statement of Work is contained within Appendix V of this re-report. Technical direction and review for this program was provided by Sandia Laboratories, Livermore, CA.

1.2 SUMMARY

1.2.1 Testing

The 1/4 MWT Solar Receiver (Figures 1-2 and 1-3) was delivered to the Advanced Component Test Facility (ACTF) at Georgia Institute of Technology (GIT) in Atlanta on 13 September. Following a week of flux measurement tests, during which the ACTF field was accurately evaluated (field sigma, σ = 11.8 to 11.9 mrad) the solar receiver was placed atop the experiment tower. First sun was directed to the receiver on 27 September 1978. Mirror field misalignment, tracking dispersion and low insolation levels reduced the power input to 20% of design levels; nevertheless air temperatures of 815^{o}C (1500^{o}F) were achieved.

The preponderance of thick haziness, typical of late summer in Atlanta, and a need for the ACTF crew to: (1) complete the shutter installation, (2) correct scanning bar malfunctions, (3) acquire tracking proficiency and (4) re-aim the more obviously divergent mirrors led to a 2-3 week test moratorium.

Prior to resuming the tests, the Sanders test crew corrected a minor cooling air control malfunction, reduced 60 Hz ripple on a transducer output line, and reduced backpressure on the terminal concentrator cooling flow.

By 18 October, the ACTF was again operational, clear fall weather had arrived, and testing resumed on the following day. Maximum temperatures of 1070^{o}C (1955^{o}F) were achieved at 10% of rated mass flow. Maximum power conversion was 121 kW during tests performed when direct insolation was 900 W/m^{2}. Steady state thermal loss data collected during the tests show the losses at design temperatures to be 50 kW. Except for second order effects, losses at rated power would be

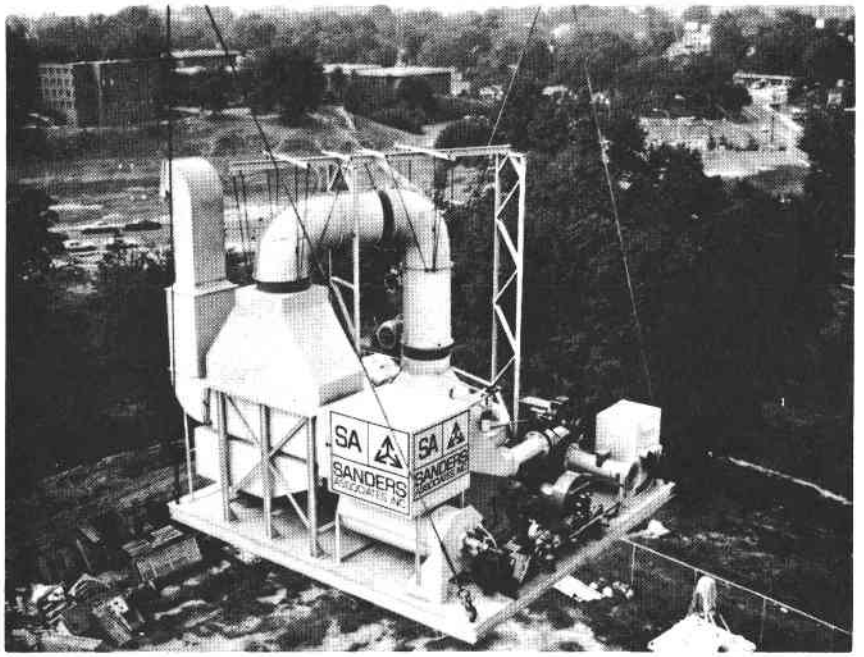

Figure 1-2. Solar Receiver Being Hoisted to ACTF Tower

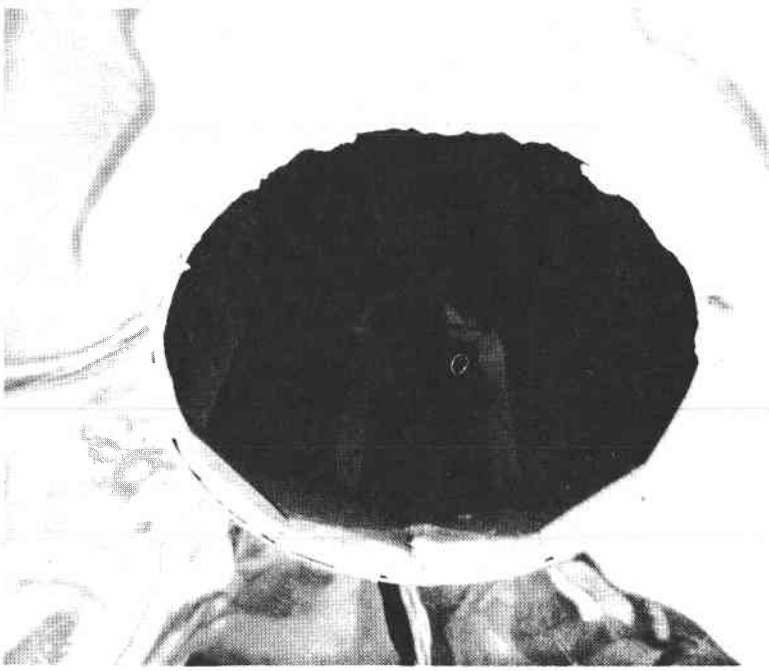

Figure 1-3. Solar Receiver Honeycomb Heated to 1000°C

identical and an efficiency of 84%[1] is projected for the Sanders receiver at rated power. These tests have shown the Sanders concept to be technically sound.

All other test objectives were met. An output power of 106 kW was achieved at an outlet operating temperature of 810°C (1486°F). Honeycomb temperatures in excess of 1100°C (2000°F) were observed during several days testing. To simulate the gas turbine temperature operating conditions, measurements were made with 650°C (1200°F) inlet air, 1070°C (1958°F) outlet air temperature and 0.38 lb/sec of air flow. Conduction and convection losses associated with the open cavity were measured. These results, when scaled to an optimum commercial size mirror field and receiver, represent a receiver collection efficiency of 85% at 2000°F and greater efficiencies at lower temperatures.

(1) $\frac{\text{Power output of receiver}}{\text{Power out of terminal Concentrator}} \times 100\% = 85\%$

SECTION 2
DESIGN DISCUSSION

2.1 RECEIVER CONCEPT

As shown in Figure 2-1, the receiver is basically a cylindrical cavity with conical ends. A reentrant cone between the aperture and cylindrical walls and a conical roof increase effective cavity absorptivity and improve energy distribution within the receiver. The cylindrical heat exchanger can be scaled to larger sizes. Present-day panel sizes can be used in commercial plants.

The air in the receiver panels flows in a direction opposite to the flow in previously designed receivers. This "reverse flow" configuration, embodied in the Sanders receiver, is somewhat analogous to a counterflow heat exchanger. Sunlight enters the receiver cavity through the (base) aperture and impinges on the inner surface of the cylindrical wall. Air enters the receiver from the outer surface of the cylindrical wall, flowing inward through the honeycomb to the cavity interior. Thus, air flow and the Poynting vectors (photon flow) are in opposite directions. This reverse flow configuration has a distinct advantage over forward flow designs; it maintains the cylindrical wall supports at or near inlet air temperatures (650^{o}C) rather than at outlet air temperatures (1100^{o}C). In fact, the receiver can tolerate even higher temperatures without affecting the integrity of the structural members.

2.2 SYSTEM DESIGN

2.2.1 General

The 1/4 MWt solar receiver was designed for an outlet temperature of 1100^{o}C (2000^{o}F) at an overall thermal efficiency of 0.84. The receiver was also designed to operate with a zero pressure differential

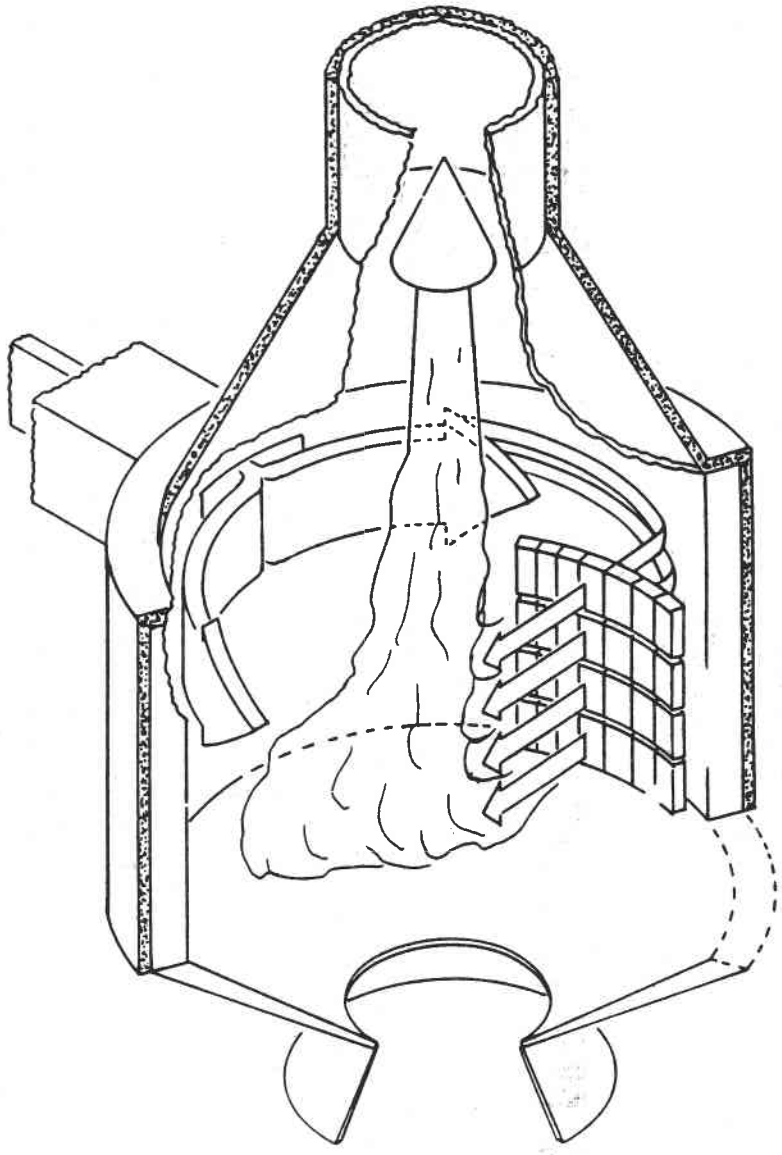

06268-46

Figure 2-1. Receiver Design

across the aperture. The receiver cavity is open, with no pressure sealing window. A terminal concentrator is integral with the design (Figure 2-2). The receiver and concentrator are designed to be compatible with the specified ACTF aim point location and mirror dispersion, σ = 6.6 mrad. The receiver system included the necessary air movers, heat load, controls, auxiliary heater, test equipment, and platform to provide a self contained system capable of demonstrating the receiver performance.

Most importantly, the experimental 1/4 MWt receiver was designed, not only to demonstrate concept validation, but also to demonstrate configuration scalability. Construction techniques are scalable to commercial, utility-sized (10, 50, 100 MWe) power tower receivers. The receiver state of the art, as advanced by this receiver, is adequate to build a large commercial receiver. Some nominal upsizing of receiver panels (from 1 ft^2 to 1 meter square, for example) is recommended since this will provide hardware and construction economies without incurring prohibitively costly manufacturing capital investments.

2.2.2 Scalability

During the contract, particular attention was directed toward aspects of scalability. The 1/4 MWt receiver is a scaled down version of a commercial receiver concept. The airtight inner receiver shell and silicon carbide panel support stanchions are mutually stiffening, not unlike a natural gas storage tank. The SiC honeycomb panels are individually supported to prevent "hydrostatic" crushing and to accommodate thermal expansions. The saffil insulation blocks are attached to the rooftop using large scale kiln (ceramic) fasteners. The receiver air distribution control system reflects the requirements of a larger system, though a more rudimentary system would have sufficed for the 1/4 MWt demonstration unit. The sizing of 24 Sic panels (1' x 1') in the 1/4 MWt receiver was dictated by a number of design and producibility considerations. The primary factors are listed in Table 2-1.

Figure 2-2. Receiver and Concentrator

TABLE 2-1. PRIMARY FACTORS FOR DESIGN AND PRODUCIBILITY CONSIDERATIONS

Factor	Impact
Producibility	Present-day size capacity of firing ovens is limited to approximately 45 cm (18 inches). Increased size capabilities are available given time and money. New technology is not required to achieve moderate scale-up. For example an oven capable of firing a 1 meter square SiC panel could be put on line in 12 months at a capital expenditure of $200K.
Thermal Stress	Thermal gradients through the thickness of the panel (axial dimension of tubes) is not a problem. Flux gradients across the face of the panel could cause differential expansions which would limit maximum panel size. Flux gradients (watts cm^{-2} per cm) are smaller in the commercial receiver so a larger panel is feasible.
Geometry	The "cylindrical" wall of the 1/4 MWt solar receiver cavity is in fact bounded by 12 discrete flat elements 0.6m high by 0.3m wide (2 ft x 1 ft). Maximum deviation from a cylinder is ± 1.7% for the 12 sided cavity. The 100 MWe receiver with linear dimensions 30-32 times those of the 1/4 MWt receiver will very nearly match a true cylinder. Given 1 m^2 panels, the large receiver will have 120 finite panels and deviation from the cylinder will be ± 0.017%. The optical model is thus more accurate for the commercial receiver; the deviation for the 1/4 MWt receiver is acceptable.

Producibility and thermal stress considerations were the driving forces for the selection of panel size in the 1/4 MWt receiver. Geometric considerations provided close approximation to the idealized cylinder.

The saffil insulation tiles were attached to the cavity rooftop by standard kiln (ceramic) fasteners. Optical scalability was achieved by matching, as closely as practicable, the flux distribution in the 1/4 MWt receiver with the flux distribution in a commercial receiver. The terminal concentrator is designed to fold in ray bundles from distant mirrors. Some of the terminal concentrator benefits are reduced by the gang-driven ACTF field constraints. The larger rim angle and computer controlled heliostats of larger commercial fields allows more terminal concentration than is presently possible at the ACTF in Georgia.

Energy balance in both the commercial and experimental receivers varies in degree but not in concept. The principal difference lies in the reradiation losses; the tighter and more optimized performance of a commercial sized heliostat field will provide higher concentration, and reradiation losses will be proportionately less.

2.3 OPTICAL DESIGN

2.3.1 Analysis and Codes

Sanders chose to optically analyze the GIT heliostat field using the HELIOS code written by Sandia Laboratories. HELIOS is a computer program for modeling the solar power received in single focal plane. The HELIOS program, as received from Sandia in Aug-Sept 1977, allowed for only one point of focus for the entire heliostat field. As computer runs were made, it appeared to be beneficial if multiple aim points could be employed to give a more even flux distribution in the focal plane. Charles Vittetoe of Sandia had just finished an update for multiple aim points and focus points, and very kindly forwarded these updates to Sanders. Computer runs were made with 180 representative heliostats divided in 22 groups, each group with its own point of focus and aim point. Tradeoffs and comparisons of such items as south

versus central tower location, angular gain factor (AGF)*, and rim angle were made. (See Tables 2-2 through 2-4).

The power available from the south tower slightly exceeds that available from the central tower. This is due to the south tower having a more favorable cosine factor. However, the comparisons show that: (1) the HELIOS integration routine tends to favor a central tower location; (2) due to the long slant range of the south tower, aiming is extremely critical; and (3) the power on the central tower target is much more concentrated, thus allowing more watts to enter a smaller aperture. This was confirmed using a new computer program (FLUXIN) which integrates the power received on the target and allows for non-rectangular targets. Outputs of the HELIOS program were input to the FLUXIN program and the FLUXIN outputs are graphically portrayed in Figure 2-3.

The FLUXIN program results indicated that a central tower would be more advantageous than a south tower. Concurrently, GIT (Georgia Institute of Technology) arrived at the same conclusion and a new central tower was designed for the GIT mirror field.

The FLUXIN program, although it calculated power received on a target (e.g., aperture plane), gave no indication as to the continuing direction of the rays and their final location (end point) within a solar receiver. Clearly, the final locations of the sun rays would determine the energy flux distribution within the receiver. Thus, the FLUXIN program was modified and expanded to trace the solar rays to their end locations within the receiver. The expanded FLUXIN program is now Sanders' FLUXGO code which was used to design the interim layout of the receiver cavity.

---

*Angular Gain Factor is a term coined to describe a particular aiming strategy. The inlet plane of the concentrator is parallel to the mirror field and is located between the mirror field and the receiver aperture. A perfectly aimed ray, from a given mirror at radius (r_f) from the tower, penetrates the concentrator entrance aperture at a smaller radius (r_c). These radii, representing bases of similar triangles, are in proportion to the vertical separation (Z) of their respective planes from the receiver entrance plane. Mathematically,

$$r_c/r_f = Z_c/Z_f \qquad \text{or} \qquad r_c = r_f Z_c/Z_f$$

The concept of the angular gain factor allows the use of a single algorithm to determine the aim point on the concentrator entrance aperture of individual mirrors. Therefore,

$$r_c = (AGF) \times r_f Z_c/Z_f$$

An AGF less than +1.0 implies that the central rays intersect the receiver optical axis at a point below the receiver aperture. From the standpoint of directing the maximum amount of energy into the concentrator and minimizing near-side spillage, an AGF of less than +1.0 is helpful.

TABLE 2-2. CENTRAL TOWER DATA

DAY OF YEAR	SOLAR TIME	RIM ANGLE (DEG)	ANGULAR GAIN FACTOR	POWER INCIDENT ON APERTURE (W)	POWER INCIDENT ON MIRRORS (W)	CAPTURE RATE (%)
June 21	10:00 AM	45	-.75	333,244	361,563	92.17
June 21	12:00 Noon	45	-.75	357,134	387,600	92.14
May 1	10:00 AM	45	-.75	363,898	394,847	92.16
May 1	12:00 Noon	45	-.75	385,721	418,736	92.11
May 1	12:00 Noon	45	-.5	383,681	418,468	91.69
May 1	12:00 Noon	45	-1.0	385,506	418,736	92.06
May 1	12:00 Noon	45	-1.25	379,493	418,736	90.63
May 1	12:00 Noon	50	-1.25	373,266	413,368	90.3
May 1	12:00 Noon	55	-1.5	371,360	407,194	91.2
May 1	12:00 Noon	55	-1.625	360,140	407,194	88.44

TABLE 2-3. SOUTH TOWER DATA

DAY OF YEAR	SOLAR TIME	ANGULAR GAIN FACTOR	POWER INCIDENT ON APERTURE (W)	POWER INCIDENT ON MIRRORS (W)	CAPTURE RATE (%)
May 1	10:00 AM	.5	367,548	403,436	91.1
May 1	12:00 Noon	.5	392,646	431,084	91.08
June 21	10:00 AM	.5	351,416	385,721	91.1
June 21	12:00 Noon	.5	378,742	415,784	91.09

TABLE 2-4. ANALYSIS GAIN DATA

TOWER LOCATION	DAY OF YEAR	SOLAR TIME	ANGULAR GAIN FACTOR	POWER INCIDENT ON APERTURE (W)	POWER INCIDENT ON MIRRORS (W)	CAPTURE RATE (%)
South	May 1	10:00 AM	.5	367,548	403,436	91.1
Central	May 1	10:00 AM	-.75	363,898	394,847	92.16
South	May 1	12:00 Noon	.5	392,646	431,084	91.08
Central	May 1	12:00 Noon	-.75	385,721	418,736	92.11
South	June 21	10:00 AM	.5	351,416	385,721	91.1
Central	June 21	10:00 AM	-.75	333,244	361,563	92.17
South	June 21	12:00 Noon	.5	378.742	415,784	91.09
Central	June 21	12:00 Noon	-.75	357,134	387,600	92.14

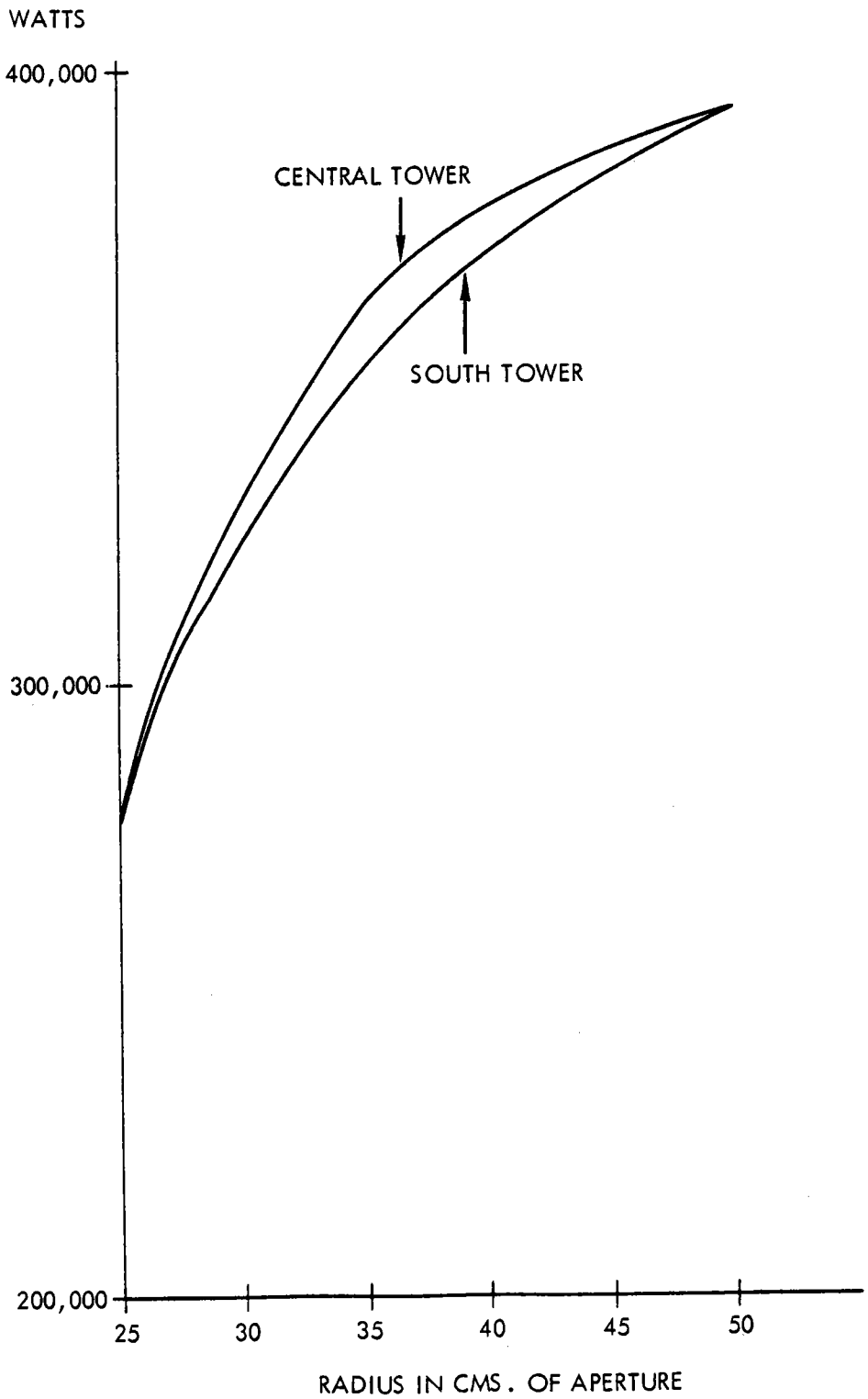

Figure 2-3. Power into Aperture

2.3.2 Commercial Design

With the aid of the FLUXGO code, Sanders optically analyzed both a commercial size 100 MWe (250 MWt) solar receiver and the scaled down 1/4 MWt GIT solar receiver. The FLUXGO code is a Monte Carlo random number generator that generates sun rays and sorts them into three categories: capture, miss or retroreflection. A retroreflection is a ray which enters the terminal concentrator or receiver and bounces back out of the receiver The rays that are captured are traced to their end locations which, if within the receiver, is where their energy is absorbed. The FLUXGO program identifies where the sun rays land in the solar receiver so that parametric analysis can assess the optimum flux distribution for maximum heat transfer and receiver longevity. An uneven flux distribution with hot spots could limit the life of some receiver components. Approximately 60% of the sun rays generated are absorbed on the receiver cylinder wall where the heat exchanger material is located (see Figure 2-7).

The commercial solar receiver was sized for a 100 MWe power output. Solar receiver aperture diameters in the range of 8 to 17 meters were compared with and without a terminal concentrator. Receivers with a terminal concentrator consistently captured 9 to 10% more flux than those without a terminal concentrator even after considering radiation losses (see Figure 2-4). The commercial solar receiver, with a 62-degree half angle terminal concentrator, captures the most flux at an aperture diameter of 12 meters (Figure 2-5). Further analysis of terminal concentrator half angle confirmed a 12-meter diameter as optimum but showed a terminal concentrator with 64-degree half angle capturing slightly more flux than a terminal concentrator with 62-degree half angle (see Figure 2-6). The commercial solar receiver designed with a 12-meter aperture diameter and a 64-degree terminal concentrator captures nearly 82% of the incident flux after accounting for radiation losses. Table 2-5 is the specification for the commercial receiver. Additional details on the costs and efficiencies of a commercial scale power plant are reported in "Final Report for A 10 KWt Solar Energy Receiver"*.

---

*Contract # EY-76-C-03-1533
Report #C000-2823-2

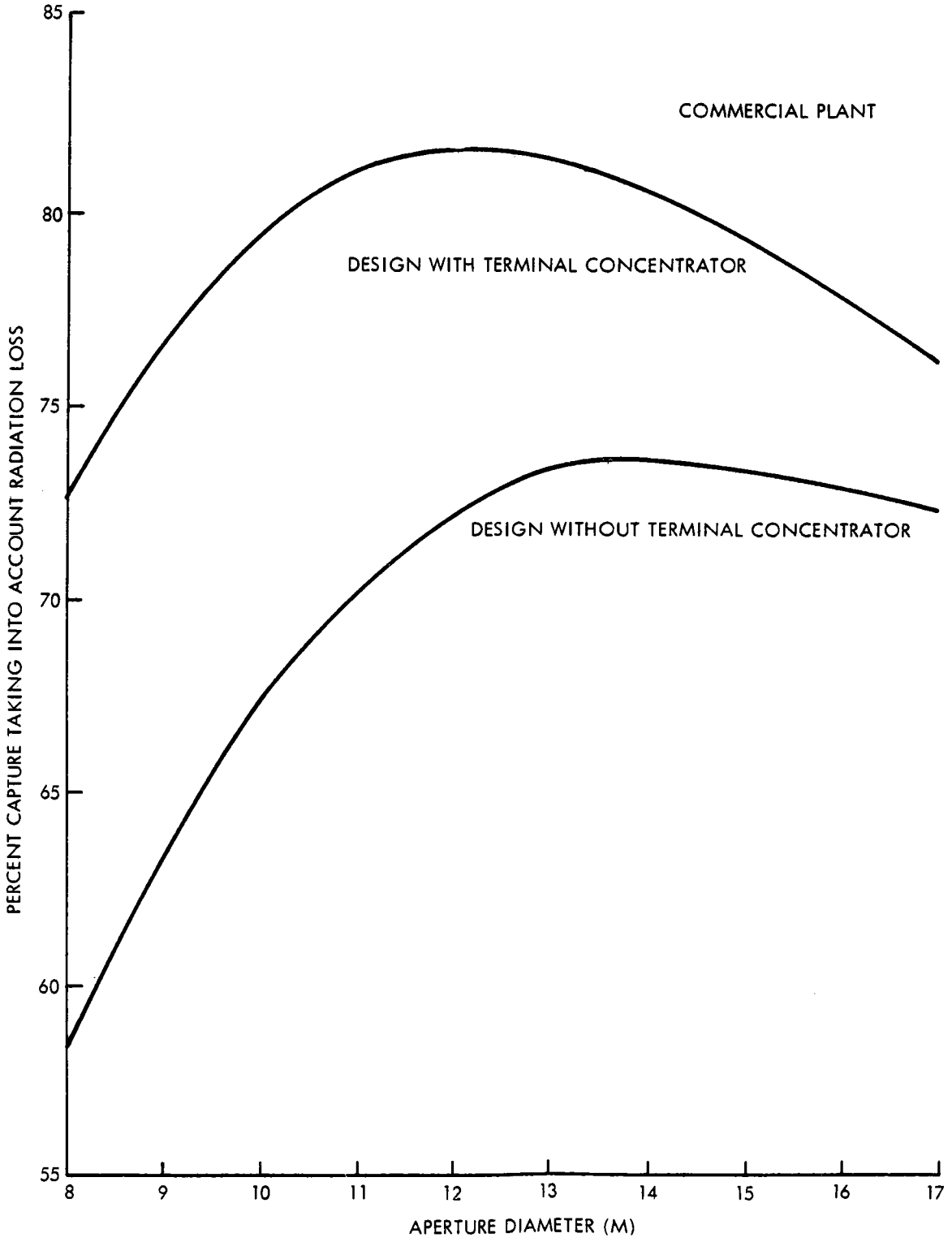

Figure 2-4. Capture Efficiency for a Commercial Size Solar Electric Power Plant

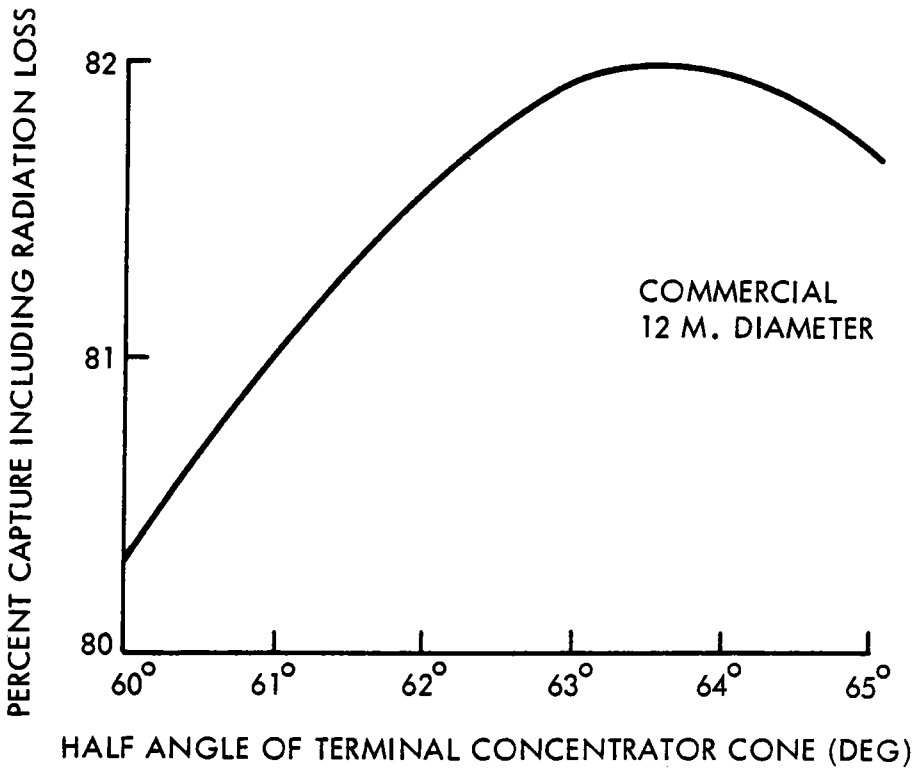

Figure 2-5. Capture Efficiency versus Terminal Concentrator Size

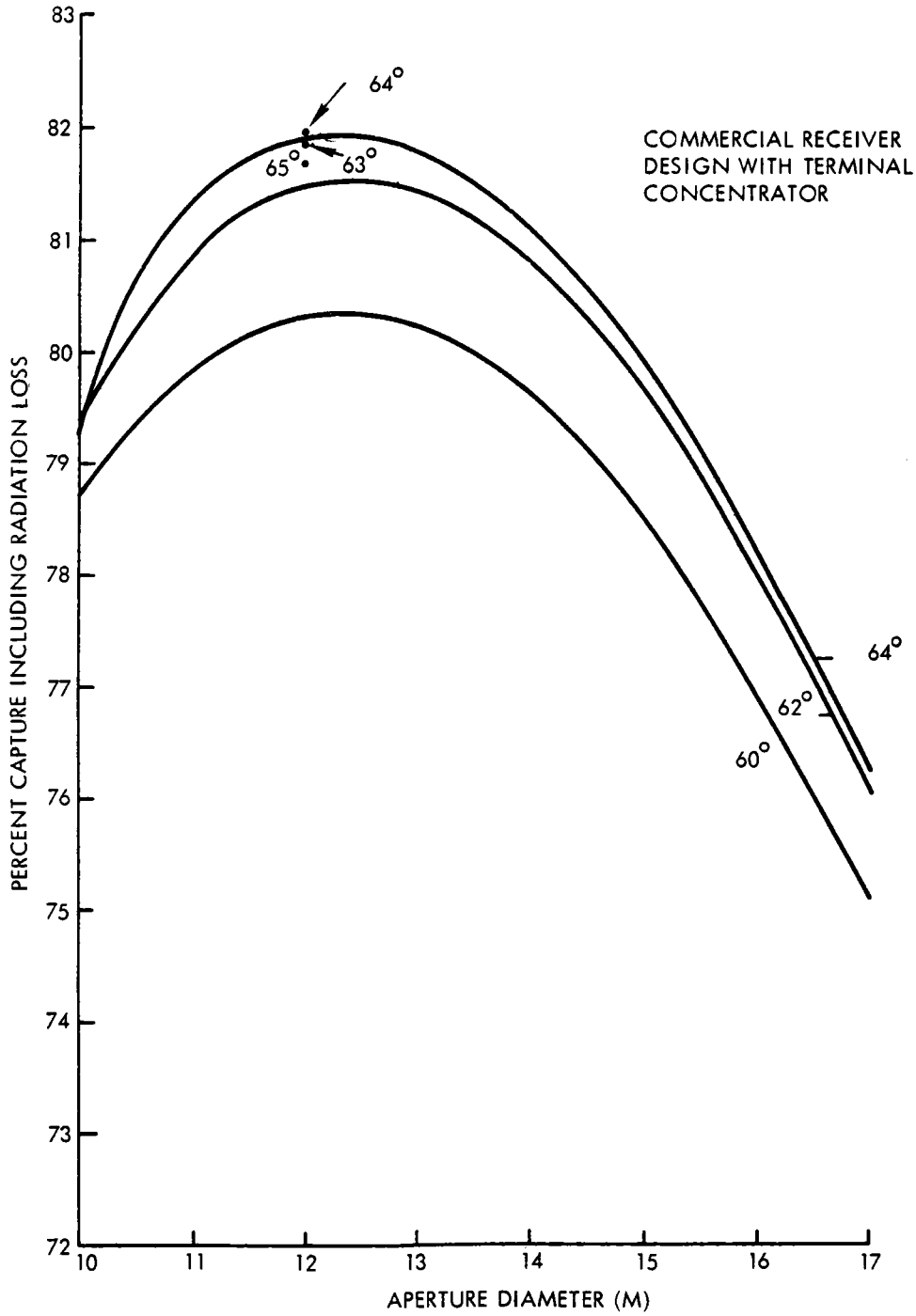

Figure 2-6. Commercial Receiver Design with Terminal Concentrator

TABLE 2-5. SPECIFICATIONS FOR SANDERS COMMERCIAL 100 MWe SOLAR RECEIVER

Receiver Input Rating (June 21)	286.00 MWt
Percent Capture (Power)	90.98
Percent Retroreflection (Power)	6.45
Percent Miss (Power)	2.57
Aperture Diameter	12m
Terminal Concentrator Diameter	37.08m
Mirror Field Diameter (Circular)	775.6m
Cylinder Diameter	25m
Aim Point Above Ground (Center of field)	241.25m
Aperture Height	239.1147m
Terminal Concentrator Aperture Height	233m
Cylinder Height (Actual)	13m
Terminal Concentrator Half Angle	64 degrees
Roof Cone Half Angle	39 degrees
Reentrant Cone Half Angle	52 degrees
Sigma Deviation (Includes sun size)	6 mrad
No. of Heliostats	11,000
Heliostat Size (each)	$37.2m^2$
Heliostat Reflectivity	0.91
Insolation	950 W/m^2

2.3.3 1/4 MWt Solar Receiver

The scaled down 1/4 MWt solar receiver tested at GIT in September 1978 was analyzed with the FLUXGO code described in Appendix I. Solar receiver apertures from 0.4 to 1.0 meter in diameter were compared versus percent flux capture with a 0.504 meter (20 inch diameter) aperture capturing the most flux. (See Figure 2-7.) Terminal concentrator angles from 50 degrees to 57 degrees with a 20 inch aperture were analyzed and a 52.5 degree terminal concentrator was found to perform best. (See Figure 2-8.) Further computer analysis yielded the optimum aim point for the GIT system at approximately 20.48 meters above ground as can be seen from Figure 2-9. A complete list of specifications for the 1/4 MWe solar receiver is given in Table 2-6.

TABLE 2-6. ORIGINAL SPECIFICATIONS FOR TESTING SANDERS 1/4 MW RECEIVER AT ACTF

Power Captured in Receiver	347 KWt
Percent Capture	82.45
Percent Retroreflection	12.90
Percent Miss	4.66
Aperture Diameter	0.508m
Terminal Concentrator Diameter	1.4206m
Mirror Field Diameter	39.622m
Cylinder Diameter	1.27m
Aim Point Above Ground	20.4810m
Aperture Height	20.36m
Terminal Concentrator Aperture Height	20.0099m
Cylinder Height (Actual)	0.6223m
Terminal Concentrator Half Angle	52.5 degrees
Roof Cone Half Angle	35 degrees
Reentrant Cone Half Angle	37.7 degrees
Sigma Deviation (Heliostats)	6.6 mrad
Mirror Reflectivity	90.0%
Insolation	950 W/m^2

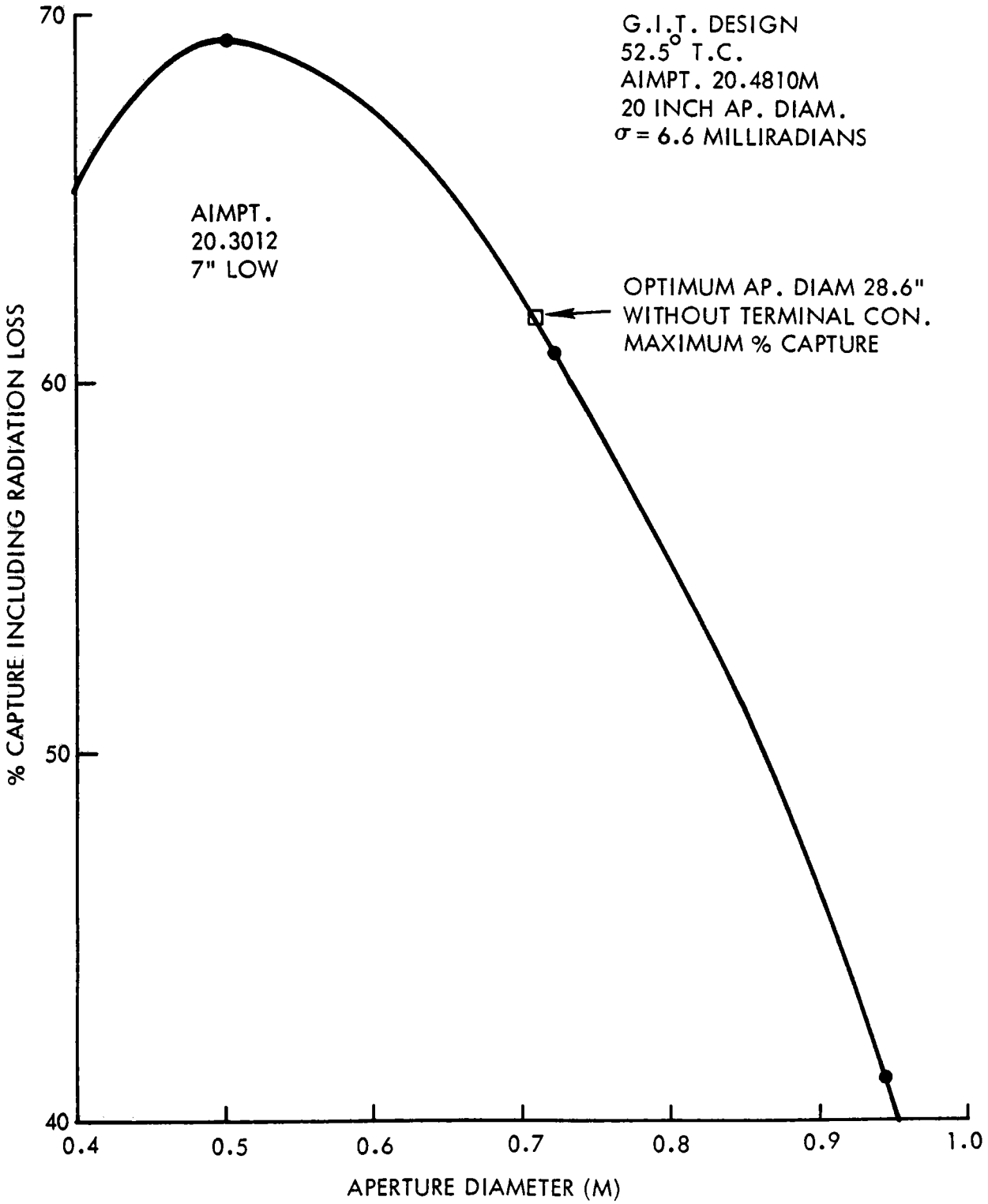

Figure 2-7. Percent Capture versus Aperture Diameter

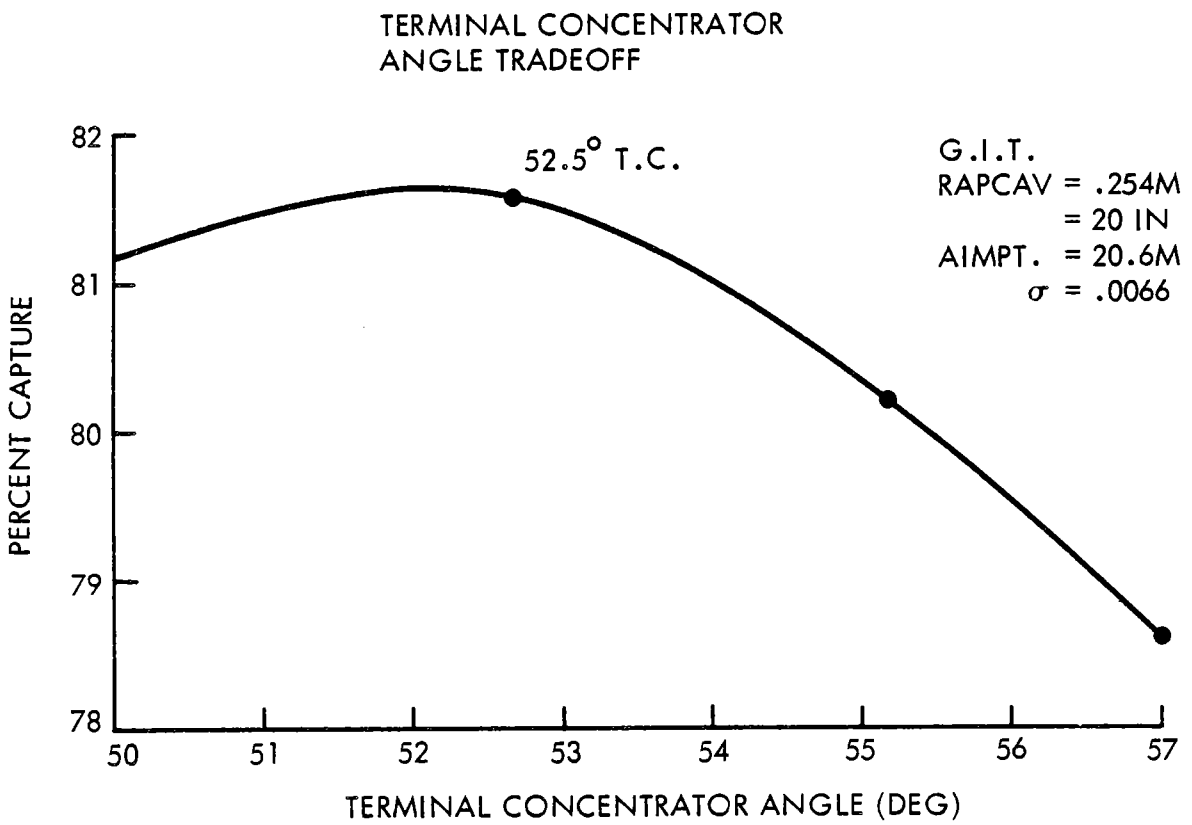

Figure 2-8. Percent Capture versus Terminal Concentrator Angle

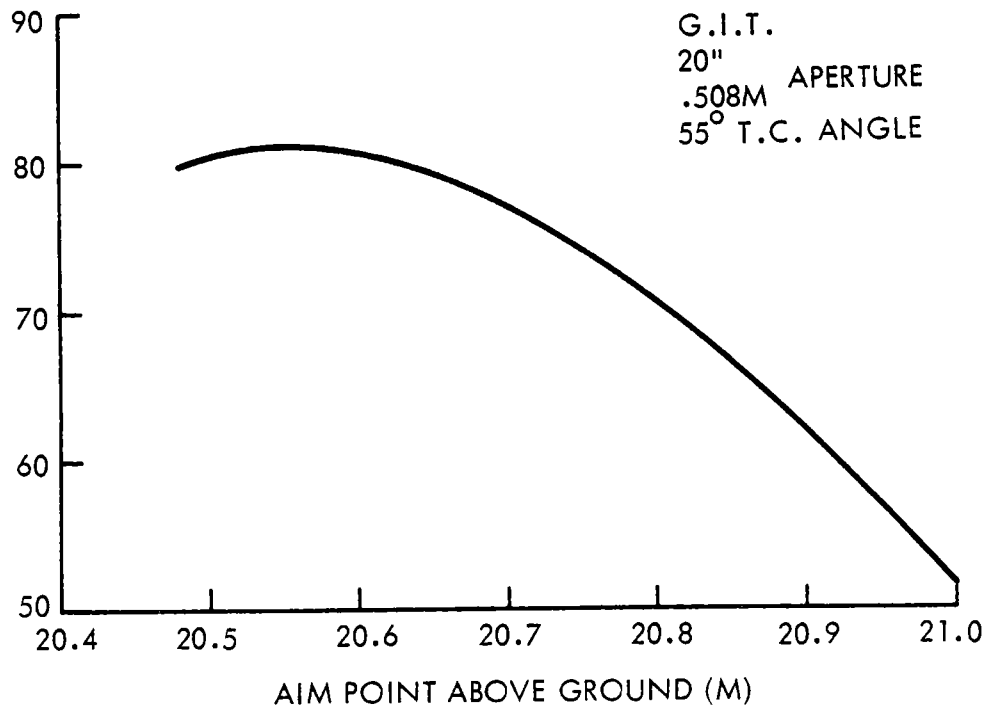

Figure 2-9. Optimum Aim Point Above Ground

2.4 THERMAL DESIGN

The commercial solar receiver is configured as a cylindrical blackbody type cavity with an active heat exchanger face/aperture area ratio of 10:1. (Total cavity wall/aperture area ratio is 18:1.) The heat exchanger, which converts incident solar radiation to thermal energy in the airstream consists of 1850m^2 of honeycomb matrix panels.

The exchanger panels may be fabricated from silicon carbide, cordierite, or other ceramic material. However, because of Sanders' experience with silicon carbide, this material is initially preferred as the honeycomb material. Cordierite, with its low thermal expansion, is a viable alternative material which may offer a more cost-effective solution where its temperature limit of 1430^{o}C (2600^{o}F) will not be exceeded.

In the conceptual receiver design (Figure 2-10) the heat exchanger panels are mounted on the cylindrical wall of the receiver. Air from the 650^{o}C (1200^{o}F) intermediate temperature stove enters the receiver via circumferential ducts external to the heat exchanger panels. The air then flows radially inward through the panels. With solar insolation incident on the inside and cooling air entering from the outside, the cylindrically-arrayed heat exchanger panels function similar to a counterflow heat exchanger (see Figure 2-11).

The two principal advantages of this configuration are: (a) the temperature gradients in the honeycomb panels during startup transients are quite linear (thermal stresses are low); and (b) the panel support structure is bathed in the relatively cool (650^{o}C) inlet air. This configuration was the basis for the 1/4 MWt receiver design.

A major design and contract goal in the 1/4 MWt receiver program was the demonstration of a scalable receiver configuration. During the course of the receiver design, solar flux profiles were determined

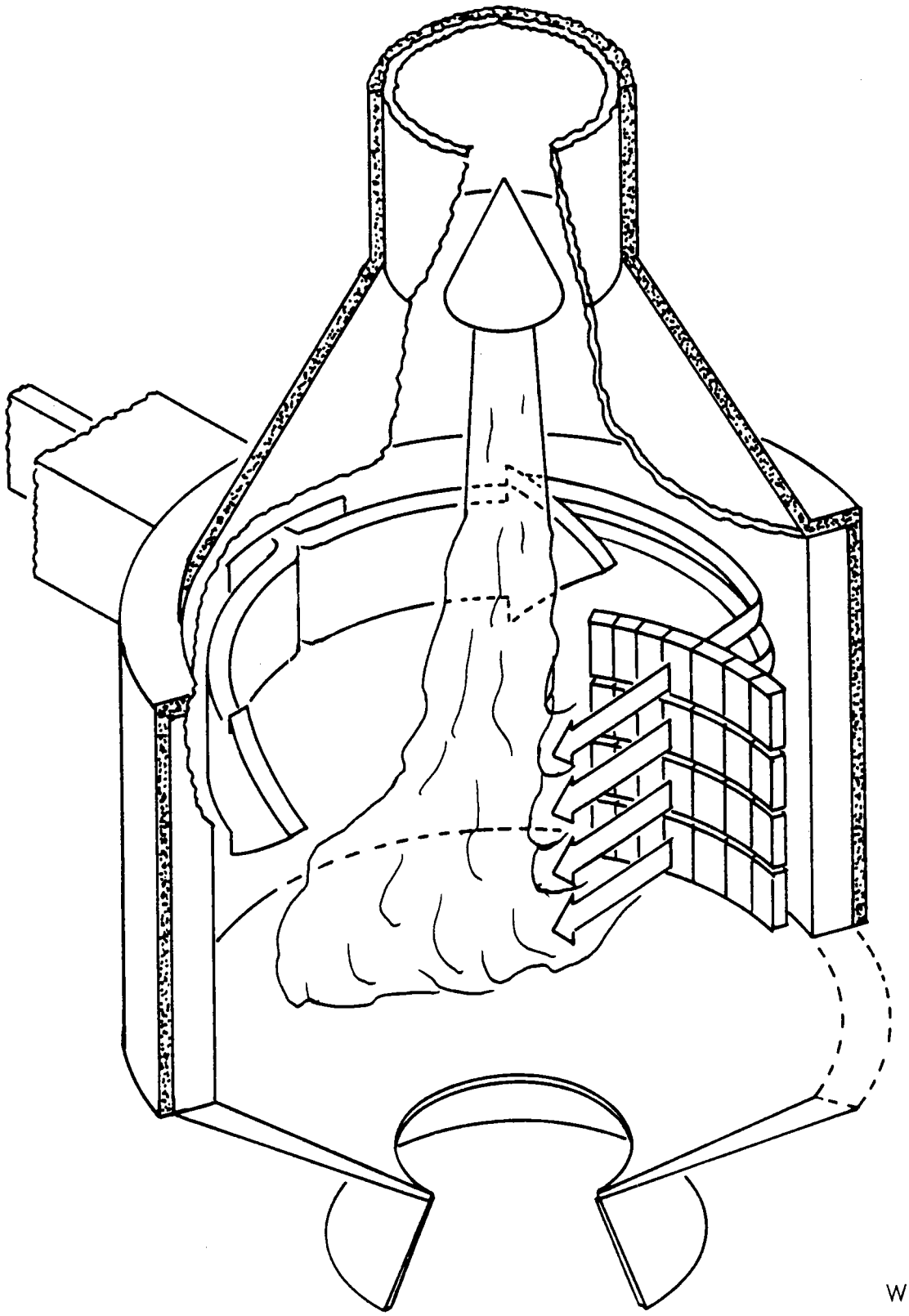

WIHYB-18

Figure 2-10. Receiver Design

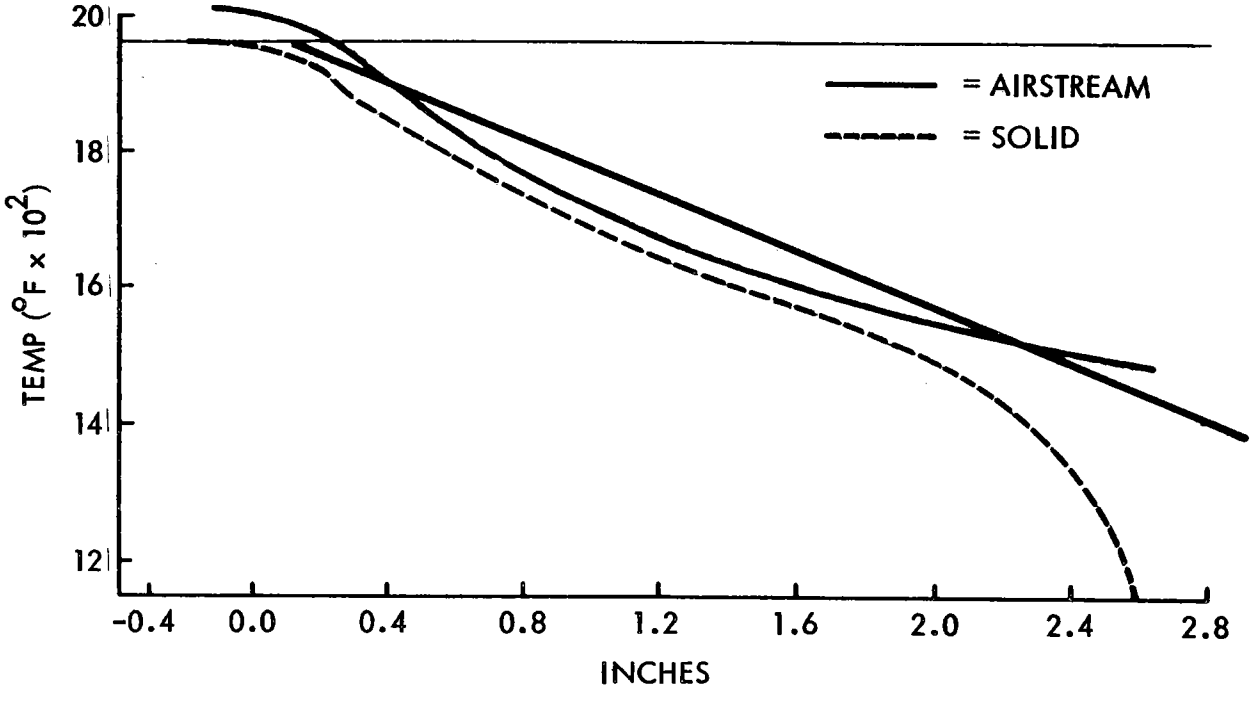

Figure 2-11. Temperature Profile, R=10, C=2000

on the ceramic matrix by using a Sanders-developed computer program called FLUXGO. From these profiles, Figures 2-12 and 2-13, the ANSYS program was used to perform heat transfer and stress analysis for both the small 1/4 MWt receiver and the commercial 100 MWe receiver. Note that the two maps shown in Figures 2-12 and 2-13 evidence similar profiles. Maximum flux levels agree within 10% and the peak/minimum flux ratios in the two receivers are similar. Previous modeling performed by Sanders has shown that even with peak/minimum flux ratios of 7:1, receiver efficiency is reduced only about one percentage point. The receiver's relative insensitivity to internal flux inequalities is characteristic of integrating blackbody-type cavities.

Stress levels in the silicon carbide honeycomb of 432 psi are well below the 24,000 psi modulus of rupture for this material. Sanders' previous experience with the silicon carbide radiation sources used in airborne infrared countermeasures (IRCM) systems has shown that even severely cracked panels survive if properly supported. The 1/4 MWt receiver utilizes a compressive preload technique which has proven successful for IRCM systems.

The compressive preload for the ceramic heat exchanger panels is achieved by a technique which takes advantage of the "counterflow" heat exchanger configuration. The rectangular (square) ceramic panels (Figure 2-14) are stacked vertically between vertical support stanchions. The panels are compressed from the side by Hastelloy-X leaf springs. The springs bear against the stanchions at two points, while the arch of the spring bears against the panel holding clamps. The spring was designed and analyzed with finite element modeling to assure that high temperature creep and yield would not diminish its effectiveness. The spring will operate at 680^{o}C (1250^{o}F), but is designed to function up to 870^{o}C (1600^{o}F). Fore and aft motion of the panel is limited by a compliant clamping arrangement designed to accommodate thermal expansion.

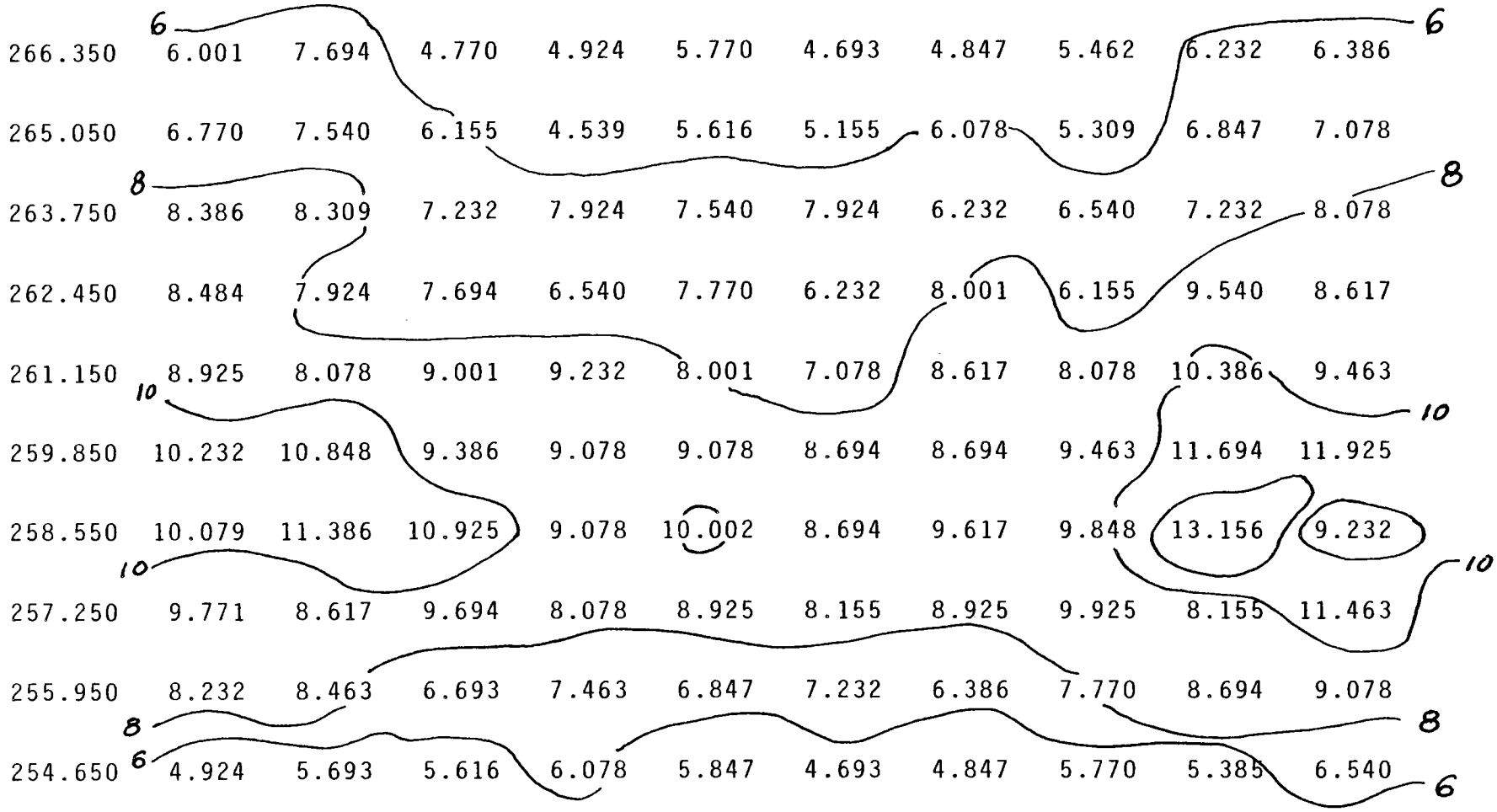

Figure 2-12. Commercial Design Flux Map

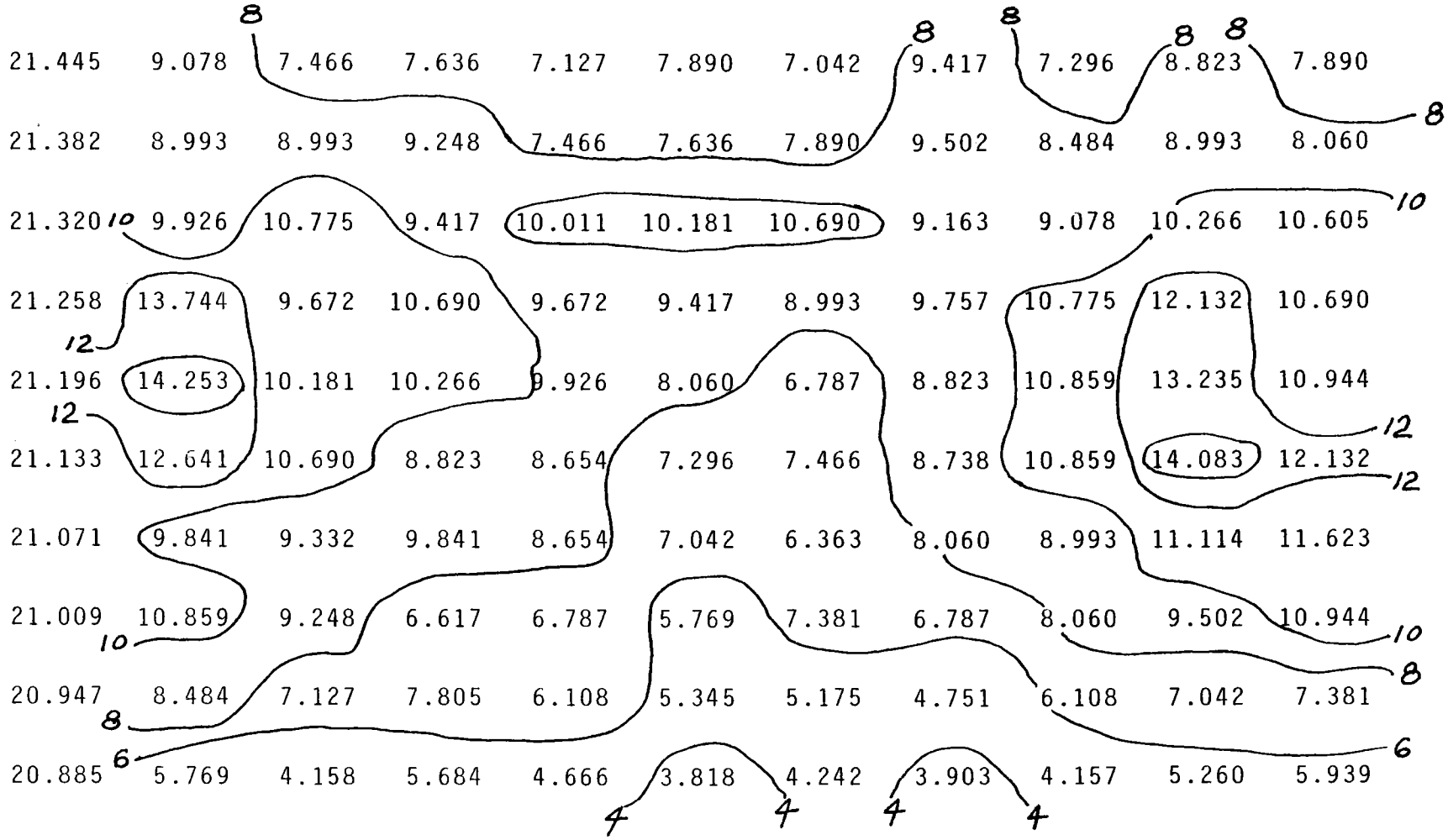

Figure 2-13. GIT Design Flux Map

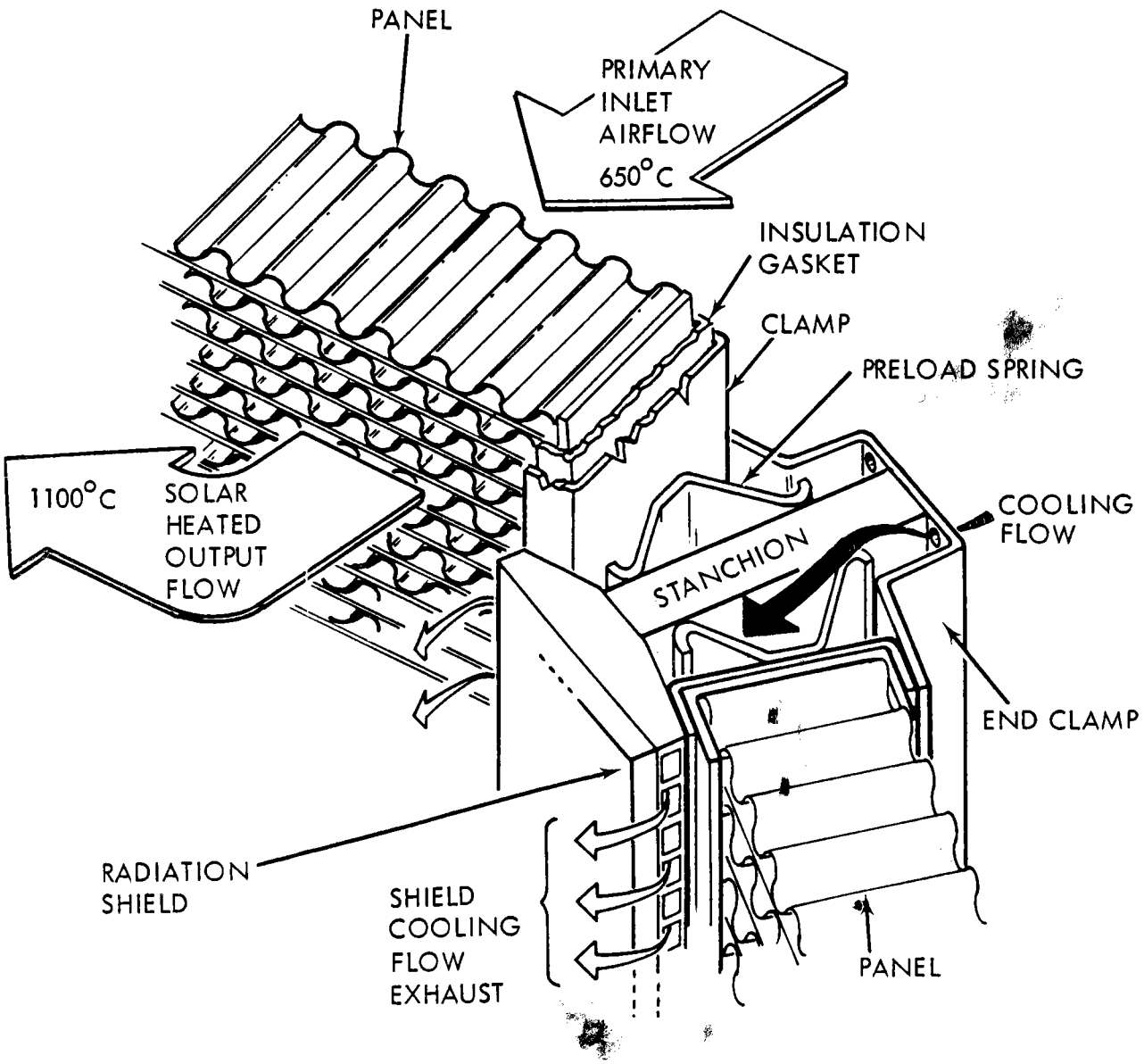

Figure 2-14. Detail of Heat Exchanger Panel Support and Airflows

Cooling is provided to the panel support components by means of bypass air. Inlet air at 650°C (1200°F) is simply diverted from the panels and flows through the panel support structure. The pressure drop through the panels provides the head necessary to drive cooling flow for the supports. This cooling technique has been rigorously analyzed with a 65 element model implementing radiation, convection, and pressure drop effects. The analysis verifies the adequacy of the cooling technique over the full range of power levels from 10% to 125% of rated conditions.

In the course of performing the 1/4 MWt solar receiver contract scalability to the utility sized (50 - 300 MWe) plant has been considered as a major design factor. Materials selected for the 1/4 MWt system are compatible with the 100 MWe system. Generally speaking, even the configuration of the components is scalable. The two exceptions to this rule are the hot pipe liners and the hot fan. In the 1/4 MWt receiver, the hot pipe liners are cylindrically formed Ceraform 2700 (1480°C) ducts with frequent expansion joints. They are 60 cm long and 30 cm ID. In a 100 MWe plant, the hot pipe is 10-12 meters in diameter; the pipe liner will consist of conveniently sized rectangular Ceraform fibrous tiles about 1 meter x 3 meters on a side. Spacing between panels will provide expansion clearance.

The solar receiver has enough intrinsic thermal capacity to withstand start up and shutdown with no special procedures required. Finite element transient analysis indicates a time constant of 5-7 minutes; near steady state conditions are achieved within 20 minutes from a step increase in insolation level. A step decrease in insolation equilibrates in about 30 minutes.

2.5 AIR FLOW AND DUCTING

In the closed loop circuit of the 1/4 MWt receiver 650°C (1200°F) air is forced through the SiC honeycomb and heated to 1100°C (2000°F).

In passing through the external heat exchanger, the air is cooled to 650°C (1200°F). The air then passes through a centrifugal hot fan and into the receiver again. Figure 2-15 shows the general configuration of the hot air circuit in the 1/4 MWt receiver.

The following parametric calculations were performed to determine the best ducting configuration in the receiver which has a low pressure drop and a low velocity through the SiC honeycomb.

The enthalpy change across the receiver is given by

$$\Delta h = c_p (T_h - T_c) - 221.6 \text{ Btu/lb}$$

where

$T_h = 2000^{\circ}F$

$T_c = 1200^{\circ}F$

c_p = (air @ $1500^{\circ}F$) = 0.277 Btu/lb$^{\circ}$F

ρ = (air @ $1500^{\circ}F$) = 0.02 lb/ft^3

Since the power (p) = 250 KWt = 14,219 Btu/min, the mass flow rate through the circuit is given by

$$\dot{m} = \frac{p}{\Delta h} = 64.16 \text{ lb/min}$$

$$= 1.07 \text{ lb/sec}$$

The average volume flow rate (Q) is given by

$$Q = \frac{\dot{m}}{\rho} = 3208 \text{ cfm}$$

Finally, the heat transfer rate (q) is given by

$$q = \dot{m} \cdot c_p \cdot \Delta T = 853{,}071 \text{ Btu/hr}$$

The frictional pressure drop (ΔP) through a pipe of circular cross section is given by

$$\Delta P = 4f \frac{L}{D} \frac{G^2}{2pg}$$

where L = pipe length

D = pipe diameter

$$G = \rho V = \frac{W}{A} = \rho \frac{Q}{A}$$

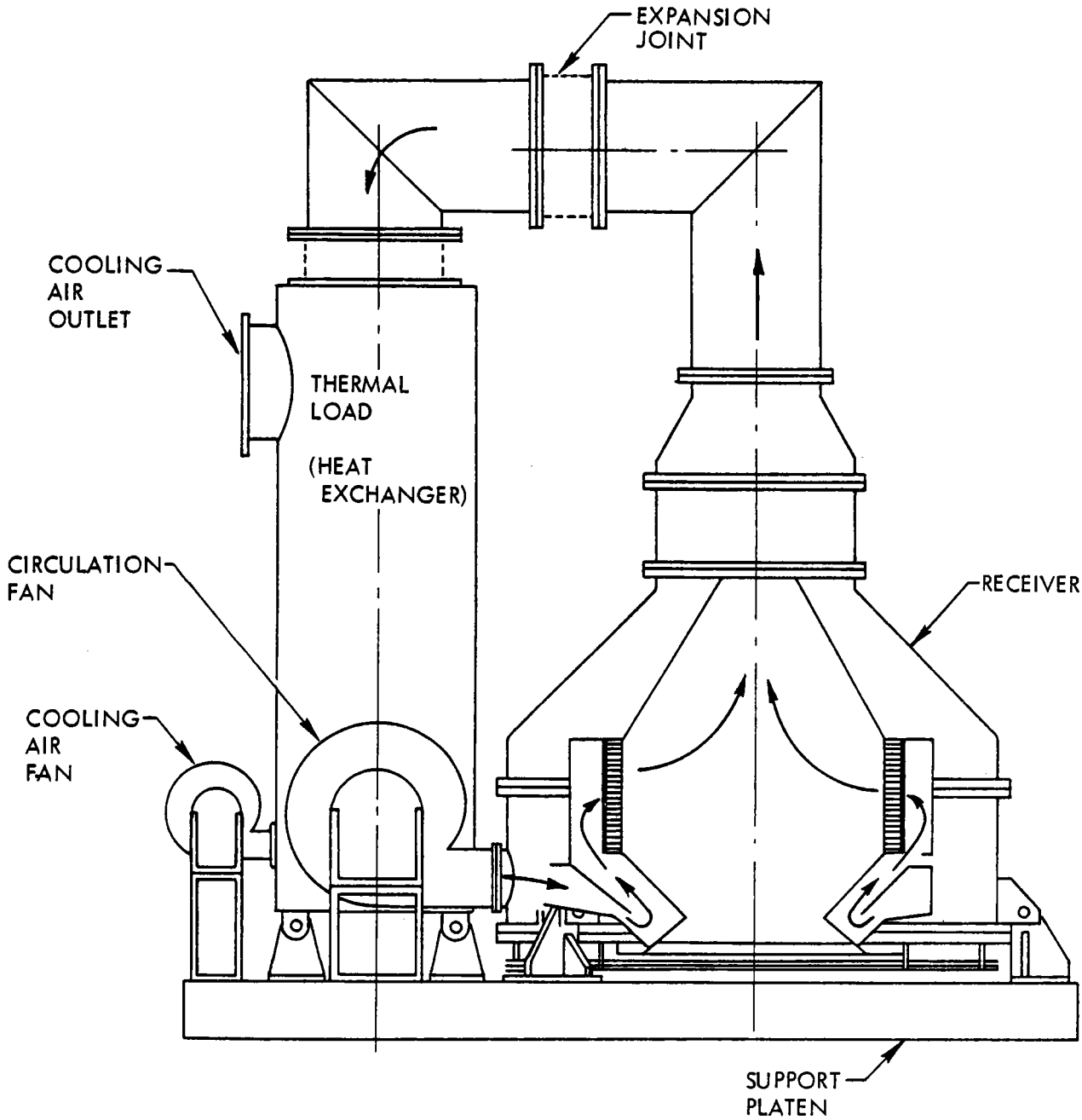

Figure 2-15. Side View of 1/4 MWt Solar Experiment (Center Tower Arrangement)

$$f = \frac{0.046}{Re^{.2}} \text{ for turbulent flow}$$

$$\left.\begin{aligned} \rho &= .0215 \text{ lb/ft}^3 \\ \mu &= .096 \text{ lb/hr ft} \end{aligned}\right\} \text{at } 650^{\circ}\text{C } (1200^{\circ}\text{F})$$

$$\left.\begin{aligned} \rho &= .018 \text{ lb/ft}^3 \\ \mu &= 0.12 \text{ lb/hr ft} \end{aligned}\right\} \text{at } 1100^{\circ}\text{C } (2000^{\circ}\text{F})$$

Frictional pressure drop within the receiver loop, which includes the ducting above the receiver, is less than 4 inches of water.

All ducting through the system was designed to minimize pressure drop (Figure 2-15). The maximum air mass velocity anywhere is less than 75 lb/sec at rated mass flow. Where heat transfer was important, such as through the silicon carbide honeycomb or the heat exchanger, the air mass velocity was held to 10 lb/sec or less. Screens were installed upstream of the silicon carbide panels to provide uniform flow through the honeycomb. Flow panels and screen adjustments were made to limit variations in air flow to less than a factor of two between the top and bottom of the panels and from panel to panel. At rated mass flow, after all flow adjustments were completed, the cold flow pressure drop across the receiver was 1.4 inches of water. The cold flow pressure drop through the honeycomb is less than 0.1 inch of water.

2.6 HEAT EXCHANGER AND FANS

2.6.1 Calculations

Heat exchanger requirements for the 1/4 MWt solar receiver are based on a peak power of 250 KWt and maximum cycle temperature drop of 450°C (800°F) (e.g. from 1100°C to 650°C). A counterflow shell and tube heat exchanger was selected to provide a heat load. The heat exchanger uses stainless steel construction with a high cooling air mass flow rate to insure a heat exchanger tube wall temperature limit of 760°C (1400°F).

A heat transfer analysis was undertaken to determine the heat exchanger requirements. During periods of maximum flux, the 1100°C (2000°F) receiver outlet air must be cooled to 650°C (1200°F). This is done in a counterflow tube and shell type heat exchanger where ambient air at 20°C (70°F) provides the required cooling.

The enthalpy change (Δh) of the receiver outlet air during the heat exchange is given by

$$\Delta h = c_p \Delta T$$

where:

$$\Delta T = 2000^{\circ}F - 1200^{\circ}F = 800^{\circ}F \ (450^{\circ}C)$$

and $c_p = 0.28$ (Btu/lb°F) at T = (1600°F)

$$\Delta h = 224 \ (Btu/lb)$$

At the maximum flux, the power output is

$$p = 250 \text{ KWt} = 14224 \text{ Btu/min.}$$

Therefore, the mass flow rate ($\dot{m}$) of air in the receiver is given by:

$$\dot{m} = \frac{p}{\Delta h} = 63.5 \text{ lb/min}$$

$$= 3810 \text{ lb/hr}$$

Finally, the heat load (q) to be removed in the heat exchanger is determined from:

$$q = \dot{m} c_p \Delta T = 853440 \text{ Btu/hr}$$

Because of the high temperatures of the receiver outlet air, it is very important to maintain the average tube wall temperature within the capabilities of stainless steel, otherwise expensive exotic

alloys would have to be used for heat exchanger construction. If maximum wall temperature is set anywhere between 700°C - 760°C (1300 - 1400°F), then sufficient quantity of cooling air must be forced through the heat exchanger to remove the heat load and exit at relatively low temperatures (Figure 2-16).

$$\text{At } T_{c\ (out)} = 340^{\circ}C\ (650^{\circ}F)$$

$$T_{max\ (wall)} = (2000 + 650)/2 = 1325^{\circ}F\ 720^{\circ}C$$

Since the maximum wall temperature is within the set limits, then

$$T_{c\ (out)} = 340^{\circ}C\ (650^{\circ}F)$$

is a suitable cooling air exit temperature

Thus, $\dot{m}_{cooling} = 6016$ lb/hr.

To provide thermal cycling and startup capabilities, the heat exchanger is also configured to add heat to the system. To heat the air in the receiver loop from ambient 650°C to (1200°F), the heat load required to raise the temperature of the 3810 lb/hr is calculated to be

$$q = \dot{m}c_p\Delta T = 1080630 \text{ Btu/hr.}$$

where:

$$c_p \text{ (at } 635^{\circ}F) = 0.251 \text{ Btu/lb}^{\circ}F$$

Therefore, a fossil fuel burner is chosen to provide the heat load necessary to raise the input air temperature from 20°C to 650°C (70°F to 1200°F). A burner downstream temperature of 815°C (1500°F) provides 165°C (300°F) thermal difference with the outlet temperature of the solar air, which is sufficient to maintain reasonable heat exchanger size. Assuming a heat exchanger effectiveness of 0.8, the combustion air outlet temperature has been determined using

$$\varepsilon = 0.8 - \frac{T_h\ (in) - T_h\ (out)}{T_h\ (in) - T_c\ (in)} = \frac{1500 - T_h\ (out)}{1500 - 70}$$

$$\therefore T_h\ (out) = 370^{\circ}F = 190^{\circ}C$$

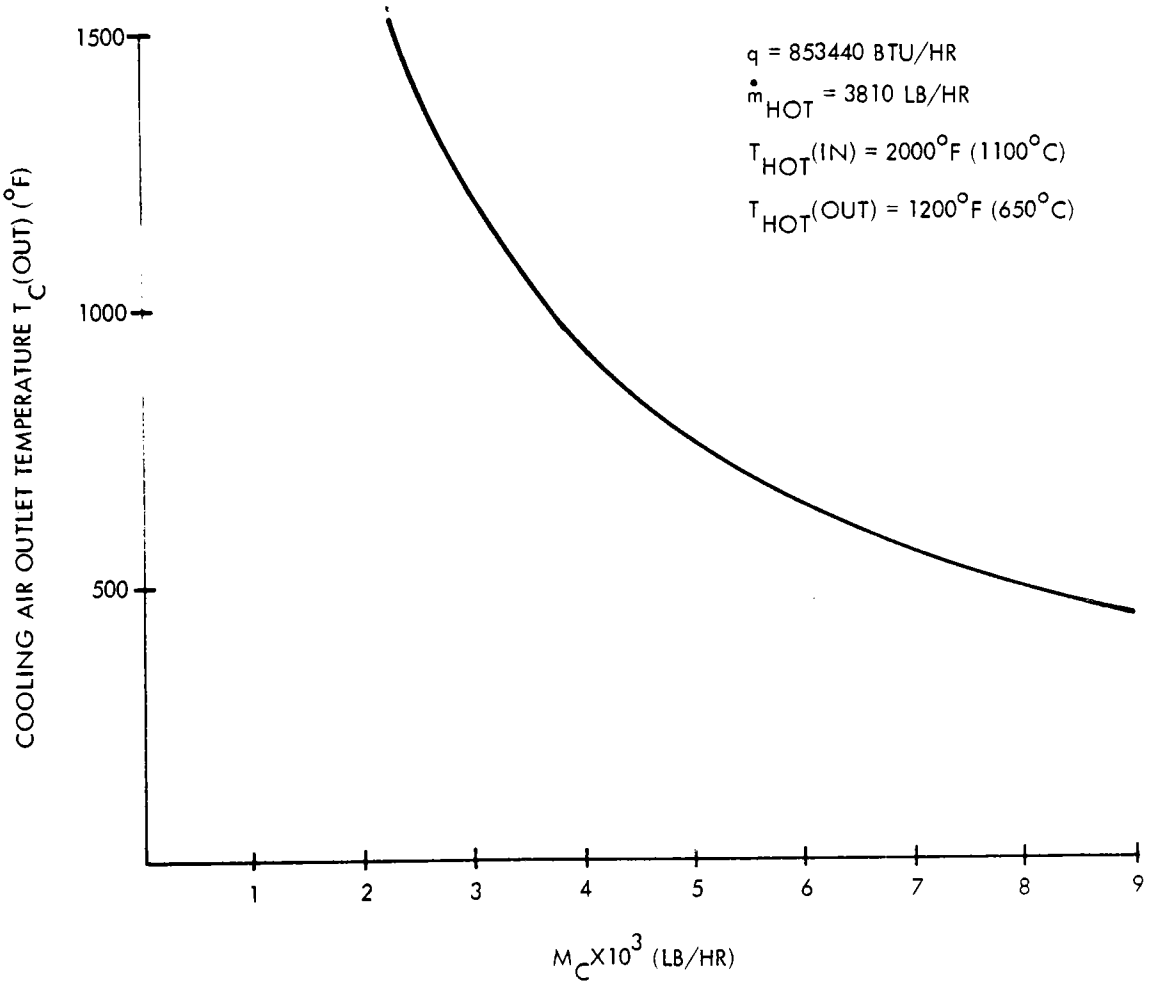

Figure 2-16. Cooling Air Outlet Temperature versus Flow Rate

Finally, the combustion air mass flow rate is

$$\dot{m} = \frac{q}{c_p \Delta T} = \frac{1080630}{0.26\ (1500-370)} = 3678\ \text{lb/hr}$$

2.6.2 Controls

A control system is incorporated in the receiver test setup to compensate for the solar flux variation during test. The purpose of the heat exchanger control mechanism is to maintain a fixed inlet air temperature. It is also possible to adjust this temperature within the range 480°C to 650°C (900°F to 1200°F). The receiver outlet temperature depends directly on the solar flux and is regulated manually by varying the mass flow rate. Most of the testing calls for establishing stable operating points and documenting performance. The burner will be used to shorten the time required to bring the equipment up to operating conditions and for checkout. The commercial equipment used to provide the auxiliary heating and cooling are described in Tables 2-7 through 2-11.

TABLE 2-7. EQUIPMENT SPECIFICATIONS AIR-TO-AIR HEAT EXCHANGER

Harris Thermal Transfer Products, Inc.

q	= 864610 Btu/hr
Heat Exchanger Heat Transfer Area	= 8.55m^2 (92 ft^2)
Overall Dimensions	= 67 cm x 85 cm x 187 cm (26-3/8" X 33-1/2" 73-1/2")
Type of Exchanger	= Shell and Tube Cross Flow Arrangement
Overall Heat Transfer Coefficient	= 7.9 Btu/hr ft^2 ^oF
No. of Tubes	= 72
Tube O.D.	= 2.5 cm (1")
Tube Length	= 1.5 m (5 ft)
Thermal Overdesign	= 33%

TABLE 2-8. COOLING FAN

Cooling Fan

New York Blower

Type - N16 P-7 1/2		
Q	=	1333 scfm at 10" H_2O
Q (available)	=	1700 scfm at ΔP = 17.7" H_2O
7.5 HP Motor	=	3600 RPM (30/440V/60 cps)

TABLE 2-9. EQUIPMENT SPECIFICATIONS GAS BURNER

Gas Burner

Pyronics, Inc.

Type - 24 XNM, Excess Air Burner

q (capacity)	=	1.5×10^6 Btu/hr
q (required)	=	1.067×10^6 Btu/hr
Q (burner air)	=	15,000 scfh = 250 scfm
Q (bypass air)	=	550 scfm
T_{max} (burner)	=	1650^oC (3000^oF)
T_{min} (burner)	=	120^oC (250^oF)
T_{max} (allowable modulated temperature)	=	815^oC (1500^oF)
ΔP_{max} (air)	=	10" H_2O
ΔP (gas)	=	4" H_2O
Q_{max} (gas)	=	1500 scfh
Q_{min} (gas)	=	50 scfh

TABLE 2-10. COMBUSTION BLOWER

Combustion Blower

New York Blower

Type - N17 P-5

Q	=	940 scfm at 21" H_2O
5 HP Motor	=	3500 RPM (3-phase/230V/460V/60 Hz)

TABLE 2-11. FANS-HOT FAN

Industrial Gas Engineering

Type - PIH-30, 75% Wheel Width.

ΔP at Hot Conditions	=	2.65" H_2O
ΔP at Standard Atmosphere	=	8.3" H_2O
Q	=	2890 cfm
Motor, 15 HP Variable Speed	=	1750 RPM
Max. Allowable Fan Speed	=	2425 RPM
HP Available to Fan Shaft at Max. Speed	=	15 HP X $\frac{1750 \text{ RPM}}{2425 \text{ RPM}}$ = 10.8 HP

2.7 INSULATION

The heat transfer (q) through a cylindrical composite wall is given by

$$q = \frac{T_i - T_o}{1/2\pi L r_1 h_i + \ell n(r_2/r_1)/2\pi L K_a + \ell n(r_3/r_2)/2\pi L K_b + 1/2\pi L r_3 h_o}$$

where,

T_i = hot side temperature

T_o = cold side temperature

L = length of wall

r = radius of cylindrical surface

K = thermal conductivity Btu/ft hr ^oF

h = heat transfer coefficient Btu/ft^2 hr ^oF

The thermal conductivity and other material properties are given in Table 2-12. The heat transfer coefficient on either side of the insulation is a function of the velocity of the heat transfer medium, in this case air, both on the inside and outside of the walls:

$h_o = 0.056\ V^{0.75}$ if $V \geq 15$ ft/sec

$h_i = 0.8 + 0.22\ V$ if ≤ 15 ft/sec

Figure 2-17 shows the simplified configuration of the receiver and the supporting structure. It is divided into two zones. The first one is below the ceramic honeycomb where entering air is at 650^{o}C (1200^{o}F) and the second one is above the ceramic where heated air is at 1100^{o}C (2000^{o}F). Finally, hot air is carried through piping, to the heat exchanger for heat removel before it enters the receiver again at 650^{o}C (1200^{o}F). Table 2-12 provides the data used in evaluating the insulation types.

TABLE 2-12. RECEIVER INSULATION PARAMETERS

	JM-23	Cerablanket
Unit Cost, $/ft^{2}in	1.30	1.50
Forming Waste Factor (Assumed)	1.1	1.5
Weighted Cost Factor $/ft^{2}in	1.43	2.25
Conductivity at 1000^{o}F K (Btu-in/ft^2 hr ^{o}F)	1.06	0.72
Cost Product $ x K ($-Btu/ft^4 hr ^{o}F)	1.52	1.62
Density (lb/ft^3)	31	8
Thickness at 3% of input heat loss (inches)	9	5
Weight (lb)	4185	600
Total Receiver Insulation Cost ($)	2316	2025
Thickness at 6% of Input Heat Loss (inches)	4.5	2.5
Weight (lb)	2090	300
Total Receiver Insulation Cost ($)	1158	1012
Thickness at 8% of Input Heat Loss (inches)	3.5	2
Weight (lb)	1627	240
Total Receiver Insulation Cost ($)	900	810

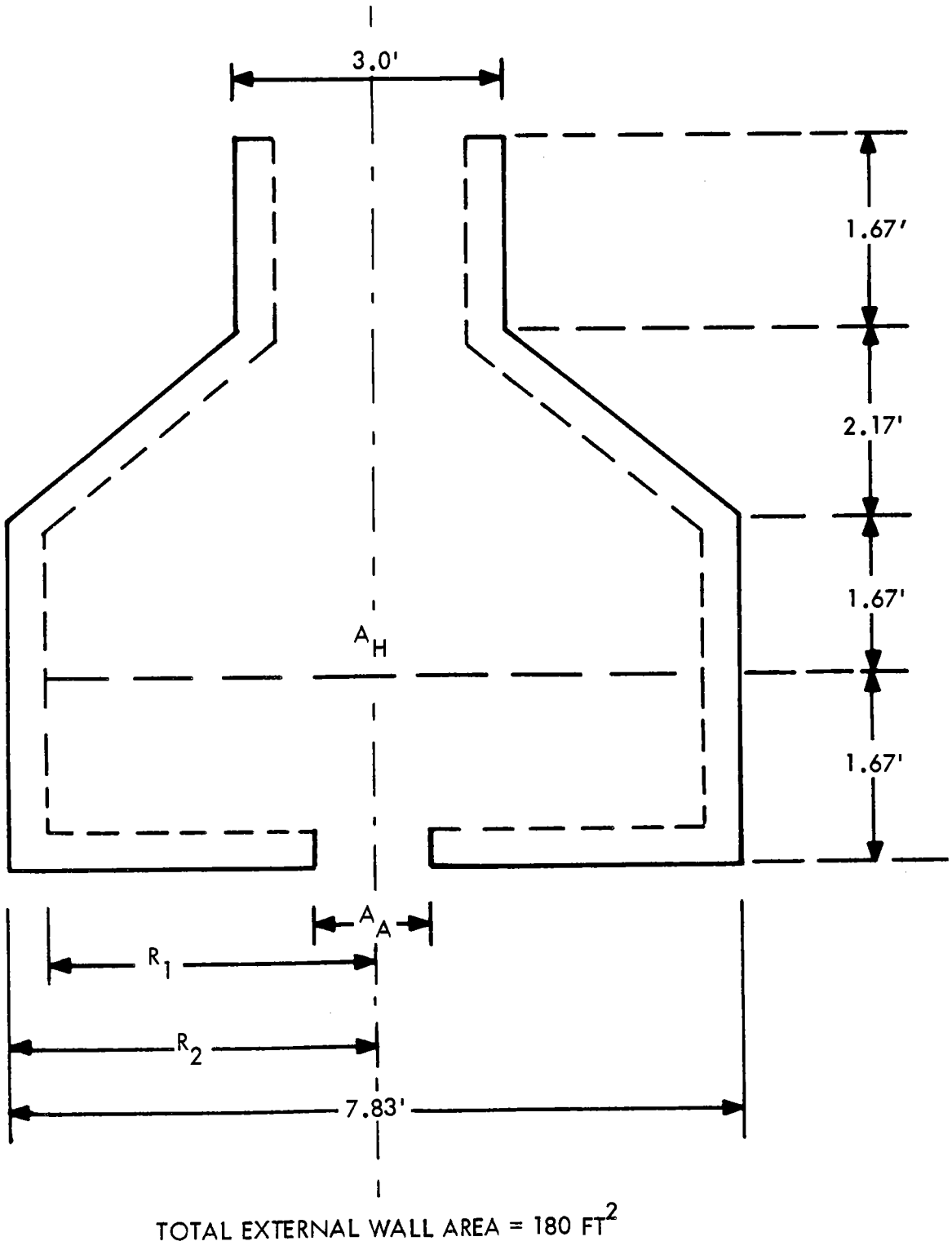

Figure 2-17. Simplified Receiver Housing Configuration

To be on the conservative side in determing the insulation thickness, the change in temperature across the wall of the receiver housing below and above the ceramic honeycomb was assumed to be 650^{o}C and 1100^{o}C (1200^{o}F and 2000^{o}F), respectively. It was also assumed that this temperature drop occurs only through the insulation without taking into account the benefit of the composite wall analysis. Furthermore, the inner and outer heat transfer coefficients have been based on 4 and 15 ft/sec of air velocity, respectively. These simplifying assumptions were used to determine the insulation heat losses under worst case conditions.

The heat loss equation was evaluated for each of the three types of Johns-Manville insulations; namely, JM-23 Firebrick, Cerablanket and MIN-K. Figures 2-18 through 2-20 represent heat loss for each type of insulation versus the insulation thickness for each of the receiver sections specified by curves A through F. The total heat loss through the receiver is also plotted to determine the overall loss as a percentage of the heat input.

For a given insulation thickness, the greatest heat loss occurs with JM-23 Firebrick and the least with MIN-K, with Cerablanket somewhere in between. If economics were not a factor in the selection process, then MIN-K would be the best choice. MIN-K costs about $140 per 18" x 36" x 1" sheet or about 31 $/ft^{2}in. JM-23 comes in 2-1/2" x 4-1/2" x 9" standard brick sizes at a cost of $900 per 1000 bricks, or 1.3 $/ft^{2}in. Finally, Cerablanket comes in sheets of 24" x 48" or 25 ft rolls in thickness ranging from 1/4" to 1-1/2" at a cost of 1.5 $/ft^{2}in.

Table 2-12 shows the parameters that would help determine the most cost effective insulation to maintain acceptable heat losses. The cost product is generally a good indicator since it relates the thermal conductivity of the insulation to its cost per unit area. Minimizing this quantity results in the optimum insulation. The table

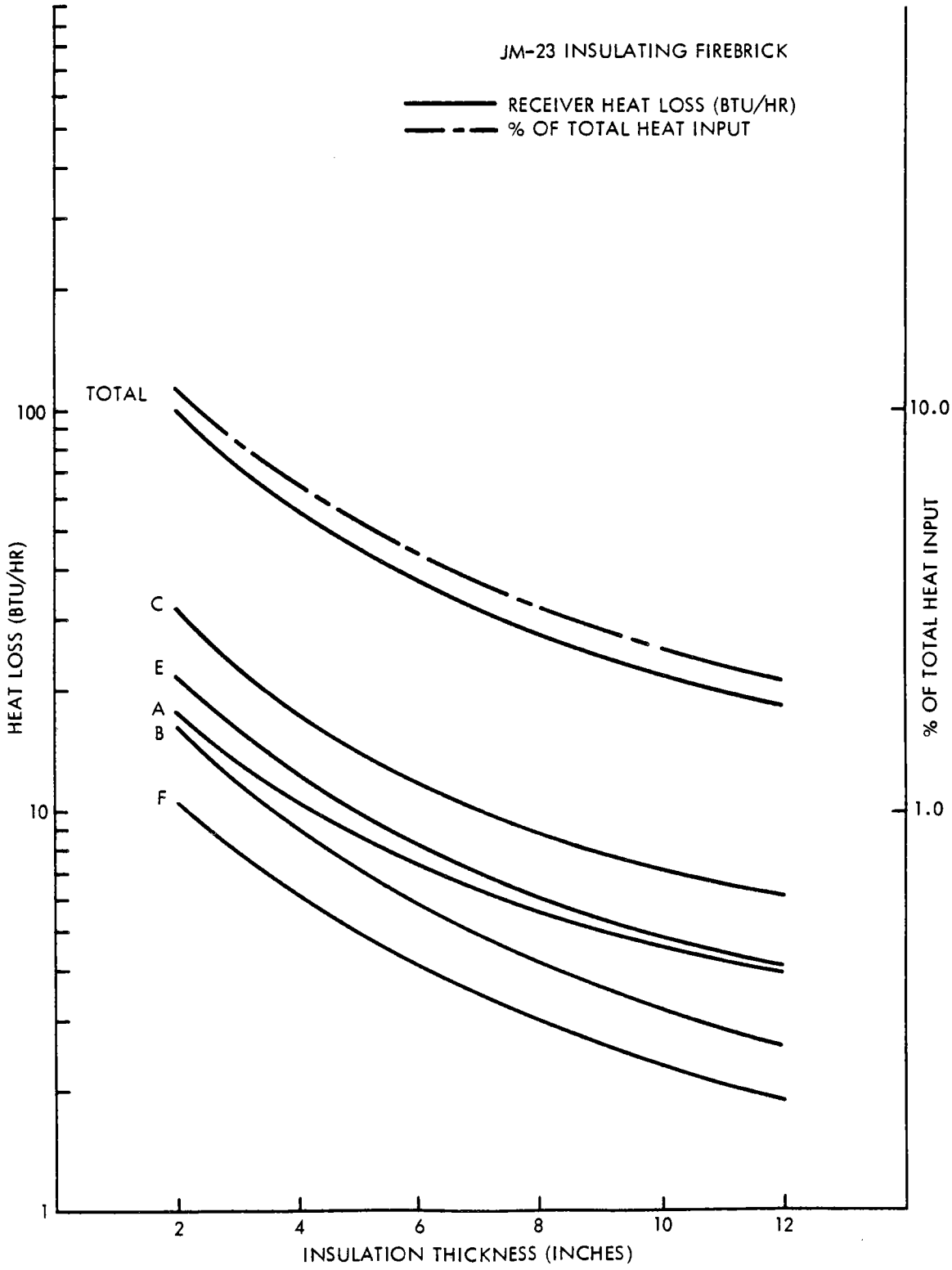

Figure 2-18. JM-23 Insulating Firebrick Characteristics

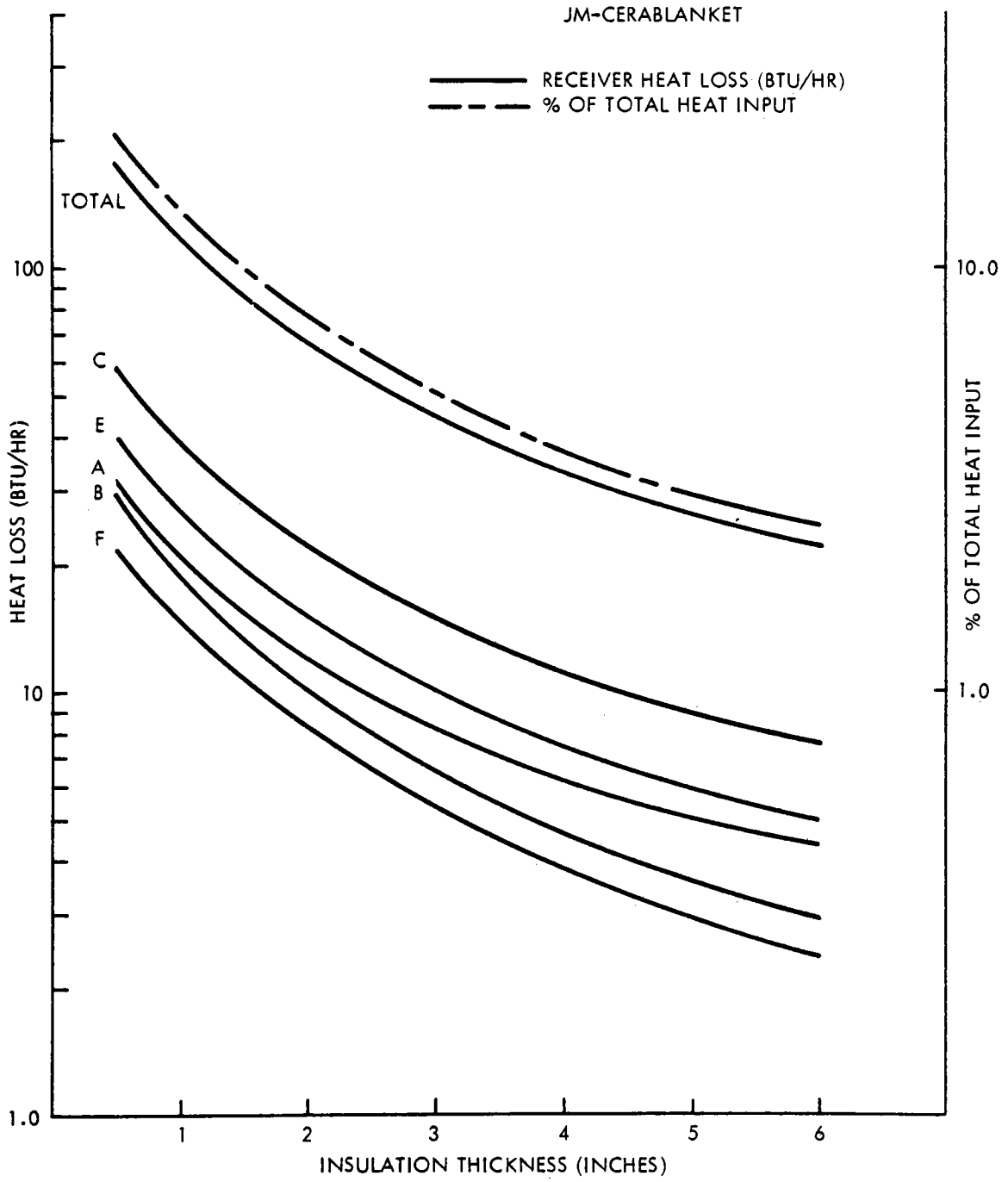

Figure 2-19. JM Cerablanket Characteristics

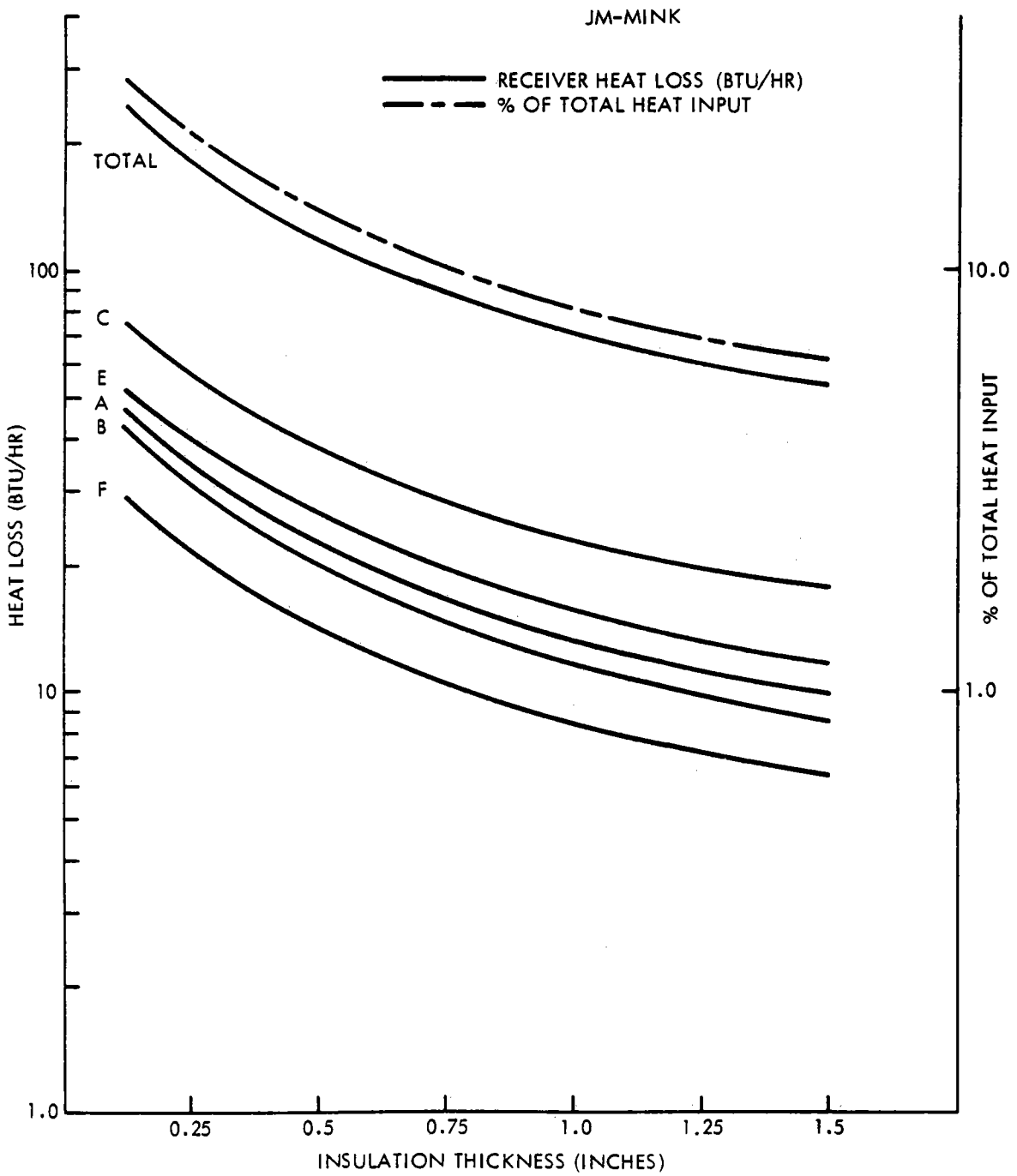

Figure 2-20. JM MIN-K Characteristics

shows that the weighted cost product of JM-23 and Cerablanket are within the same range, whereas, that of MIN-K is very high. If maximum allowable heat losses are 3, 6, or 9% of the heat input, then the table also compares the insulation thickness and the total cost of all the types analyzed. It becomes clear that with these thicknesses, MIN-K is virtually eliminated as a possible contender because of its high cost factor. The choice between JM-23 and Cerablanket is further narrowed down by the light weight and ease of handling of the Cerablanket resulting in its selection for the receiver housing insulation.

In addition to the receiver housing, the interconnecting pipes between the receiver and the heat exchanger must be insulated. In this instance the temperature difference is also assumed to be 1100^{o}C (2000^{o}F) and the heat loss per linear foot is shown in Figure 2-21 for pipe radii 38 cm to 63.5 cm (15" to 25") with Cerablanket and MIN-K as the insulating materials. Again, Cerablanket was chosen for the pipe insulation. Assuming an outer radius of 38 cm (15 in), the heat loss for 10 cm(4 in) insulation of Cerablanket is 2000 Btu/hr/ft. If the cumulative length of the pipe is 6.1 m (20 ft), then the total heat loss would be 40,000 Btu/hr or 4.6% of the heat input. Adding the percentage of receiver and pipe heat losses the final amount is about 7.6 to 8%, i.e., about 68,000 Btu/hr.

A section of the fabricated insulation ducting (Figure 2-22) contains Ceraform sections two inches thick, which have been impregnated with Cerapreg to provide a harder, abrasive-resistant surface. A metal container around the outside provides the air seal. The properties of this insulation are presented in Table 2-13.

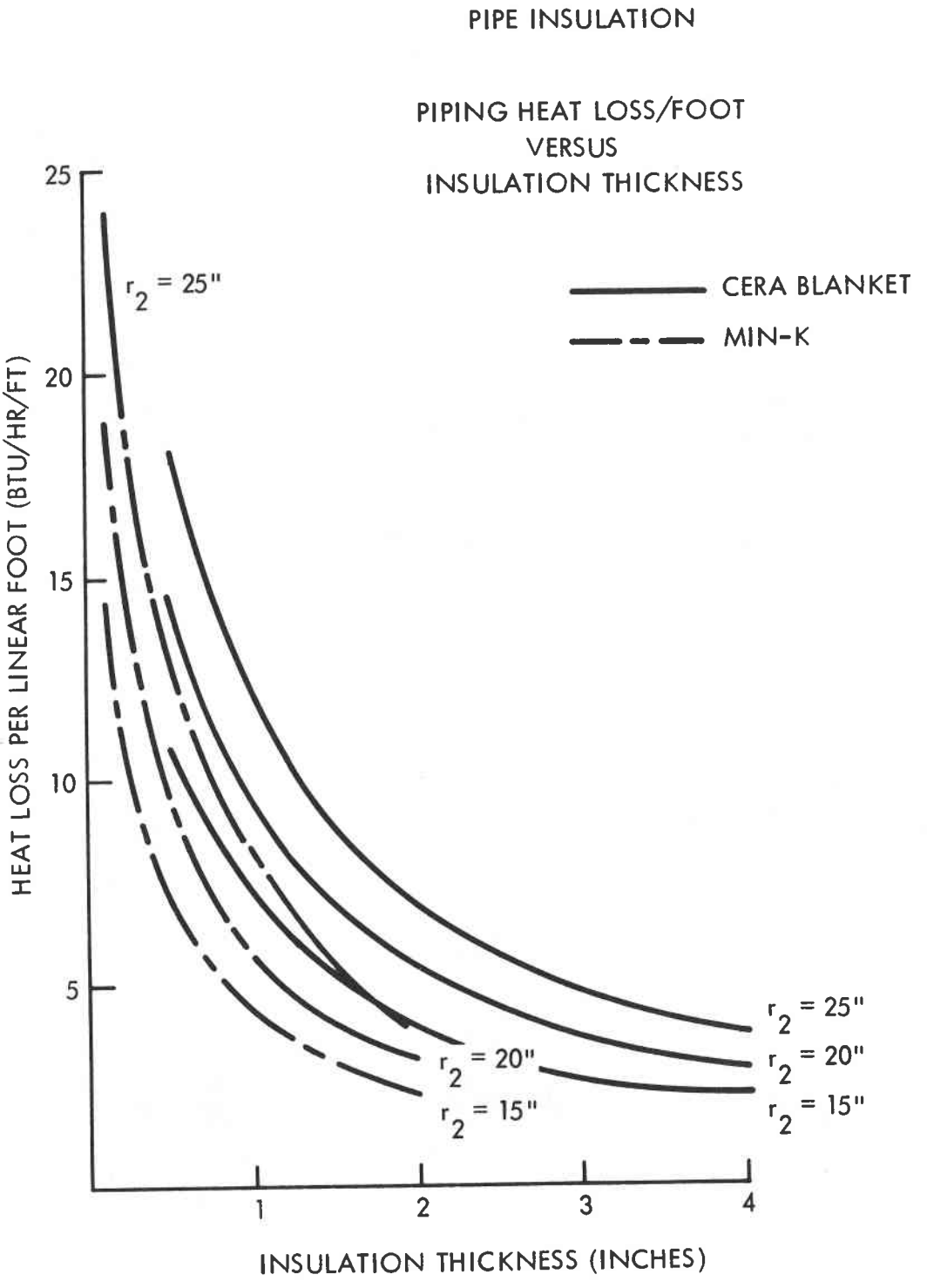

Figure 2-21. Pipe Insulation Characteristics

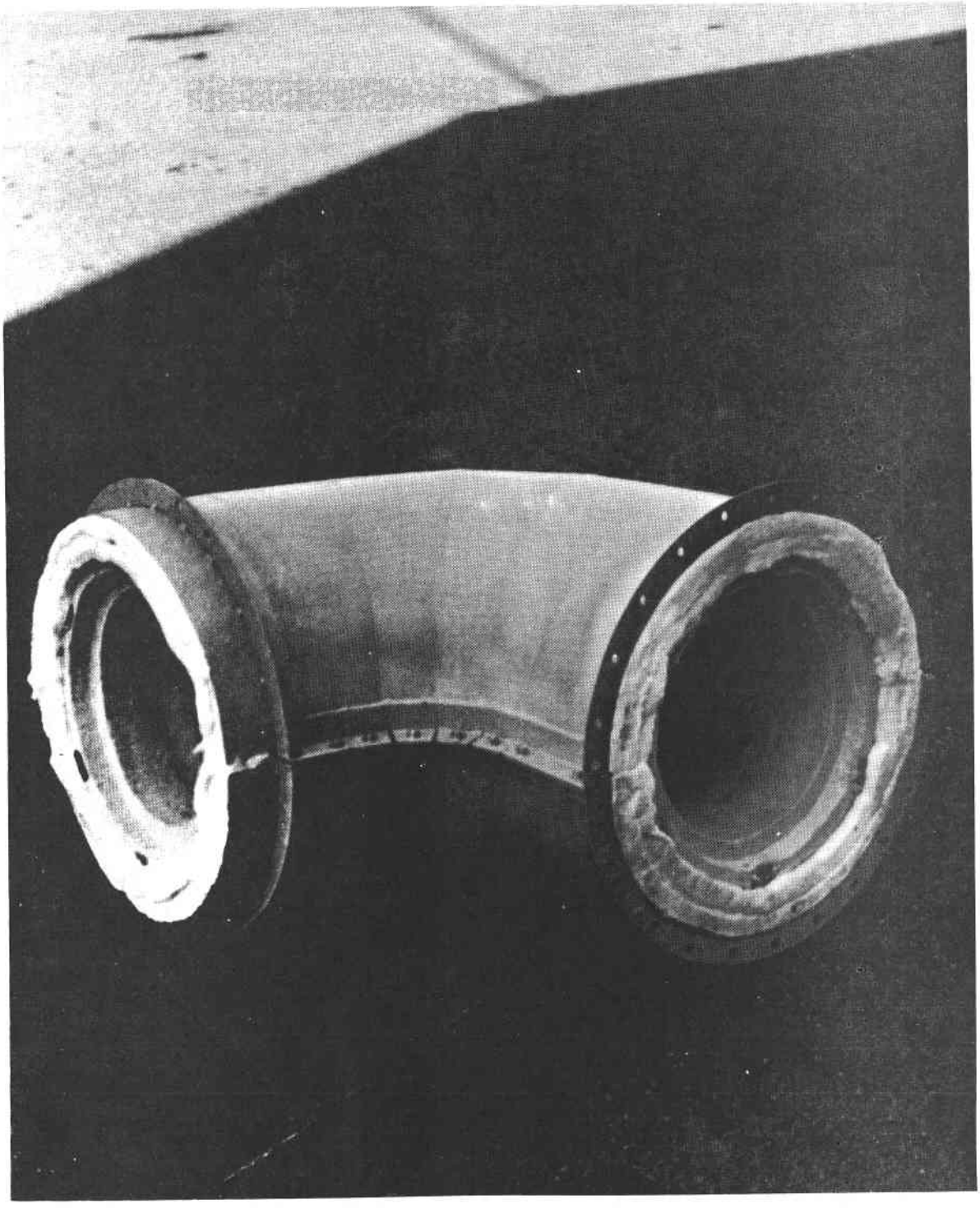

Figure 2-22. 90 Degree Ducting at Top of Receiver

TABLE 2-13. HOT PIPE LINER

Hot Pipe Liner

Type - Johns Manville Ceraform

Thickness	= 5 cm (2 in)
Temperature Limit	= 1260°C (2300°F)
Thermal Conductivity at 1000°F	= 0.71 $\frac{\text{Btu in}}{\text{ft}^2\text{hr }^\circ\text{F}}$
Linear Shrinkage at 2300°F	= 3.2%
Density	= 13 lb/ft^2
Required Quantity	= 2 elbows, 5 sleeves, 1 spacer

Liner is coated on hot side by Cerapreg to provide a harder, abrasive-resistant surface.

Inside Diameter	= 29 cm (11.5 in)

2.8 CONTROL SYSTEM

The electrical control system consists of a control console on the ground, a subcontrol chassis, burner control chassis, and various watertight boxes housing pressure transducers, power supplies, and thermocouple/transducer terminations mounted on the tower platform.

2.8.1 Control Console

The control console (Figures 2-23 and 2-24) provides all remote operational functions for the receiver and associated tower mounted equipment. It is connected by a 84m (275 ft), 80 wire cable, to a subcontrol console on the tower. The subcontrol console acts as both a distribution box for the tower platform and an electrical equipment container.

The control console has four major control panels with the following functions:

1. Tower Power Panel

    a. ON/OFF switch and indicator for 115V, 60 Hz, single phase. Used for control power and for control relays, power contactors, indicator lights, audio alarms, solenoids, and primary power to ac/dc power supplies for transducers.

    b. ON/OFF switch and indicator for 230V, 60 Hz, 3-phase. Used for blower motors and primary source for dc speed control of the hot fan.

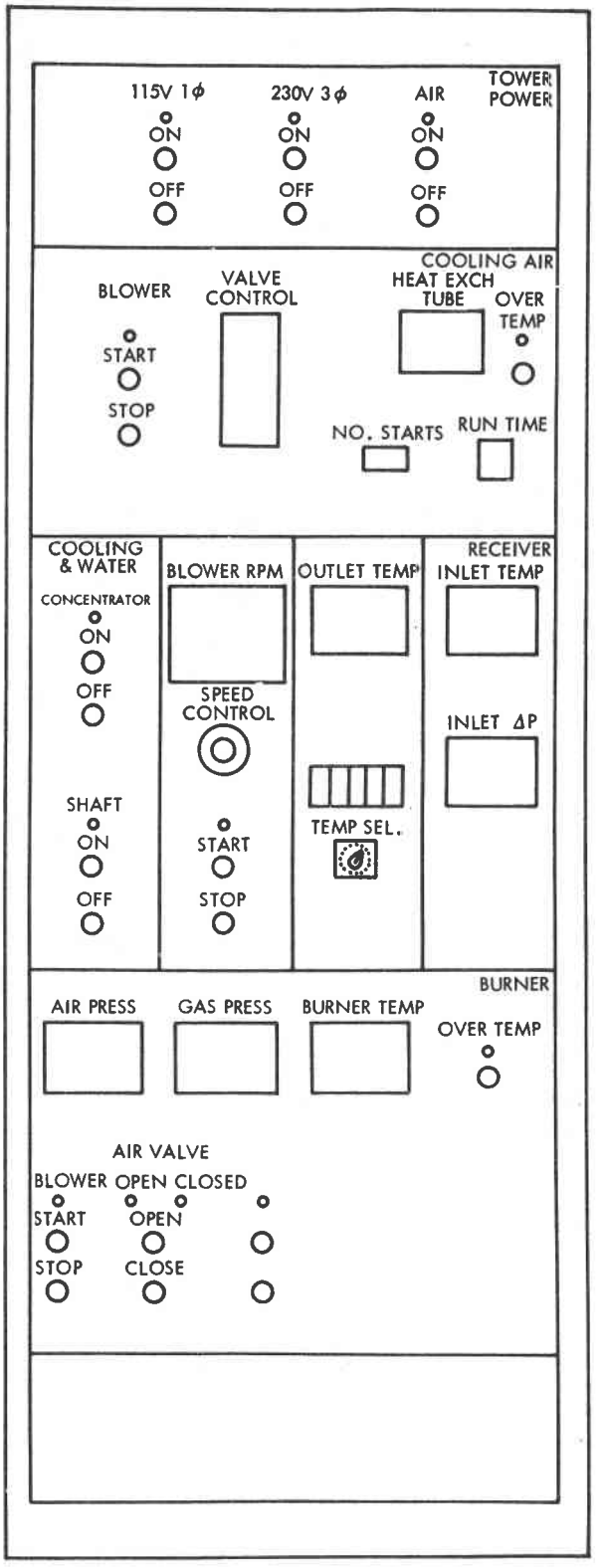

Figure 2-23. Control Console

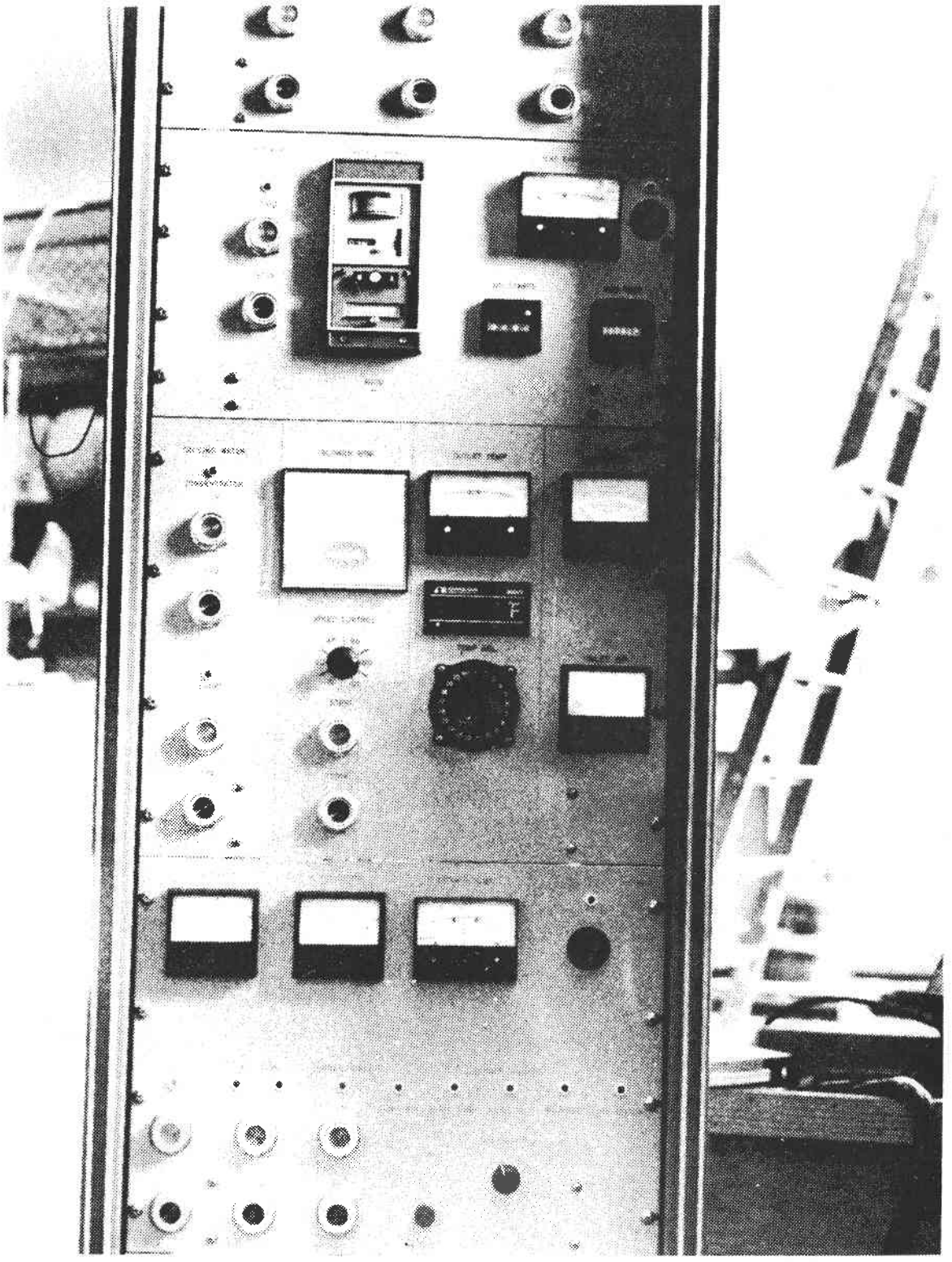

Figure 2-24. Control Console Photo

c. ON/OFF switch and indicator for air. Used as the valve operating air for both cooling blower butterfly control valve and the combustion air blower valve.

2. Cooling Air Panel

a. ON/OFF switch and indicator for cooling air blower.

b. Valve controller for controlling the butterfly valve position which varies the flow of cooling air to the heat exchanger. In the automatic mode, the controller has a thermocouple sensor located in the hot air stream and depending on the desired temperature setting will vary an electro-pneumatic converter allowing the service air to vary the position of the butterfly valve in the cooling air blower ducting. In the manual position, the cool air valve position is varied by adjusting the controller above or below the thermocouple reading.

c. A meter relay which indicates the temperature of the heat exchanger tube. There are two variable set points on this meter relay. The low set point is set at approximately 93°C (200°F) and energizes the "number of starts" counter and the running time meter. The upper set point is set to the maximum allowable heat exchanger tube temperature and at that point will energize the over-temperature alarm (audio and visual).

3. Receiver Panel

This panel is divided into four sections:

a. Cooling Water - contains ON/OFF switches for water line solenoids for both concentrator and hot fan shaft. The indicators for the appropriate flows are controlled by flow switches in the individual water lines.

b. Blower Control - contains ON/OFF switch and indicator for hot air blower. Also contains the speed control and a direct readout of the blower impeller RPM.

c. Outlet Temperature Meter and a digital temperature readout with switch for selecting 24 remote thermocouples.

d. Contains two meters: one for Inlet Temperature and the second for Inlet ΔP.

4. Burner Control Panel

The burner control panel has individual meters for measuring combustion air pressure, gas pressure (propane), and burner air temperature. The burner temperature meter is a meter relay and the high set point may be set to energize alarms at desired temperatures. The blower ON/OFF switch starts and stops the combustion air blower. The air valve control switches open or close the butterfly air valve; indicator lights are use to show its status. (Note: This is not proportionally controlled and is normally either open or closed.) The burner ON/OFF switches control the burner and a series of pilot lights indicate its status as it goes from purge cycle to combustion. If the burner does not ignite by the end of its combustion cycle, the yellow RESET switch will be lighted and is used to reset and start new cycle.

2.8.2 Subcontrol Console

The subcontrol console is mounted on the tower platform and connected to the control console by an 80-wire control cable. It contains the power supply and electronics for the hot blower variable speed drive, power contactors for 110V, 230V, and blower motor contactors.

All power, 115V and 230V supplied by GIT for system operation is routed into this console. This console also contains terminal strips for interconnection of control cable to tower platform components.

2.8.3 Burner Control Console

The burner control console is mounted on the platform adjacent to the subcontrol panel and contains the electronics and control system for the propane burner. These controls are in parallel with the burner controls on the control console (on the ground). The burner may be operated locally from this unit to aid in repair or troubleshooting.

2.8.4 Transducers

All but three pressure transducers, are mounted with their power supplies in a metal box on the south side of the platform. The other three transducers, which are used for combination air pressure, gas pressure (propane), and operating air pressure are mounted in waterproof boxes on the north side of the platform. All wiring is routed through conduit and all electrical terminations and interconnects are made in waterproof boxes.

All thermocouples, except those imbedded in the silicon carbide bricks and honeycomb supports, are sheathed, ungrounded, chromel-alumel (Type K). The thermocouples in the SiC bricks (TC-18 through TC-29) and those welded to the honeycomb supports (TC-15, TC-16, and TC-17) are glass insulated chromel-alumel (Type K).

All interconnections for all transducers are made in waterproof boxes and terminated in a large waterproof box on the south end of the heat exchanger mounting. There is a cable provided to interconnect this box to the GIT Instrument Building, where these signals go to the Data Logger.

SECTION 3
TEST PROGRAM AND RESULTS

3.1 GENERAL

The test plan is contained in Appendix II. The testing program began with hot tests of the unit at the Sanders test facility in Merrimack, NH. These tests were primarily to check out all equipment, test apparatus, and controls. During this period, the flow adjustments were made in the receiver to even the airflow throughout the ceramic honeycomb area. Temperatures in excess of 1000^{o}F were reached throughout the receiver area.

After trucking the assembly to Atlanta, Georgia, it was assembled and cycled with the burner on the ground before installing on the tower, Figure 3-1. While the receiver was being assembled on the ground, calibration tests of the terminal concentrator were conducted on the tower, Figure 3-2. The Sanders flux rake, containing 25 calorimeters, rotates ±180 degrees at a controlled rate and measures the flux throughout the receiver cavity. Comparisons of the integrated flux from the Sanders flux rake with that of the GIT flux rake located below the terminal concentrator (see Appendix IV) provides a calibration for the terminal concentrator.

In one day, a crane removed the Sanders flux rake pallet and placed the 13,000 pound receiver pallet on the tower, Figure 3-3. After several days of hookup and checkout procedures, the equipment was ready for test the last week in September. Due to the poor weather patterns in Atlanta during September, the tests were rescheduled for later in October when weather patterns were more favorable for solar testing. The test program was completed during five consecutive clear days, October 19 through 23.

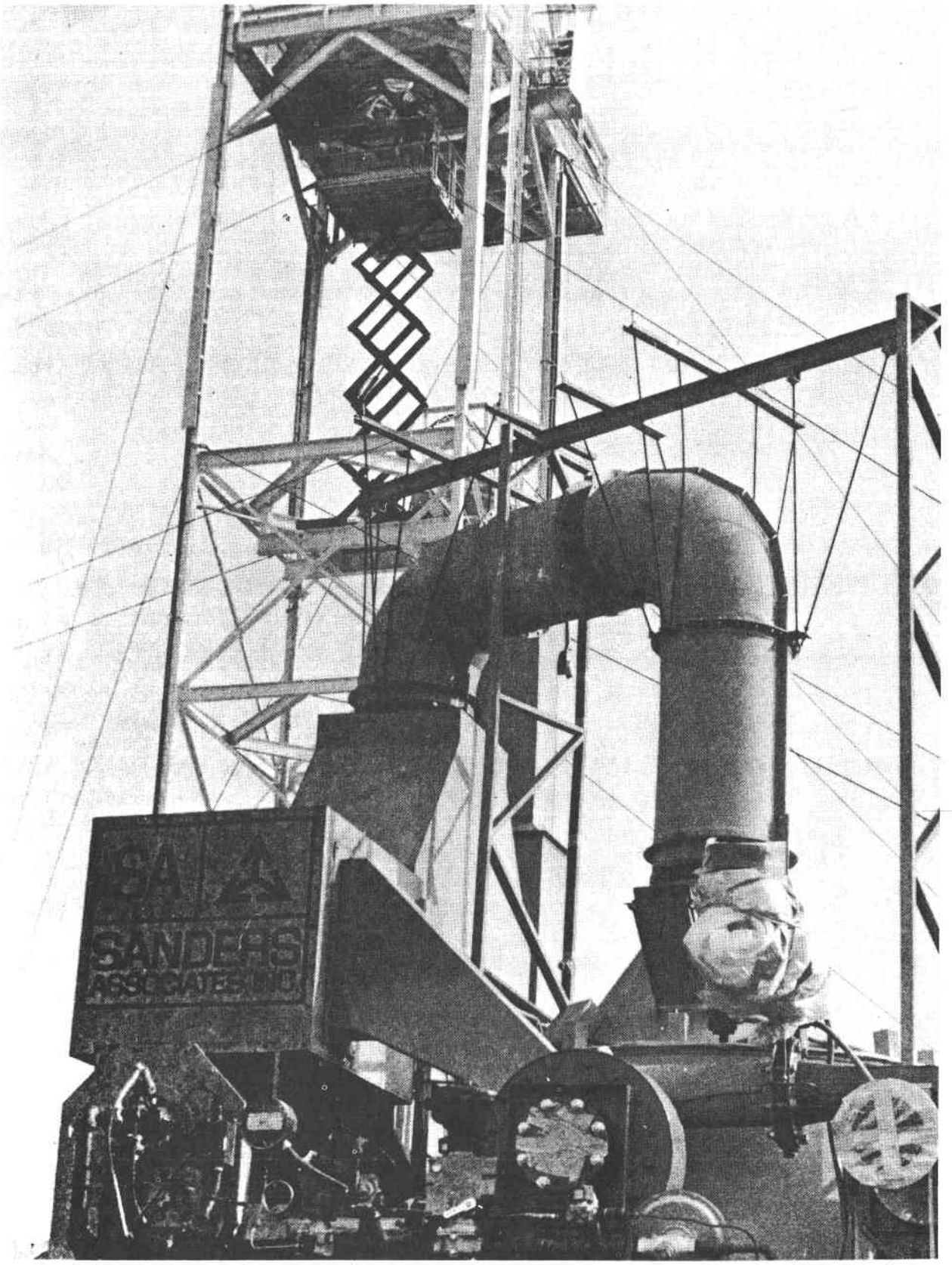

Figure 3-1. Ground Operation of Receiver Assembly Prior to Installation on the Tower

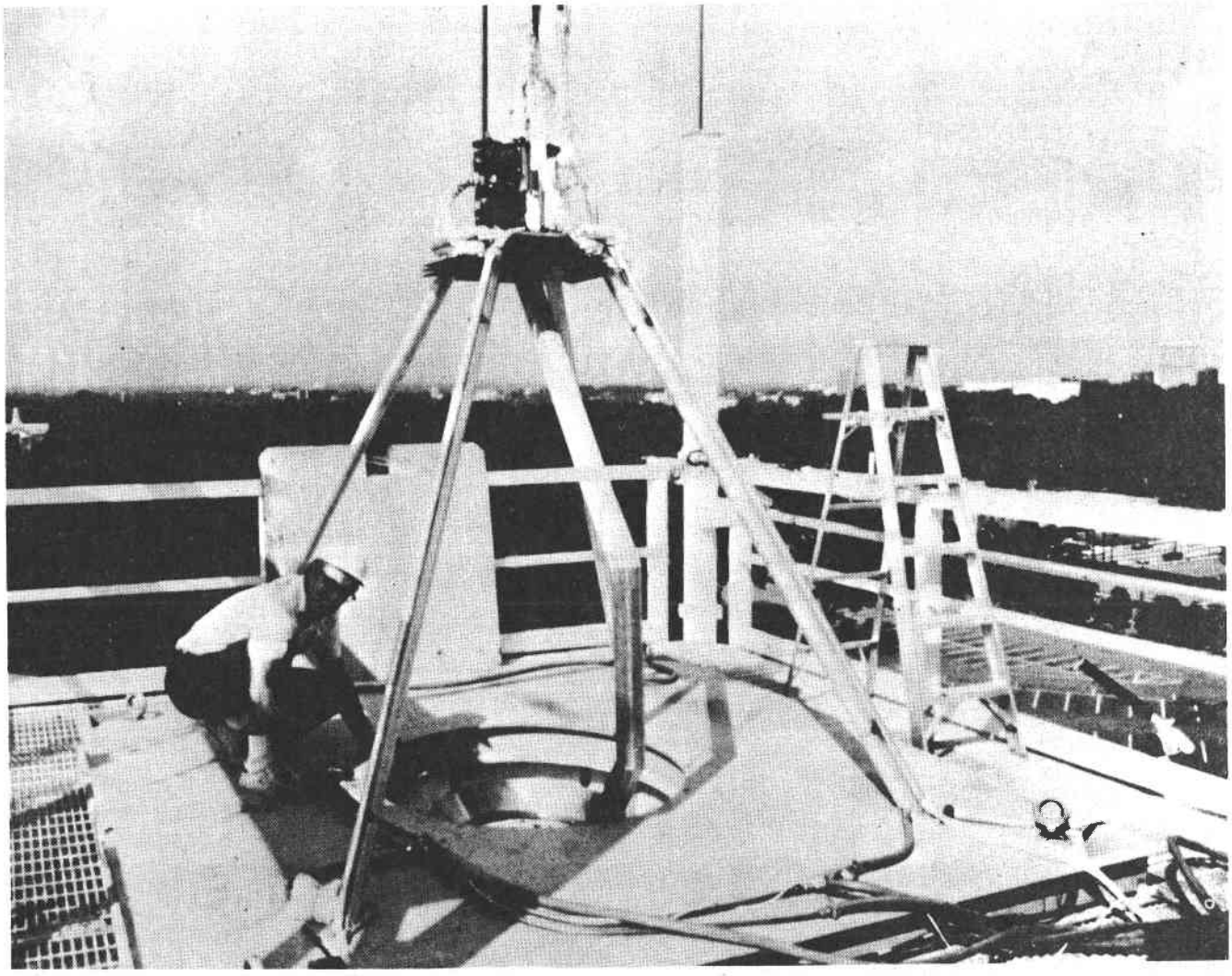

Figure 3-2. Flux Rake and Terminal Concentrator Test Equipment

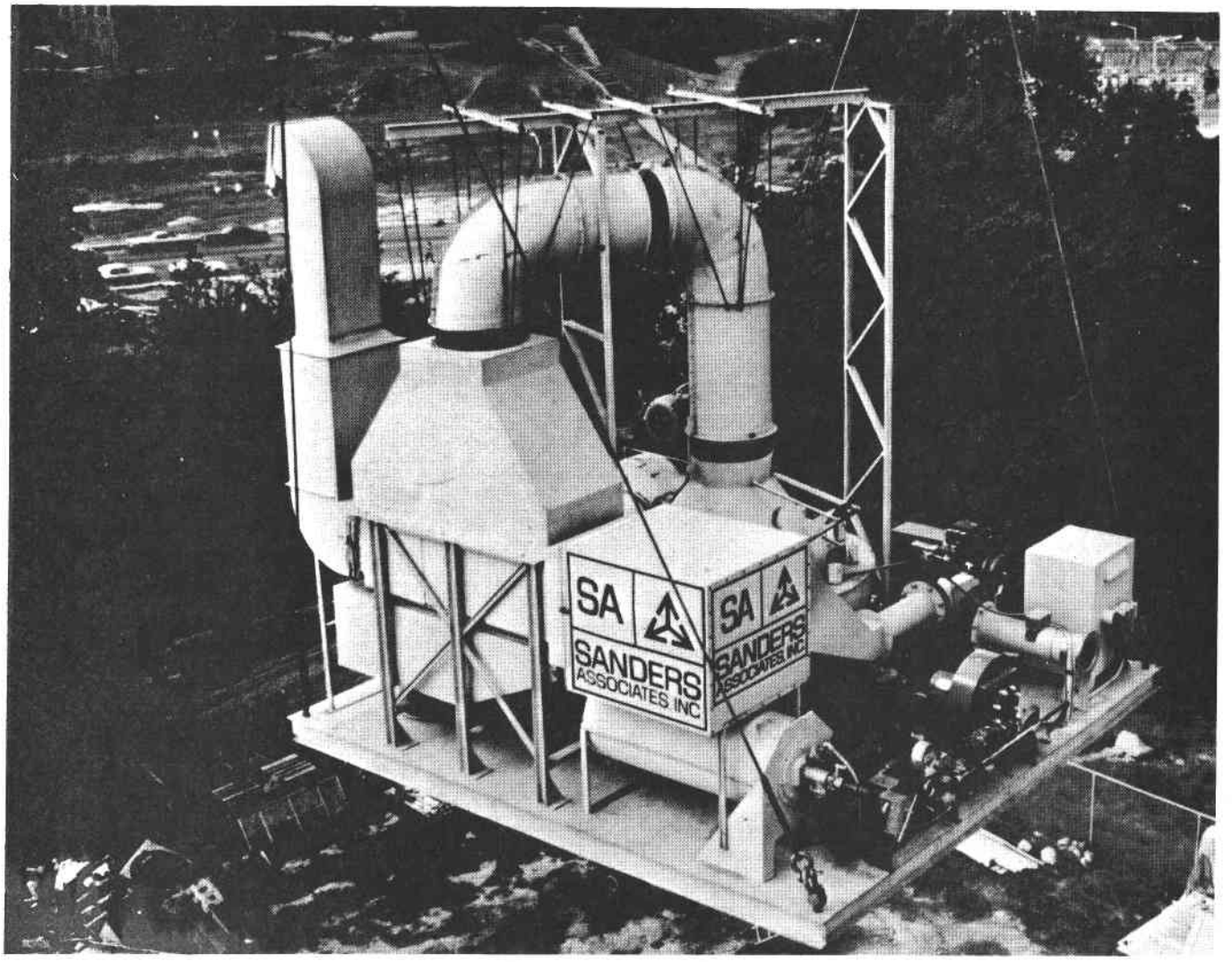

Figure 3-3. Receiver Assembly being Lifted to Tower

3.2 TEST OBJECTIVES

The five objectives of this test program were:

a. Measure the efficiency with which the receiver collects solar energy

b. Measure the convective heat loss associated with an open cavity air receiver

c. Demonstrate the scalability of the receiver concept to larger sized receivers

d. Demonstrate the structural integrity of the receiver design at air temperatures to 1100°C (2000°F)

e. Demonstrate the ability to provide constant outlet air temperature as insolation varies with time.

The test program described in Appendix II was designed to accomplish all the objectives. Receiver efficiency measurements required the measurement of both the air mass flow through the receiver and the air temperature achieved after passing through the ceramic honeycomb. The efficiency was calculated as the quotient of the heat added to the air divided by the solar energy input.

A potential problem in an open cavity receiver in the loss of efficiency due to convective heat transfer to the ambient. A special test program was conducted early in the contract to evaluate this convective heat loss mechanism (see Appendix III). These tests, simulating a hot receiver in a 25 mph wind, showed the convective loss to be 2 to 3% of the receiver output power. Additional measurements were made during the ACTF test to confirm these results. The procedure, which uses an oxygen concentration measuring apparatus and

nitrogen as a diluent gas, was developed too late in the program to be included in the test plan of Appendix II. However, it was tested during the receiver hot test at Sanders and was incorporated in the ACTF test program.

3.3 TEST RESULTS

3.3.1 Power Into Cavity

Receiver performance evaluation requires an accurate measurement of solar flux entering the receiver. The terminal concentrator, with its unknown performance, located between the receiver cavity and the ACTF flux rake, necessitated a preliminary calibration test to compare the ACTF flux rake measurements with the flux entering the cavity. Therefore, Sanders constructed a separate rotating rake located on its own test platform. The rake was designed to sweep the total internal surface of the receiver with calibrated calorimeters at the same time that the terminal concentrator and the ACTF flux rakes were in position but before the receiver unit was installed.

As reported in Appendix IV, the flux rake data was corrected for time of day and insolation. Data for both rakes as a function of time (Figure 3-4) shows average transmission through the terminal concentrator. These measurements indicated a maximum input to the receiver cavity of only 139 kW at an insolation value of 900 W/m^2, compared with the design value of 300 kW (see Table 3-1). Using the FLUXGO program to analyze the data, this low value was deduced to be due to a much lower mirror reflectivity than anticipated (0.65 versus 0.90) and a greater dispersion (11.5 mrad versus 6.6 mrad) than predicted for the ACTF. This reduced input had a major impact on the tests by limiting the mass flow and the power output at the design honeycomb temperatures of 1100°C (2000°F).

Other objectives, such as measuring the convective loss, structural and thermal stresses at 1100°C (2000°F), and the operational

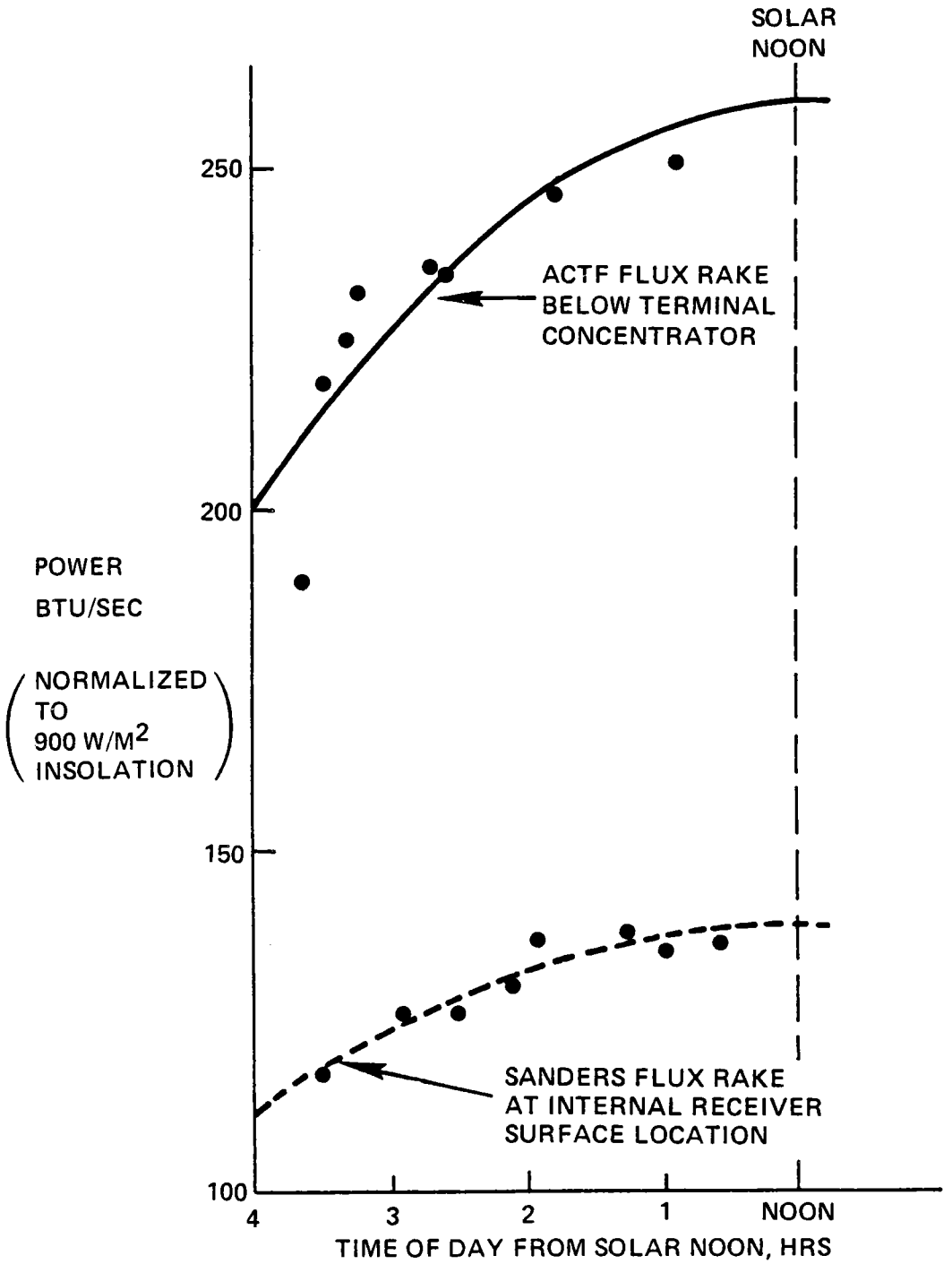

Figure 3-4. Solar Flux Passing Through Terminal Concentrator

TABLE 3-1. COMPARISON OF COMMERCIAL DESIGN WITH ACTF MIRROR FIELD

	Commercial (100 MWe)	ACTF	
	Design 950 W/m^2	Design 900 W/m^2	Experimental 900 W/m^2
Field angle (deg)	62	45	45
Sigma (mrad)	6.0	6.6	11.5
Heliostat reflectivity (%)	91	90	65
Terminal concentrator reflectivity (%)	91	91	91
Concentration ratio	2000	1600	750
Max power entering TC	362 MWt	378 KWt	260 KWt
Power passing into cavity through TC (%)	94	79	54
Max power into receiver cavity	340 MWt	300 KWt	139 KWt
Maximum collector temperature (^{o}F)	2100	2100	2100
Maximum power out of receiver	286 MWt	250 KWt	100 KWt
Receiver output / T.C. input	0.79	0.66	0.384
Receiver output / T.C. output	0.84	0.83	0.72

performance in a solar environment, were achieved during the test program. Terminal concentrator performance was adversely affected because the actual dispersion (11.5 mrad) was far greater than that for which the concentrator was designed (6.6 mrad). Therefore, the terminal concentrator was not included in the receiver performance calculations. Accordingly, a correction factor, described in Figure 3-4, was incorporated in the data analysis to account for power actually entering the receiver cavity. In this way, the receiver performance has general applicability and scalability to commercial sizes.

To explain the discrepancy between design and actual performance, Sanders made some additional computer runs with the FLUXGO code at various values of sigma and reflectivity. The first objective was to use the computer model to duplicate the flux patterns which were measured with both the GIT flux rake at a plane five inches below the terminal concentrator and the Sanders flux rake above the terminal concentrator. When the flux patterns measured by both rakes can be reproduced with the same input conditions, the field sigma and reflectivity are uniquely determined for the given set of optical parameters. This coincidence occurred for a mirror field sigma of 11.9 mrad and for an average reflectivity of 62.5%. Since the staff at ACTF had independently measured mirror reflectivity to be 63% to 68% on several mirrors, there was reasonably good agreement between experiment and simulation. Furthermore, under these conditions the terminal concentrator has a theoretical capture ratio of 49% which also agrees well with the average value of 54% derived from Figure 3-4. In summary, the actual specifications for the testing of the 1/4 MWt solar receiver, as tested at ACTF, differ from that in Table 3-1 as shown in Table 3-2.

TABLE 3-2. SPECIFICATIONS FOR SANDERS' 1/4 MWe SOLAR RECEIVER AS TESTED AT ACTF

Power Captured	139 kW
Percent Capture	49.97
Percent Retroreflection	40.80
Percent Miss	9.23%
Aperture Diameter	0.508m
Terminal Concentrator Diameter	1.4206m
Mirror Field Diameter	39.622m
Cylinder Diameter	1.27m
Aim Point Above Ground	20.3032m
Aperture Height	20.36m
Terminal Concentrator Aperture Height	20.0099m
Cylinder Height (Actual)	0.6223m
Terminal Concentrator Half Angle	52.5 deg
Roof Cone Half Angle	35.0 deg
Reentrant Cone Half Angle	37.7 deg
Sigma Deviation (Heliostats)	11.8 mrad
Mirror Reflectivity	62.5%
Insolation	900 W/m^2

3.3.2 Receiver Performance

3.3.2.1 Air Temperatures

Receiver performance data was obtained during five consecutive clear days, October 19 - 23, Figures 3-5 through 3-9, respectively. Runs were begun by using the propane burner as a preheater, then both solar heat and the propane burner were used until the maximum temperature of the solar burner was reached. At that point, all heat came from the solar input and all cooling air was shut off. Tests were made at different receiver loop fan speeds according to the objective of the test plan. For example, on October 20, the insolation was the highest of the five days and the test objective was to operate at maximum temperature. These tests were run by reducing the receiver loop fan speed to a point consistent with maintaining a safe 650°C (1200°F) inlet air temperature to the fan. During four of the five days of operation, receiver outlet air temperatures exceeded 980°C (1900°F) for a total operating time of five hours. The maximum outlet air temperature reached was 1070°C (1958°F) with an inlet air flow of 1800 CFM.

3.3.2.2 Honeycomb Temperatures

A series of 12 thermocouples, six on the front surface of the honeycomb and six on the rear, supplied data on honeycomb temperatures and temperature gradients during the test. A sequence of one minute readings over 2-1/2 hours of operation on October 20th (Figure 3-10) covers the period when the highest temperatures were reached. The highest temperature of 1190°C (2180°F) was reached at 14:00. Also shown on the figure is the fan speed and the receiver inlet air temperature as measured by the thermocouples located in the air flow upstream of the instrumented honeycomb panels. The temperature difference across the honeycomb is approximately 97°C (200°F) for a fan speed of 1000 rpm (1800 CFM) and less for lower fan speeds. As fan speed is reduced, both front and rear honeycomb temperatures increase and the inlet air temperature decreases because of conduction losses in the ducts.

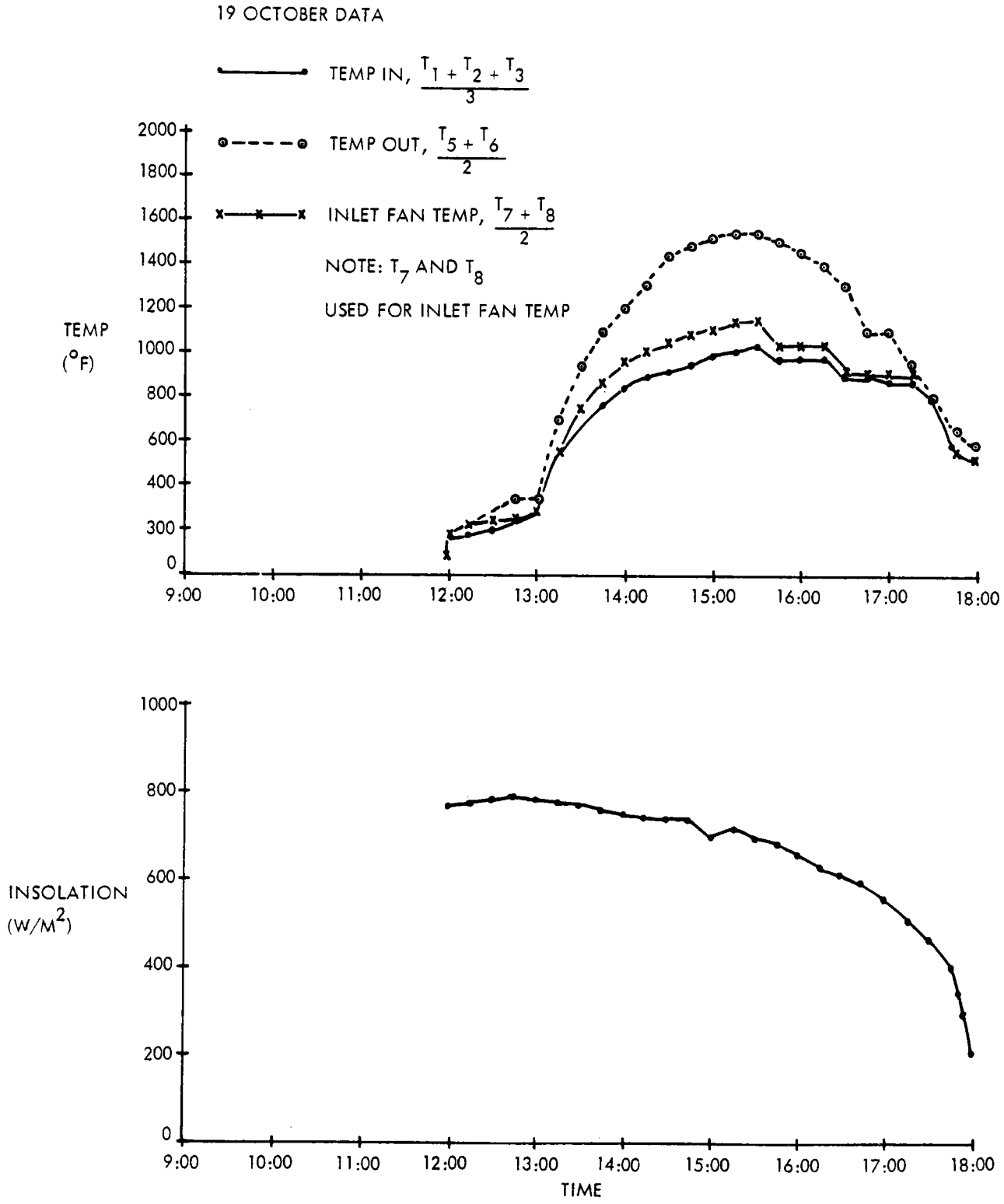

Figure 3-5. Test Data 10/19

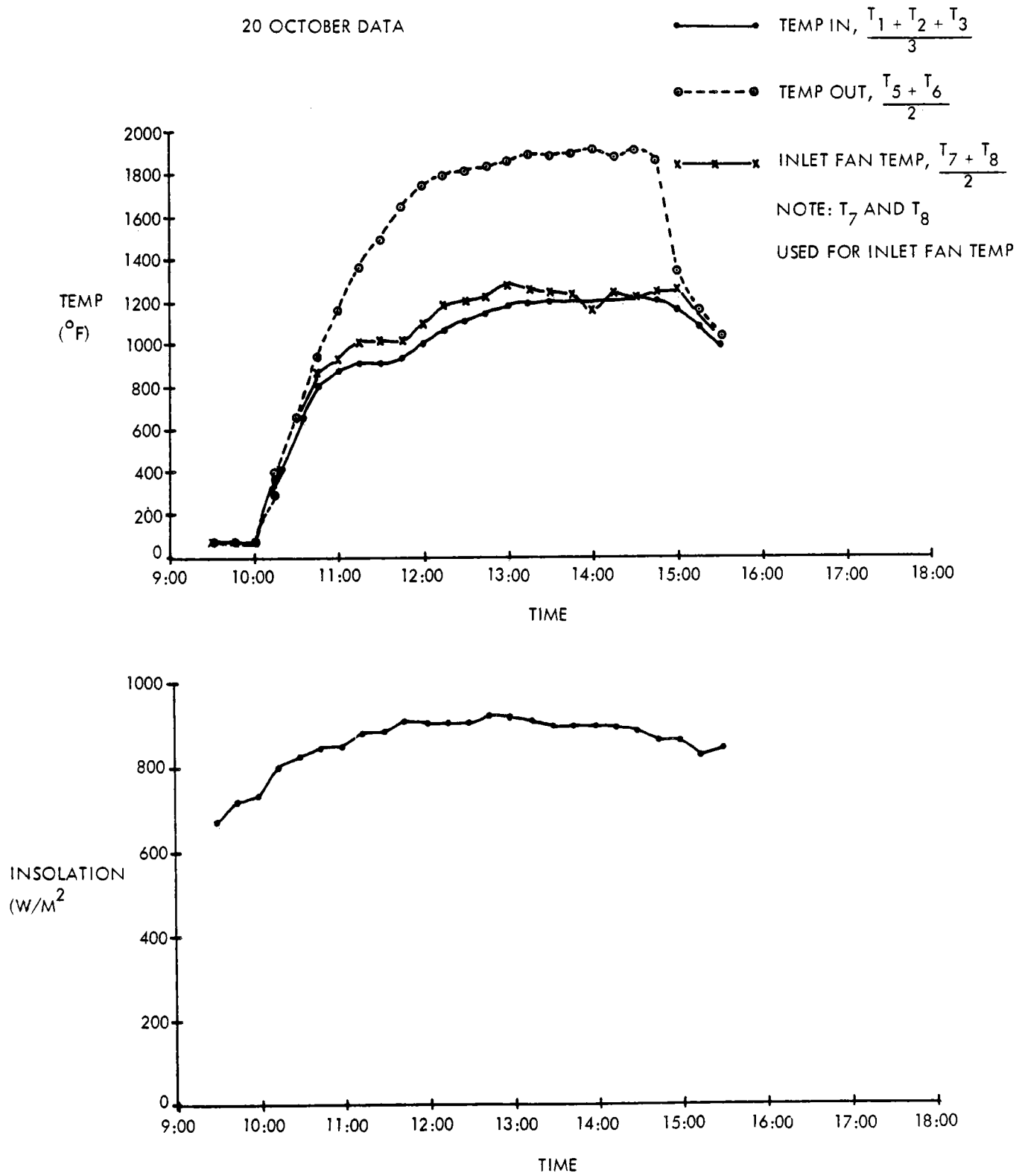

Figure 3-6. Test Data 10/20

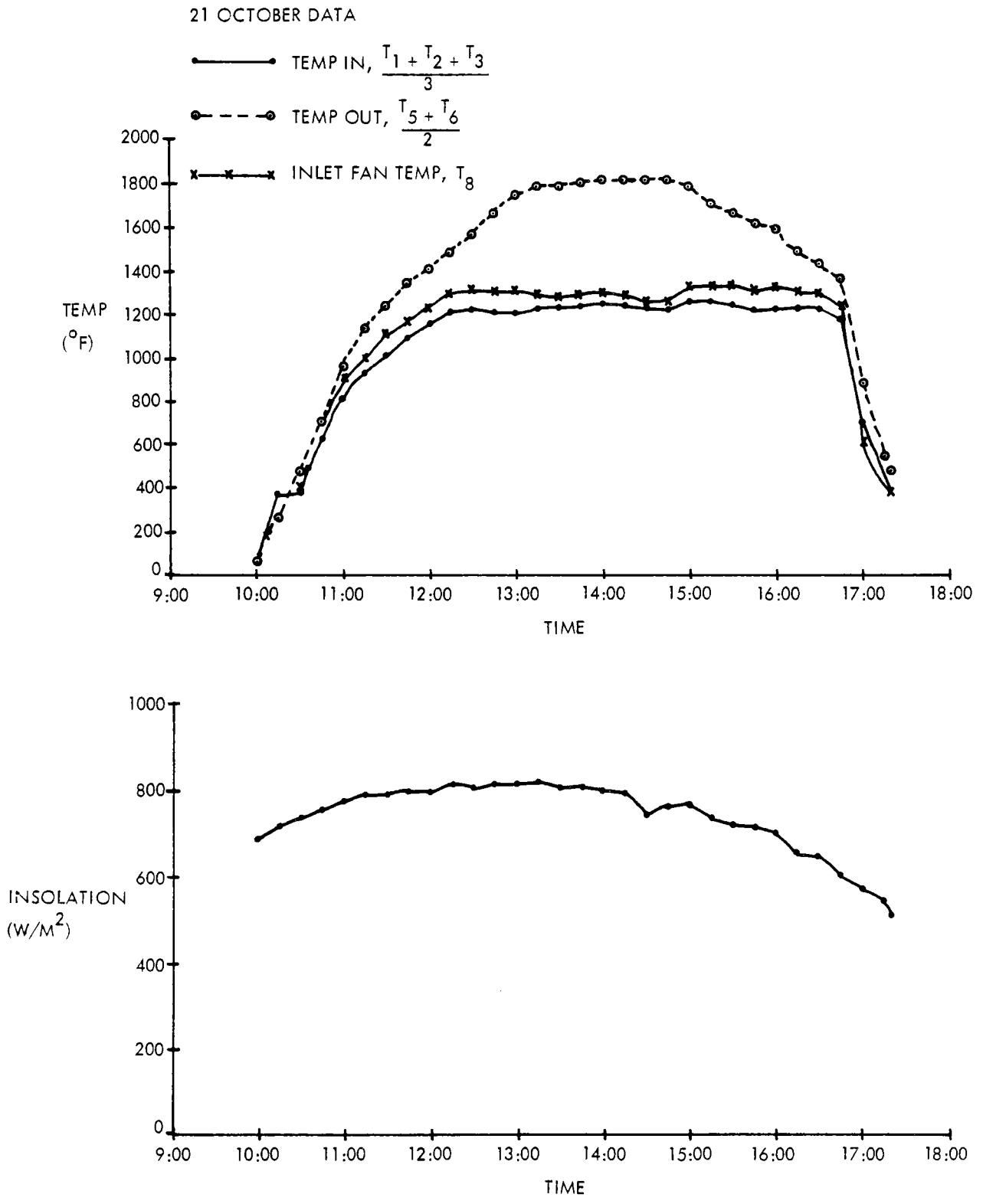

Figure 3-7. Test Data 10/21

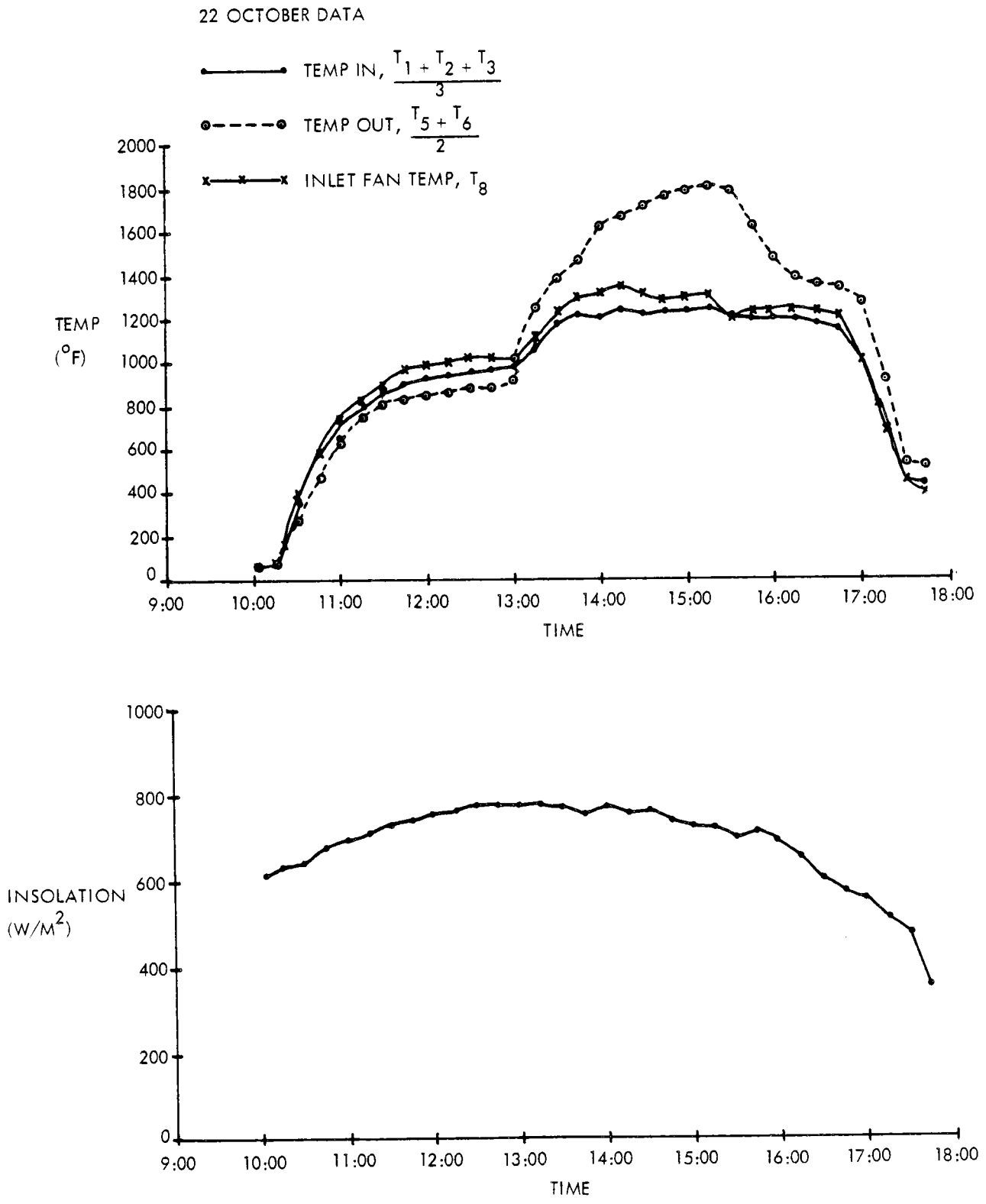

Figure 3-8. Test Data 10/22

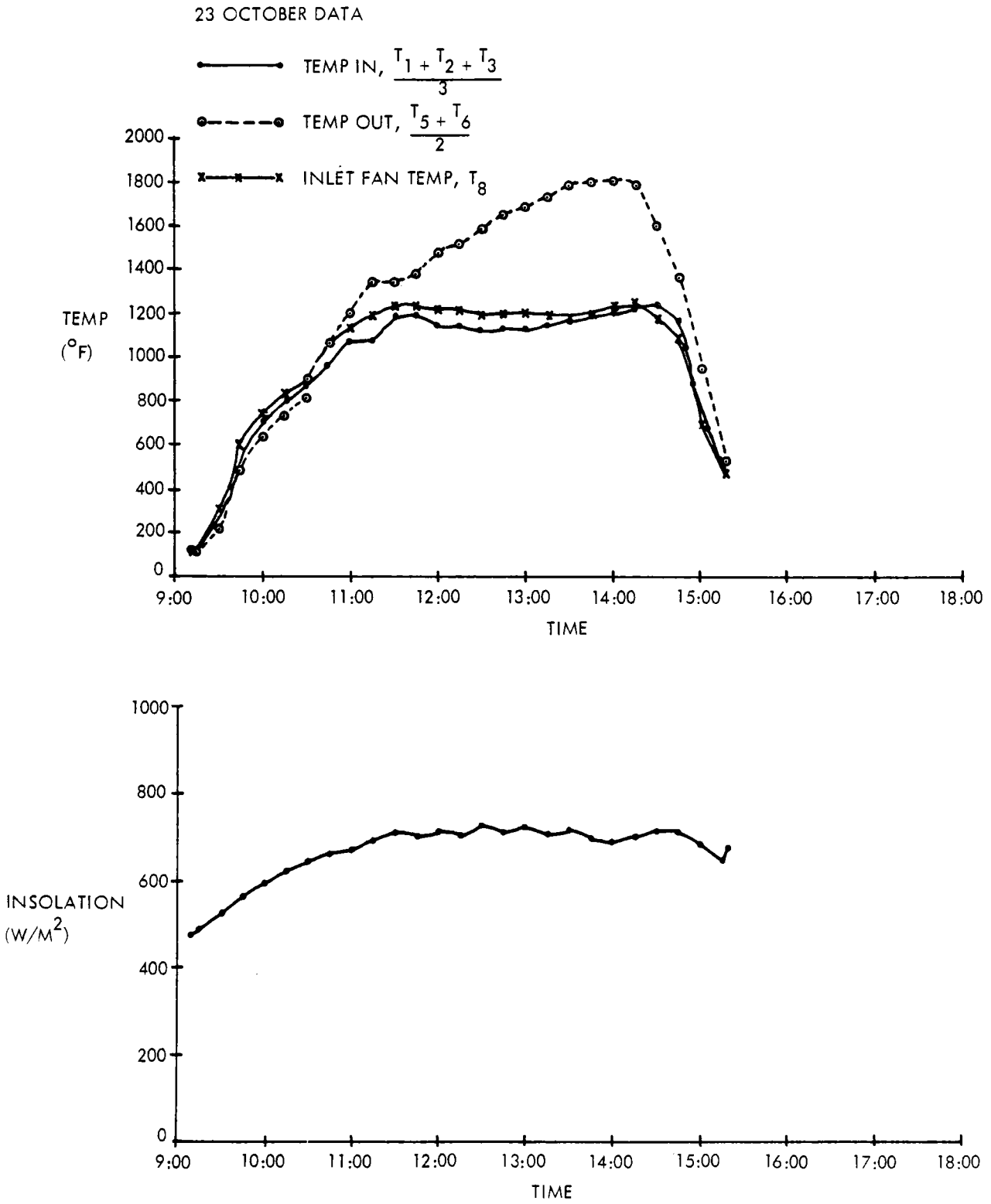

Figure 3-9. Test Data 10/23

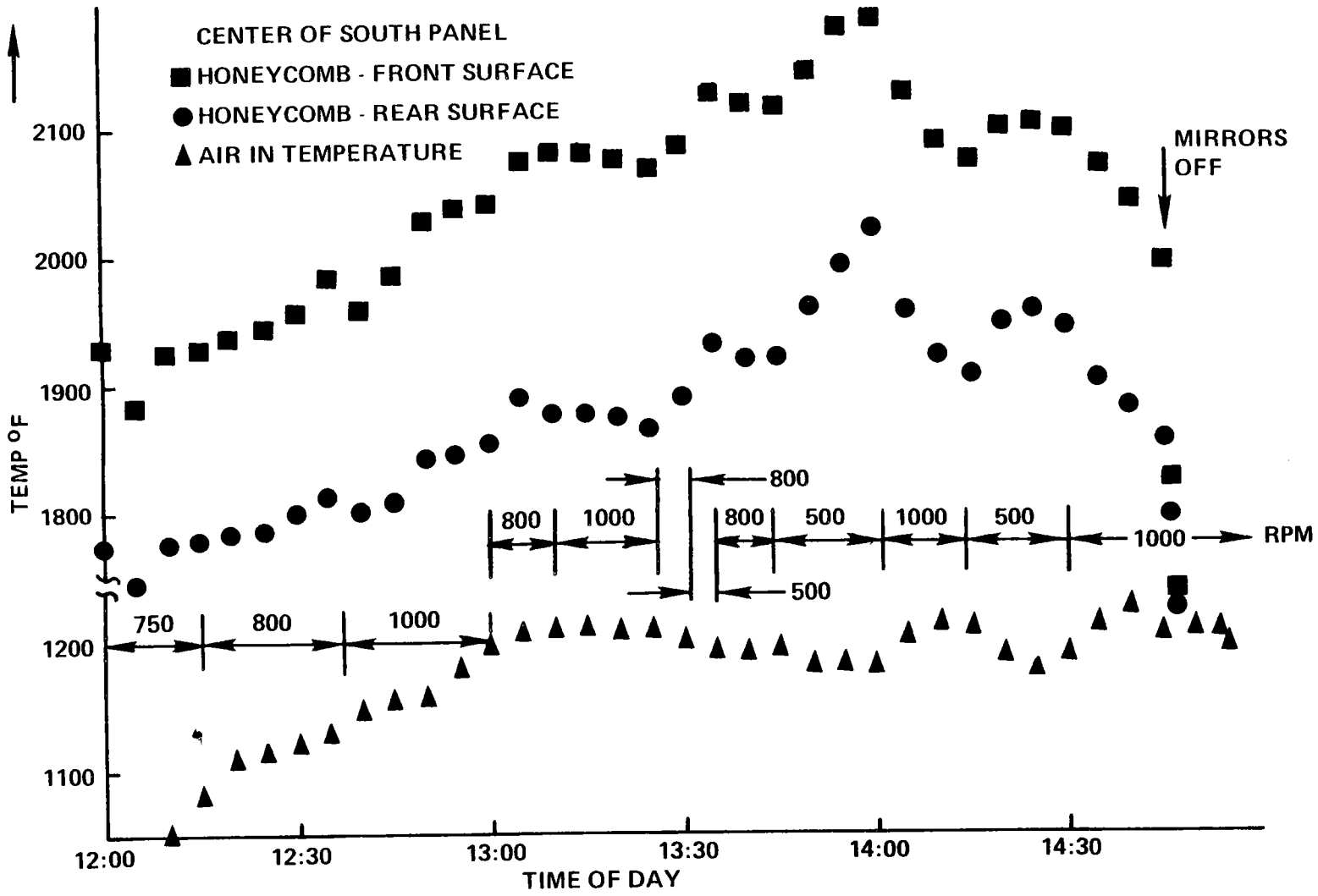

12078-59

Figure 3-10. Typical Receiver Temperatures

A second sequence of temperatures representing the honeycomb front and rear surface immediately after scramming the mirror field and removing flux from the receiver is shown in Figure 3-11. Within one minute of system shutdown (including all fans), the honeycomb cross section is nearly uniform in temperature and the air temperature above the honeycomb has decreased below the maximum temperature of the honeycomb parts. After ten minutes, an approximate drop in temperature of 220°C (400°F) was observed.

3.3.2.3 Mass Flow

The instrumentation for measuring air mass flow was designed to provide an accurate duct profile of dynamic pressure at design mass flow at a position located at the end of six diameters of a straight section, and positioned one diameter ahead of the hot fan. For the higher rpm (1800 and above) this instrumentation worked well; but for lower values of rpm, the flow was too low to measure accurately. To improve the accuracy of the data at reduced rpm, the standard air mass flow was plotted versus fan speed (Figure 3-12). This curve was used with air temperature and rpm to obtain mass flow.

3.3.2.4 Heat Flow

The net heat added to the air flowing through the receiver cavity was determined, as described in Appendix II, by subtracting the total enthalpy of the air entering the receiver from that leaving the receiver. When these calculations are made under stable temperature conditions, no accounting should be needed for heating or cooling of receiver components. Examples of stable operating points from 10/22 and 10/23, Figures 3-13 and 3-14, were selected for further analysis. Each sequence shows a minute by minute record of receiver and hot fan air temperatures on one scale and the measured insolation on another scale. During a one hour sequence in Figure 3-13, two ten minute periods are indicated during which the ACTF rake made a traverse across the terminal

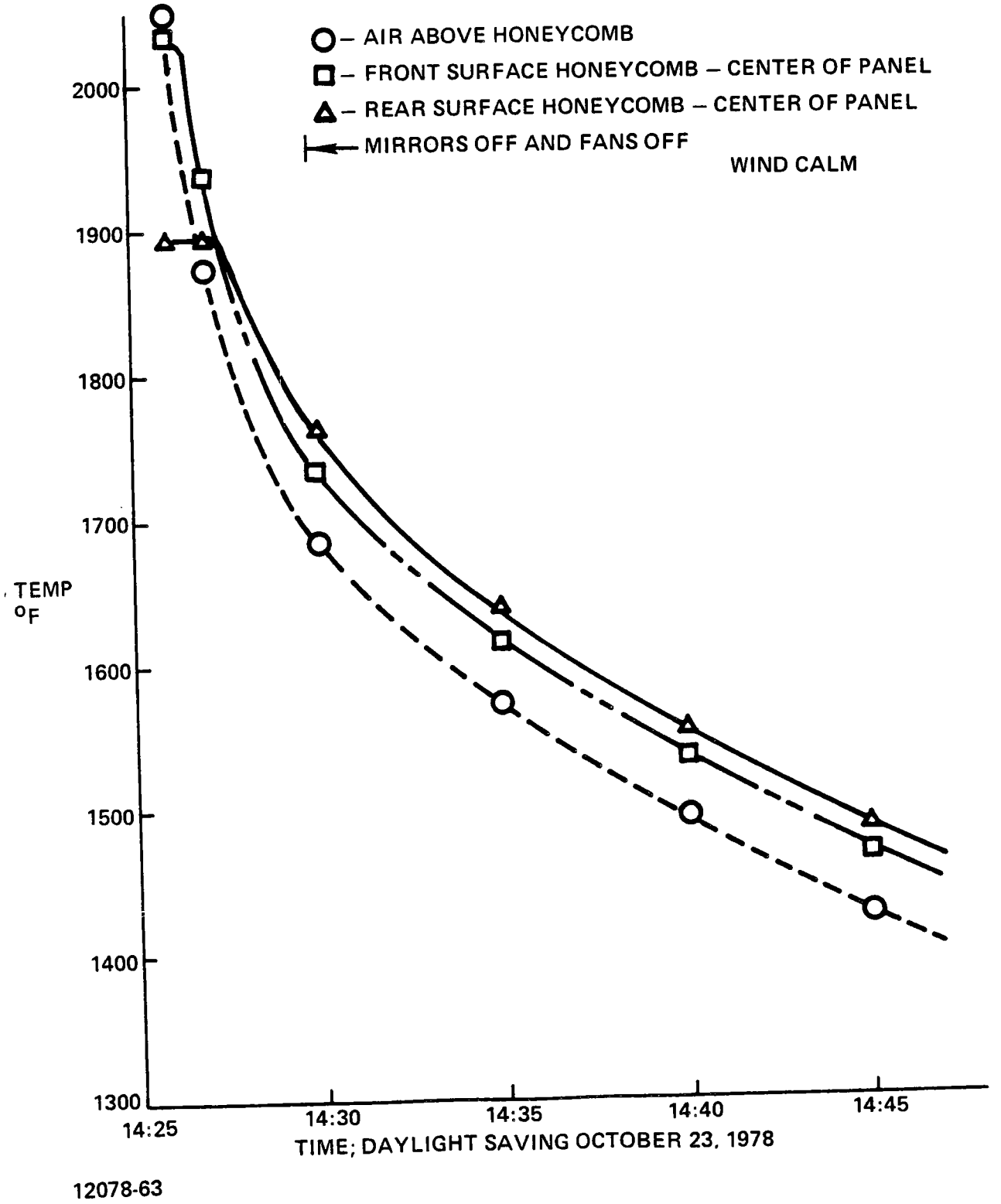

Figure 3-11. Honeycomb Cooling

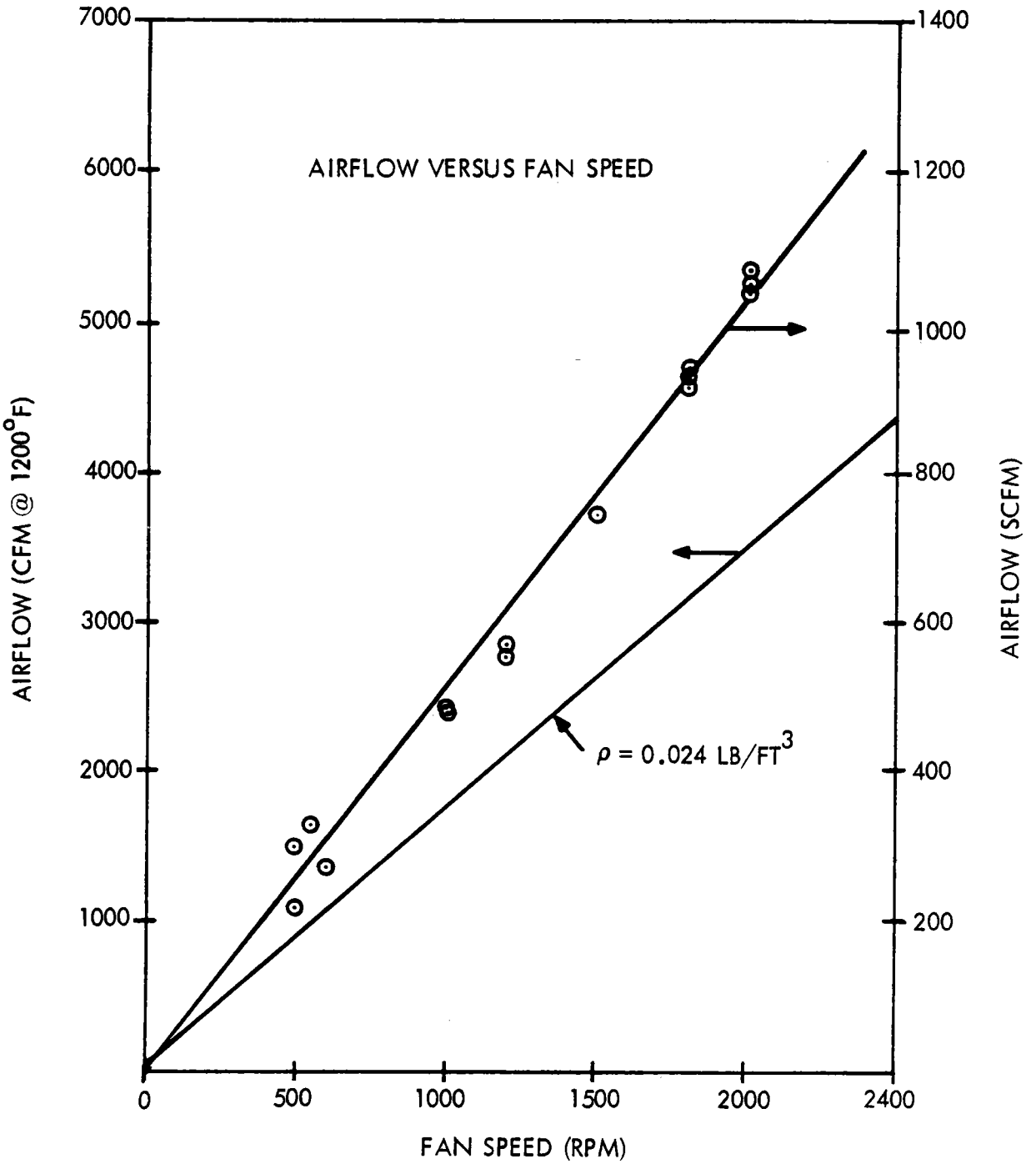

Figure 3-12. Airflow versus Fan Speed

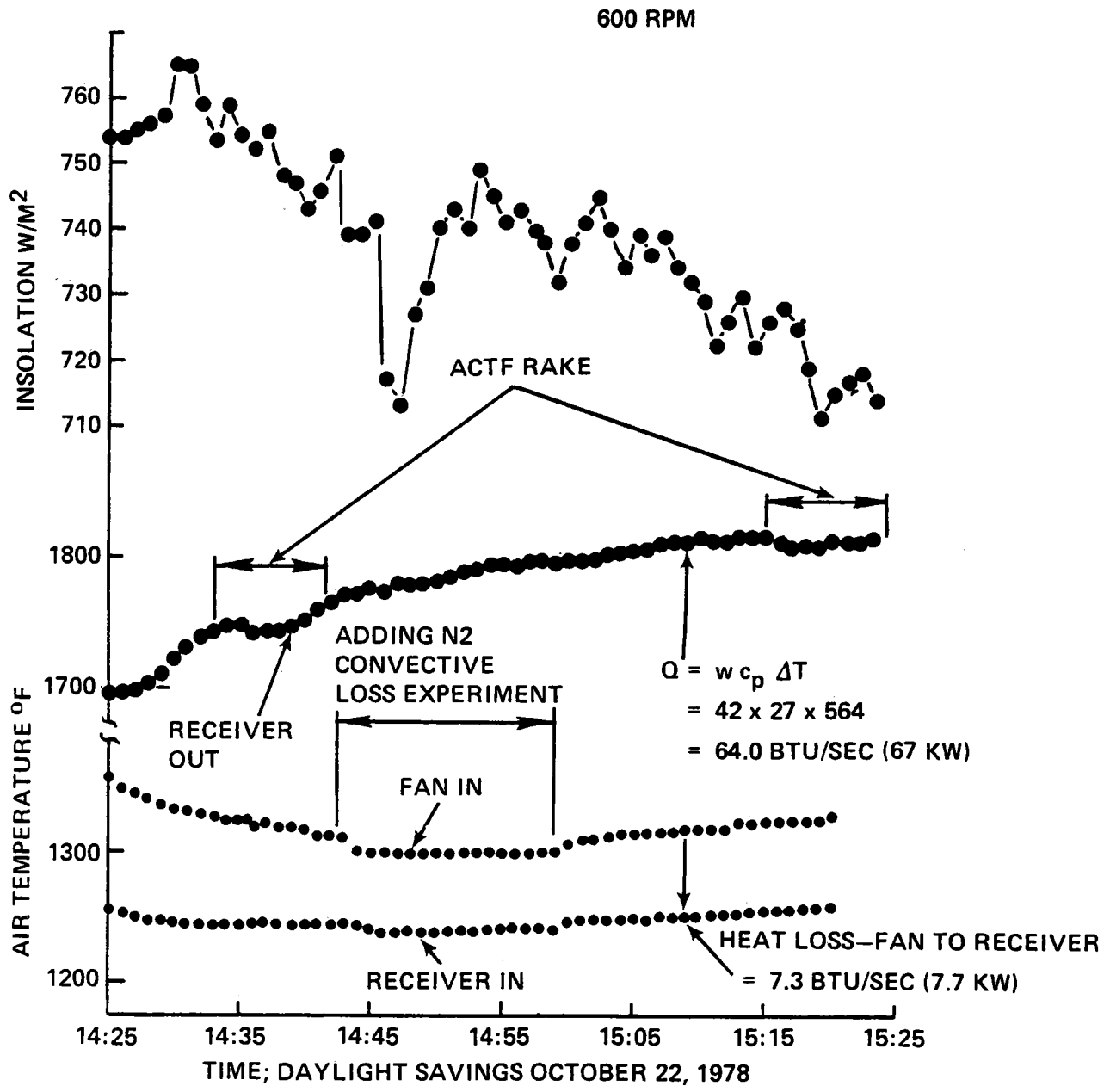

12078-58

Figure 3-13. Receiver Temperatures and Insolation - Case 1

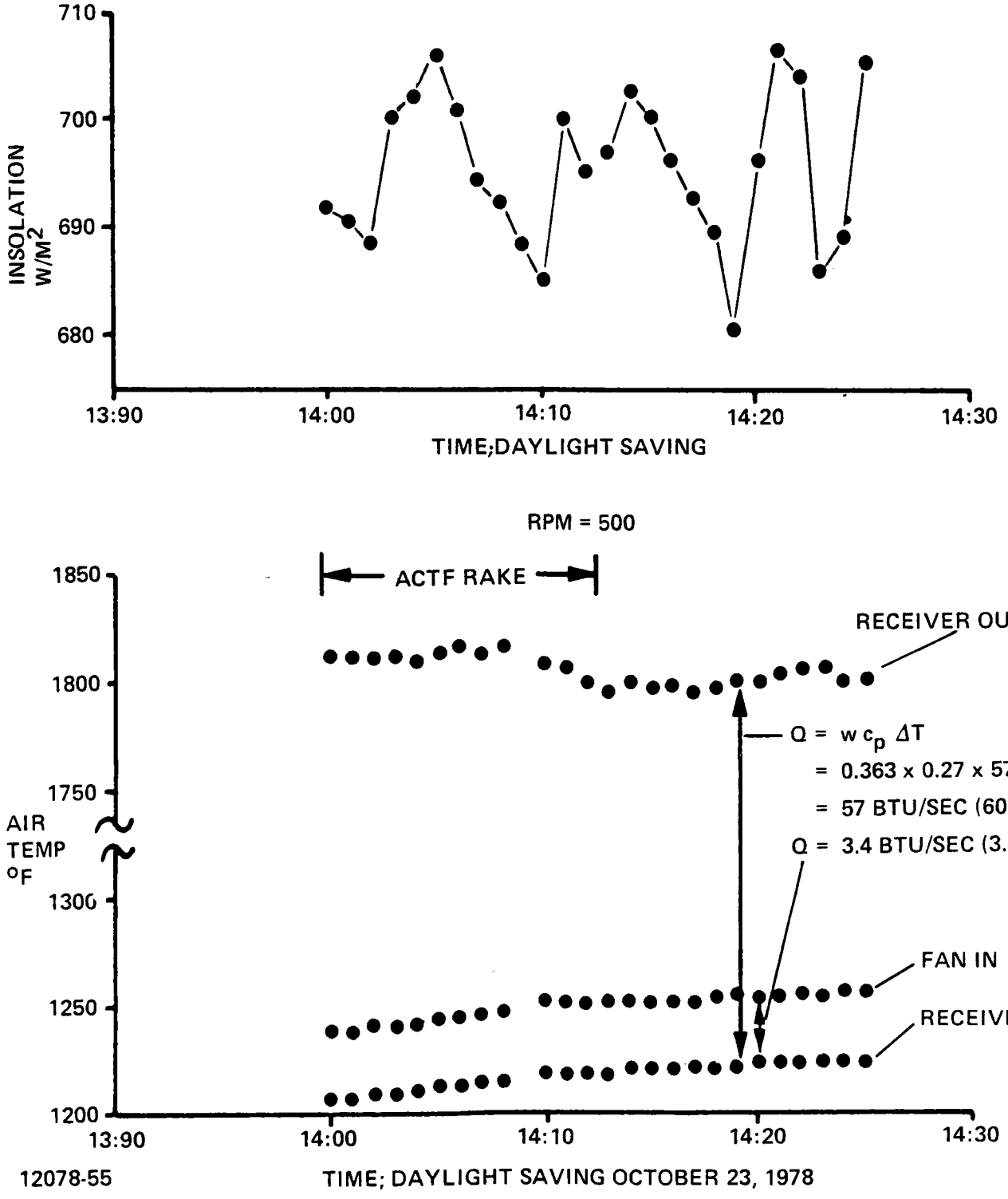

Figure 3-14. Receiver Temperature and Insolation - Case 2

concentrator measuring the flux in and the centroid of the flux from the mirror field. The only mechanical equipment operating during this one hour period was the hot fan running at 600 rpm.

These measurements show a reduction in receiver outlet temperature of 10-15^{o}F as the ACTF rake passes across the terminal concentrator. This decrease is due to the reduced energy input resulting from reflection from the rake. The net heat output of the receiver is 68 kW. Temperature drop occurred between the hot fan inlet station and the receiver inlet. This temperature drop represents a heat loss of 7.7 kW as shown below:

$$(Q = w\ C_p\ \Delta T = 0.42 \times 0.27 \times 64 = 7.26 \text{ Btu/sec or } 7.7 \text{ kW})$$

During this stable measurement period, there was a sudden drop of 6% in insolation extending over a five minute period. Almost instantaneously there was a small but perceptable change in receiver outlet temperature. Another observation of sensitivity to change occurred when the nitrogen was injected into the system as part of the convective loss experiment. Both the fan inlet air temperature and the receiver inlet air temperature dropped a few degrees.

On October 23, stable operation at 500 rpm occurred from 14:00 to 14:25 (Figure 3-14). The receiver outlet air temperature was again 980^{o}C (1800^{o}F) and the insolation was somewhat less than the previous day. The net heat output was 60 kW compared with 67 kW obtained during the previous day. Losses between the fan air flow measuring station and the receiver air inlet were less than half the losses measured on October 22, which is explained by the fact that a cooling water leak in the area around the outside of the terminal concentrator developed during the test on October 22 and was fixed prior to testing on October 23. The leak caused additional cooling of the inlet air.

A third example of system operation (Figure 3-15) is representative of conditions where the airflow is high (200 rpm fan speed) but the ΔT is low and temperatures in the entire system are rising rapidly. Over a period of 30 minutes when the insolation was nearly constant at 800 W/m^2, the receiver inlet temperature increased about 80^oC (150^oF). The heat output was also nearly constant at 95 kW, 24 kW of which were lost in the heating and conduction losses within the ducting from the fan inlet station to the receiver inlet station.

3.3.2.5 Heat Balance

The three examples of heat flow (Figure 3-12 through 3-14) were analyzed in an attempt to correlate with predicted heat losses. Data are summarized in Table 3-3.

Solar flux into the terminal concentrator, as determined from the ACTF flux rake, was normalized to 900 W/m^2. Normalized input varied from 244 kW to 251 kW, representing a variation of 3% after correcting for time differences between the experiment and solar noon (cosine effect). The actual heat flux into the cavity was obtained by multiplying the normalized flux by 0.54, which is the experimentally-determined transmission factor for the terminal concentrator (Figure 3-4).

Measurements of losses and heat flows were summed in an attempt to account for the flux which enters the cavity. Heat flow out of the cavity was computed from measured mass flows and temperatures at the inlet and outlet to the receiver. The losses due to radiation, convection, and conduction must be added to this heat flow. Radiation losses were determined by assuming the 50.8 cm (20 inch) diameter aperture was radiating at a uniform temperature equal to the average temperature of the six thermocouples recording the front surface temperatures of the silicon carbide honeycomb panels (Figure 3-16).

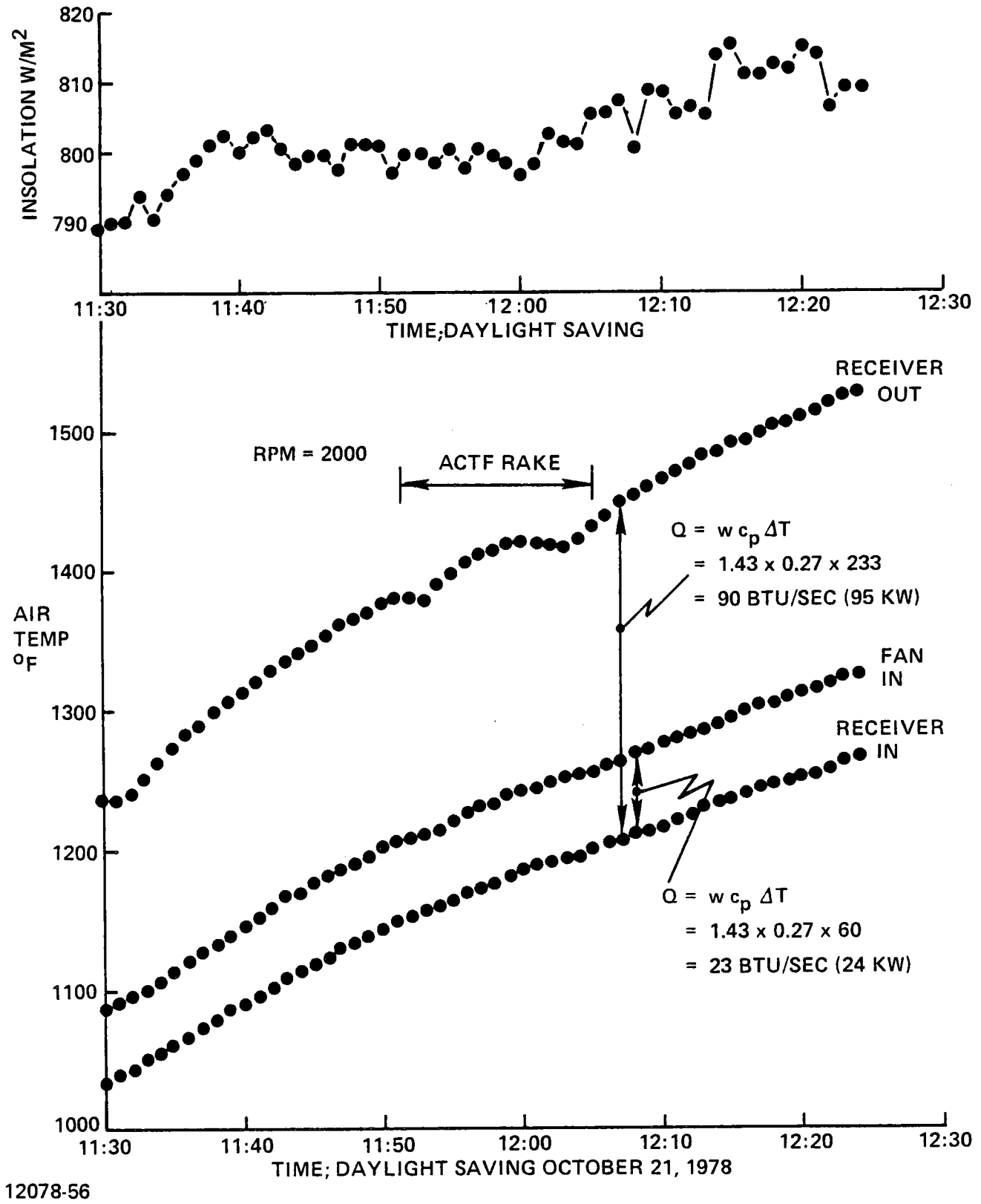

Figure 3-15. Receiver Temperature and Insolation - Case 3

TABLE 3-3. SUMMARY OF HEAT BALANCE MEASUREMENTS

Heat Flow In	Case 1	Case 2	Case 3
Terminal concentrator inlet (kW) (normalized to 900 W/m^2)	244	251	251
Actual Terminal Concentrator (kW) (corrected for insolation)	200	194	224
Into Cavity (kW) (corrected for terminal concentrator transmission, 54%)	108	105	122
Heat Flow Out			
Receiver Air (kW) (measured)	67	60	95
Receiver Radiation (kW) (calculated)	29	29	15
Receiver Convection (kW) (measured)	1.4	1.2	4
Receiver Conduction (kW) (calculated)	5	5	5
Base Conduction (kW) (measured)	2	2	2
Total kW	104.4	97.2	121
Discrepancy (%)	-4	-3	-1
Operating Conditions			
Time and date	15:00 10/22	14:20 10/23	12:07 10/21
Cavity average temp (^oF)	1800	1800	1448
Air flow (lb/sec)	0.42	0.36	1.40

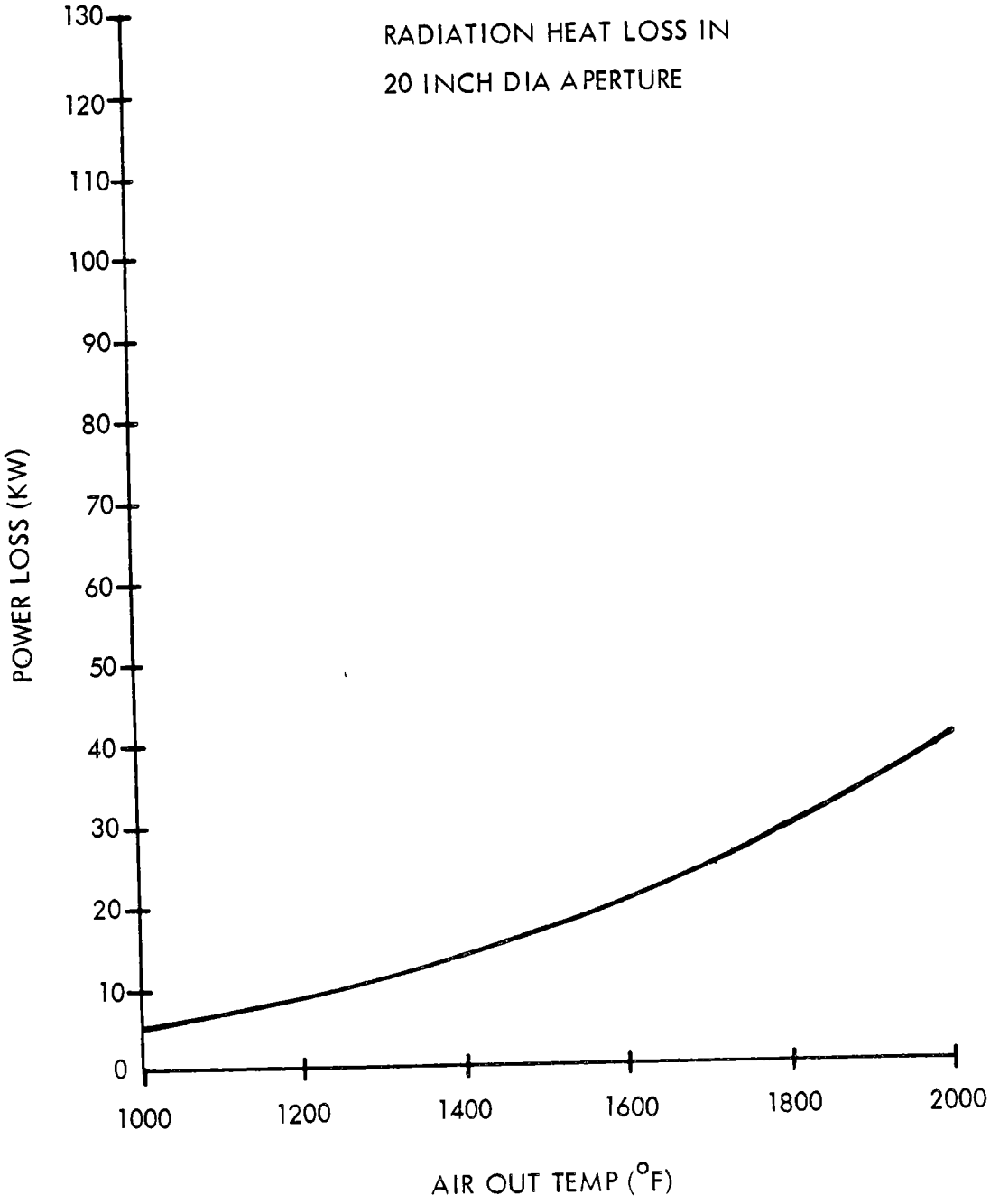

Figure 3-16. Radiation Heat Loss in 20-inch Diameter Aperture

Convective heat flow was obtained from the total measured mass loss rate (Figure 3-19), assuming that the lost air was at the receiver outlet temperature. Heat loss through conduction was determined partly from known R values for the insulation. An additional conduction loss was unpredicted and was caused by poor insulation in the base which supports the receiver. A direct conduction loss to the platform was calculated using the receiver air flow and temperature differences measured around the receiver inlet station. When the inlet temperatures were close to 650°C (1200°F), a base conduction loss of 2 kW was estimated for each case.

The discrepancy between the heat flow into the receiver cavity and the sum of the receiver losses is 4% or less for the three cases compared in Table 3-3. In extending these measurements to apply to a full-scale commercial system, the receiver performance is directly applicable but significant corrections to the terminal concentrator performance are needed. This terminal concentrator was designed for a thruput of 82% with a 45 degree mirror field having σ = 6.5 mrad as was initially projected for the ACTF. The actual thruput was reduced to 54% as a result of the reduced mirror field performance σ = 11.5 mrad. The terminal concentrator used in a commercial system would have a field angle of 62 degrees, a total sigma of 6.0 mrad and a thruput of 94%. By extrapolation of these test results to a commercial size receiver and mirror field, the projected power out of the receiver is 84% of the power entering the terminal concentrator (see Table 3-1).

3.3.3 Convective Loss

3.3.3.1 Experiment

The thermal loss (Q_{loss}) due to convective exchange through the open aperture of the 1/4 MWt solar receiver can be directly related to the mass flow of air lost through the receiver as follows:

$$Q_{loss} = \dot{m}\, C_p\, \Delta T$$

where C_p = heat capacity of hot air

ΔT = T operation - T ambient

$\dot{m}$ = mass flow

and % energy lost = $\frac{Q \text{ lost}}{Q \text{ delivered}} \times 100$

The mass flow loss was measured by isolating a particular gas with which the receiver was charged and observing the change in gas concentration due to exchange mechanisms as a function of time. Typically, the gas within the receiver was composed of 21% oxygen. The test was designed to dilute the oxygen concentration by injecting nitrogen into the receiver. In this manner, since the molecular weight of air and nitrogen are similar, little variation in flow properties would occur. The mass flowing out of the receiver was determined by observing the decay in the nitrogen concentration in the receiver and the measured increase in oxygen concentration. An oxygen analyzer was employed to measure the concentration of oxygen within the receiver.

3.3.3.2 Oxygen Analyzer

The commercial oxygen analyzer is a galvanic cell with a solid electrolyte, zirconium oxide (ZrO_2), which is pervious to oxygen ions (Figure 3-17). An electromotive force (EMF) is developed due to the difference in oxygen potential or concentration across the electrolyte. Air ($C_o = 0.21$) is used as a reference state and the EMF is related to the measured oxygen concentration by:

$$EMF = \frac{-RT}{4F} \ln \frac{P_{O_2}}{0.21}$$

R = universal gas constant

F = Faraday's constant

T = temperature

P_{O_2} = Oxygen partial pressure

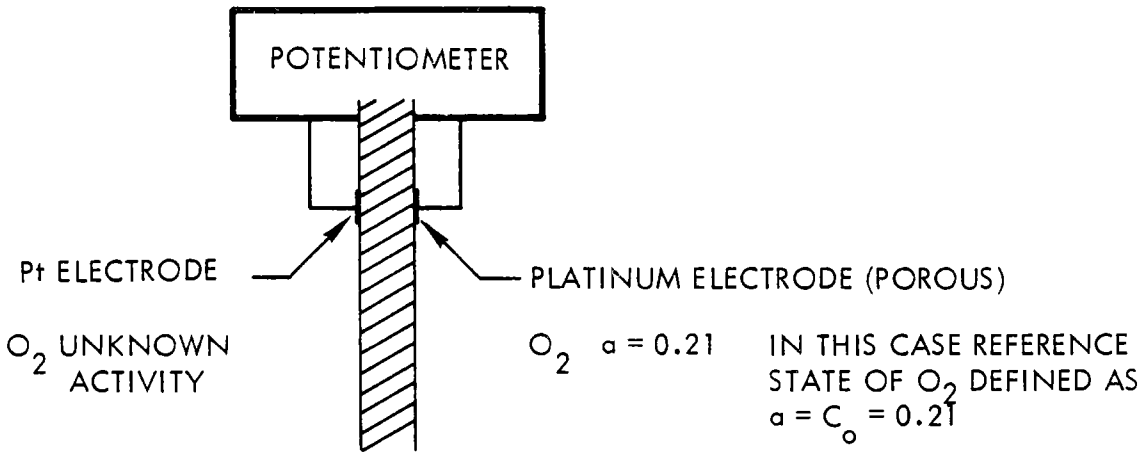

IONIC TRANSFER OCCURS WHEN $C_o \neq C_o^*$

$$\Delta G = RT \text{ LN } C_o/C_o^*$$

$$\Delta G = (-nF)(+EMF) \qquad n = 4 \text{ FOR A TRANSFER OF 1 MOLE OF } O_2$$

$$EMF = \frac{-RT}{4F} \text{ LN} C_o/C_o^*$$

$$C_o = C_o^* \exp\left[\frac{-EMF\,(4F)}{RT}\right]$$

WHERE:

ΔG = GIBB'S FREE ENERGY
T = TEMPERATURE ^{o} KELVIN
R = UNIVERSAL GAS CONSTANT
F = FARADAY'S CONSTANT

Figure 3-17. Schematic of Oxygen Analyzer

The temperature of the ZrO_2 electrolyte is maintained between 650^oC and 850^oC. At this temperature, response time ranges between 3 and 5 seconds, depending on the path which the unknown gas must travel to the cell.

3.3.3.3 Model for Oxygen Concentration with Volumetric Change

The transient of the rise in oxygen concentration of air in a reduced state in an open container can be described phenomenologically, assuming ideal mixing occurs and that segregation of an existing species does not occur. Both assumptions are valid in this case as the atomic weights of the species involved are similar:

$$dV_o = (0.21-C_o)dV_a$$

$$dC_o = \frac{dV_o}{V_{tot}}$$

$$(0.21-C_o)dV_a = dC_o\ V_{tot}$$

$$\frac{dC_o}{0.21-C_o} = \frac{dV_a}{V_{tot}}$$

Integrating this from limits of C_o to C_o obtains:

$$C_o = 0.21 + (C_o' - 0.21)\ \exp\left(\frac{-V_a}{V_{tot}}\right) + K$$

With boundary conditions at:

$$C_o' = 0$$
$$C_o = 0$$
$$V_a = 0$$

then $K = 0$

$$C_o = 0.21 + (C_o' - 0.21)\ \exp\left(\frac{-V_a}{V_{tot}}\right)$$

where C_o' = initial concentration of oxygen at time, t = o

C_o = concentration of oxygen at time t

V_a = volume of air exchanged

V_{tot} = total volume of system

This equation may be expressed with time as a variable:

$$V_a = Q_\ell t$$

Q_ℓ = volume of gas exchanged/time

t = time

and $$C_o = 0.21 + (C_o' - 0.21) \exp \frac{-Q_\ell t}{V_{tot}}$$

The oxygen concentration (C_o) of the system at time (t) is exponentially related to the air flow into the system due to leaks or convective loss.

An experiment can be designed with a reduced atmosphere ($C_o < 0.21$) in a container with a leak or open port in which air ($C_o = 0.21$) may enter. To maintain this reduced atmosphere, nitrogen must be added to the system continuously to compensate for the change in concentration due to the leak.

Two mechanisms are taking place:

1. Introduction of nitrogen ($Q_{nforced}$) which results in an equal flow of gas, concentration C_n, out of the container.

2. Exchange of gas, Q_{loss}, due to leaks and convective loss to ambient. Nitrogen concentration of gas moving out of the container is C_n, nitrogen concentration of gas transporting into container is 0.79 (concentration of inert components in air 0.78 nitrogen and 0.01 argon, for this experiment considered 0.79 nitrogen).

$Q_{\text{nitrogen flow out of container}} (Q_{n_{out}}) = Q_{n_{forced}} (C_n) + C_n(Q_{loss})$

$Q_{\text{nitrogen flow into container}} (Q_{n_{in}}) = Q_{loss} (0.79) + Q_{n_{forced}} (1.0)$

at steady state: $Q_{n_{in}} = Q_{n_{out}}$

$$Q_{n_{forced}} + 0.79 (Q_{loss}) = C_n (Q_{loss} + Q_{n_{forced}} (1.0)$$

$$= \frac{Q_{n_{forced}} (1-C_n)}{C_n - 0.79}$$

and $C_n = 1 - C_o$

$$Q_{loss} = \frac{Q_{n_{forced}} (C_o)}{(0.21 - C_o)}$$

Charge Cycle

The volume of nitrogen required to fill the receiver can be expressed as follows:

$$C_n = 1 + (C_n' - 1) \exp \frac{-V_n}{V_{tot}}$$

or $$C_o = C_o' \exp \frac{-V_n}{V_{tot}} \quad \text{where } V_n = Q_{nt}$$

$$C_o = C_o' \exp \frac{Q_{nt}}{V_{tot}}$$

where C_o' = initial concentration of oxygen at t = o

C_o = concentration of oxygen at time (t)

Q_n = flow rate of nitrogen into receiver

t = time

V_{tot} = system volume

This expression will be true as long as

$$Q_n \gg Q_\ell$$

Q_ℓ = loss flow out of receiver

If $Q_n \geq Q_\ell$ then the exponential term must include a correction factor to reduce the rate of change in oxygen concentration. The effect of the loss flow will be minimized if the time of charging is minimized. The transient equation for the reduction in oxygen concentration was used only as an estimate of time to obtain a specific oxygen concentration.

3.3.3.4 Test Procedure

The test apparatus was installed just upstream of the hot fan in the receiver. Figure 3-18 illustrates the experimental setup. Nitrogen flow was controlled and monitored by a needle valve and flow meter. Nitrogen was introduced downstream from the gas sampling station to allow proper mixing. A sample stream of 0.5 liter/min was continuously extracted from the hot air duct and evaluated for oxygen concentration. This value was recorded as a function of time on a strip chart recorder. After sampling, the gas was exhausted.

The mass flow and temperature were monitored continuously at station three. Thermocouples were also located just above the aperture to determine the average temperature of the hot air stream. Once the system was at equilibrium, nitrogen would be introduced into the hot stream and charging would continue until the oxygen concentration reached steady state. At this time the nitrogen flow was stopped and the oxygen concentration was continuously monitored. Convection loss

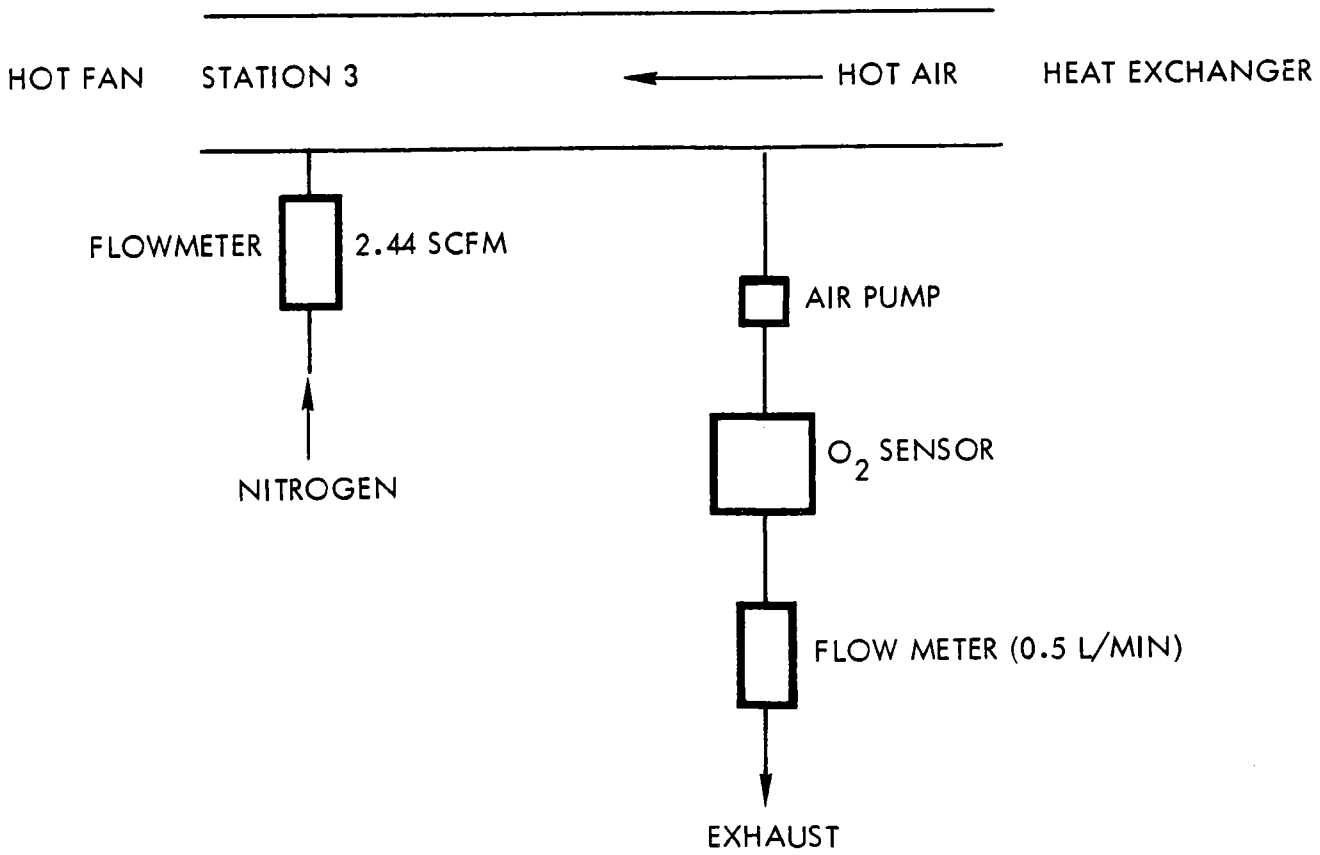

Figure 3-18. Convective Loss - Test Apparatus

runs were performed at fan speeds of 600, 1200, 1800, and 2400 rpm. Tare runs were performed to determine leakage rates. The aperture was closed and the system was heated with the propane burner. The loss in the tare runs was related to system leakage. Tare leakage rates were factored out of the total loss data to obtain convective loss values.

3.3.3.5 Results

Figure 3-19 illustrates the plot of oxygen concentration as a function of time at a fan speed of 1200 rpm. This fan speed represents a system mass flow of 0.80 lbm/sec. Curve 1 is the actual decay in the oxygen concentration during the discharge cycle of the receiver as recorded. The response time of the test apparatus, 3 to 5 seconds, allows excellent accounting of concentration changes as a function of time. The time constant for the gas exchange was in the order of 180 to 300 seconds.

The total loss curve (Curve 1) was fit to the decay function described earlier to determine the total mass flow (Q_ℓ) of gas exchanged. Q_ℓ was corrected for system leakage determined in the tare runs to calculate the mass flow loss due to convective mechanisms (Curve 2).

The steady state case was used to check the measurements. A constant oxygen concentration (C_0) was maintained by a steady inflow of nitrogen to compensate for the convective exchange. The nitrogen was maintained at a O_2 maintained constant mass flow. The mass flow loss due to convective mechanisms was again determined by subtracting the tare losses from the total calculated loss. The loss values determined through the two approaches usually were within 10% of the average value.

Table 3-4 summarizes the convective loss data from the tests on the 1/4 MW_t receiver at GIT. Tare runs at fans speeds of 1200 rpm and 2400 rpm were performed at about 540°C (1000°F). This relates to

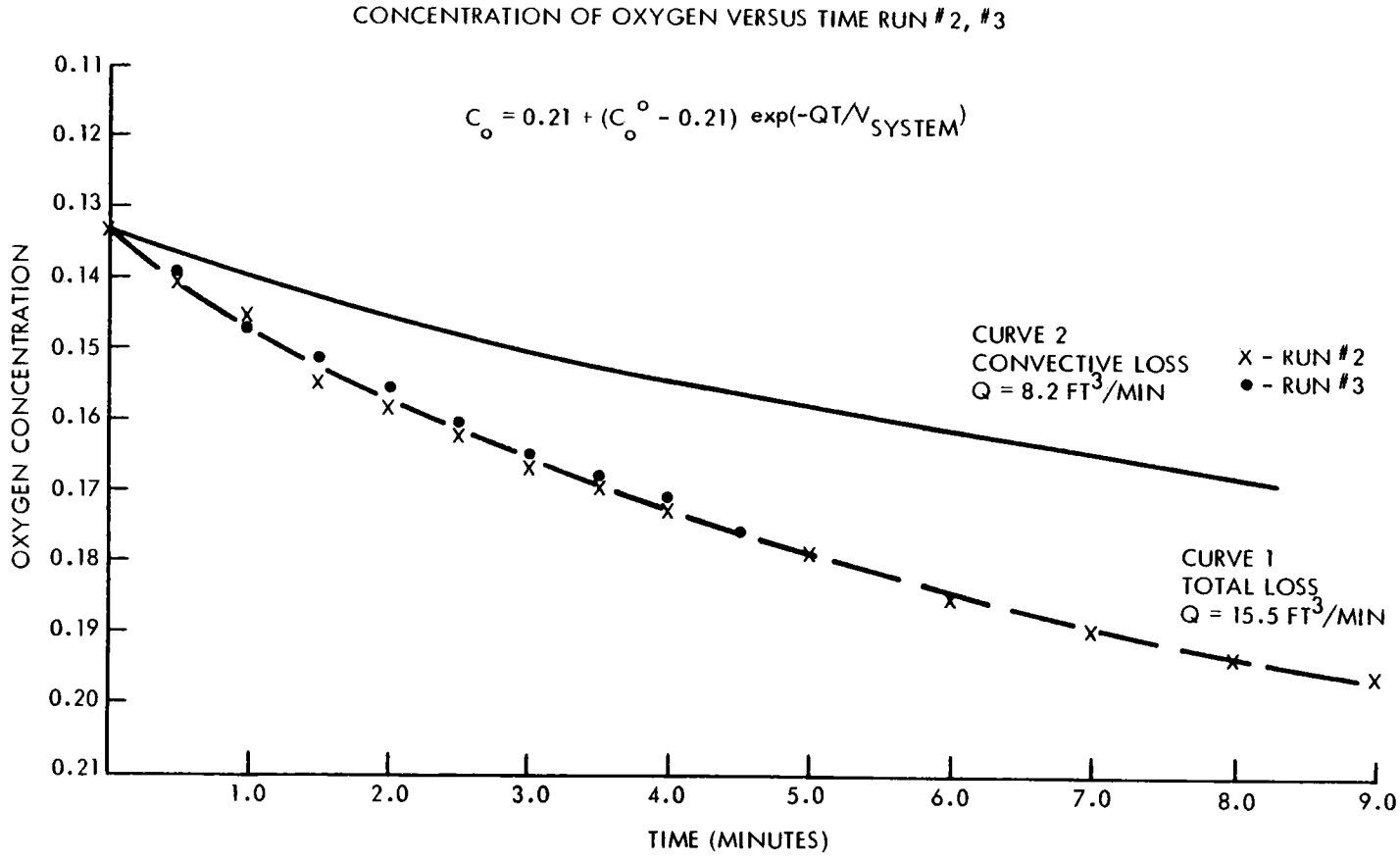

Figure 3-19. Concentration of Oxygen versus Time

TABLE 3-4. CONVECTIVE LOSS DATA
GIT 10/20/78

RPM	Run	Av. Cavity Temp (^{o}R)	System Mass Flow (lbm/sec)	Total Loss (lbm/sec)	Convective Loss (lbm/sec)
600	Test	1950	0.42	0.0037	0.0020
1200	Tare	1450	1.00	0.0038	-
1200	Test	1850	0.80	0.0058	0.0023
1800	Test	1704	1.30	0.0107	0.0050
2400	Tare	1250	2.30	0.0115	-
2400	Test	1697	1.75	0.0137	0.0060

system mass flows of 1.00 lbm/sec and 2.30 lbm/sec, respectively. Also noted are system mass flows for test runs at specific fan ratings. Total loss and convective loss values are reported as mass flow and illustrated in Figure 3-20. The loss due to convective mechanisms varies linearly with system mass flow. It appears that system leakage rates are of the same magnitude as the convective losses.

The results of the GIT experiment are compared to the previous experiment at Wolfeboro in Figure 3-21. The percent of energy lost was calculated by obtaining the convective loss rate (0.0049 lmb/sec) for the system design mass flow of 1.4 lbm/sec, operating from 650°C to 1100°C (1200 to 2000°F). The data on convective loss was measured at a system output power level of 70 kW, therefore, the data was extrapolated to the system design of 250 kW. From the present data, it appears that the thermal influence on the loss mechanism is a secondary consideration and that the extrapolation is reliable. The ΔT of the gas lost through convective mechanisms was assumed to be 600°C (1100°F) based on gas temperature measurements inside the receiver near the aperture. Employing

$$Q_{loss} = m_L \cdot C_p \cdot \Delta T$$

convective loss was 1.3 kW or 0.5% of design energy (250 kW). The experiment at GIT was performed with a fairly constant wind speed of 5.2 mph. Data from the two tests fit a linear function reasonably well; however, only three data points are available. In comparing data from the two experiments, it should be noted that the terminal concentrator configuration and aperture size were similar, however, due to the tower configuration at GIT, the wind flow pattern around the aperture may have been modified.

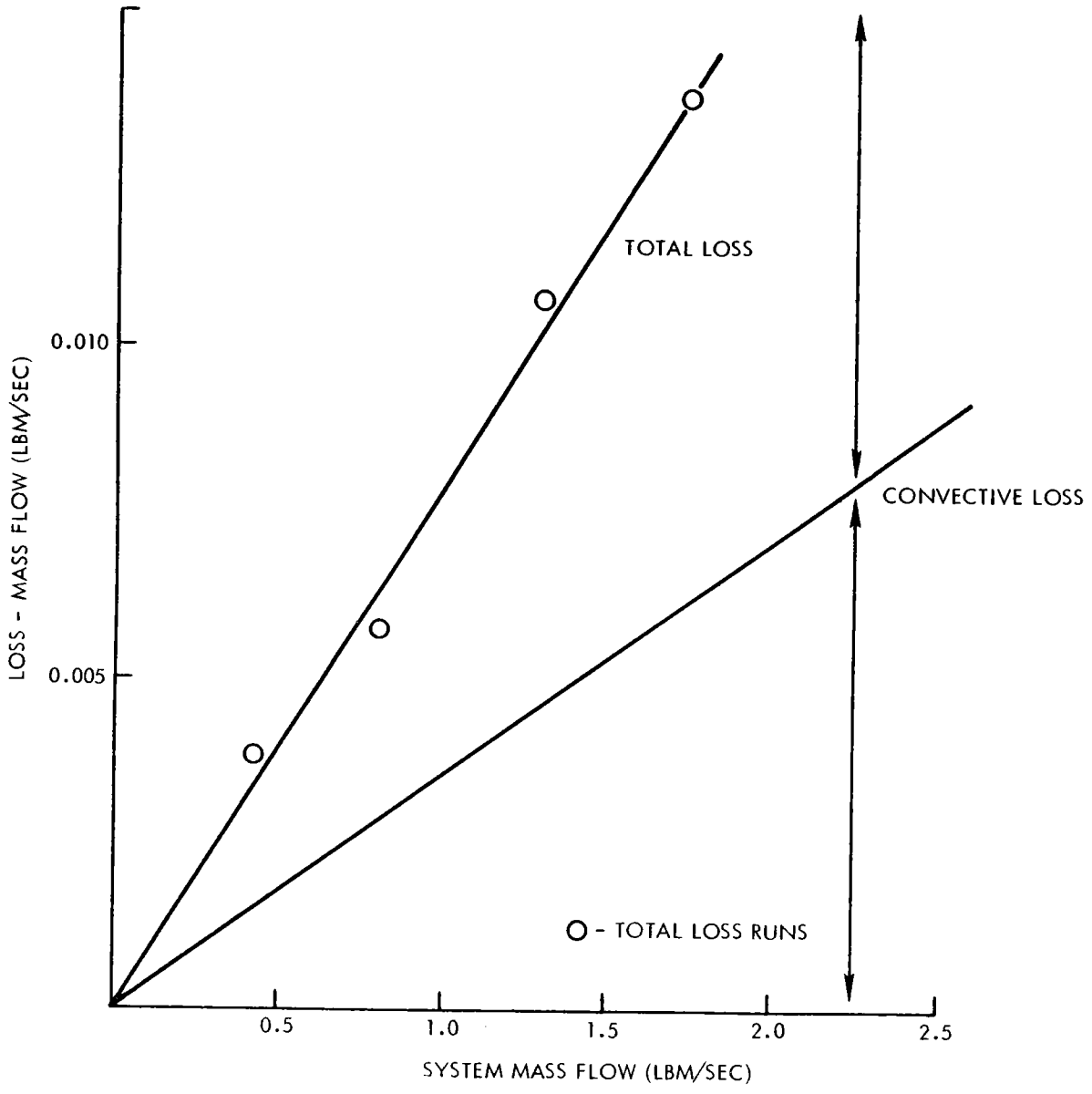

Figure 3-20. Loss versus Mass Flow

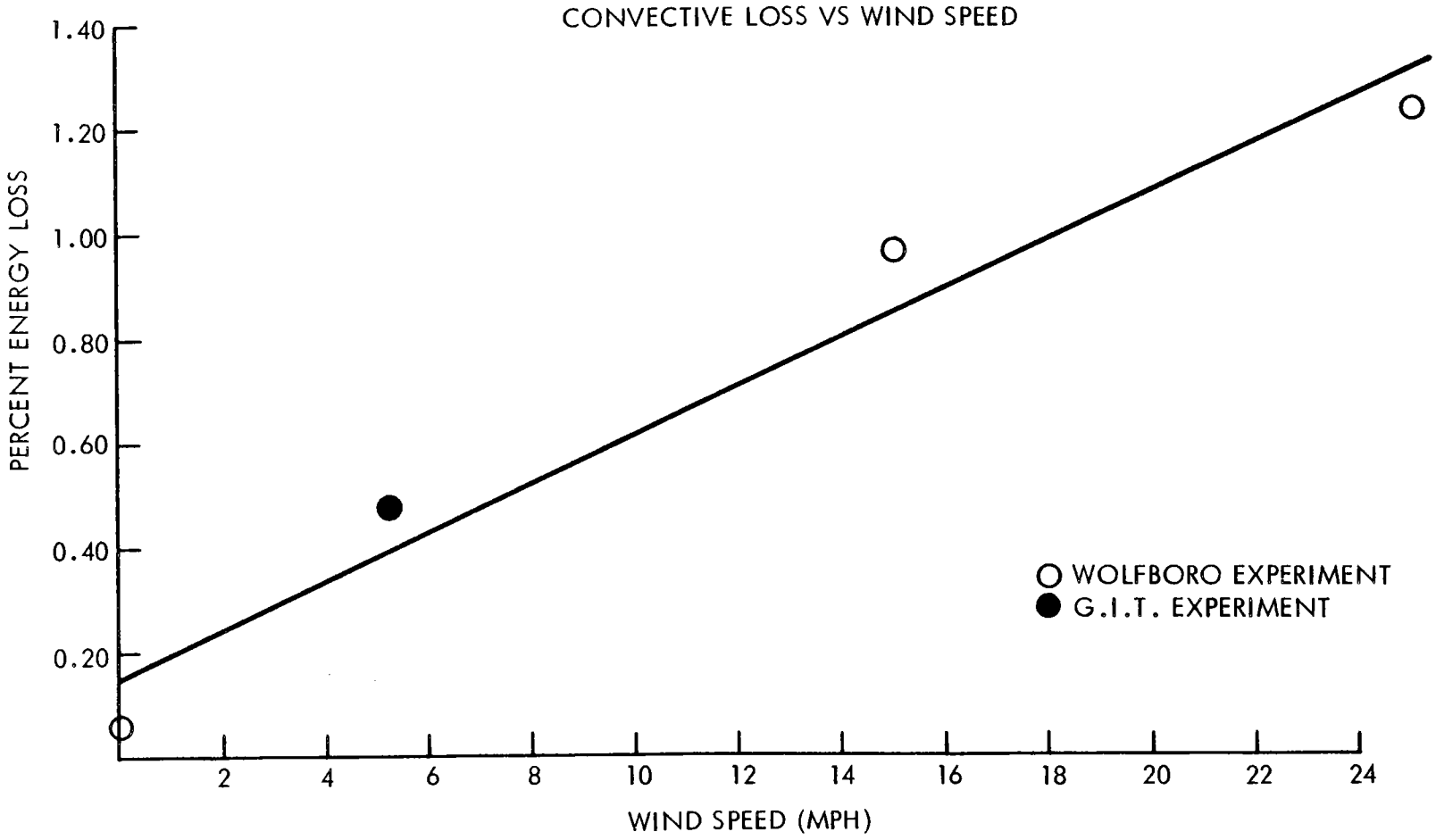

Figure 3-21. Convective Loss versus Wind Speed

SECTION 4
CONCLUSIONS AND RECOMMENDATIONS

During this program, a 1/4 MWt solar receiver was designed, fabricated and successfully tested at the design temperature of 1100°C (2000°F). No structural difficulties were encountered. In addition, direct measurements of convective heat loss from the open cavity receiver confirmed and validated the previous loss measurements, and showed the loss for a wind velocity of 5 mph to be less than 1% of rated thermal power.

This receiver design is scalable to a 300 MWt commercial size receiver. The tests have shown that the performance projected for the commercial receiver are achievable.

Although the solar receiver tests conducted at ACTF were limited by the mirror field performance to reduced mass flow conditions, the data has been conservatively extrapolated to predict and verify thermal efficiency at design input power conditions. When the ACTF mirror field aiming and tracking performance is improved, a new series of tests is recommended with the receiver operating at the design mass flow.

The 1/4 MWt receiver was designed to maintain a constant outlet air temperature during periods of varying insolation by varying the air flow. The experience obtained at the ACTF has demonstrated that this approach is easily implemented so that it will consistently provide the constant temperature gas needed to fully charge the thermal storage device.

APPENDIX I

SOLAR FLUX AND RECEIVER HEAT TRANSFER COMPUTER MODELS

APPENDIX I
SOLAR FLUX AND RECEIVER HEAT TRANSFER COMPUTER MODELS

I.1 SUMMARY

Sanders used the HELIOS, FLUXGO and ANSYS computer codes to determine the aperture and internal cavity flux distributions for both the commercial 100 MWe and GIT 1/4 MWe solar receivers.

The HELIOS code, a FORTRAN program written by Sandia determines the flux received on a plane. This code was used to study the flux distribution obtained with both a south tower and central tower mirror field. The results showed that the central tower mirror field outperformed the south tower mirror field. Independently, the staff of the ACTF (Advanced Components Test Facility) at GIT came to the same conclusion. Thus, the decision was made by GIT that the receiver tower would be located at the central field location.

The FLUXGO code, written by Sanders, tracks and maps the final location of the entering sun rays, thus determining the flux distribution within the solar receiver. The FLUXGO code with an extremely versatile input capability was used to analyze the parameters of the solar receiver (e.g., terminal concentrator angle, aperture diameter, and roof cone). An optimum receiver design for maximum heat transfer and ultimate efficiency was chosen with the aid of the FLUXGO code.

The ANSYS model, written by Swanson Associates, takes over where the FLUXGO code leaves off in that it traces heat flows within the system. The ANSYS model takes into consideration the distribution of energy within the receiver structure, its transfer to an airstream, and the radiation emitted by the receiver.

Thus, the combination of the HELIOS, FLUXGO and ANSYS solar flux computer models enabled Sanders to simulate and trace sun rays entering

the terminal concentrator, impinging on the receiver, and ultimately, absorbed by the airstream, in order to design an optimum solar receiver for both 100 MWe and 1/4 MWe power output.

I.2 HELIOS

The HELIOS computer program, written by Sandia Laboratories in early 1977, evaluates designs of power tower solar energy systems.

Sanders chose to use the HELIOS program to determine power received on its receiver for the GIT 1/4 MWe experiment. The HELIOS program can locate hot spots, verify aiming strategy and test if the design will meet specification. The program also gives the flux on a target. The target may be either the solar receiver or the frontal plane of a terminal concentrator. The program does not include a terminal concentrator routine.

The HELIOS code consists of seven groups of input data:

(1) Problem and Input Type Data
(2) Sun Parameter Data
(3) Receiver Data
(4) Facet Data
(5) Heliostat Positioning Data
(6) Time Data
(7) Atmospheric Data

The first group, Problem and Input Type Data, controls computer options such as short or detailed analysis and printout. The second group defines sun parameter data. Sanders chose to employ the sun parameters including sunshape recommended by GIT. The third group, Receiver Data, is particular to the Sanders design. Receiver data includes tower height, tower location in the field, target orientation,

point of focus and target shape and extent. Group four, Facet Data, is particular to the GIT heliostats. Each heliostat has one facet, 0.555m on a side with a reflectivity of 62.5%. The center is slightly depressed with a pull-down radius of 0.065m. The fifth group, Heliostat Positioning Data, gives the coordinates of the heliostats in the solar field. The origin is at the base of the south tower location with sign convention east and north as positive. The GIT heliostat field in the Fall of 1977 consisted of approximately 540 heliostats. Sanders, for economic reasons, chose a representative 180 heliostats. Group six, time data, is the solar time at which the HELIOS program is to compute the power received on the target. Group seven, Atmospheric Data, is particular to the Georgia area. Direct normal insolation was assumed at 900 W/m^2.

*Measured reflectivity of the unwashed mirrors.

I.3 FLUXGO

I.3.1 Introduction

FLUXGO is a 700 line FORTRAN computer program written at Sanders Associates to aid in the design of a central tower solar receiver. Developed early in 1978, the program, is adaptable to almost any solar receiver design. A random number generator is used to generate a given number of sun rays, which the program then traces to individual end locations. The printout, listing the end location of the sun rays, indicates parameter changes to achieve a desired flux distribution. The printout also states the percent capture, percent miss, percent retroreflection and power (in kilowatts) into the receiver for a particular design. FLUXGO thus aids optimum design of central tower solar receivers to meet the required specifications.

I.3.2 FLUXGO Design and Modeling

Sanders solar receiver, depicted in Figure I-1, consists of a roof cone, cylinder, reentrant cone, aperture and terminal concentrator. The numbers 0 through 6 in Figure I-1 identify the various sections of the solar receiver in the computer program. The design of any section may be changed as long as that section is not totally eliminated. A virtually non-existent terminal concentrator one millimeter larger in radius than the aperture radius, and one millimeter lower in height than the aperture is permissible. Figure I-2 shows the FLUXGO block diagram.

I.3.3 FLUXGO Applications

The FLUXGO program is a cost effective means of evaluating solar receiver design trade-offs. The program will accommodate virtually any possible receiver design. Given a set of input values, the program uses a random number generator to simulate sun rays, and calculates the

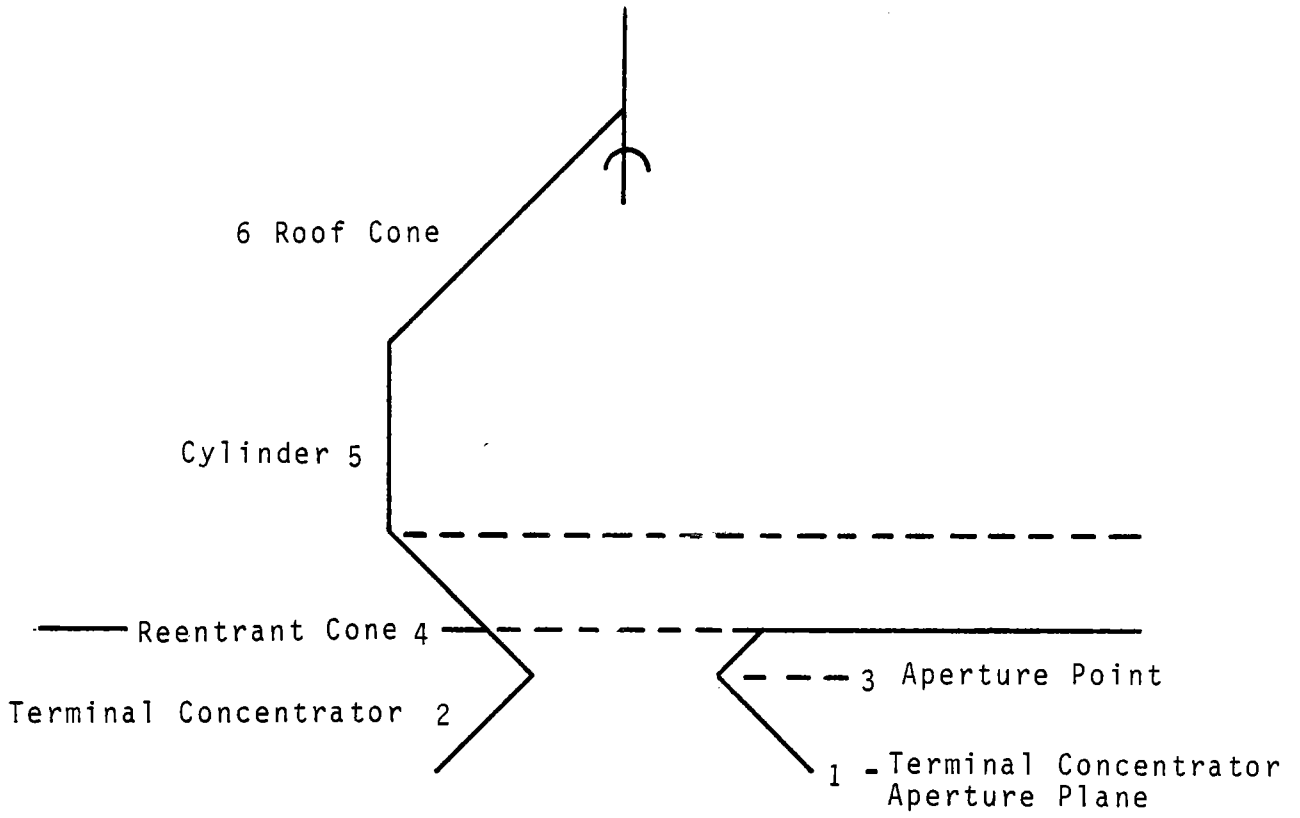

Figure I-1. Solar Receiver Model and Section Numbering

power (in kw) intercepted by the receiver. The program traces each sun ray to its end location, which may occur after a number of bounces (reflections) within the receiver. The computer then tabulates the rays' end locations and calculates the percent capture, percent miss and percent retroreflection of a particular receiver design.

The FLUXGO program, with input variations, can model insolation for various locations, seasons and times of day. Heliostat field specifications such as number of mirrors, size, reflectivity and optical quality may also be changed. The solar receiver design and dimensions may all be changed as long as a section of the solar receiver, as explained in Section I.3.1, is not removed. Receiver parameter optimization such as aperture size, aim point location, terminal concentrator angle and overall receiver proportions is easily accomplished using the program.

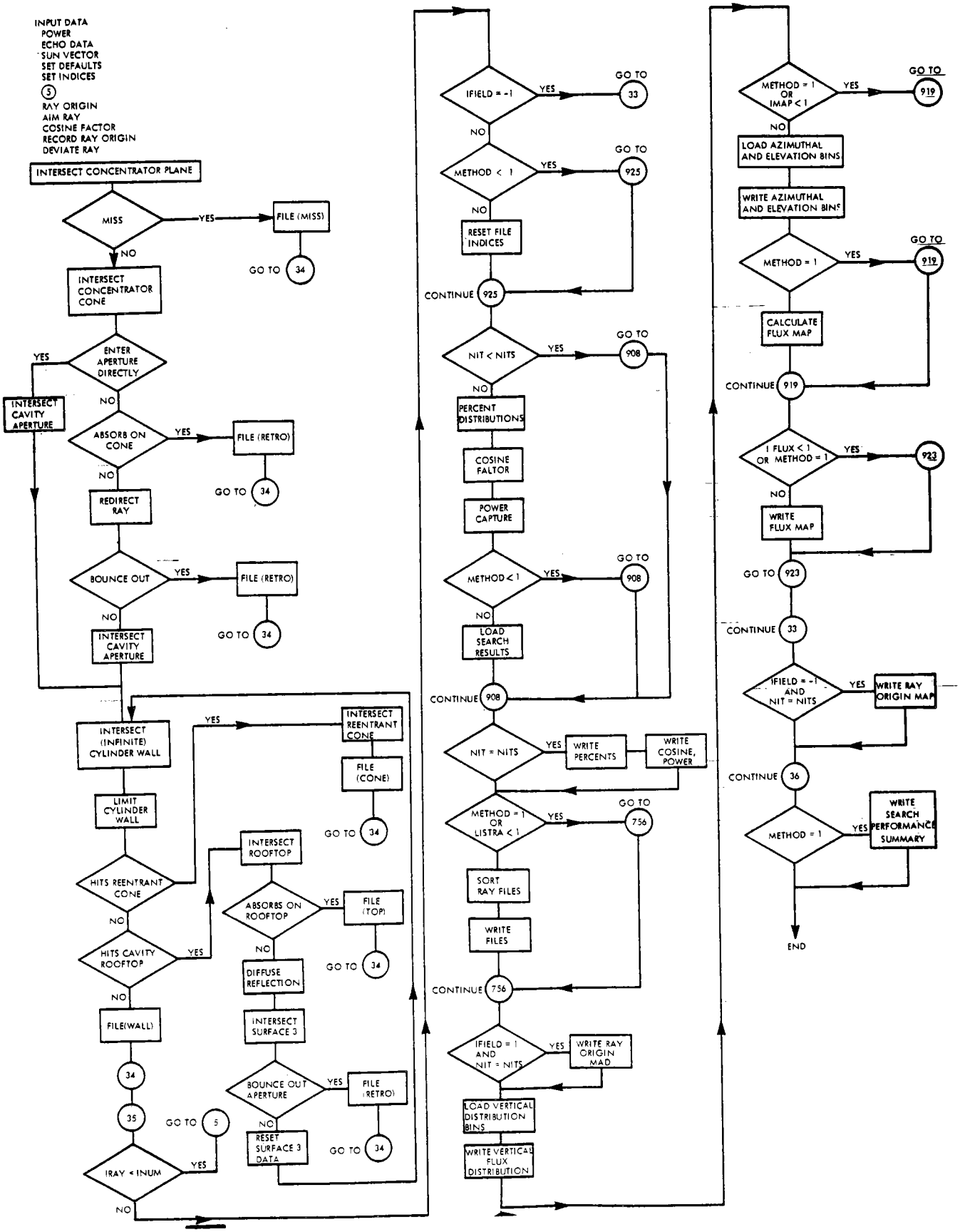

Figure I-2. FLUXGO Block Diagram

In FLUXGO, angles are measured in degrees, except where noted, and all scalar measurements are in meters with an origin at the base of the solar receiver tower. The input labels such as THA4, the tangent of the half angle of receiver section four, are the actual variables read by the computer in the FLUXGO program and may be found in the program listing. The input card deck consists of 23 cards, which are divided into five groups as described in Tables I-1 through I-3.

I.3.4 Sample FLUXGO Program

The sample FLUXGO program, reprinted in the following pages, is a solar receiver design for Sanders' 1/4 MWt Air Cycle Solar Receiver program. The design is for a receiver with a 73 cm diameter aperture, 52.5 degree terminal concentrator angle, and an aim point 20.6 meters above the ground.

The first page of the printout is a listing of the entire input deck of 23 data cards. Page 2 shows: (a) the overall flux distribution from the heliostat field, and (b) the total power captured by the receiver. Pages 3 through 9 list, in matrix form, the flux in W/cm^2 received on various parts of the solar receiver. This particular run had each part of the receiver divided into a ten by ten matrix for flux examination since NTFINE, NWFINE and NCFINE were all chosen as ten on the control card.

I.3.5 Interpreting the Results

The computed results of the FLUXGO program begin on page 2 of the computer printout. Page 2 lists the percent capture, percent retroreflection and percent miss of the random generated sun rays. The percent capture is further divided as to capture location; the percent capture on the roof of the receiver, wall of the receiver and terminal concentrator are listed. The cosine factor and total power (in kW) captured by the receiver is also shown. The map on page 2 is a flux distribution of the actual number of rays coming from various sections of the heliostat field.

```
 INUM  METHOD LISTRA  IMAP  IFLUX  NTFINE NWFINE NCFINE  NITS  IFIELD
500     -1      0.      1      1      10     10     10     40     1
     .0066    0.0000  20.5000
   19.8110     .7645
    0.0000     .6700    0.0000
    0.0000   20.1299
   20.7594    1.3032     .3500
     .3628   20.4310
   20.3534   21.4757     .6350
   19.9846     .7309
   22.3826     .7002     .2100
    0.0000
    0.0000
    0.0000
    0.0000
    0.0000
    0.0000
    0.0000
    0.0000
    0.0000
    0.0000
     .9672     .9000  550.0000
     .9500
    3.1416    1.0472
454.83
.22741E-01
     .5913
```

6' T.T.
38 ft. Dia...
50.5° T.C.

CAPTOR	PCTDET	PCTFLS
87.91	9.3%	3.0%

PCTTOP	PCTWAL	PCTCON
12.8%	56.82	17.96

AVERAGE FIELD COSINE FACTOR IS .927. TOTAL POWER CAPTURED IS 369. KILOWATTS.

0	0	0	0	0	0	0	0	0	0	0	0	1	4	13	11	15	21	18	22	15	17	8	10	3	0	0	0	0	0	0	0	0	0	0	0	0	0	0
0	0	0	0	0	0	0	0	0	0	0	2	12	24	15	10	12	18	27	8	20	25	18	15	20	8	26	7	2	0	0	0	0	0	0	0	0	0	0
0	0	0	0	0	0	0	0	0	3	11	17	19	11	15	11	20	10	13	13	14	17	13	20	14	15	19	24	18	15	0	0	0	0	0	0	0	0	0
0	0	0	0	0	0	0	0	5	16	14	20	13	17	20	23	16	18	18	20	14	18	17	16	7	22	12	22	22	21	15	4	0	0	0	0	0	0	0
0	0	0	0	0	0	0	17	17	11	13	12	15	18	11	28	11	20	19	16	18	17	20	12	18	13	10	22	10	8	14	19	7	0	0	0	0	0	0
0	0	0	0	0	2	10	16	17	23	11	14	17	20	19	15	19	20	14	22	22	18	23	19	12	14	20	15	10	21	22	14	15	13	1	0	0	0	0
0	0	0	0	0	10	24	13	17	18	13	16	10	20	14	28	22	11	24	18	20	20	18	16	17	15	17	16	14	12	23	22	11	11	13	0	0	0	0
0	0	0	0	11	23	11	21	13	16	13	18	23	16	31	15	16	13	16	17	32	18	17	17	17	20	23	13	19	18	25	18	17	15	10	9	0	0	0
0	0	0	11	17	14	13	15	20	23	25	19	21	18	14	10	15	13	13	13	18	12	14	16	18	15	20	20	18	19	22	18	18	13	15	14	4	0	0
0	0	1	13	17	19	14	19	16	16	17	17	12	25	12	19	19	27	11	10	22	19	20	21	17	21	18	22	20	9	16	13	12	21	20	19	17	4	0
0	0	12	27	10	12	12	19	15	19	14	18	16	18	11	17	25	12	15	12	19	14	18	15	15	26	16	17	25	10	18	20	19	15	15	14	15	9	0
0	5	17	13	9	24	13	12	30	13	17	16	19	15	19	15	17	18	13	16	26	20	13	21	16	19	15	17	17	14	17	22	13	12	13	18	12	14	1	0
0	11	21	20	21	21	16	20	19	17	20	23	29	14	22	14	21	17	13	19	30	18	13	21	16	15	17	15	23	15	17	21	24	19	25	11	12	20	8	0
0	16	28	21	15	15	17	16	21	11	28	14	19	26	9	23	19	14	21	32	17	12	21	21	16	19	22	12	20	19	24	22	17	18	18	15	17	15	13	0
6	13	21	20	19	19	23	18	21	22	17	15	21	28	17	17	11	15	11	19	17	16	15	13	13	18	15	21	11	16	18	22	17	14	14	18	19	11	17	6
14	16	19	15	19	15	20	20	13	15	18	19	20	22	18	16	15	25	19	20	21	16	16	18	21	19	21	11	16	14	21	14	17	14	17	21	13	14	17	9
4	18	20	14	15	19	16	19	16	13	18	17	10	16	19	23	22	16	17	14	12	13	22	17	19	15	22	22	16	13	16	14	12	12	13	23	24	15	24	10
11	14	11	16	25	12	6	11	10	16	11	24	9	18	17	16	16	13	5	0	1	8	16	16	21	11	21	15	26	9	12	13	10	9	18	24	14	16	20	12
11	8	18	9	22	15	14	12	15	25	11	14	20	15	23	16	20	7	0	0	0	0	11	15	14	17	15	16	21	16	17	17	19	16	25	14	10	13	20	19
14	17	14	16	12	15	13	10	17	17	24	15	19	17	25	20	16	1	0	0	0	0	0	14	11	17	23	12	15	25	11	12	14	24	11	12	17	13	13	25
13	15	16	14	12	8	22	15	18	16	14	18	15	14	17	22	14	0	0	0	0	0	2	17	15	23	18	12	16	19	11	16	21	16	18	8	14	13	11	9
9	12	16	16	21	11	15	16	15	15	15	15	23	18	18	12	17	4	0	0	0	0	8	10	21	18	14	11	19	22	14	18	9	13	17	12	19	12	11	16
12	19	19	9	15	11	17	11	15	16	18	13	14	6	18	6	13	15	11	0	0	3	8	14	14	25	28	17	15	13	14	25	20	16	13	17	12	12	17	16
16	15	19	19	17	17	13	9	16	17	22	19	17	17	11	16	14	16	20	21	13	12	20	23	17	22	12	17	15	16	14	18	15	18	20	22	20	11	14	17
12	13	22	21	17	15	22	15	14	18	11	16	19	18	15	9	12	18	19	15	12	9	17	19	17	21	14	16	13	15	15	21	14	13	13	17	16	14	13	13
4	17	15	16	17	10	22	16	17	11	19	11	13	15	16	18	17	17	16	25	11	16	10	17	12	17	15	23	17	12	14	12	14	15	23	15	21	14	22	1
0	8	16	20	15	12	20	9	7	12	18	15	25	22	19	12	27	11	18	13	14	17	14	17	15	11	8	16	19	9	15	22	16	16	14	22	13	16	23	0
0	17	22	14	18	15	18	14	21	15	16	18	14	14	16	15	15	12	15	25	14	14	13	15	11	22	17	13	22	11	12	17	20	18	23	24	17	14	4	0
0	4	16	24	17	19	16	17	17	16	10	16	10	19	12	15	17	10	13	16	24	20	19	15	13	15	14	16	15	11	10	21	12	18	20	20	10	13	2	0
0	0	6	11	15	14	21	11	4	16	11	17	14	12	18	16	17	10	17	18	13	13	13	19	16	10	19	14	12	12	15	19	17	20	18	14	15	12	0	0
0	0	0	19	14	11	15	7	24	17	16	19	13	19	13	9	17	22	16	12	22	28	19	14	11	15	12	11	13	15	15	14	25	14	19	20	16	1	0	0
0	0	0	2	13	15	17	8	10	18	18	13	18	17	10	16	10	14	17	15	9	18	14	14	14	18	14	8	18	17	11	25	18	5	21	15	5	0	0	0
0	0	0	0	10	10	15	15	11	14	15	15	14	14	14	16	13	12	19	16	21	12	20	11	20	16	15	17	12	11	17	13	10	13	10	3	0	0	0	0
0	0	0	0	1	8	14	13	9	13	19	12	19	10	15	15	16	23	10	11	14	8	16	18	12	28	18	13	11	12	16	20	14	13	12	1	0	0	0	0
0	0	0	0	0	0	9	14	15	21	16	17	19	15	14	17	11	18	18	21	17	15	12	12	10	22	19	18	8	13	16	13	16	12	1	0	0	0	0	0
0	0	0	0	0	0	1	12	22	21	12	15	21	12	18	14	9	16	16	14	14	18	13	16	17	15	15	10	15	9	13	15	7	0	0	0	0	0	0	0
0	0	0	0	0	0	0	0	7	11	19	9	15	13	15	7	13	16	23	10	14	13	17	17	11	12	15	11	21	11	14	9	0	0	0	0	0	0	0	0
0	0	0	0	0	0	0	0	0	3	7	13	15	17	13	20	15	10	19	20	15	23	16	14	14	11	12	14	8	9	0	0	0	0	0	0	0	0	0	0
0	0	0	0	0	0	0	0	0	0	0	1	9	5	14	12	13	11	13	20	16	20	17	12	12	16	13	7	2	0	0	0	0	0	0	0	0	0	0	0
0	0	0	0	0	0	0	0	0	0	0	0	0	0	0	6	10	11	8	15	18	19	11	14	10	2	0	0	0	0	0	0	0	0	0	0	0	0	0	0

ENERGY DISTRIBUTION ON THE CAVITY ROOFTOP:

6	22.34
33	22.25
46	22.15
111	22.07
167	21.97
239	21.84
297	21.79
425	21.70
543	21.61
701	21.52

ENERGY DISTRIBUTION ON THE CYLINDER WALL=

1420	21.44
1461	21.38
1369	21.32
1324	21.25
1217	21.20
1126	21.13
1010	21.07
821	21.01
850	20.95
765	20.88

ENERGY DISTRIBUTION ON THE REENTRANT CONE:

448	20.83
457	20.80
447	20.75
420	20.72
427	20.69
383	20.65
309	20.61
279	20.57
229	20.54
192	20.50

ENERGY DISTRIBUTION AT THE CAVITY ROOFTOP:

22.337	2	0	0	1	0	1	1	0	0	1
22.247	2	6	3	4	6	3	2	2	2	3
22.156	3	8	4	5	7	3	4	4	6	2
22.065	10	7	10	5	18	14	9	16	12	10
21.974	18	12	16	21	12	15	16	18	20	19
21.884	27	23	26	17	23	32	26	19	22	24
21.793	34	32	31	34	19	25	22	40	33	27
21.702	49	41	37	44	40	50	44	43	38	39
21.612	53	58	56	52	41	59	63	51	57	53
21.521	76	65	75	51	71	68	63	71	77	84

ENERGY DISTRIBUTION ON THE CYLINDER WALL=

21.445	161	140	130	146	116	123	133	154	165	150
21.382	186	151	142	125	125	136	142	139	160	155
21.320	173	139	136	123	116	98	135	132	173	144
21.258	184	143	113	118	93	103	106	147	149	163
21.196	134	144	118	109	91	95	108	119	138	156
21.133	131	116	120	97	96	93	96	109	137	131
21.071	120	114	97	111	77	87	83	109	102	110
21.009	96	97	84	69	66	63	63	79	87	117
20.947	103	92	96	67	72	79	56	85	94	106
20.885	81	77	76	70	76	68	65	71	87	94

ENERGY DISTRIBUTION ON THE REENTRANT CONE:

20.835	48	48	36	42	27	53	47	56	37	54
20.798	48	50	46	39	50	45	43	49	39	48
20.760	47	49	43	45	50	56	34	42	42	39
20.723	41	31	35	52	45	43	44	50	37	42
20.686	35	43	44	50	40	35	38	55	38	49
20.649	34	33	39	33	35	39	53	51	34	32
20.611	34	27	28	22	28	39	27	36	35	29
20.574	24	21	27	22	33	28	35	35	24	30
20.537	27	22	25	18	15	28	26	23	21	24
20.500	18	19	19	18	23	24	21	14	22	14

ENERGY DISTRIBUTION ON THE CAVITY ROOFTOP:

-3.142 V	-2.513 V	-1.885 V	-1.257 V	-0.628 V	0.000 V	0.628 V	1.257 V	1.885 V	2.512 V	3.142 V
22.337	1.909	0.000	0.000	.954	0.000	.954	.954	0.000	0.000	.954
22.247	.636	1.909	.954	1.272	1.909	.954	.536	.636	.536	.954
22.156	.573	1.527	.763	.954	1.336	.573	.763	.763	1.145	.382
22.065	1.363	.954	1.363	.682	2.454	1.909	1.227	2.181	1.536	1.363
21.974	1.909	1.272	1.696	2.227	1.272	1.590	1.696	1.909	2.121	2.015
21.884	2.342	1.995	2.256	1.475	1.995	2.776	2.256	1.648	1.909	2.082
21.793	2.496	2.349	2.276	2.496	1.395	1.835	1.515	2.936	2.422	1.982
21.702	3.117	2.608	2.354	2.799	2.545	3.181	2.799	2.736	2.417	2.481
21.612	2.975	3.256	3.143	2.919	2.301	3.312	3.536	2.863	3.200	2.975
21.521	3.817	3.265	3.767	2.561	3.566	3.415	3.164	3.566	3.857	4.219

ENERGY DISTRIBUTION ON THE CYLINDER WALL=

	-3.142 V	-2.513 V	-1.885 V	-1.257 V	-0.628 V	0.000 V	0.628 V	1.257 V	1.885 V	2.512 V	3.142 V
21.445	13.837	11.884	11.035	12.393	9.847	10.441	11.290	13.073	14.006	12.733	
21.382	15.789	12.818	12.054	10.611	10.611	11.545	12.054	11.799	13.582	13.157	
21.320	14.685	11.799	11.545	10.441	9.847	8.319	11.460	11.205	14.685	12.224	
21.254	16.048	12.139	9.592	10.017	7.894	8.743	8.998	12.478	12.648	13.837	
21.196	11.799	12.224	10.017	9.253	7.725	8.064	9.168	10.102	11.714	13.242	
21.133	11.120	9.847	10.186	8.234	8.149	7.894	8.149	9.253	11.629	11.120	
21.071	10.186	9.677	8.234	9.422	6.536	7.385	7.046	9.253	8.658	9.338	
21.009	8.149	8.234	7.130	5.857	5.603	5.348	5.348	6.706	7.385	9.932	
20.947	8.743	7.810	8.149	5.687	6.112	6.706	4.754	7.215	7.979	8.998	
20.885	6.876	6.536	6.451	5.942	6.451	5.772	5.518	6.027	7.385	7.979	

RAD. AP = .3628 m (28.6")

ENERGY DISTRIBUTION ON THE REENTRANT CONE:

-3.142 V	-2.513 V	-1.885 V	-1.257 V	-0.628 V	0.000 V	0.628 V	1.257 V	1.885 V	2.512 V	3.142 V
20.835	5.617	5.617	4.213	4.915	3.160	6.203	5.500	6.554	4.330	5.320
20.798	5.875	6.119	5.630	4.773	6.119	5.508	5.263	5.997	4.773	5.875
20.760	6.028	6.285	5.515	5.772	6.413	7.183	4.361	5.387	5.387	5.002
20.723	5.524	4.177	4.716	7.006	6.063	5.794	5.928	6.737	4.985	5.659
20.686	4.966	6.101	6.243	7.094	5.676	4.966	5.392	7.804	5.392	6.953
20.649	5.095	4.945	5.844	4.945	5.245	5.844	7.942	7.642	5.095	4.795
20.611	6.033	4.286	4.445	3.493	4.445	6.191	4.286	5.715	5.556	4.604
20.574	4.051	3.544	4.557	3.713	5.570	4.726	5.907	5.907	4.051	5.063
20.537	4.864	3.964	4.504	3.243	2.702	5.044	4.684	4.144	3.793	4.324
20.500	3.477	3.671	3.671	3.477	4.443	4.636	4.057	2.705	4.250	2.705

TABLE I-1. FLUXGO INPUT DATA DECK SET GROUPING

CARDS	SET NAME	FUNCTION
1	Control	Determines number of rays (sample size) and controls processing and output options.
2-10	Geometry	Describes the geometry of the optical model.
11-20	Aiming	Defines the target bands for execution of a multiple aim point analysis.
21	Heliostats	Defines field reflectivity and surface area.
22-23	Solar	Defines solar power constant and sun angle.

TABLE I-2
FLUXGO INPUT DECK FORMATS AND VARIABLE NAMES

CARD NO.	FORMAT	VARIABLE NAMES	MEANINGS
1	10I4	INUM	Number of rays processed per iteration
		METHOD	Aiming method key; search, multiple or single
		LISTRA	Ray listing option key
		IMAP	Cavity ray hit mapping key
		IFLUX	Cavity flux mapping key
		NTFINE	Number of horizontal bins on cavity roof top
		NWFINE	Number of horizontal bins on cavity wall
		NCFINE	Number of horizontal bins on reentrant cone
		NITS	Number of program iterations (Multiplier for INUM)
		IFIELD	Mirror field brightness display key
End Set 1, Control			
2	3F10.4	SIGMA	Field aiming error deviation, spot radius, radians
		APTILT	Aperture tilt, northward from vertically downward, radians
		AIMPT	Height of aim point in global Z coordinates, meter
3	2F10.4	RNORM0	Normalizing radius of heliostat field, meter
		RNORM1	Normalizing radius of concentrator mouth, meter
4	3F10.4	XCEN0	Global X, (easterly) coordinate of center of field, meter
		ZOG	Global Z, (vertical) coordinate of heliostat plane, meter
		YCEN0	Global Y, (northerly) coordinate of center of field, meter
5	2F10.4	YCEN1	Global Y, (northerly) coordinate of center of concentrator, meter
		ZCEN1	Global Z (vertical) coordinate of center of concentrator mouth, meter
6	3F10.4	ZVRTX2	Global Z coordinate of vertex of concentrator cone, meter
		THA2	Tangent of half angle of concentrator cone
		REFL	Reflectivity of concentrator
7	2F10.4	RAPCAV	Radius of aperture of cavity, meter
		HAPCAV	Global Z coordinate (height) of aperture of cavity, meter
8	3F10.4	ZMIN5	Global Z coordinate of base of cavity wall, meter
		ZMAX5	Global Z coordinate of top of cavity wall, meter
		RCYL	Cylindrical radius of cavity wall, meter
9	2F10.4	ZVRTX4	Global Z coordinate of vertex of reentrant cone, meter
		THA4	Tangent of half angle of reentrant cone

TABLE I-2
FLUXGO INPUT DECK FORMATS AND VARIABLE NAMES (Cont'd)

CARD NO.	FORMAT	VARIABLE NAMES	MEANINGS
10	3F10.4	ZVRTX6	Global Z coordinate of vertex of cavity roof top cone, meter
		THA6	Tangent of half angle of cavity roof top cone
		EMIS	Emissivity of cavity roof top
End Set 2, Geometry			
11	F10.4	AIM(1)	Rl if .15 < RZERO < .3468
12	F10.4	AIM(2)	Rl if .3468 < RZERO < .4669
13	F10.4	AIM(3)	Rl if .4669 < RZERO < .5619
14	F10.4	AIM(4)	Rl if .5619 < RZERO < .6430
15	F10.4	AIM(5)	Rl if .6430 < RZERO < .7150
16	F10.4	AIM(6)	Rl if .7150 < RZERO < .7804
17	F10.4	AIM(7)	Rl if .7804 < RZERO < .8407
18	F10.4	AIM(8)	Rl if .8407 < RZERO < .8969
19	F10.4	AIM(9)	Rl if .8969 < RZERO < .9499
20	F10.4	AIM(10)	Rl if .9499 < RZERO < 1.000
End Set 3, Aiming			
21	3F10.3	AREAMR	Area of individual mirror, meter^2
		REFMIR	Reflectivity of mirror
		QTYMIR	Number (quantity) of mirrors in field
End Set 4, Heliostats			
22	F10.4	SOLAR	Solar Constant, kilowatts meter^{-2}
23	2F10.4	SUNAZ	Sun azimuth, measured from north, radians
		SUNEL	Sun elevation, measured from horizon, radians

TABLE I-3

CONTROL PROCESSING AND OUTPUT OPTIONS

INUM	Number of rays per iteration. A limit of 500 rays per iteration is imposed by storage limitations. (Total number of rays processed is INUM times NITS). INUM resets to 500 if INUM is input greater than 500.
METHOD	Determines aim point calculation routine
1	Activates search aiming routine. Performs 100 runs where ten radial bands of field aim at 10 bands of radius. (This is used to facilitate identification of efficient multiple aim point strategies).
0	Activates multiple aim point strategy wherein radial bands of the field are aimed at specified radial bands of the terminal concentrator. The field bands and concentrator bands are specified and correlated by ten cards of the input data deck; cards numbered 11-20 inclusive.
1	Activates single point aim strategy wherein all mirrors are aimed at a single point on the optical axis of the concentrator. The Z coordinate (height) of the aimpoint is specified by the third entry on the second card of the input data deck.
LISTRA	
0	Suppresses the detailed ray history listing.
1	Activates the detailed ray history listing. NOTE: LISTRA overrides to zero if NITS is set greater than 1.

TABLE I-3

CONTROL PROCESSING AND OUTPUT OPTIONS (Cont'd)

IMAP

0 Suppresses ray count map inside cavity

1 Activates ray count map inside cavity

NOTE: If IFLUX is to be set at 1 then IFLUX must be 1.

IFLUX

0 Suppresses Flux Map

1 Activates Flux Map

NOTE: It is not necessary to call IFLUX if only IMAP is wanted.

NTFINE

1 < NTFINE < 20 (usually NTFINE = 10)

Divides cavity roof top into NTFINE vertically separated zones (or bins).

NWFINE

1 < NWFINE < 20 (usually NWFINE = 10)

Divides cavity wall into NWFINE vertically separated zones.

NCFINE

1 < NCFINE < 20 (usually NCFINE = 10)

Divides reentrant cone into NCFINE vertically separated zones.

NITS

1 < NITS < 9999 (NITS usually 1 or 40)

Sets number of iterations for program.

TABLE I-3

CONTROL PROCESSING AND OUTPUT OPTIONS (Cont'd)

NOTE: NITS should be used with discretion if INUM = 500 and NITS = 1, then 500 rays are processed and this is sufficient for a ray history type output. If INUM = 500 and NITS = 40 then 20,000 rays are processed and this is sufficient for a ray count for Flux Map. Since this program uses Monte Carlo techniques, the random errors generally vary as $(\text{INUM} * \text{NITS})^{-1/2}$. Therefore, for example, if INUM = 500 and NITS = 80 then run time is doubled but accuracy only increases from about 98.5% to 99%.

IFIELD

-1 Suppresses all output except mirror field display. Mirror field display shows effect of cosine factor on distributed field brightness. Insofar as there are approximately 1200 active field bins the product of INUM * NITS should be at least 20,000 for this output option to be meaningful. This option provides an economical means of mapping field brightness without processing ray histories.

0 Suppresses mirror field display. Does not affect other program options.

1 Activates mirror field display but does not affect other program options.

Page 3 of the printout lists the number of sun rays incident at different heights within the receiver. The numbers on the right (20.50-22.34) are the heights in meters above the ground, and the numbers to their left are the number of sin rays incident on the receiver in the band located at the indicated height level. As can be noticed, the greater majority of sun rays land on the cylinder wall for optimum heat transfer and maximum receiver efficiency.

Two dimensional flux distribution of the number of sun rays on various receiver sections are also available (see printout pages I-12 through I-14). The numbers on the far left are height in meters above the ground. The two-dimensional array is a ten by ten since NTFINE, NWFINE and NCFINE were chosen as 10 on the control card. Further magnification of flux distribution is limited only by the number of characters per printed line (132 on the CDC system).

Printout pages I-16 and I-17 also show a two-dimensional flux distribution of the receiver; but instead of the matrix numbers representing number of sun rays, they are the actual flux in W/cm^2.

I.4 ANSYS

The ANSYS Engineering Analysis Software has been applied to the solar receiver design shown in Figure I-3. This simulation performs all the relevant heat transfer calculations encountered in solar receiver design to the accuracy required by a given design problem.

I.4.1 Design Preparation

Given the surface distribution of input heat fluxes on the receiver structure (e.g., honeycomb), the resulting temperature distributions and heat outputs for an airstream in contact with this structure can be determined by the analysis of many simultaneous local convection,

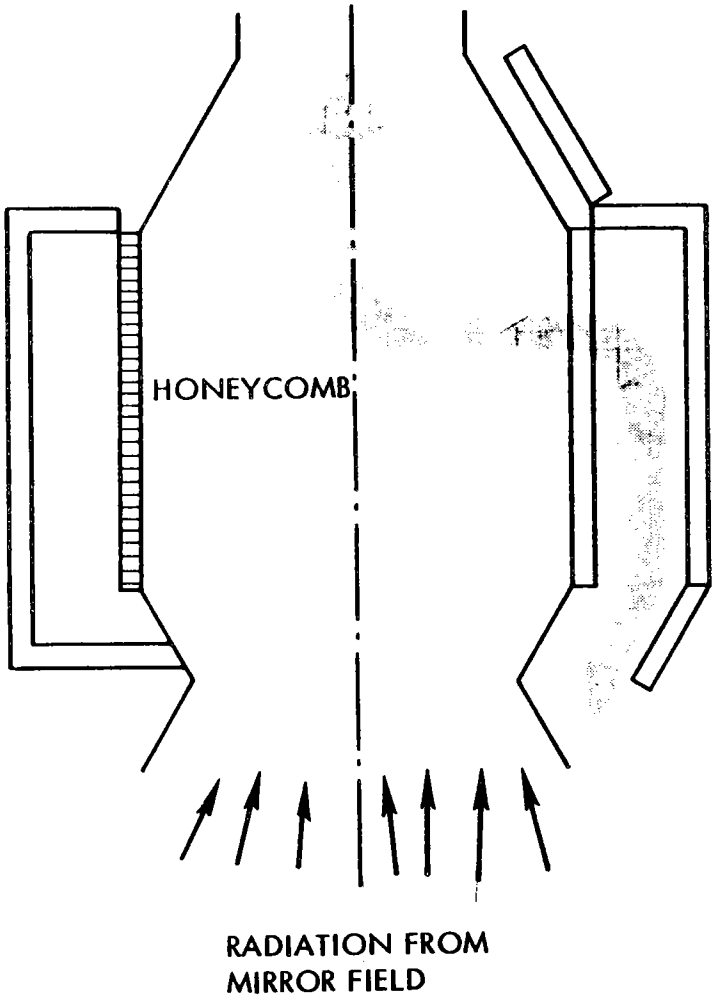

PRINCIPAL PARAMETERS MODELED

HONEYCOMB EMISSIVITY	:	0.90
APERTURE AREA	:	0.203 M^2 (2.18 FT^2)
HONEYCOMB AREA	:	2.04 M^2 (22 FT^2)
CAVITY RATIO	:	10
TUBE DIAMETER	:	1.97 MM (0.0774 IN)
SOLID FRACTION	:	0.352
TUBE LENGTH	:	61 MM (2.4 IN)
INSOLATION	:	384 KW (1.309 X 10^6 BTU/HR)
CONCENTRATION RATIO	:	2000 (NOMINAL FOR GIT MIRROR FIELD)

Figure I-3. Cylinder Design for Honeycomb, Reverse Flow

conduction and radiation processes. The ANSYS Engineering Analysis Software, developed by Swanson Analysis Systems, is suitable for both this thermal analysis and any subsequent mechanical stress analysis.

In this simulation, each honeycomb element in the receiver is modeled by a tube with a specified diameter and length. Each tube is then divided into a specified number of segments joined by nodes. The analysis then treats each segment separately and later combines the results to form the model.

I.4.1.1 Input

The input to the solar receiver simulation is a representation of solar energy input to the system. This radiant energy from sunlight focused on the receiver cavity is represented as a specified heat input at the irradiated model nodes. Since the net radiation input to the nodes is specified, any thermal reradiation toward the focusing mirror areas should be omitted. This condition is satisfied through corresponding reductions in the configuration factors of the elements that reradiate in the direction of the mirror field.

I.4.1.2 Nodes

The node is the basic partitioning element in the solar receiver simulation. Each node represents a region with a distinct temperature. The temperature region between nodes should be represented by a linear function. Thus, temperature differences, which are generally nonlinear, can be represented by a series of nodes connected by straight line segments. The accuracy with which the temperature is represented is dependent on the number of nodes selected to represent the model. The more nodes chosen, the more accurate (and refined) will be the simulation.

I.4.1.3 Heat Balance Equations

Following the selection of nodes, a set of heat balance equations must be formulated consistent with the set of nodes. Heat balance equations are expressions of conservation of energy. For each element (heat flow path between nodes), there is an equation of the form:

$$\dot{Q}_{ij} = f\ (T_i,\ T_j)$$

where

i and j are the nodes at each end of the element

T_i is the higher temperature

T_j is the lower temperature

$\dot{Q}_{ij}$ is the heat flow from i to j

Energy (or heat) is transferred by four processes:

Conduction: $Q_{ij} = KA\ (\text{grad } T) - \frac{KA}{x}\ (T_i - T_j)$

Convection: $Q_{ij} = LA\Delta T = LA\ (T_i - T_j)$

Fluid Flow: $Q_{ij} = \frac{dm}{dt}\ c_p\ (T_i - T_j)$

Radiation: $Q_{ij} = \sigma EAF_{ij}\ (T_i^4 - T_j^4)$

where:

K = Conductivity

h = Film coefficient for convection

$\frac{dm}{dt}$ = mass flow rate

ΔT = Temperature difference from i to j = $T_i - T_j$

c_p = heat capacity

σ = Stefan-Boltzmann constant

E = Emissivity

F_{ij} = radiation configuration factor

x = separation between i and j

A = cross sectional area for heat flow

By applying these equations to every element in a model, and observing all the "network laws" (Kirchoff's Laws), a set of simultaneous equations can be developed which couple the heat flows to the node temperatures. Using this theory, boundary conditions or constraints, such as values of temperature or heat flow, are maintained constant.

If all the heat transfer processes occur together, the heat transfer equations are nonlinear. Fluid flow rates may also be coupled to pressure gradients, requiring additional simultaneous equations. In addition, the material properties (such as c_p, h or K) may be temperature dependent, adding further nonlinearity.

Finally, time dependence may be involved, adding terms of the form

$$m_i \; c_p \; \frac{\partial T_i}{\partial T}$$

at each node (i) to which a mass (m_i) is ascribed.

Radiant energy from sunlight focused on the receiver cavity is represented as a specified heat input at the irradiated model nodes. The flux distribution on the surfaces of the receiver honeycomb are calculated by Monte Carlo techniques. An earlier Sanders study* showed that for silicon carbide (SiC), with emissivity greater than 0.9, an adequate approximation could be obtained by curve fitting to Monte Carlo samples. This empirical formula can be stated as follows:

---

*Final Report for a 10 KWt Solar Energy Receiver
DOE Contract #EY-76-C-03-1533
Report #COO-2823-2

$$\dot{q}_i = \frac{\dot{Q}(1-f)}{r_c} \int_{Z_i}^{Z_{i+1}} \exp\left(-Z^2/2\sigma^2\right) \qquad (1)$$

$$\dot{q}_o = \frac{\dot{Q}f}{r_c} \qquad (2)$$

$$\sigma = 50N_F/2 \qquad (3)$$

where: f = solid fraction of honeycomb

N_F = effective f/number of incoming radiation at average tube location

$$N_F = \frac{1}{2 \tan \theta_{MAX}}$$

$\theta_{MAX} = \frac{1}{2}$ (maximum angular subtense of incoming radiation at average tube)

D = diameter of honeycomb tube

$\dot{Q}$ = total solar energy entering receiver aperture

r_c = cavity ratio = $\frac{\text{active nominal honeycomb face area}}{\text{aperture area}}$

Z_i = distance of a given node from front of honeycomb tube, i = 1 is first, i = 2 is second node, etc. (not same as node numbers in ANSYS model)

q_o = solar heat input at front face of honeycomb tube

$\frac{1}{2}q_1$ = solar heat input at first node inside honeycomb tube

$\frac{q_i + q_i\text{-}1}{2}$ = solar heat input at nodes beyond first node inside honeycomb tube (i = 2, 3, 4,....)

(Terms less than about ($q_{iMAX}/100$) are ignored.)

These equations can be used to find the heat inputs to various nodes on the tube model, with SiC as honeycomb material. For general use and to avoid an empirical curve fit, a FORTRAN program (TFLUX) was written to calculate the heat flux inputs directly for each ANSYS model node. These inputs are based on input values of emissivity (E) which can be any value between 0 and 1, solid fraction (F), f/number (FNO) and tube diameter (D).

The configuration factor is one of the parameters required to characterize any thermal radiation link. This factor is a geometric integral for which values are tabulated in many heat transfer handbooks.

Where A_1 and A_2 are the two areas connected by the radiation link, the configuration factor (F_{1-2}) is

$$F_{1-2} = \frac{1}{A_2} \int_{A_1} \int_{A_2} \frac{\hat{n}_1 \cdot \vec{r}\vec{r} \cdot \hat{n}_2}{r^4} \, dA_1 \, dA_2$$

$$= \frac{1}{A_2} \int_{A_1} \int_{A_2} \frac{\cos \theta_1 \cos \theta_2}{r^2} \, dA_1 \, dA_2$$

where

r = distance between area elements dA_1 and dA_2

$\vec{r}$ = vector from element dA_1 to dA_2

$\hat{n}_1$ = unit vector normal to dA_1

$\hat{n}_2$ = unit vector normal to dA_2

θ_1 = angle between $\hat{n}_1$ and $\vec{r}$

θ_2 = angle between $\hat{n}_2$ and $\vec{r}$

dA_1 = area element of surface 1 at one end of the radiation link

dA_2 = area element of surface 2 at other end of the radialion link

Where either A_1 or A_2 includes a mirror field at one end and a heat flux input at the other, the mirror area is estimated and subtracted or removed from the integration zone. This adjustment is consistent with the assumption that the heat input is a net value, and therefore is not subject to reradiation loss back to either the sun or the focusing mirrors which are in the ray paths. By arbitrary choice, in the current model the adjustments are applied to the configuration factor, while the true areas are input without modification. Configuration factors are listed in Table I-4.

I.4.2 Solutions

The solution is divided into two parts: (a) a temperature/pressure part, and (b) a heat flow part. Typical of plots of temperature and pressure profiles through the honeycomb are shown in Figures I-4 and I-5.

An illustration of outlet air temperature variation for a receiver under transient conditions is shown in Figure I-6.

TABLE I-4. ESTIMATES OF CONFIGURATION FACTORS FOR SOLAR RECEIVER DESIGN MODEL

1. Between model segments inside a honeycomb tube

- Tube diameter = D
- Segment length (equal for both segments) = ΔZ

$$F = 1 - \frac{\left(\frac{\Delta Z}{D}\right)^3 + \frac{3}{2}\frac{\Delta Z}{D}}{\left[\left(\frac{\Delta Z}{D}\right)^2 + 1\right]^{3/2}}$$

Typical Values:

$\frac{\Delta Z}{D}$	F
0.1	0.85
0.2	0.71
0.3	0.58
0.4	0.47
0.5	0.37
0.6	0.30
0.75	0.21
1.0	0.116
1.5	0.040
2.0	0.016

2. From inside first segment of tube to cavity

(crude estimate)

- x = cavity diameter
- D = honeycomb tube diameter
- Length of segment less than D

TABLE I-4. ESTIMATES OF CONFIGURATION FACTORS FOR SOLAR RECEIVER DESIGN MODEL (Continued)

$$F \approx \frac{1}{2}\left[\frac{\left(\frac{x}{D}\right)^2 + \frac{1}{2}}{\sqrt{\left(\frac{x}{D}\right)^2 + 1}} - \frac{x}{D}\right]$$

Sample values

$\frac{x}{D}$	F
0.5	0.17
0.75	0.10
1	0.061
2	0.012
3	0.004
5	0.00096
10	0.000125
20	0.000016

3. From front face of tube to cavity and to aperture

Note: approximation considered to hold only if $r_c > 5$

(a) Spherical Matrix Arrangement

r_c = cavity ratio

θ_{RIM} = half angle of mirror field

β = half angle of sphere measured from its radius

direct through aperture

$$F_{AP} \approx \sin\left\{\tan^{-1}\left[\frac{\text{radius aperture}}{\text{distance:aperture-apex of honeycomb}}\right]\right\}$$

TABLE I-4. ESTIMATES OF CONFIGURATION FACTORS FOR SOLAR RECEIVER DESIGN MODEL (Continued)

$$\approx \sin\left\{\tan^{-1}\left[\frac{1}{\sqrt{\frac{r_c}{2(1-\cos\theta_{RIM})}} - \frac{1}{\tan\theta_{RIM}}}\right]\right\}$$

To rest of honeycomb

$$F_{self} \approx \frac{\Omega}{4\pi} = \frac{1}{2}\cos\left(\frac{\pi-\beta}{2}\right)$$

To cavity

$$F_{CAV} = 1-F_{AP} - F_{self}$$

(b) Cylindrical Matrix Arrangement

A_{AP} = aperture area

d = diameter of cylinder

r_c = cavity ratio

θ_2, θ_1 = angles of cavity aperture extremes from normal at average honeycomb tube

through aperture:

$$F_{AP} \approx \sin\theta_2 - \sin\theta_1$$

TABLE I-4. ESTIMATES OF CONFIGURATION FACTORS FOR SOLAR RECEIVER DESIGN MODEL (Continued)

$$\gtrsim \sin\left\{\tan^{-1}\left[\frac{r_c\ A_{AP}}{\pi d^2}\right]\right\}$$

(correction for reradiation to mirrors applies here)

$$F_{self} \approx 2 \sin\left\{\tan^{-1}\left[\frac{r_c\ A_{AP}}{2\pi d^2}\right]\right\}$$

$$F_{CAV} = 1 - F_{AP} - F_{self}$$

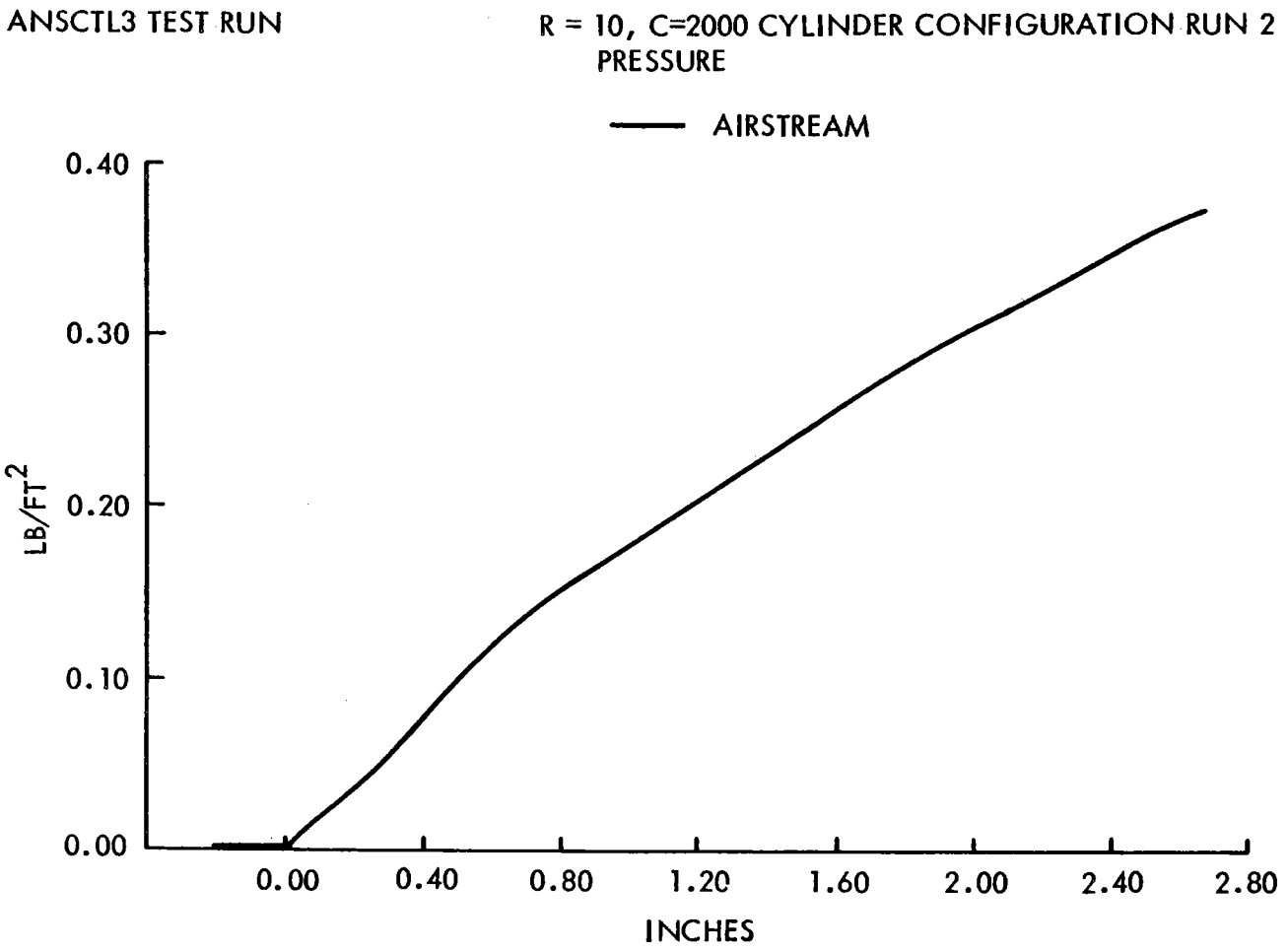

Figure I-4. R=10, C=2000; Cylinder Configuration, Run 2, Pressure

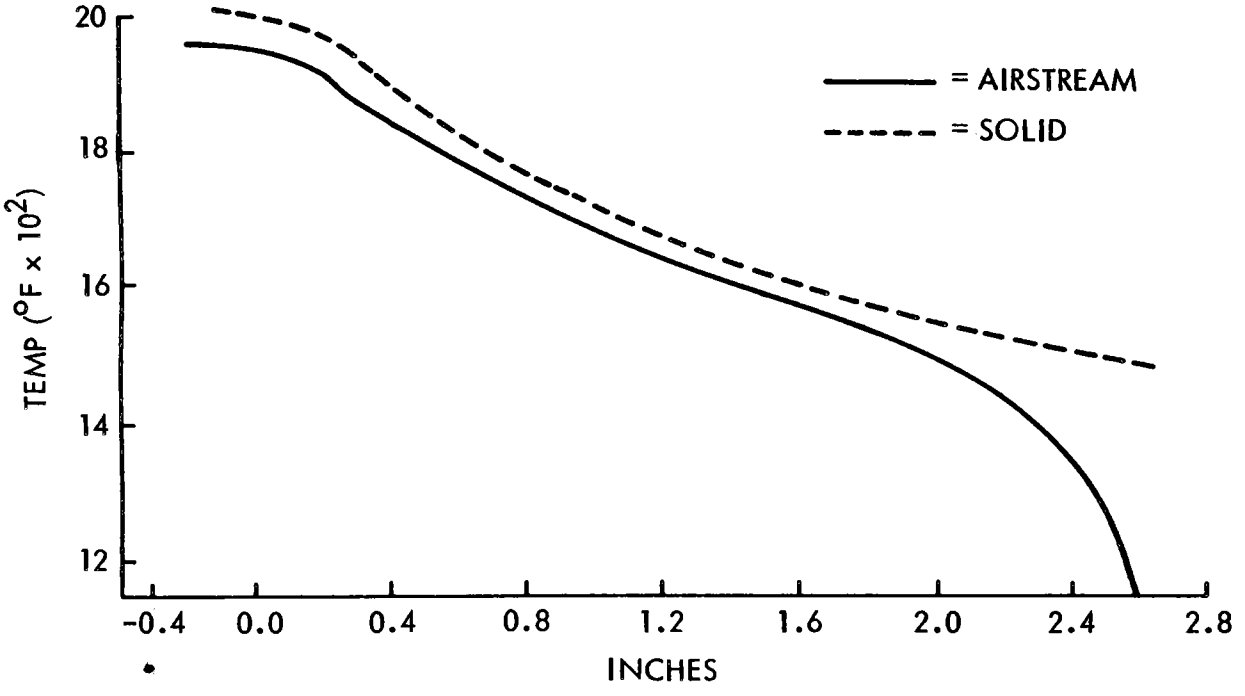

Figure I-5. R=10, C=2000; Cylinder Configuration, Run 2, Temperature Profiles

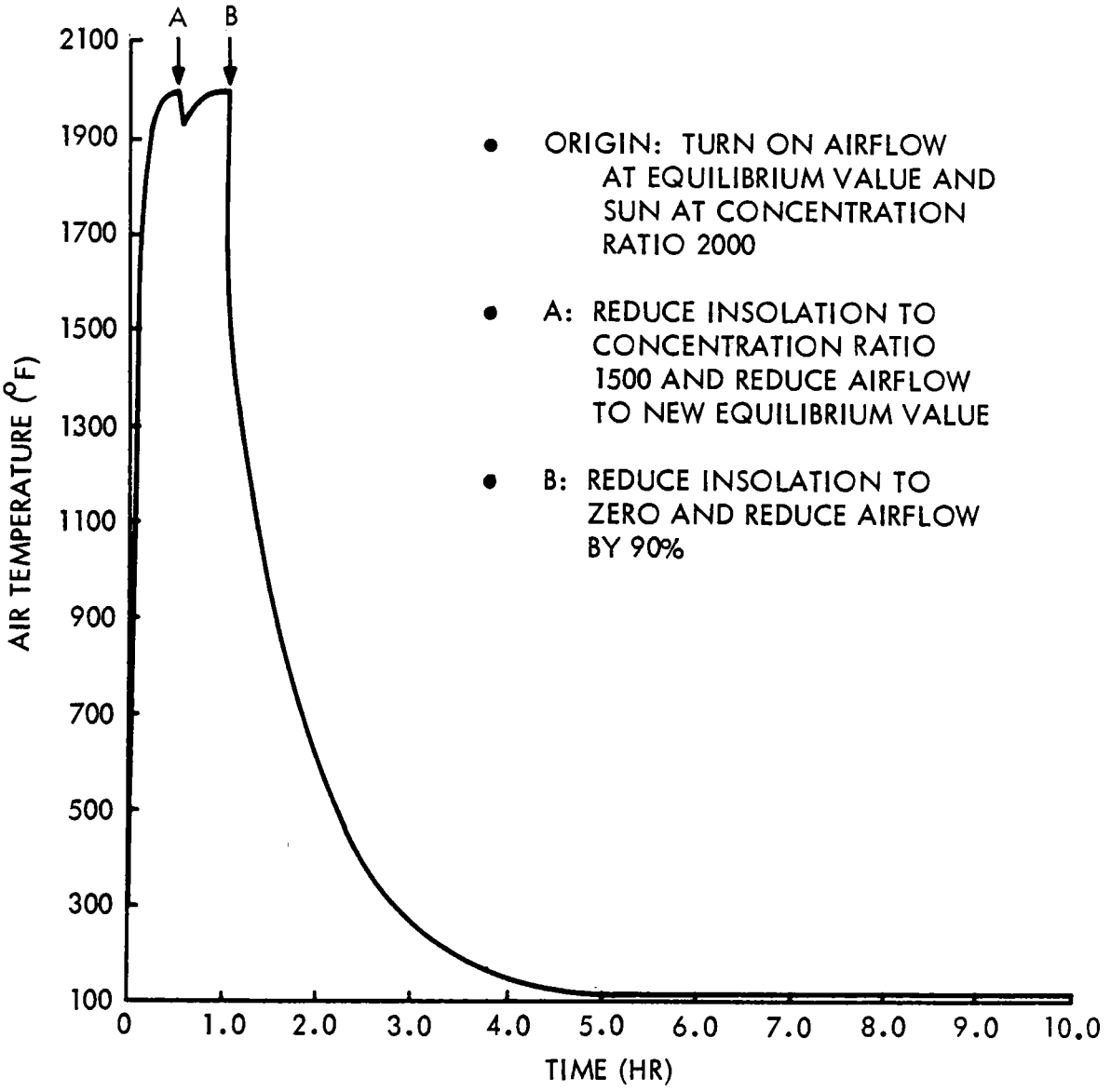

Figure I-6. Transient Simulation in Reverse Flow Cylinder Solar Receiver Design

APPENDIX II

TEST PLAN FOR 1/4 MWt SOLAR RECEIVER AT ACTF

TABLE OF CONTENTS

TABLE OF CONTENTS (Continued)

ATTACHMENTS

LIST OF ILLUSTRATIONS

LIST OF TABLES

SECTION 1
INTRODUCTION

Under contract to the Department of Energy (DOE), Sanders Associates, Inc., is developing a solar receiver and air heat exchanger unit (receiver) for use in advanced solar powered, electric generating plants. The function of the receiver is to absorb the concentrated solar energy focused on it by a large mirror field and transfer this energy to an airstream, where eventually it will drive an open cycle Brayton turbine powered generator. Described in this test plan is the program to measure the performance of a 1/4 MWt model of the receiver at the Advanced Components Test Facility (ACTF) located at the Georgia Institute of Technology in Atlanta, GA. The plan for preliminary testing at Sanders Associates, Inc., prior to shipping to GIT is also included in this plan.

SECTION 2
OBJECTIVES

The objectives of this test program are as follows:

a. Measure the efficiency of the receiver in the collection of solar energy

b. Measure the convective heat loss associated with an open cavity air receiver

c. Design and test a receiver concept which is scalable to larger receivers

d. Demonstrate structural integrity of receiver design at air temperatures up to 1100^{o}C

e. Demonstrate a mode of operation where the outlet air temperature is held constant as insolation varies with time

SECTION 3
TEST ARTICLE

A Sanders platform will be mounted at the top of a 76 foot tower located in the center of the mirror field. On the platform are three assemblies (see Figure 3-1 block diagram) connected by 275 feet of cable to a remote control panel capable of operating the receiver from the control room at the bottom of the tower. The three platform assemblies are:

- Receiver assembly
- Burner assembly
- Cooling air assembly

3.1 PLATFORMS

The Sanders platform is approximately 4 meters square, constructed of I-beams and channels, and serves as the foundation for mounting the solar receiver assembly, burner and cooling air supply (see Figure 3-2). The weight of the hardware fully assembled is approximately 5500 kg. It will be shipped to Georgia Institute of Technology after shakedown and calibration testing at Sanders in Merrimack, NH. A separate shutter assembly, mounted on the GIT tower below the plane of the terminal concentrator, is required along with the test platform. This shutter will provide another level of safety in case of equipment malfunction.

A second test platform will be supplied by Sanders to be used during the calibration phase to obtain the flux distribution on the plane of the solar absorption panels when the terminal concentrator is in place. On top of this platform is mounted the Sanders' rotating flux rake and below it is the water-cooled terminal concentrator.

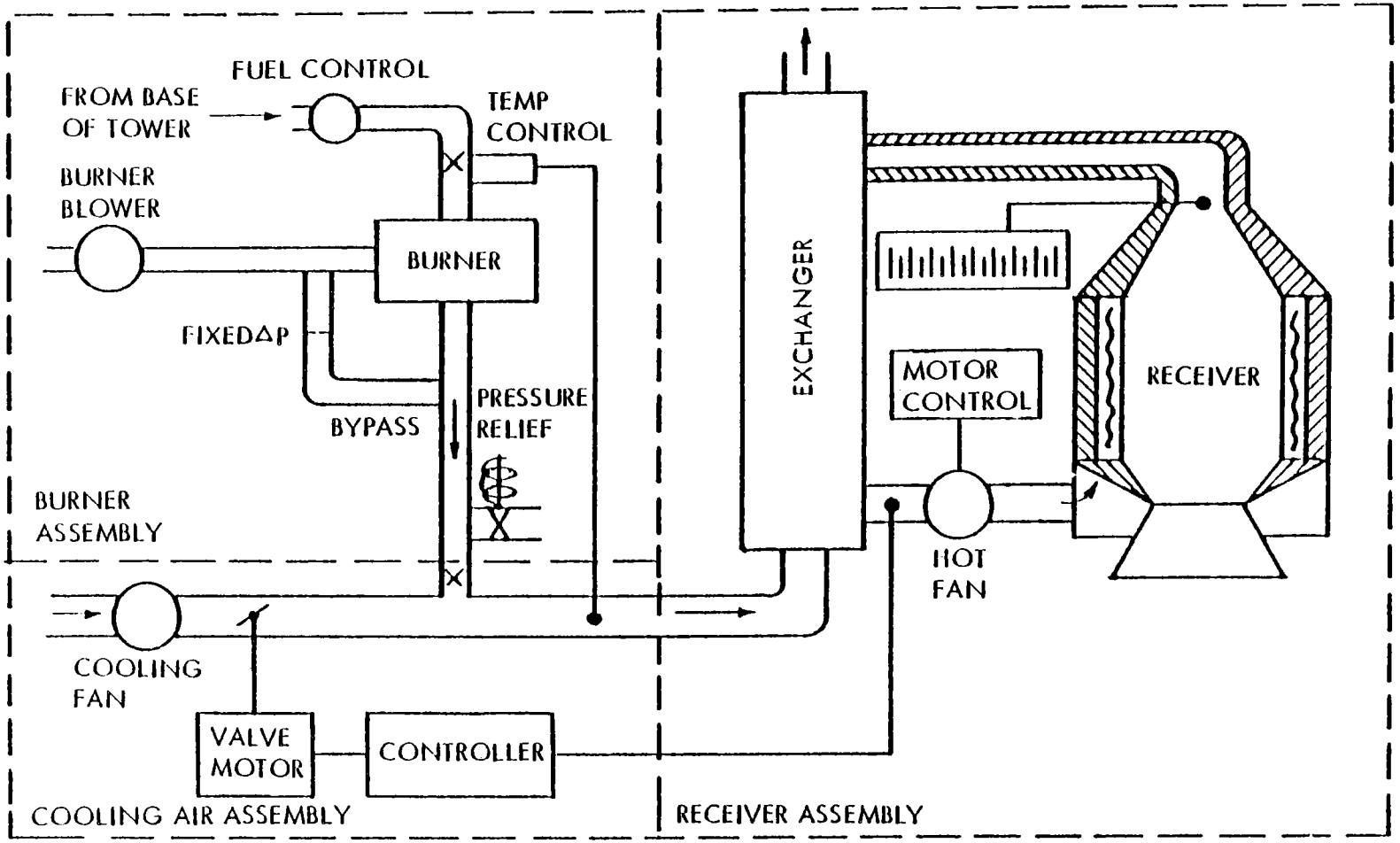

Figure 3-1. 1/4 MWt Receiver Block Diagram

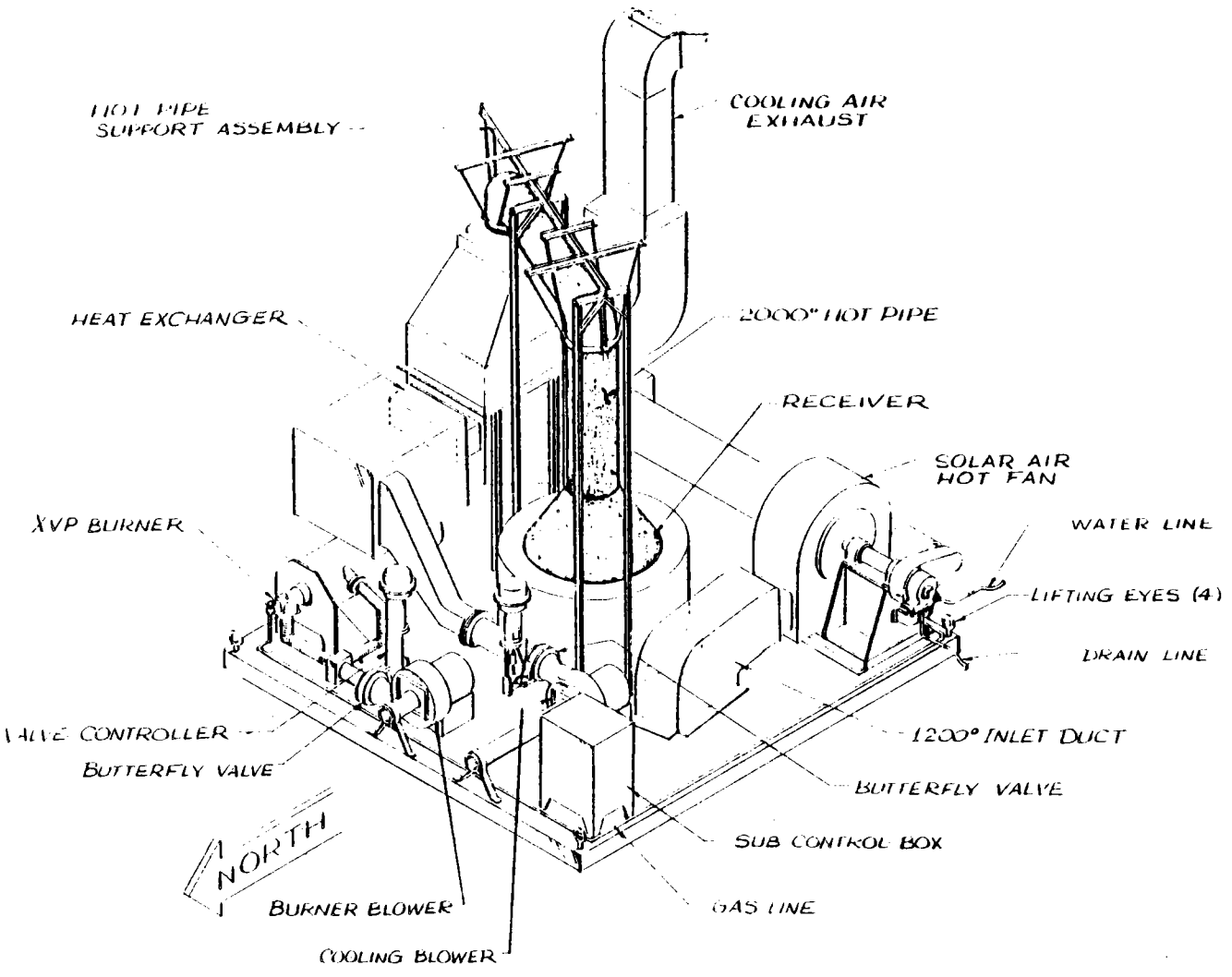

Figure 3-2. Platform

3.2 SOLAR RECEIVER ASSEMBLY

Solar energy enters the open cavity of the receiver and is absorbed in the ceramic matrix structure. Air from the high temperature fan is heated by passing through the ceramic and is then circulated to the air-to-air heat exchanger where it is cooled prior to re-entering the fan and receiver. A separate water cooling system is mounted on the platform to maintain the fan bearings at a safe operating temperature and prevent overheating of the terminal concentrator.

The inlet air temperature to the receiver is limited to 650^{o}C by the temperature limitation on the 15 hp hot air fan. Airflow can be varied from 0.0 kg/sec to 0.57 kg/sec by controlling the speed of the fan motor. Maximum outlet temperature of the receiver is limited to approximately 1150^{o}C.

3.3 BURNER

The gas-fired hot air supply is needed to check out the equipment prior to shipment to GIT. It will also be available at GIT for bringing the equipment up to test temperatures prior to bringing the mirror field into position (soft start).

The hot air supply consists of a gas burner, blower and controls. The output temperature of the burner is approximately 1400^{o}C, which must be cooled by excess airflow to a maximum of 800^{o}C prior to entering the heat exchanger. Fuel for the burner is piped from a 500/1000 pound tank on the ground. The maximum heat input to the receiver system is 440 kW.

3.4 COOLING AIR SUPPLY

The solar heat received in the ceramic matrix is removed from the receiver assembly by the cool air which passes through the heat

exchanger. Supplying the cool air is a circulating fan and a motorized flow control valve which controls the volume of ambient air passing through the heat exchanger. The airflow is controllable from 0 to 0.9 kg/sec and can be supplied simultaneously with the hot air supply.

3.5 CONTROL PANEL

The control panel is hard-wired to the platform and contains all the switches, meters, and controls needed to start up, operate, and shut down the equipment. Safety alarms and the switches for key pressures and temperatures are mounted on the control panel. Safety alarms sound when an over-temperature occurs in: (a) the bearings, (b) receiver outlet temperature, and (c) burner outlet temperature.

Further thermal analysis of receiver performance will be available from a long wavelength imaging receiver filtered to view both the front and rear surfaces of the honeycomb in the 2.75μ to 2.85μ spectral band. This unit will be mounted outside the receiver and will view its ceramic matrix through quartz windows.

3.6 FLUX RAKE

The flux rake, supplied by Sanders, will use 25 HYCAL-1112-B calorimeters mounted on a water-cooled beam to sweep out the plane of the inside of the receiver and measure the solar flux distribution and its variations throughout the day. The location of each sensor is designed to measure the total flux coming in which can then be compared with the values measured with the Georgia Tech flux rake located just below the plane of the terminal concentrator.

The instrumentation details are described in Table 3-1.

DATE_____

TRANSDUCER LABEL	TRANSDUCER LOCATION
TC-1	Receiver Inlet - North
TC-2	Receiver Inlet - South (also on control)
TC-3	Receiver Inlet
TC-4	Receiver Outlet - South
TC-5	Receiver Outlet - Center Tube (also on control console)
TC-6	Receiver Outlet
TC-7	Hot Air Flow - Into Fan - On Wall
TC-8	Hot Air Flow, Into Fan - On Center Line
TC-9	Heat Exchanger Air Inlet - Cooling
TC-10	Heat Exchanger Cooling Air Inlet
TC-11	Heat Exchanger Cooling Air Outlet
TC-12	Heat Exchanger Cooling Air Outlet
TC-13	Heat Exchanger Tube Surface
TC-14	Heat Exchanger Tube Surface
TC-15	S_iC Honeycomb Support - Top, wire #40
TC-16	S_iC Honeycomb Support - Center, wire #41
TC-17	S_iC Honeycomb Support - Bottom, wire #42
TC-18	S_iC Honeycomb, Top Panel, Front Face, Top Position, wire #43
TC-19	S_iC Honeycomb, Front Face, Middle of Top Panel, wire #45
TC-20	S_iC Honeycomb, Front Face, Bottom of Top Panel, wire #45
TC-21	S_iC Honeycomb, Front Face, Top of Bottom Panel, wire #46
TC-22	S_iC Honeycomb, Front Face, Middle of Bottom Panel, wire #43

DATE_____

TRANSDUCER LABEL	TRANSDUCER LOCATION
TC-23	S_iC Honeycomb, Front Face, Bottom of Bottom Panel, wire #48
TC-24	S_iC Honeycomb, Rear Face, Top of Top Panel, wire #49
TC-25	S_iC Honeycomb, Rear Face, Middle of Top Panel, wire #50
TC-26	S_iC Honeycomb, Rear Face, Bottom of Top Panel, wire #51
TC-27	S_iC Honeycomb, Rear Face, Top of Bottom Panel, wire #52
TC-28	S_iC Honeycomb, Rear Face, Middle of Bottom Panel, wire #53
TC-29	S_iC Honeycomb, Rear Face, Bottom of Bottom Panel, wire #54
TC-30	Air Above Honeycomb - North
TC-31	Air Above Honeycomb - South
TC-32	Air Above Honeycomb - East
TC-33	Air Above Honeycomb - West
TC-34	
TC-35	Ambient Cooling Air - Fan Inlet
TC-36	Terminal Concentrator - North
TC-37	Terminal Concentrator - NW
TC-38	Terminal Concentrator - West
TC-39	Terminal Concentrator - SW
TC-40	Terminal Concentrator - South
TC-41	Terminal Concentrator - SE
TC-42	Terminal Concentrator - East
TC-43	Terminal Concentrator - NE
TC-44	Terminal Concentrator - H_2O Out

DATE_____

TRANSDUCER LABEL	TRANSDUCER LOCATION
TC-45	Terminal Concentrator - H_2O In
TC-46	Receiver Metal Cone Temperature
TC-47	Inside Metal Surface, Cone
TC-48	Hard Insulation, Cone
TC-70	ACTF Scanner Outlet H_2O
TC-71	ACTF Scanner Position #34
TC-72	ACTF Scanner Position #38
TC-73	ACTF Scanner Back of #34
TC-74	ACTF Scanner Back of #36
TC-75	ACTF Scanner Back of #38
PS-1	Static Pressure, Recur. Inlet - North
PS-2	Static Pressure, Recur. Inlet - South
PS-3	Static Pressure, Recur. Inlet - East
PS-4	Static Pressure, Recur. Inlet - West
PS-5	Static Pressure, Recur. Outlet - North
PS-6	Static Pressure, Recur. Outlet - South
PS-7	
PS-8	
PS-9	Static Pressure, Hot Fan Inlet (wall) Flow
PS-10	Static Pressure, Hot Fan Inlet (wall) Flow
PS-14	Static Pressure, Cooling Air Inlet
PS-26	Barometric Pressure
PT-11	Dynamic Pressure, Hot Fan Inlet

DATE_____

TRANSDUCER LABEL	TRANSDUCER LOCATION
PT-12	Dynamic Pressure, Hot Fan Inlet
PT-13	Dynamic Pressure, Hot Fan Inlet
CAL-1	ACTF Cal #1 (South)
CAL-3	ACTF Cal #3
CAL-5	ACTF Cal #5
CAL-7	ACTF Cal #7
CAL-9	ACTF Cal #9
CAL-11	ACTF Cal #11
CAL-13	ACTF Cal #13
CAL-15	ACTF Cal #15
CAL-17	ACTF Cal #17
CAL-19	ACTF Cal #19
CAL-21	ACTF Cal #21
CAL-23	ACTF Cal #23
CAL-25	ACTF Cal #25
CAL-27	ACTF Cal #27
CAL-29	ACTF Cal #29
CAL-31	ACTF Cal #31
CAL-33	ACTF Cal #33
CAL-35	ACTF Cal #35
CAL-36	ACTF Cal #36 (Center)
CAL-37	ACTF Scanner #37
CAL-39	ACTF Scanner #39

DATE_____

TRANSDUCER LABEL	TRANSDUCER LOCATION
CAL-41	ACTF Scanner #41
CAL-43	ACTF Scanner #43
CAL-45	ACTF Scanner #45
CAL-47	ACTF Scanner #47
CAL-49	ACTF Scanner #49
CAL-51	ACTF Scanner #51
CAL-53	ACTF Scanner #53
CAL-55	ACTF Scanner #55
CAL-57	ACTF Scanner #57
CAL-59	ACTF Scanner #59
CAL-61	ACTF Scanner #61
CAL-63	ACTF Scanner #63
CAL-65	ACTF Scanner #65
CAL-67	ACTF Scanner #67
CAL-69	ACTF Scanner #69
CAL-71	ACTF Scanner #71 (North)
HSCNR	ACTF Scanner Pot
DIR S	Direct Solar Isolation
TOT S	Total Isolation

SECTION 4
OPERATION PROCEDURES

4.1 GENERAL

4.1.1 Test Platform

A test platform (see Figure 4-1) will be provided prior to receiver tests in order to calibrate the performance of the mirror field. Mounted below the platform is the terminal concentrator surrounded by the Georgia Tech flux rake assembly. Above the platform is a Sanders flux rake, capable of measuring the flux distribution in the plane of the ceramic receiver elements. This equipment will measure the actual test conditions in order to compare them with the theoretical flux distributions assumed in the receiver design. A further objective is to make simultaneous measurements with the Sanders and Georgia Tech flux scanners so that during subsequent receiver tests, when only the GIT flux scanner is available, there is a verification of unchanging performance of the mirror field.

Operation of the flux rake requires approximately 6 gallons per minute of water flow in parallel through the rake and the terminal concentrator. A small control box operates the variable speed motor for rotating the flux arm at speeds which vary from 80 sec/rev to 360 sec/rev. A swing switch limits the arm rotation to $\pm$180 degrees. Position readout is provided by a 20 turn potentiometer connected to a 12 volt power supply. A calibration curve measured in situ is incorporated in the computerized data reduction procedures.

4.1.2 Receiver Platform

The three component parts of the receiver test platform are: burner assembly, cooling air assembly, and the receiver assembly.

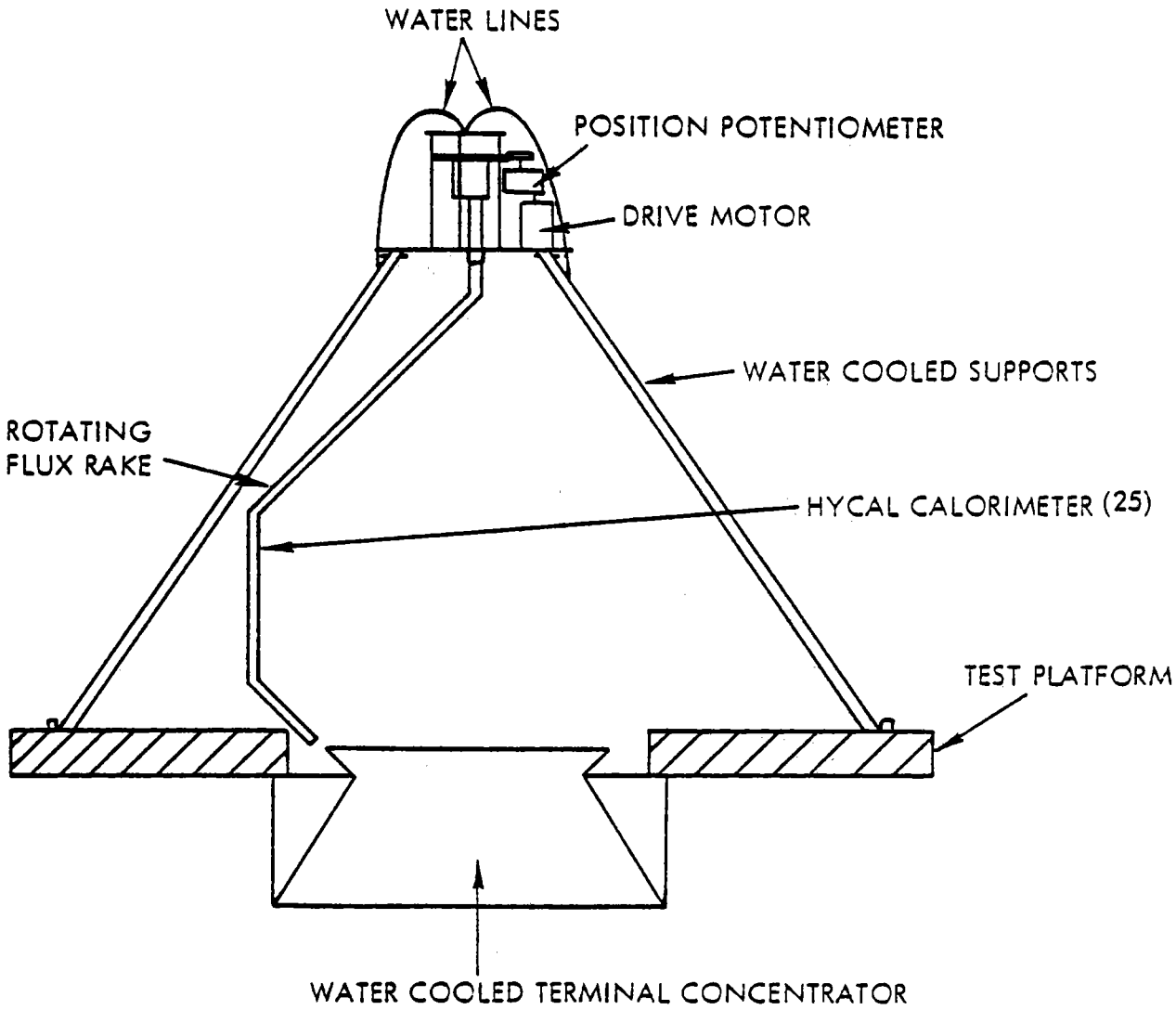

Figure 4-i. Sanders' Test Platform

Each assembly may be started and run from the control panel (Figure 4-2) as a separate system for the purposes of test, calibration, and checkout. However, when operated in conjunction with the mirror field, a detailed sequence of startup and shutdown steps are necessary. The checklists for the operation of the three components as a complete system are detailed in Tables 4-1 and 4-2; refer to Figure 4-2 for the control panel layout.

4.2 OPERATIONAL PROCEDURES

4.2.1 Test Platform

Below are the setup and operation procedures for the flux rake measurement program.

Setup:

1. Assemble rake to platform.
2. Mount terminal concentrator to platform.
3. Connect all water lines and check for flow and leaks.
4. Connect electrical leads.
5. Check operation of motor and rake.
6. Check response of each thermocouple.
7. Mount on tower and connect controls and instrumentation.
8. Operate in cold conditions.

Operation:

1. Turn power on.
2. Turn water on.
3. Check rotation flux arm through several cycles.
4. Check water flow.
5. Check instrumentation.
6. Open shutter.
7. Record flux profiles at three rotation rates:
    a. 80 sec/scan
    b. 160 sec/scan
    c. 320 sec/scan
    d. 600 sec/scan

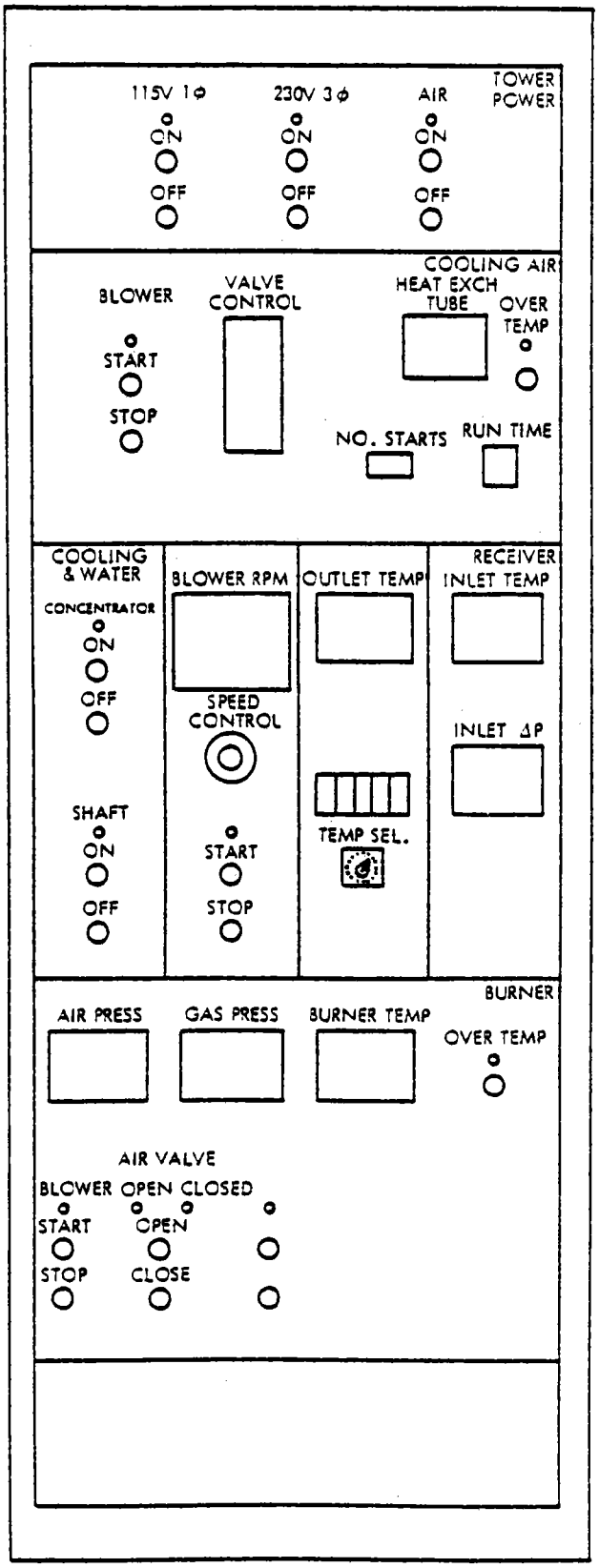

Figure 4-2. Control Console

4.2.2 Receiver Platform

The control panel contains all the signals, meters and control functions needed to operate the three independent assemblies on the receiver platform. These controls are grouped on the control console according to the assemblies they operate (see Figure 4-2 and Table 4-3). Power switches are located on the top of the console and must be turned on before any other operation can be performed.

The cooling air assembly is controlled from the second chassis in the console. Start and stop switches operate the blower and a valve control regulates the airflow needed to maintain a set temperature for the receiver air. The temperature at the critical heat exchanger is displayed,as is the number of starts and running time on the heat exchanger.

Receiver operation is controlled from the third chassis of the console. Remote control of cooling water to the hot fan shaft and the concentrator is also provided. Mass flow through the receiver is maintained by setting the speed control of the hot fan motor. Inlet and outlet receiver temperatures are displayed to aid in setting airflow. Several other critical temperatures can be selected by the operator and displayed on a digital readout.

For calibration and soft start purposes, a hot gas burner assembly can be operated from the fourth chassis. This unit requires a rigidly specified startup procedure which functions automatically once the start button is pushed. Meters and lights keep track of the various steps in the startup and shutdown sequences.

All instrumentation needed in computing receiver performance is provided by the solar facility digital data logging and computing system.

Preliminary procedures for turn on and off are presented in Tables 4-1 and 4-2.

TABLE 4-3

CONTROL PANEL INSTRUMENTATION

ASSEMBLY	ITEM	INSTRUMENTATION
Burner	Combustion air blower	ON-OFF switch, pilot light
	Combustion air valve	Open-close switches, open-close light
	Purge start	Pilot light
	Purge end	Pilot light
	Gas valve	Open-close switches, open pilot light
	Fuel valve controller	Meter, control switch
	Outlet temperature	Meter
	Air pressure	Meter
	Gas pressure	Meter
	Ignition	ON-OFF switch, pilot light
	Over temperature	Alarm and pilot light
Cool Air	Fan Motor	ON-OFF switch, pilot light
	Controller	ON switch, temperature adjust meter, mode switches
	Valve position	Open-closed
	Automatic manual mode	Pilot light
Receiver	Hot fan	ON-OFF switch, pilot light
	Valve position	Open-closed
	Controller	ON switch, meter, flow control, mode switch
	Automatic or manual mode	Pilot light

TABLE 4-3

CONTROL PANEL INSTRUMENTATION (Continued)

ASSEMBLY	ITEM	INSTRUMENTATION
	Temperature in	Meter
	Temperature out	Meter
	Cooling water to bearings	ON light, ON-OFF switch
	Cooling water to concentrator	ON light, ON-OFF switch
	Temperature at heat exchanger	Meter
	Over temperature	Alarm, light
	Elapsed time indicator	Meter
	Number of hot starts	Meter
	Cooling water to bearings	ON light
		ON-OFF switch
	Cooling water to concentrator	ON light
		ON-OFF switch
	Temperature at heat exchanger	Meter
	Over temperature	Alarm, light
	Elapsed time	Meter
	Number of hot starts	Meter

SECTION 5
REQUIRED SUPPORT FACILITIES

Sanders will provide all the instrumentation and associated calibration data for the receiver and all controls for operating the solar receiver. All recorded data such as temperatures and pressures will be sent to the facility data logging equipment for processing, recording and display. Sanders understands that measurement requirements for insolation will be provided by GIT. "First-look" data reduction will also be provided and displayed in real time at the control center by the facility data logging equipment.

A separate control panel is connected to the receiver platform by about 80 meters of cable which carries all instrumentation, control signals, and controls for operating the receiver system. Sanders will provide two cables for insertion into the tower facility conduits: one contains all power lines and control and the other contains low voltage sensor lines. The only connection for electrical power will be on the tower at the fixed electrical distribution box.

There is a limitation of approximately 30 meters on the length of cable which connects the IR cameras to their respective displays. Accordingly, a "bomb shelter" is needed at the base of the tower large enough to house three or four people and a table containing two video displays. Communication between the control room tower platform and the shelter is also needed.

Sanders will need space on the ground near the tower where the complete system can be assembled and checked out using all facilities; water, power, and gas, but not necessarily data logging equipment.

SECTION 7
TEST PLAN

7.1 TEST AT SANDERS ASSOCIATES, INC.

The program at Sanders is for the checkout and calibration of all the equipment to be sent to Georgia Institute of Technology. In addition, tests will be performed at temperatures in excess of 540°C in order to verify performance at elevated temperatures.

The following is a tentative schedule of runs to be made:

- Cooling air system operation
  - check for leaks
  - check airflow controls
  - calibrate airflow

- Hot air system operation
  - check gas supply valves
  - check for leaks
  - check airflow volume and pressure drop
  - check temperature adjustment
  - check safety features
  - connect to cooling air system and calibrate temperature controls

- Receiver assembly operation
  - check hot fan over flow (cold) range
  - add heated air and check operation
  - set inlet temperature at 540°C and measure airflow, air temperature, heat losses
  - calibrate airflow
  - check for leaks
  - check instrumentation

- check controller operation
- measure time constant for system
- measure heat loss with and without an open cavity over the range of inlet air temperatures from 480°C - 650°C and airflows of 0.35, 0.45, 0.55 kg/sec

7.2 TEST AT GEORGIA INSTITUTE OF TECHNOLOGY

Phase I - Calibration

a. Calibrate three mirror field configurations designated by Sanders as:

1. 50% (nominal 96 w/cm^2 at aperture, -12 cm below focal plane)

2. 75% (nominal 135 w/cm^2 at aperture, -12 cm below focal plane)

3. 100% (nominal 180 w/cm^2 at aperture, -12 cm below focal plane)

with flux rake located at the O and R positions of Figure 7-1.

b. Measure flux distribution at three additional stations, with mirror field configuration No. 3 (see Figure 7-1).

1. Plane of concentrator entrance - 18.54"

2. Plane of aperture - 4.76". Install terminal concentrator and Sanders flux rake

3. Vertical plane of ceramic matrix simultaneously with "R" position at several times throughout the day.

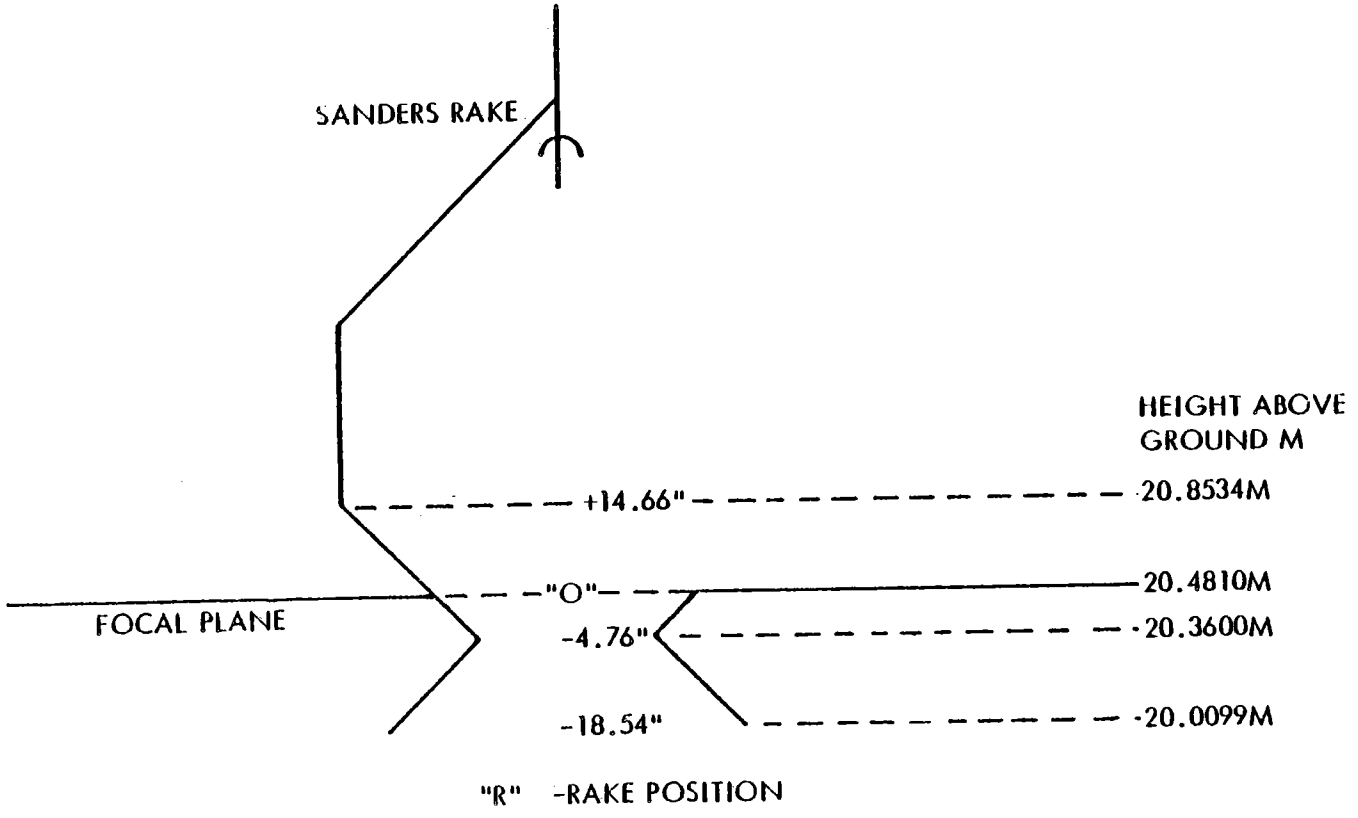

Figure 7-1. Flux Calibration Positions

Phase II - Determine Effect of Design Parameters on Efficiency

Set			Measure			
Mirror Plan	T_{in} (°C)	W_a (kg/sec)	T_{out}	Ins.	ΔP_s	T_1----T_h
1	500	0.35				
	550					
	600					
	650					
	700					
2	500	0.35 0.45				
	550					
	600					
	650					
	700					
3	500	0.35 0.45 0.55				
	550					
	600					
	650					
	700					
3	$\frac{T_{in}}{700}$	$\frac{T_{out}}{1100^{\circ}C}$	W_a	Ins.	ΔP_s	T_1----T_h
			T_{out}	Ins.	ΔP_s	T_1----T_h

As required, repeat Item C-9 in Section 7.1 to measure convective and conductive heat losses of the system.

Phase III - Analyze Limits of Performance

Set			Measure
Mirror Plan	T_{in} °C	T_{out} °C	IR Profiles, W_a, Ins., ΔP, T_1----T_h
Modified C	700	1100	

Display in real time (4 minute increments or less), the following performance parameters:

- mass flow - lb/sec
- inlet air temperature - °F
- outlet air temperature - °F
- power in - w
- efficiency - %
- ΔP at Station 3 - inches H_2O

7.3 DATA REDUCTION

7.3.1 Total Flux Determination

For the sake of error analysis, an algorithm for the total flux input to the receiver as a function of the HYCAL calorimeter readings and their displacements is provided.

At the recommended 5° reading interval, at the design rate of 80 seconds for full scan, each calorimeter will represent at most a 2° smear, which is judged not serious. If a check at a lower scan rate shows no significant difference, then we can reliably use the design rate for further measurements. With the .1% linearity, .01% repeatability of the monitor helipot, keeping $\Delta\theta_i$ to the suggested 5° is expected to be straightforward.

Since all the dimensions are assumed as in the design, the tolerances allowed on delivery will determine whether we can maintain a nominal 1% for this overall measurement. Note that errors in the local incremental area (which are 2 x linear dimension tolerances) are multiplied by an outside limit of $f_{MAX}/f_{AVERAGE}$ in the overall flux determination. Thus, with the present design of $f_{MAX}/f_{MIN} = 3:1$ (to be verified by the maps resulting from this experiment), $f_{MAX}/f_{AVERAGE} \sim 1.73$. Thus, the maximum error is 2 x 1.73 x δ1. To be sure of a 1% error in total flux, we must have all linear dimensions within 0.3%. At the maximum radius of 24.9", this implies a 0.075" dimensional measurement accuracy.

- Quantities for use in program, as based on Figure 7-2.

S_i = array	ΔS_i = array
$S_1 = 0$	$\Delta S_1 = 2.24 + \frac{4.750}{2} = 4.6150$
$S_2 = 4.750$	$\Delta S_2 = 4.750$
$S_3 = 2 \times 4.750 = 9.5000$	$\Delta S_3 = 4.750$
$S_4 = 3 \times 4.750 = 14.2500$	$\Delta S_4 = \frac{4.750}{2} + .9756 = 3.3506$
S_5	$\Delta S_5 = .83 + \frac{1.940}{2} = 1.8000$
not used in algorithm	ΔS_6 … $\Delta S_{15} = 1.940$
S_{16}	$\Delta S_{16} = \frac{1.940}{2} + .83 = 1.8000$
$S_{17} = 8 \times 5.312 = 42.4960$	$\Delta S_{17} = 1.184 + \frac{5.312}{2} = 3.8400$

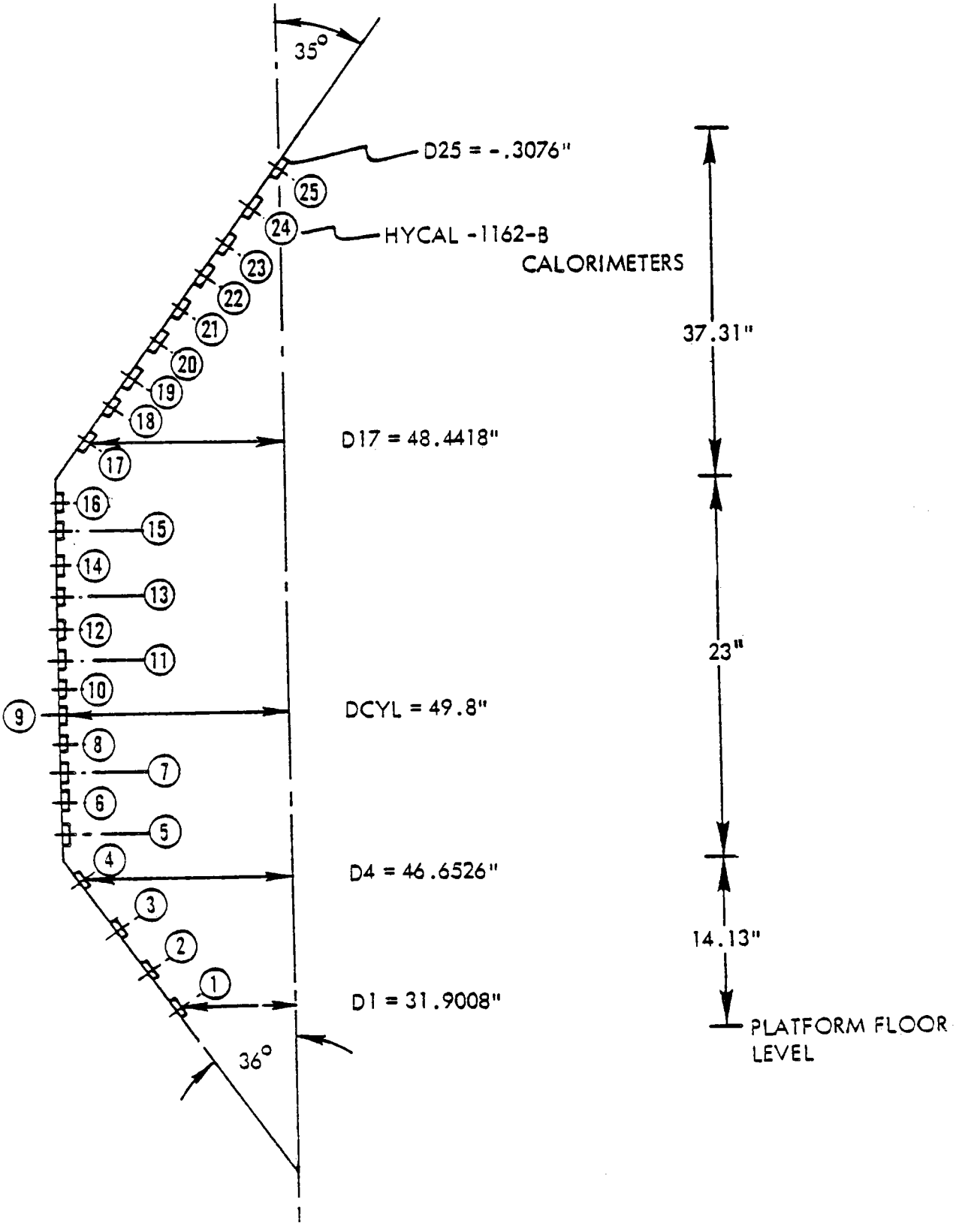

Figure 7-2. Sensor Locations

$S_{18} = 7 \times 5.312 = 37.1840$ $\quad \Delta S_{18}$

$S_{19} = 6 \times 5.312 = 31.8720$

$S_{20} = 5 \times 5.312 = 26.5600$

$S_{21} = 4 \times 5.312 = 21.2480$ $\quad = 5.312$

$S_{22} = 3 \times 5.312 = 15.9360$

$S_{23} = 2 \times 5.312 = 10.6240$

$S_{24} = 5.312$ $\quad \Delta S_{24}$

$S_{25} = 0$ $\quad \Delta S_{25} = \frac{5.312}{2} + 1.87 = 4.526$

$D_1 = 2*[24.9 - (0.976 + (3 * 4.750)) * \sin 36^\circ] \simeq 31.9008$

$D_4 = 2*(24.9 - 0.976 * \sin 35^\circ) \simeq 46.6526$

$D_{CYL} = 24.90 \times 2 = 49.8000$

$D_{17} = 2*(24.9 - 1.184 * \sin 35^\circ) \simeq 48.4418$

$D_{25} = 2*[24.9 - (1.184 + 8 \times 5.312) * \sin 35^\circ] \simeq -.3076$

$\Delta\theta_K$ = constant for all K, suggest $5^\circ = .08727$ radians

$N = \frac{2\pi}{\Delta\theta} = 72$ = number of angle readouts in sweep

(N should be an integer)

$$\frac{D_4 - D_1}{S_4 - S_1} \simeq 2 * \sin 36^\circ \quad , \quad \frac{D_{25} - D_{17}}{S_{25} - S_{17}} = 2 * \sin 35^\circ$$

$$= 1.1756 \qquad\qquad = 1.1472$$

- Algorithm for total flux in terms of calorimeter readings and dimensions.

$$\dot{Q}_{IN} = \frac{1}{144 \times 2} \sum_{\substack{i=1 \\ K=1}}^{\substack{K=N \\ L=4}} f_i\,(\theta_K) * (D_1 + \frac{D_4 - D_1}{S_4 - S_1} * S_i)\,\Delta S_i\,\Delta\theta_K$$

$$+ \frac{144}{144 \times 2} \sum_{\substack{i=5 \\ K=1}}^{\substack{K=N \\ i=16}} f_i\,(\theta_K) * D_{CYL} * \Delta S_i * \Delta\theta_K$$

$$+ \frac{1}{144 \times 2} \sum_{\substack{i=16 \\ K=1}}^{\substack{K=N \\ L=25}} f_i\,(\theta_K) * (D_{25} + \frac{D_{25} - D_{17}}{S_{25} - S_{17}} * S_i)\,\Delta S_i\,\Delta\theta_K$$

Units

Flux values should be in BTU/sec-ft^2 to get Q_{IN} in BTU/sec.

Cross Check

Set all $f_i\,(\theta_K) = 1$. Should get $\dot{Q}_{IN}$ numerically equal to surface area in ft^2. A hand calculation gives 63.64 ft^2 for use in comparison with computer test runs.

NOTE

If θ_K values are well controlled so that $\Delta\theta_K$ values are all within 1%, the $\Delta\theta_K$ constant may be factored out of all three sums.

7.3.2 Data Reduction

Test data will be entered on a disc at the end of each day. A 300 BAUD phone line will write a tape at the campus computer center. This tape, when completed, will be read back and compared with the disc before any erasure of the disc data. Sanders will have a copy of this tape for later data analysis.

On-line processing will be performed directly from the disc by the computer located in the control center. The present inputs to on-line data reduction are:

- Energy input - This quantity is to be obtained from the pyroheliometer reading plus a correction factor obtained from the most recent calorimeter data. With the 3% accuracy, 0.5% repeatability of the calorimeters, this quantity dominates the overall measurement error.

- Static pressure (P_{s3}) - Barometric pressure to be supplied by facility instrumentation in units of lb/ft^2.

- Dynamic pressure (P_{d3}) - The measuring instrument provides inches H_2O on a 0-10V scale. Its calibration needs multiplication by 5.200 to convert to lb/ft^2 (see Table 4-1 for sensor list).

- Temperatures (T_{t1}, T_{t2}, T_{t3}) - See Table 7-1 for sensor listings.

TABLE 7-1a

INSTRUMENTATION SENSORS - THERMOCOUPLES (REVISED 6/14/78)

STATION	DESCRIPTION	REFERENCE	DESCRIPTION	MAX SIGNAL MV	RESOLUTION	TEMPERATURE
1	RECEIVER INLET	150°F	TC-1 N	33.913	.01%	1500°F
	$T_{t1} = \frac{(TC-1)+(TC-2)}{2}$	150°F	TC-2 S	33.913	.01%	1500°F
		150°F	TC-3 E	26.975	.01%	1800°F
2	RECEIVER OUTLET	150°F	TC-4 S	53.000	.01%	2400°F
	$T_{t2} = \frac{(TC-4)+(TC-5)}{2}$	150°F	TC-5 N-S	53.000	.01%	2400°F
		TC-3	TC-6 E-W	26.975	.01%	1800°F
3	HOT AIRFLOW	150°F	TC-7 WALL	33.913	.01%	1500°F
	$T_{t3} = (TC-8)$	150°F	TC-8 C	33.913	.01%	1500°F
6	HEAT × AIR INLET	150°F	TC-9	22.666	.01%	150°F
		150°F	TC-10	2.666	.01%	150°F
7	HEAT × AIR OUTLET	150°F	TC-11	33.913	.01%	1500°F
		150°F	TC-12	33.913	.01%	1500°F
8	HEAT × TUBE	150°F	TC-13	53.000	.01%	1500°F
		150°F	TC-14	53.000	.01%	1500°F
9	HONEYCOMB	150°F	TC-15-34	53.000	.01%	2400°F
10	COOLING AIR	150°F	TC-35	53.00	.01%	150°F

(1) IR Camera with spectral filter 2.75μ-2.85μ
* TDIF (direct reading)

TABLE 7-1b

INSTRUMENTATION SENSORS - PRESSURE TRANSDUCERS

STATION	DESCRIPTION		TYPE	DESIGNATION	MAX SIGNAL	RESOLUTION	MAX PRESSURE
1	RECEIVER INLET	N	LFE	PS-1	60 mv	1%	0-20" H_2O
		S	LFE	PS-2	60 mv	1%	0-20" H_2O
		E	LFE	PS-3	60 mv	1%	0-20" H_2O
		W	LFE	PS-4	60 mv	1%	0-20" H_2O
2	RECEIVER OUTLET	N	LFE	PS-5	60 mv	1%	0-20" H_2O
		S	LFE	PS-6	60 mv	1%	0-20" H_2O
		E	LFE	PS-7	60 mv	1%	0-20" H_2O
		W	LFE	PS-8	60 mv	1%	0-20" H_2O
3	HOT AIRFLOW		LFE	PS-9	60 mv	1%	0-20" H_2O
	P_{S3} = PS-9		MKS	PS-10	10 v	0.1%	0-10" H_2O
			MKS	PT-11	10 v	0.1%	0-10" H_2O
	$P_{D3} = \frac{PT-(11)+(12)+(13)}{3}$		MKS	PT-12	10 v	0.1%	0-10" H_2O
			MKS	PT-13	10 v	0.1%	0-10" H_2O
	$P_{t3} = P_{S3}+P_{D3}$						
4	COOLING AIR INLET		LFE	PS-14	60 mv	1%	0-20" H_2O
			LFE	PS-15	60 mv	1%	0-20" H_2O
			LFE	PS-16	60 mv	1%	0-20" H_2O
5	BURNER AIR INLET		LFE	PS-17	60 mv	1%	0-20" H_2O
			LFE	PS-18	60 mv	1%	0-20" H_2O

TABLE 7-1b

INSTRUMENTATION SENSORS - PRESSURE TRANSDUCERS (Continued)

PRESSURE TRANSDUCERS

STATION	DESCRIPTION	TYPE	DESIGNATION	MAX SIGNAL	RESOLUTION	MAX PRESSURE
6	WIND N	LFE	PT-17	60 mv	1%	0-20" H_2O
	WIND E	LFE	PT-18	60 mv	1%	0-20" H_2O
	WIND S	LFE	PT-19	60 mv	1%	0-20" H_2O
	WIND W	LFE	PT-20	60 mv	1%	0-20" H_2O
7	HEAT EXCHANGER HOT FLOW	LFE	PS-21	60 mv	1%	0-20" H_2O
		LFE	PS-22	60 mv	1%	0-20" H_2O
		LFE	PS-23	60 mv	1%	0-20" H_2O
		LFE	PS-24	60 mv	1%	0-20" H_2O
			PS-25	60 mv	1%	0-20" H_2O

TABLE 7-2. PREFERRED DATA FORMULAS

lb/ft^2 (1) $P_{t3} = P_{s3} + P_{d3}$ $\quad g = 32.17$, $R = 53.48$, P in $lb/ft^2 = 70.58x"Hg = 5.200x"H_2O$

lb/ft^3 (2) $\rho = \dfrac{P_{t3}}{RT_{t3}}$

All T Values in ^oR

ft^3/sec (3) $V = \sqrt{\dfrac{2P_{d3}\ T_{t3}\ gR}{P_{t3}}}$ $\quad c_p = 0.219 + \dfrac{0.342}{10^4} T_{t3} - \dfrac{0.293}{10^8} T_{t3}^2$

---- (4) $M = \sqrt{\dfrac{2}{\gamma}\ \dfrac{P_{d3}}{P_{t3}}}$ (4a) $\gamma = \dfrac{1}{1-R/Jc_p}$; $R/J = 0.068552$

lb/sec (5) $\dot{m} = A\sqrt{\dfrac{2g}{R}\ \dfrac{P_{d3}\ P_{t3}}{T_{t3}}} \left\{ 1 + \dfrac{\gamma - 1}{\gamma} \dfrac{P_{d3}}{P_{t3}} \right\} \dfrac{1}{2} \dfrac{1+\gamma}{1-\gamma}$

BTU/lb (5) $H_1 = T_{t1} \left[0.219 + T_{t1} \left[\dfrac{0.342}{2x10^4} - \dfrac{0..293}{3x10^8} T_{t1} \right] \right]$

BTU/lb (7) $H_2 = T_{t2} \left[0.219 + T_{t2} \left[\dfrac{0.342}{2x10^4} - \dfrac{0.293}{3x10^8} T_{t2} \right] \right]$

BTU/lb (8)

$$\Delta H = H_2 - H_1 = (T_{t2} - T_{t1}) \left[0.219 + \frac{0.342}{2x10^4} (T_{t2} + T_{t1}) - \frac{0.293}{3x10^8} (T^2_{t2} + T_{t2} T_{t1} + T^2_{t1}) \right]$$

BTU/sec (9) $Q_{out} = \dot{m}\Delta H$

---- (10) $\eta = \dfrac{\dot{m}\Delta H}{Q_{in}}$

Sample Calculation

INLET TEMP = $\frac{1140.5}{(t_{t1}-459.7)}$ DEG F, = $\frac{1600.2}{T_{t1}}$ DEG R, = $\frac{616.0}{(5T_{t1}/9-273)}$ DEG C, T1

OUTLET TEMP = $\frac{2000.7}{(T_{t2}-459.7)}$ DEG F, = $\frac{2459.7}{T_{t2}}$ DEG R, = $\frac{1093.5}{(5T_{t2}/9-273)}$ DEG C, T2

FLOW TEMP = $\frac{1196.1}{(T_{t3}-459.7)}$ DEG F, = $\frac{1655.8}{T_{t3}}$ DEG R, = $\frac{646.89}{(5T_{t3}/9-273)}$ DEG C, T3

OUT-IN TEMP = $\frac{859.0}{(TDIF)}$ DEG F, = $\frac{477.22}{(5*TDIF/9)}$ DEG C, TDIF

STATIC PRESSURE = $\frac{2069.02}{(P_{s3})}$ LB/FT^2, = $\frac{99064.68}{(47.88*P_{s3})}$ N/M2, = $\frac{0.9777977 \text{ ATM}}{(P_{s3}/2116)}$ ATM, P_{s3}

DYNAMIC PRESSURE = $\frac{52.1}{(P_{d3})}$ LB/FT^2, = $\frac{250.3}{(47.88*P_{d3})}$ N/M2, $\frac{.0267}{(P_{d3}/2116)}$ ATM, PD3

(1)
TOTAL PRESSURE = $\frac{2121.12}{(P_{t3})}$ LB/FT^2, = $\frac{101559.2}{(47.88*P_{t3})}$ N/M2, = $\frac{0.97945}{(P_{t3}/2116)}$ ATM, PT3

(2)

DENSITY = $\frac{.02395}{(RHO)}$ LB/FT^3, = $\frac{.38404}{(16.033\ RHO)}$ KG/M3, RHO

(3)

VOLUME FLOW = $\frac{374.09}{(VDOT)}$ FT^3/SEC, = $\frac{10.594}{(VDOT/35.31)}$ M3/SEC, VDOT

(4)

MACH NO. = $\frac{.2196}{(MACH)}$, MACH (see footnote (†))

(4a)

GAMMA = $\frac{1.3444}{(GAMMA)}$, GAMMA (see footnote (††))

(5)

MASS FLOW = $\frac{1.30019}{(MDOT)}$ LB/SEC, = $\frac{.59029}{(0.454*MDOT)}$ KG/SEC, MDOT

(6)

ENTHALPY IN = $\frac{387.92}{(H1)}$ BTU/LB, $\frac{901458}{(2323.8*H1)}$ JOULES/KG, H1

(7)

ENTHALPY OUT = $\frac{622.15}{(H2)}$ BTU/LB, = $\frac{1445757}{(2323.8*H2)}$ JOULES/KG, H2

(8)

ENTHALPY DIFF = $\frac{237.23}{(HDIF)}$ BTU/LB, = $\frac{551276}{(2323.8*H2)}$ JOULES/KG, HDIF

(Note: This differs from 7-6. See DIF in 8)

- $\overline{A}$ (see 5) is taken as .14823 ft^2 for this sample calculation. Proper value will be determined after calibration test at Sanders. As default, use .7854 ft^2.

†† C_p = .2676

- FROM LAST CALIBRATION/PYRHELIOMETER COMBINATION

$$Q_{IN} = \frac{363.61}{(Q_{IN})} \text{ BTU/SEC}, = \frac{344.65}{(Q_{IN}/1.055)} \text{ KW}, Q_{IN}$$

(9)
$$Q_{OUT} = \frac{308.444}{(Q_{OUT})} \text{ BTU/SEC}, = \frac{295.069}{(Q_{OUT}/1.055)} \text{ KW}, Q_{OUT}$$

(10)
$$\text{EFFICIENCY} = \frac{.84828}{(Q_{OUT}/Q_{IN})}, \text{ ETA}$$

Symbols

A - duct area (ft^2)

g - gravitational constant (lb_m-ft/lb_f-sec^2)

H - enthalpy (BTU/lb)

M - mach number

$\dot{m}$ - mass flow rate (lb_m/sec)

P - pressure (lb_f/ft^2)

Q - heat rate (BTU/hr)

R - specific gas constant (lb_f-ft/lb_m-^oR)

T - temperature (^oR)

V - velocity (ft/sec)

γ - isentropic exponent for air

η - receiver efficiency

ρ - air density (lb_m/ft^3)

Subscripts

t1, t2, t3	Total conditions at stations no. 1, 2, 3
s1, s2, s3	Static conditions at stations no. 1, 2, 3
d1, d2, d3	Dynamic conditions at stations no. 1, 2, 3
1, 2, 3...N	Instrument numbers
IN	Inlet conditions
OUT	Outlet conditions

7.4 ERROR ANALYSIS

Included in the error analysis are the factors which contribute to errors, temperatures, pressure, area and solar flux.

Simple Form

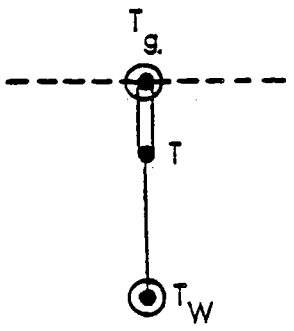

$$T = \frac{h A_{t.c.} T_g + \frac{KA_x}{L} T_w}{hA_{t.c.} + \frac{KA_x}{L} T_w}$$

$$= T_g (1-n) + T_w n$$

$$\text{with } n = \frac{\frac{KA_x}{LhA_{t.c.}}}{\frac{KA_x}{LhA_{t.c.}} + 1}$$

Where:

T = thermocouple reading

T_g = gas temperature

T_w = wall temperature, which causes deviation of T from T_g if not equal to T_g

L = length of thermocouple leads

A_x = cross section of thermocouple leads/sheath

$A_{t.c.}$ = surface area of thermocouple and/or sheath exposed to and sensitive to gas pressure

n = "conduction effectiveness" of thermocouple leads

Improved Form

Though harder to derive, a form in general use, and easy to justify, as well as leading to smaller corrections, is

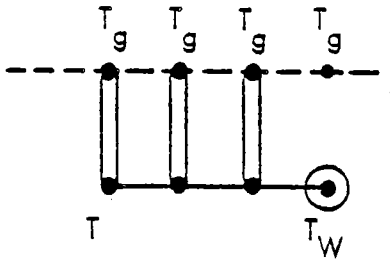

$$T = T_g (1-\eta) + T_w \eta$$

$$m = \sqrt{\frac{hp}{KA_x}}$$

p = perimeter of sheath exposed to gas temperature

L = length of leads/shield from wall to thermocouple

$$\eta = \frac{\tanh mL}{mL}$$

Sample Numbers

h~7 BTU/h ft^2 (typical of exposure to 30 FPS flow velocity)

$$p = \pi \times \frac{0.0625}{12} = 0.01636 \text{ ft}$$

$$A_x = 2 \times \frac{\pi}{4} \times \left(\frac{.01}{12}\right)^2 + \pi \times \frac{0.0625}{12} \times \frac{0.010}{12} = 1.473 \times 10^{-5} \text{ ft}^2$$

K~10 average for inconel (K=7.5) with 1/5 the area in highly conductive leads (K=100)

m = 27.9

L Inches	η
3	.1435
6	.0717
12	.0359
18	.0239

With

$$\eta = .0717$$

$$T_g = 2460^{\circ}R$$

$$T_w = 2260^{\circ}R$$

$$T = 2460\ (1 - .0717) + 2260\ (.0717)$$

$$= 2445.66$$

error in T_g as measured by T is

$$\varepsilon = 2460 - 2445.66 = 14.3^{\circ}$$

percent error

$$\delta\varepsilon = \frac{14.3}{2460} \times 100 = 0.58\%$$

In summary, 6" lead length or more insures conduction error is less than 0.6% when wall temperatures are as much as 200° below T_g.

Radiation Correction

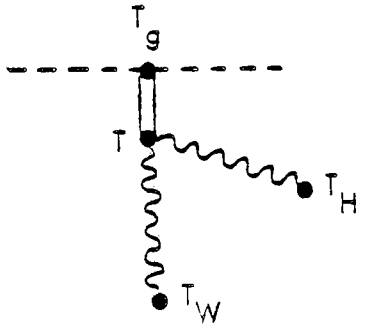

General

$$T = WAT_g + \sigma\varepsilon A \left\{ F_{t-w} \overline{(T_w^2 + T^2)}\ \overline{(T_w + T)}\ T_w + F_{t-h}\ \overline{(T_h^2 + T^2)}\ \overline{(T_h + T)}\ T_h \right\} \div hA + \sigma\varepsilon A \left\{ F_{t-w}\ (T_w^2 + T^2)\ (T_w + T) + F_{t-h}\ \overline{(T_h^2 + T^2)}\ \overline{(T_h + T)} \right\}$$

Assumptions

- Emissivities at wall, W, and at hot spot, H, greatly exceed value ε at thermocouple
- $\bar{T}$ is a non-critical average value of T, which may be guessed with broad tolerance in calculating T and its relation to T_g.

In present experiment, there is no significant area at T_h.

Using the form

$$T = T_g (1-n_R) + T_w n_R$$

for the radiation correction, and defining m_R and n_R as follows

$$m_R = \frac{\sigma \varepsilon F \overline{(T_w^2 + T^2)} \; \overline{(T_w + T)}}{h}$$

$$n_R = \frac{m}{1+m}$$

$$m = \frac{1.73 \times 10^{-9} \times .3 \times 1.0 \times (2460^2 + 2460^2)\,(2460 + 2460)}{7}$$

$$= \frac{4.42}{7} = .63$$

$$n_R = .38$$

Since

$$\frac{\delta T}{T} = \frac{T_w - T_g}{T_g} n_R$$

Then

$$\frac{\delta T}{T} = < .5\% \text{ if } T_w - T_g < \frac{T_g}{n} \left(\frac{\delta T}{T}\right) = 32^o$$

When a larger temperature difference occurs, either a radiation shield or a suitable adjustment for T_w in data reduction will be needed.

$$T_g = \frac{T - n_R T_w}{1 - n_R} \sim T + n_R (T - T_w) + \ldots$$

In summary, the thermocouples will be so located that they can not directly view either the solar flux or solar heated parts of the receiver.

Within the limits of the above analysis, we expect a temperature error to be primarily random, of $\pm 15^o$, or 0.6% in the absolute temperature. For the temperature difference, $T_2 - T_1$, which requires no reference junction, $\pm 4^o$ or 0.2% of the difference is the expected error.

Pressures

The critical values of dynamic pressures will all be measured with instruments rated to $\pm 0.1\%$. The static pressure will be measured as the barometric pressure, probably to far better than 0.1%.

Cross Sectional Area

While random errors in area can be kept under 0.2% with reasonable caution (based on ±.010 inch dimensions), the systematic error in this quantity will dominate (to be discussed).

Energy Flux Input

The basic random error of the HYCAL calorimeters is stated at 0.5%. Since the flux measurement is not at the desired location (at the mouth of the receiver aperture), and must be referred to another flux measurement made during a separate calibration phase, a ±0.7% repeatability or random error is the best that can be assigned to this measurement.

Systematic Errors

Temperature - None are expected if the probes are properly placed following preliminary experiments, and if radiation and lead conduction corrections can be safely ignored, as discussed above under random errors.

Pressure - No significant systematic errors are expected in pressure as read at the probe. For the assumed mass flow formula, error will result from the fact that the pressure profile will be inhomogeneous across the duct. An independent calibration experiment is planned to calculate the mass flows based on the observed profile of dynamic pressure. Discrepancies from the assumed formula will be resolved by: (a) choice of the point at which pressure will be measured during (non-calibration) runs, and (b) use of an effective value for cross sectional area differing from the true dimensions. This will account for the ineffectiveness of the boundary layer zone in the mass flow formula.

Since the velocity profile depends on the square root of the measured pressures, the pressure profile accuracy is improved by a factor of 2. Since, however, the measurement depends on a separate calibration, the random error or repeatability is degraded. We anticipate at 3% consistency in pressure probe measurement and averagine, thus a ±1.5% mass flow systematic error. A repeatability of ±0.5% is expected to provide a generous allowance for the random errors in the separate calibration.

Energy Flux Input

The calibration accuracy is ±3% for the calorimeters, based on an BNS traceable standard. This imposes the strongest limit on the overall experimental accuracy. Deviations of angular sensitivity of the HYCAL calorimeters from Lambertian (i.e., from being proportional to the cosine of the angle of incidence) have been supplied by HYCAL. By obtaining graphically the range of incidence angles for different sections of the "flux rake", we have modified the flux algorithm to increase each reading by the average shortfall predicted from HYCAL's curve for the range of incidence angles involved. These corrections amount to less than 4% up to 60^{o} angles off the normal. They increase glancing angles ($80\text{-}90^{o}$). The largest corrections averaged to 22%. Since they apply to a part of the rake expected to receive less than 20% of the total flux, the net impact of this total correction remains under 3%.

Error Propagation Formulas

Outside Limit Form:

$$\delta\eta = \delta Q_{in} + 1/2 \left(\delta P_{d3} + \delta P_{s3} + \delta T_3\right) + \delta\left(T_2 - T_1\right) + \delta A$$

Gaussian Form

$$\sigma\eta = \sqrt{\sigma Q_{in}^2 + 1/4 \left(\sigma P_{d3}^2 + \sigma P_{s3}^2 + \sigma T_3^2\right) + \sigma\left(T_2 - T_1^{\,2}\right) + \sigma A^2}$$

Numerical Values

Using the random errors discussed above in the Gaussian error propagation, we get a repeatability for the experiment as follows:

$$\sigma_n = \sqrt{(.5)^2 + 1/4\ (0.1^2 + 0.1^2 + .6^2) + (.2)^2 + (.2)^2}$$

$$= 0.65 \text{ percent repeatability}$$

Using the outside limit form, we get a worst case repeatability of

$$\sigma_n = .5 + 1/2\ (0.1 + 0.1 + 0.6) + 0.2 + 0.2$$

$$= 1.3 \text{ percent repeatability - worst case}$$

For the systematic errors, where we can only justify use of the worst case error propagation, we must use the ±3% error inherent in the flux calibration - the best level for which NBS certification is available for light flux. We must also use the expected mass flow error of 1.5% in place of the cross sectional area of the duct (which is the quantity to be adjusted in the calibration experiment). Thus,

$$\sigma_n = 3.0 + 1/2\ (0.1 + 0.1 + 0.6) + 0.2 + 1.5$$

$$= 5.1 \text{ percent error - systematic}$$

Thus, we anticipate an overall measurement accuracy of ±5%, repeatable to 0.7% in standard deviation to 1.3% as an outside limit.

SECTION 8
SAFETY

Factors of prime consideration in evaluating the safety of the receiver test program are the dangers arising from fires and exposure to hot parts. Propane gas for the heater is the only combustible material which will be on the tower. It will be supplied to the gas control system from a tank on the ground which maintains a pressurized flow of propane at 10 psig. Should a leak develop on the tower, the fuel supply can be shut off completely from the ground.

There is a danger to personnel working on the receiver before it has been properly cooled. Therefore, the cooling air system and the hot fan in the receiver assembly are used to cool parts prior to allowing workmen on the tower.

8.1 PRELIMINARY SAFETY STATEMENT

8.1.1 Gas - Fuel (Propane)

1. The gas (propane) tank at base of tower has a ten-pound pressure regulator and a manual shut-off valve.

2. The piping to the burner includes dual solenoid shut-off valves with a solenoid vent valve between.

3. Built into the gas control system are safety features which will cause burner shutdown and stop gas flow. They are as follows:

   a. High gas pressure
   b. Low gas pressure
   c. Pilot failure to light
   d. Over temperature
   e. Burner or pilot light cannot be ignited until purge cycle is complete

NOTE

See attachment A for NFPA code summary.

8.1.2 Electrical

1. The 440V line is protected by heaters in magnetic contactors in all three (3) blower motor starters. 110V lines will be protected by fusing as required.

2. All electrical wiring will be in conduits.

3. All electrical equipment susceptible to weather will be housed in protective enclosures.

4. All electrical controls will be so interlocked that, in the event of a power failure, all systems shut down and will not self-start when power is returned.

5. All critical functions are monitored at Sanders' control panel by meters or indicators, and also provides status of the system.

6. All power to Sanders' system (tower) will be controlled (ON/OFF) from a Sanders control console.

7. All power to Sanders' control console issues from the tower.

NOTE

This is relatively low current as it is used for controls and indicators only.

8. The control to defocus mirrors or close the shutter in the event of an emergency shutdown is to be provided by GIT.

9. There will be a written procedure/checklist detailing the startup, operate, and shutdown procedures. This checklist is to be followed step-by-step, and any deviation from the list is only to be by agreement between Sanders personnel and GIT personnel, except under emergency conditions.

APPENDIX III

CONVECTIVE LOSS EXPERIMENT
TEST RESULTS

SECTION 2
CONVECTIVE LOSS EXPERIMENT/APPROACH

2.1 APPROACH

Sanders' solar receiver design embodies an open cavity concept. Solar energy is transmitted through an aperture open to the ambient and absorbed by an air-cooled heat exchanger located within the receiver cavity. This concept eliminates the requirement for a "windowed" aperture with its associated structural and thermodynamic problems. However, the nature of this design requires an experimental determination of the thermal energy loss that may exist at the aperture due to wind driven forced convection.

2.2 EXPERIMENT

The experiment utilized a unique modeling technique for estimating the magnitude of the convective heat losses arising from an air exchange occurring at the solar receiver's aperture, where receiver inlet air at 1200^{o}F may be exchanged with cold ambient air. Figure 2-1 schematically represents this concept.

A cold mixture of helium and air was used as the working fluid for simulating the properties of hot air at 1200^{o}F. The use of helium conveniently accommodates the requirements of both simulating the physical properties (density) of hot air, and allowing leakage rates to be determined by measuring the resultant variation in the helium concentration.

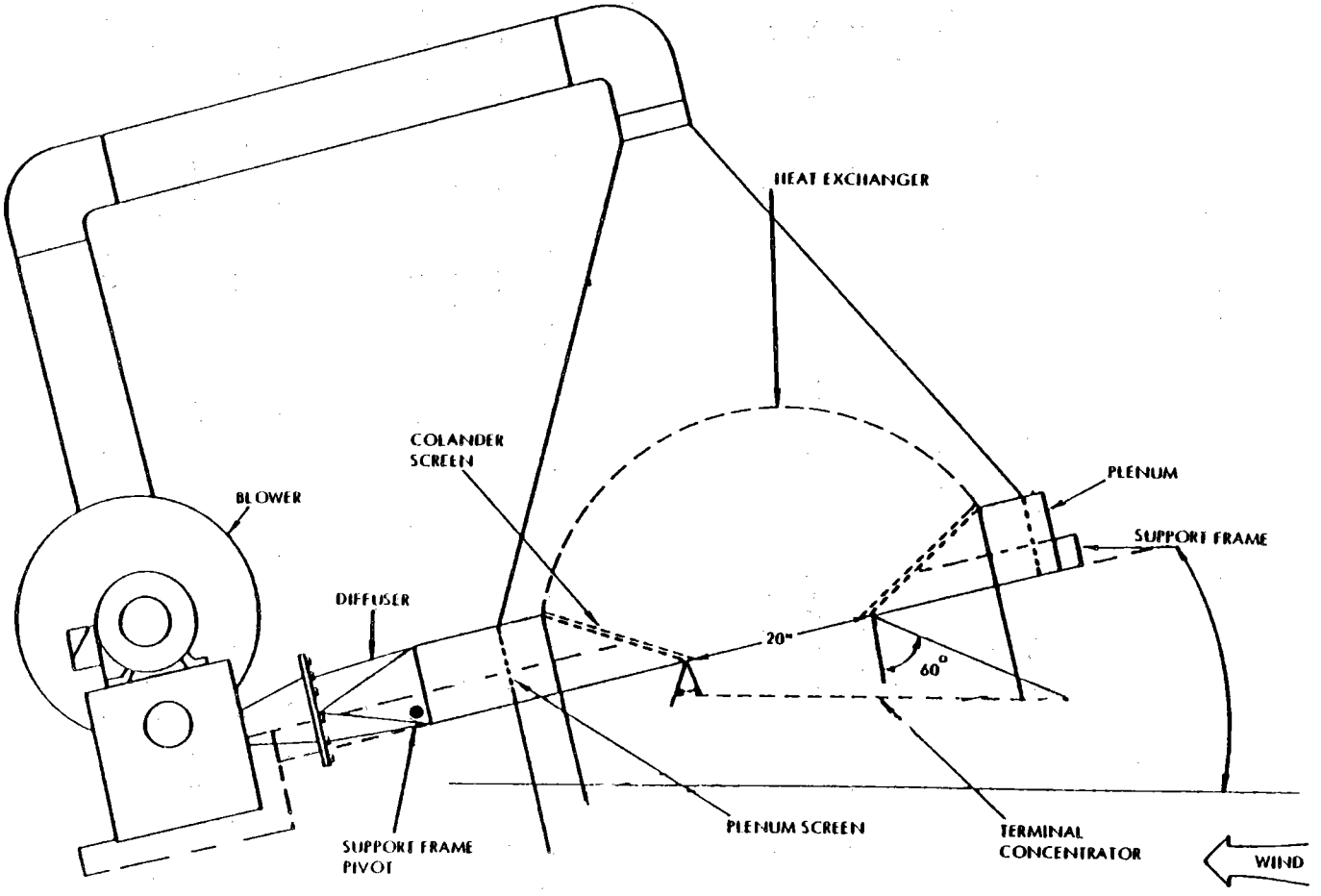

05028-6

Figure 2-1. Convective Loss Apparatus

The convective loss test was accomplished using a simple sheet metal cold flow version of the 1/4 MWt Solar Receiver, which accurately simulated the local internal and external airflows at the solar aperture. The cold flow receiver was built and set up on a standard flatcar rented from the Wolfeboro Railroad. A diesel engine pushed the test apparatus ahead of it, thus generating uniform winds of 0 to 25 MPH on demand. Figure 2-2 and 2-3 show the apparatus installed on the flatcar.

In order to obtain a realistic convective loss picture at the solar aperture, proper simulation of the detailed local flows and their fluid properties was required. Local flow circulations at or near the solar aperture are responsible for gas mixing and subsequent thermal energy losses between system and ambient. These flows are influenced by both the internal fluid gas properties and the ambient wind conditions. The aperture region required detailed simulation of the local flows. Consequently, the cold flow model's working fluid consists of a homogeneous mixture of helium and air whose density equals that of the 1200^{o}F receiver inlet air, with velocities matched to those expected during solar testing.

2.3 ACOUSTIC GAS ANALYZER

Sanders designed and built an acoustic gas analyzer to measure helium concentration when no commercial device was available. Figure 2-4 is a schematic of this unique device. The instrument determines helium concentrations by measuring the speed of sound in a sample of the gas being analyzed. The principle is one of creating a closed Helmholtz resonator by utilizing a tube terminated by a speaker and transmitting sound through the gas sample to the microphone. Thus oscillations are induced at the tube's resonant wavelength. Changes in the volumetric helium concentration or density of the gas mixture determine the change

Figure 2-2. Solar Test Appparatus on Railroad Car View 1

Figure 2-3. Solar Test Apparatus on Railroad Car View 2

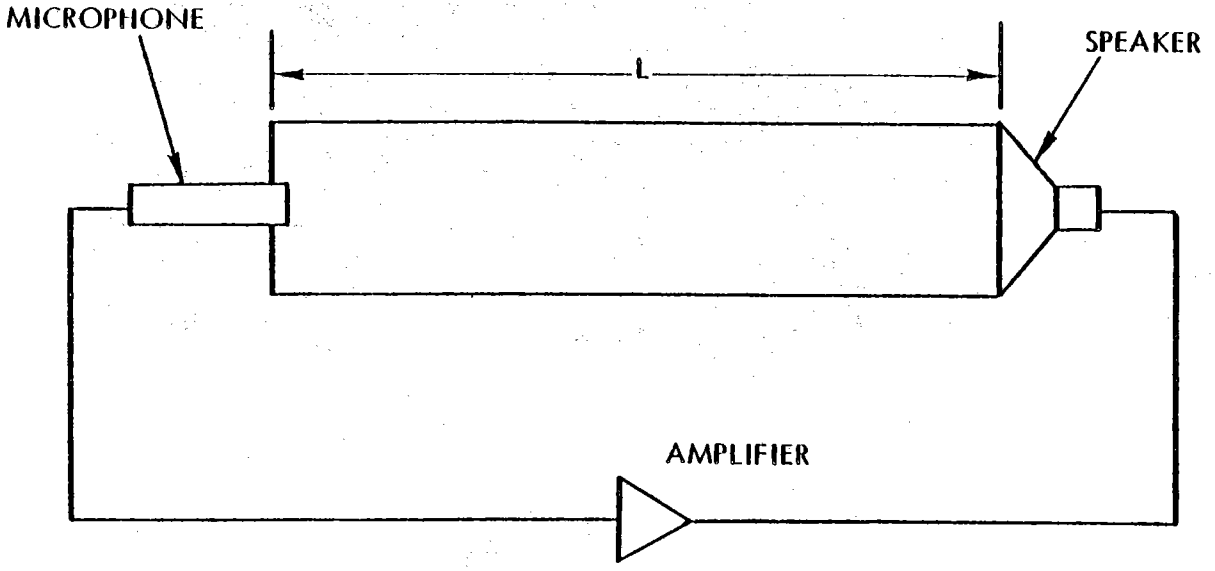

$$f = \frac{v_S}{2L}$$

$$v_S = \left(\frac{\delta P}{\rho}\right)^{1/2}$$

05028-7

Figure 2-4. Schematic of Acoustical Gas Analyzer

in speed of sound in the tube, causing a discrete change in the resonant frequency of the system. The frequency is calibrated against volumetric helium concentration thus resulting in an accurate determination of concentration of the test mixture. Figure 2-5 is the calibration curve, for gas temperatures of 30°F and 60°F. These temperatures are representative of the temperature variation experienced during the convective experiment and appear to have a negligible effect on the calibration.

2.4 FLOW VISUALIZATION

Flow visualization studies were conducted during the test. Both smoke flares and tufts of yarn were used as an aid in observing the flow phenomenon in the vicinity of the solar aperture. These flow studies immediately pointed to the existence of a problem with the experimental setup. The flatcar's aerodynamic interference effects were more severe than originally anticipated and caused the airflow to divert both around and up- and- over the front end of the car. This effectively created a local flow with a large effective angle of attack. The airflow splitter plate shown in Figure 2-3 was introduced and satisfactorily remedied the problem. All subsequent testing was then conducted with the splitter plate in place.

2.5 TEST PROCEDURE

Typically, for a selected constant train speed, a test run begins with the opening of the aperture for a short time period of say 15 seconds, after which it is quickly closed. Helium concentration is monitored at convenient time intervals prior to opening at t=0. After closing the aperture, data is collected at intervals of 15 seconds until an equilibrium concentration is obtained. This somewhat complex procedure accommodates the longer-than-desired time constant of the helium concentration monitor, and permits accurate data reduction.

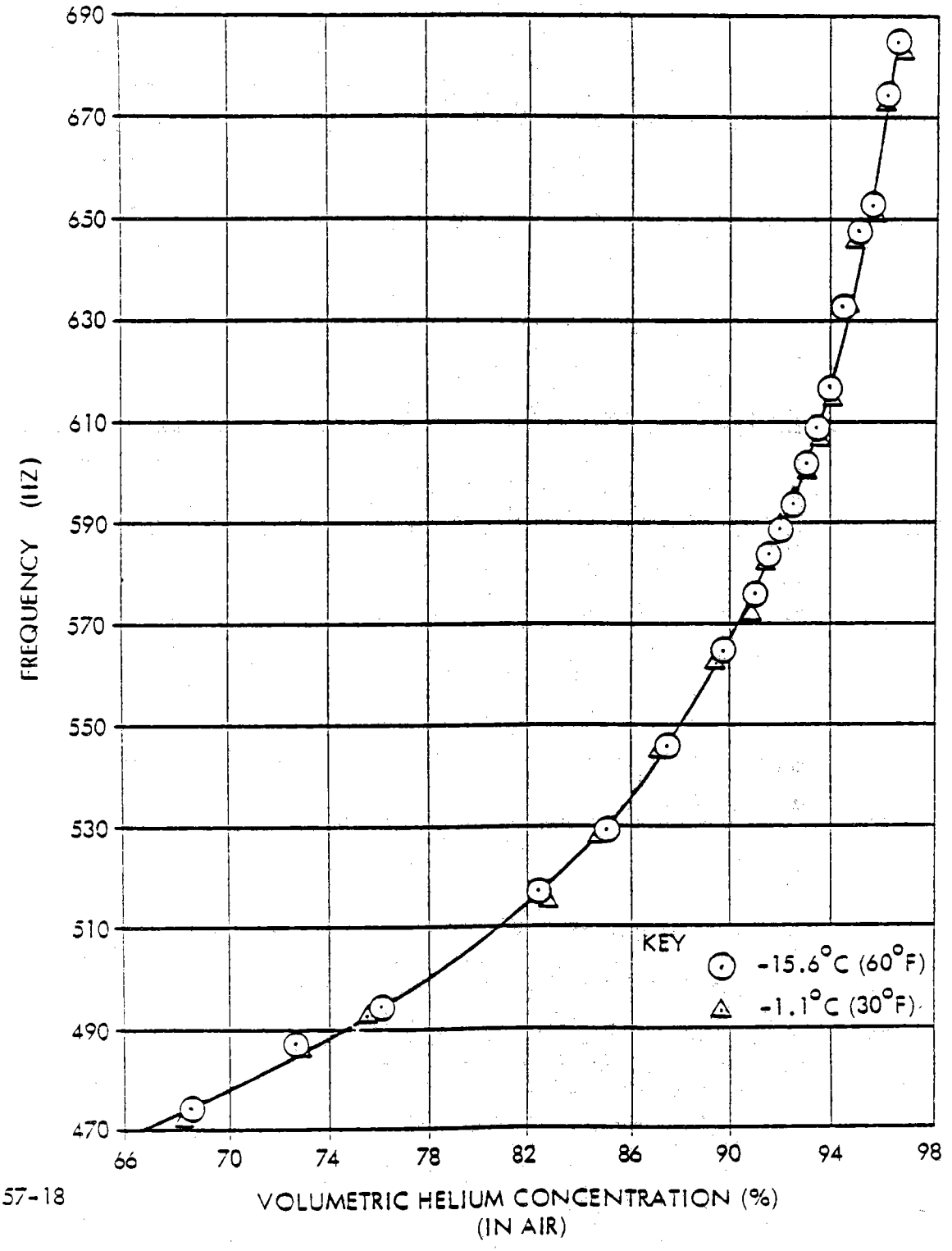

Figure 2-5. Calibration Curve for Acoustical Gas Analyzer

SECTION 3
RESULTS

A typical graph from a series of runs, Figure 3-1, is examined in order to illustrate the graphical data reduction technique utilized. The data plotted along a particular line represents a single test run. The figure indicates that two 15-second "time freeze" sampling runs were performed to ascertain measurement repeatability. Then, test runs sampling at 33 and 45-seconds were each performed. The figure shows the data points from each sampling run plotted, then curve fitted (using the slope as represented by the "tare" run which represents system leakage) and extrapolated to the time when the aperture was closed for sampling. These resultant extrapolated points enabled the fitting of a curve whose slope represented the actual helium leakage rate of the configuration tested.

Tare runs are necessary for this data reduction procedure because they establish the base leakage slope rate of the receiver system for a particular configuration. The data points must be extrapolated because of the gas analyzer's time constant which appears to be 15 seconds by virtue of the extrapolation time required.

Figure 3-2 summarizes the results for the configurations tested and shows that convective energy losses are under 2.5% for all cases investigated. No attempt was made to reduce the loss through external aerodynamic design.

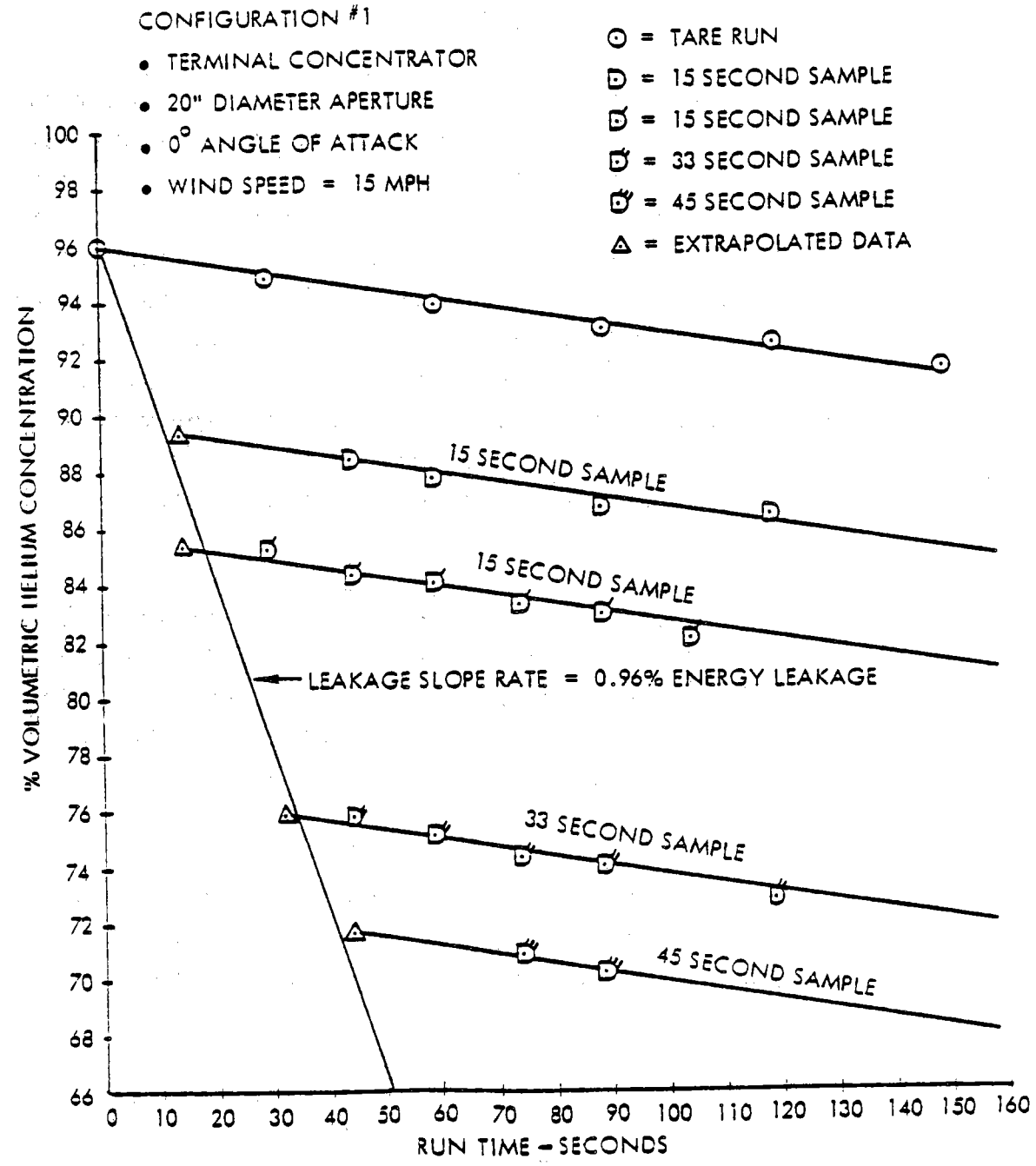

12207-4b

Figure 3-1. Convective Loss Experiment Helium Concentration versus Run Time

SYSTEM	CONFIGURATION			% ENERGY LEAKAGE
	TERMINAL CONCENTRATOR	α (DEG)	WIND SPEED (MPH)	
1	YES	0	0	0.06
2	YES	14	0	0.06
3	NO	0	0	0.06
4	NO	14	0	0.09
5	YES	0	15	0.96
6	YES	14	15	1.09
7	NO	0	15	0.63
8	NO	14	15	0.43
9	YES	0	25	1.23
10	YES	14	25	2.46
11	NO	0	25	0.95

12207-1

Figure 3-2. Convective Loss Experiment Summary of Test Results

APPENDIX IV

1/4 MWt SOLAR RECEIVER TESTS

FINAL REPORT

FINAL REPORT

SOLAR TEST OF SANDERS ASSOCIATES ¼ MWt RECEIVER AT THE ADVANCED COMPONENTS TEST FACILITY

(Georgia Institute of Technology effort)

January 8, 1979

Prepared By

Energy & Chemical Systems Division
Applied Sciences Laboratory
Engineering Experiment Station
Georgia Institute of Technology
Atlanta, Georgia 30332

TABLE OF CONTENTS

LIST OF ILLUSTRATIONS

(Continued)

LIST OF ILLUSTRATIONS (Continued)

1.0 INTRODUCTION

Under contract to the U. S. Department of Energy, Georgia Institute of Technology's Engineering Experiment Station operates the Advanced Components Test Facility (ACTF) on the campus in Atlanta, Georgia. The primary mission of the ACTF is to encourage research and development in the area of high temperature solar technology by providing an intermediate size facility available to the scientific community.

This report describes ACTF activities associated with the testing of a ¼ MWt receiver designed and constructed by Sanders Associates, Inc. of Nashua, New Hampshire.

The downward facing receiver, designed to provided heated air at 2000°F, operates at ambient pressures and has an open aperture. The receiver employs silicon carbide honeycomb as a heat eschange surface with cool side air heated as it passes through the solar radiated honeycomb panels in the walls of the receiver cavity.

The receiver assembly tested at the ACTF included an air-to-air heat rejection system, an L.P. gas fired pre-heating system and necessary controls and instrumentation transducers.

1.1 Test Objective

The objective of the test program was to characterize the Sanders Associates receiver assembly under varied solar powered operating conditions. The test plan also included evaluation of receiver operation using L.P. gas pre-heating and quantification of convective losses across the windowless aperture during solar operation. In support of this activity, ACTF responsibilities included:

1.1.1 Characterize and transmit to Sanders Associates the optical characteristics of the ACTF as related to the specific requirements of the Sanders test.

1.1.2 Provide Sanders Associates with support and interface information regarding thermal shielding, computer data system characteristics, utility service availability, etc.

1.1.3 Maintain interface control documentation and drawings with Sanders Associates in order to eliminate possible hardware interference and system modifications.

1.1.4 Provide and approve jointly with Sanders Associates, receiver test procedures and check lists to be used during all phases of testing.

1.1.5 Manage the ACTF mirror field, data system and various support utilities during testing, as well as assist Sanders personnel as required.

1.1.6 Tailor the general purpose ACTF data acquisition system to collect and rapidly analyze test data, including calculation of receiver efficiency, beam centroid and integrated flux.

1.1.7 Process and transmit all data gathered during testing for reduction and analysis by Sanders Associates.

1.1.8 Document the results of the tests with regard to the performance of all ACTF systems.

1.2 Organization

A system of close communication and documentation was established between Sanders and ACTF personnel to define control system interfaces and responsibilities prior to and during receiver testing. This effort included monthly coordination meetings at which problems were resolved, a Document of Understanding defining responsibilities of and constraints on each organization, a detailed Operational Test Procedure including check lists, which was followed in each day's testing, and Interface Control Drawings which defined mechanical electrical, pneumatic, hydraulic, etc. system interfaces between ACTF and Sanders Associates hardware.

1.3 Summary of Results

At the beginning of the two month test period, the receiver was checked out on the ground where hardware was available. On ground checkout was undertaken in order to recognize and correct any possible damage to the unit during shipment to the test site. The receiver package was then installed on the test tower and, after additional connection of systems and checkout, was subjected to various combinations of both solar and/or LP gas heating cycles. The solar portion of the test included the accumulation of 28 hours and 9 minutes of receiver solar radiation at daily peak incident insolation levels from 559 W/m^2 to 920 W/m^2. Maximum heat rate input into the terminal concentrator of 255 kW, as measured by the ACTF scanning calorimeter, was achieved on October 20, 1978. The Sanders receiver reached design temperature of 2000^{o} F during these tests.

2.0 ADVANCED COMPONENTS TEST FACILITY

Major components of the ACTF include a collector mirror field, an experiment platform located above the center of the mirror field, an instrument and control building, and a computerized data acquisition system. The octagonally shaped mirror field contains 550 mirrors that focus sunlight into a focal zone 21.1 m (69.2 ft) above the center of the field. The mirrors are driven by their electric motor powered mechanical supports (kinematic motion devices) so that the focal zone remains stationary throughout the day. The maximum radiation flux density in the central focal zone is of the order of 150 W/cm^2* and the corresponding maximum total power into the focal zone is approximately 325 kW* for an insolation of 900 W/m^2. The central test stand is a rigid tower capable of supporting a 9100 kg (20,000 lb) test device). Figures 1, 2 and 3 depict the ACTF as configured for the Sanders Associates receiver test.

2.1 ACTF Optical Configuration

The mirror field is arranged in an octagonal pattern in a horizontal plane. Mirrors are mounted on tracking devices (mechanical couplings similar in design to an equatorial mount) that rotate the mirrors so that sunlight reflected from each mirror will pass through a stationary focal zone throughout the day. The tracking devices are driven by a controlable electric clockwork mechanism and are designed so that all the mirrors can be focused in a zone over the center of the field. The rim angle of the mirror field is approximately 0.79 radians (45 degrees).

*Seasonly dependent.

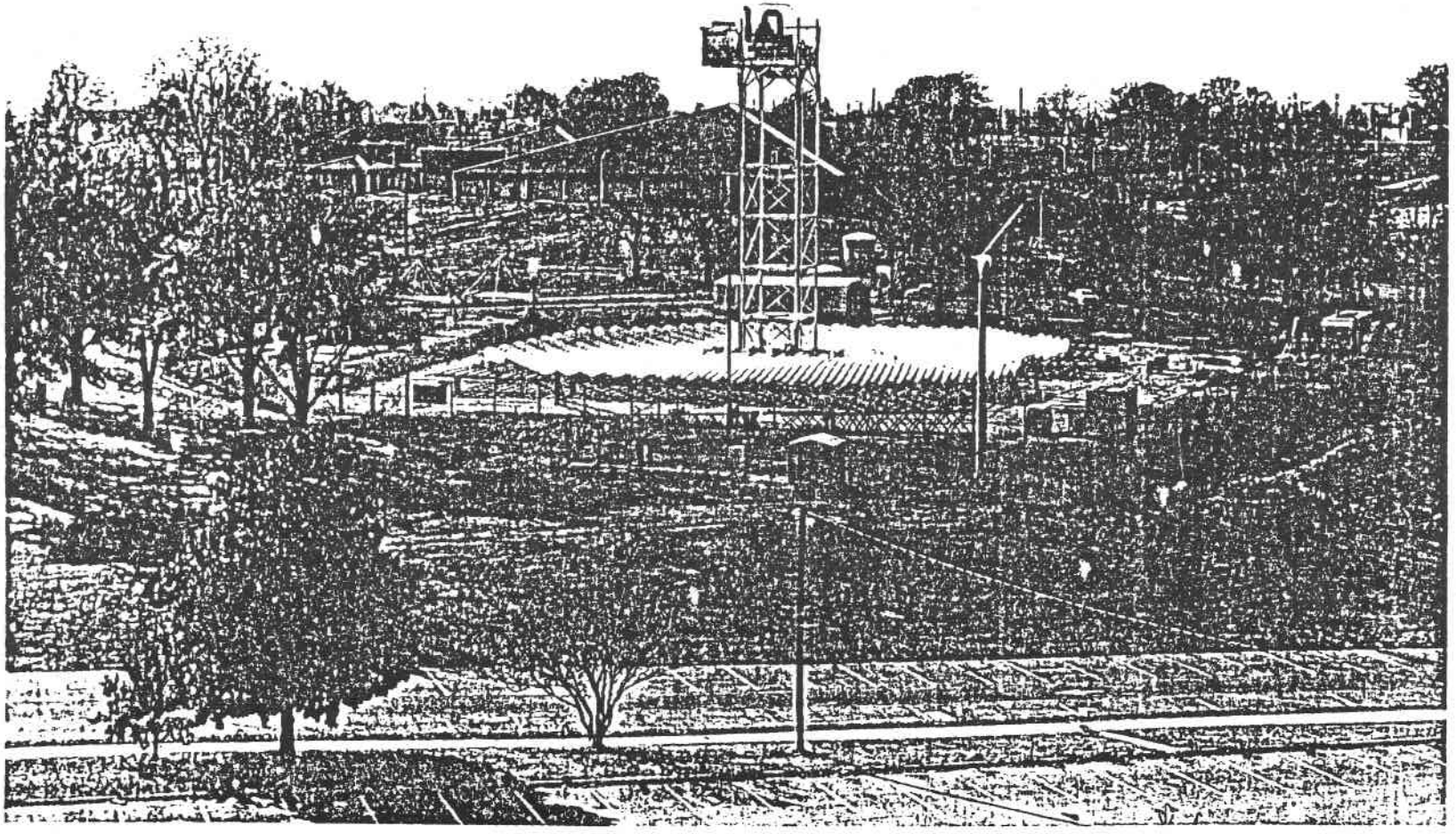

Figure 1. Westerly View of ACTF.

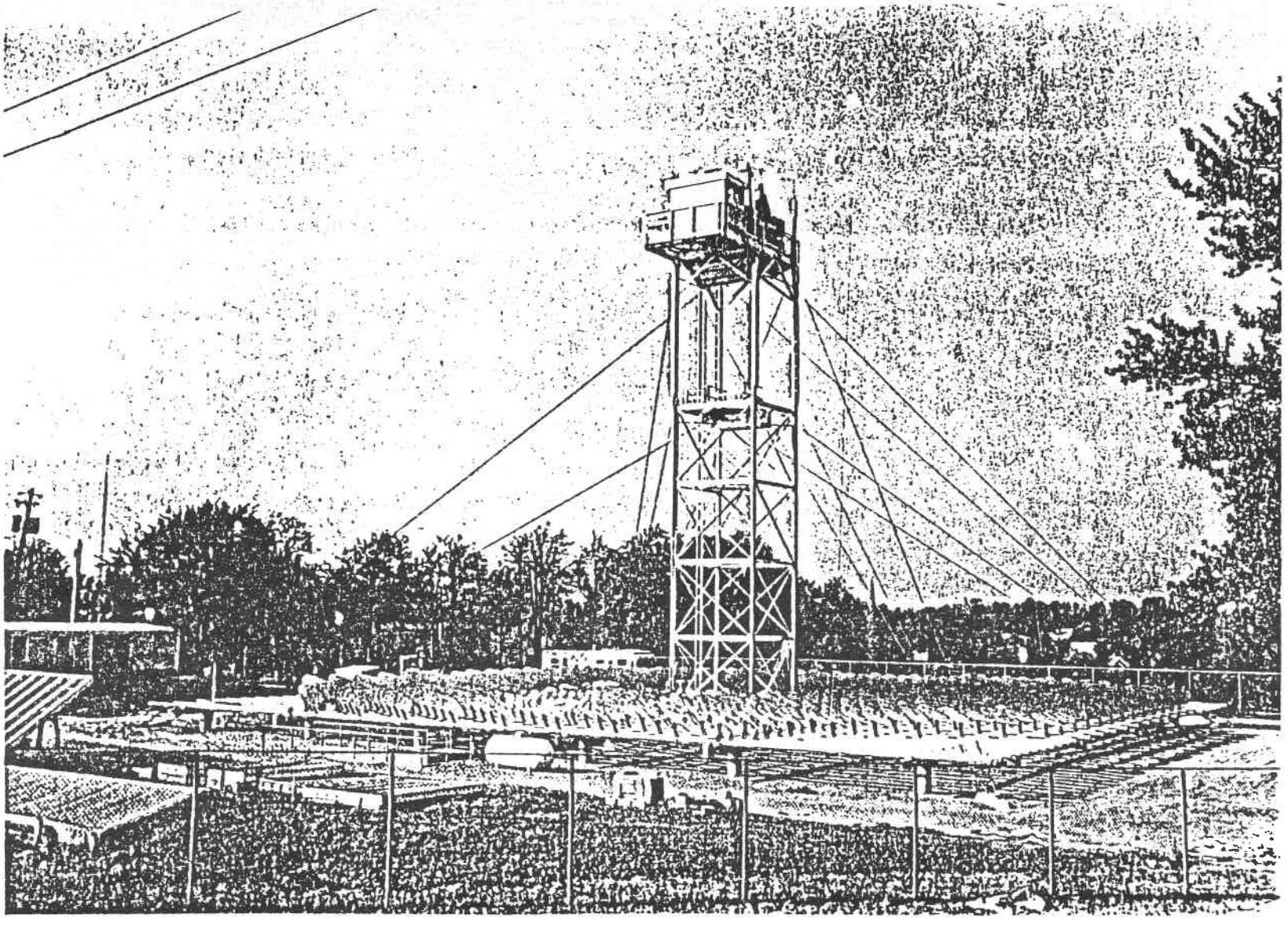

Figure 2. Northerly View of ACTF.

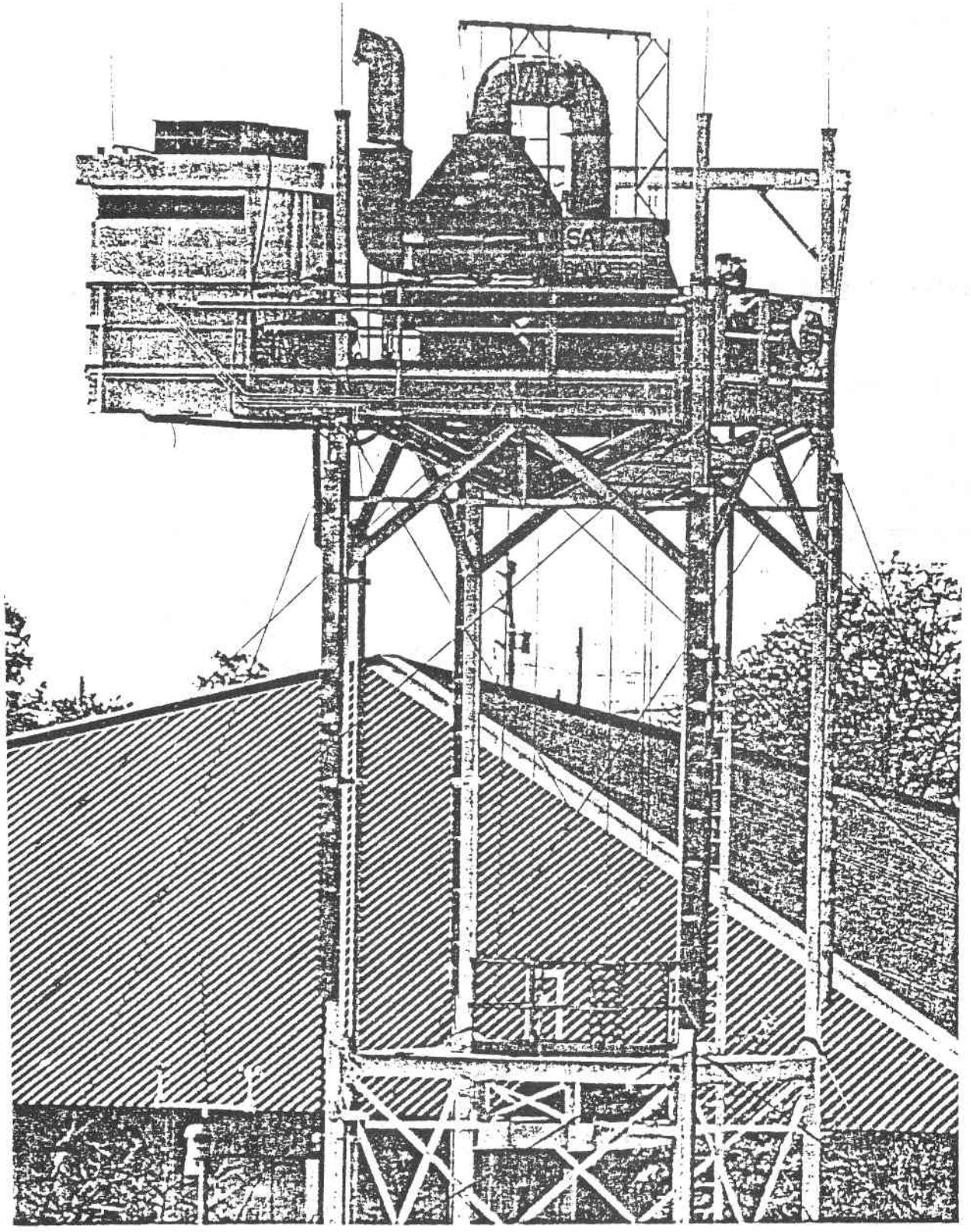

Figure 3. View of the ACTF Test Stand with Sanders Receiver Assembly Installed.

The mirrors are circular, second surface silvered reflectors 111 cm (43.7 in.) in diameter and are made from 3 mm (1/8 in.) low iron, drawn glass. All mirrors were operated in the focused condition, with each mirror focused according to its slant range to the tower.

2.2 Tracking

Mirror field tracking was accomplished with the aid of an optical device attached to one of the tracking arms (modified kinematic motion device) near the mirror field control station. This device employs a 30 cm focal length glass lens at the upper end of a tracking arm which focuses the sun's image on a target at the lower end of the arm. A micrometer positioned line on this target is used as a reference point for monitoring tracking accuracy.

Tracking corrections were made by (1) determining beam centroid error from scanning calorimeter data, (2) calculating correction value using ratios and correction curve, and (3) positioning tracking lens image at the corrected reference line on the tracking device.

2.3 ACTF Test Stand

The ACTF test stand (Figure 4) supported the Sanders Associates assembly during the solar portion of the testing. The nominal focal point of the heliostat array is over the geometric center of the field and 18 cm (7.1 in.) below the top of the work platform. Four support points for test apparatus are located on the work platform on 2.64 m (8.67 ft) centers, equidistant from the focal point. The receiver viewed the mirror field through a 2.44 m x 2.44 m (8 ft x 8 ft) opening in the center of the platform.

SANDERS ASSOCIATES RECEIVER ON DOE ACTF TOWER

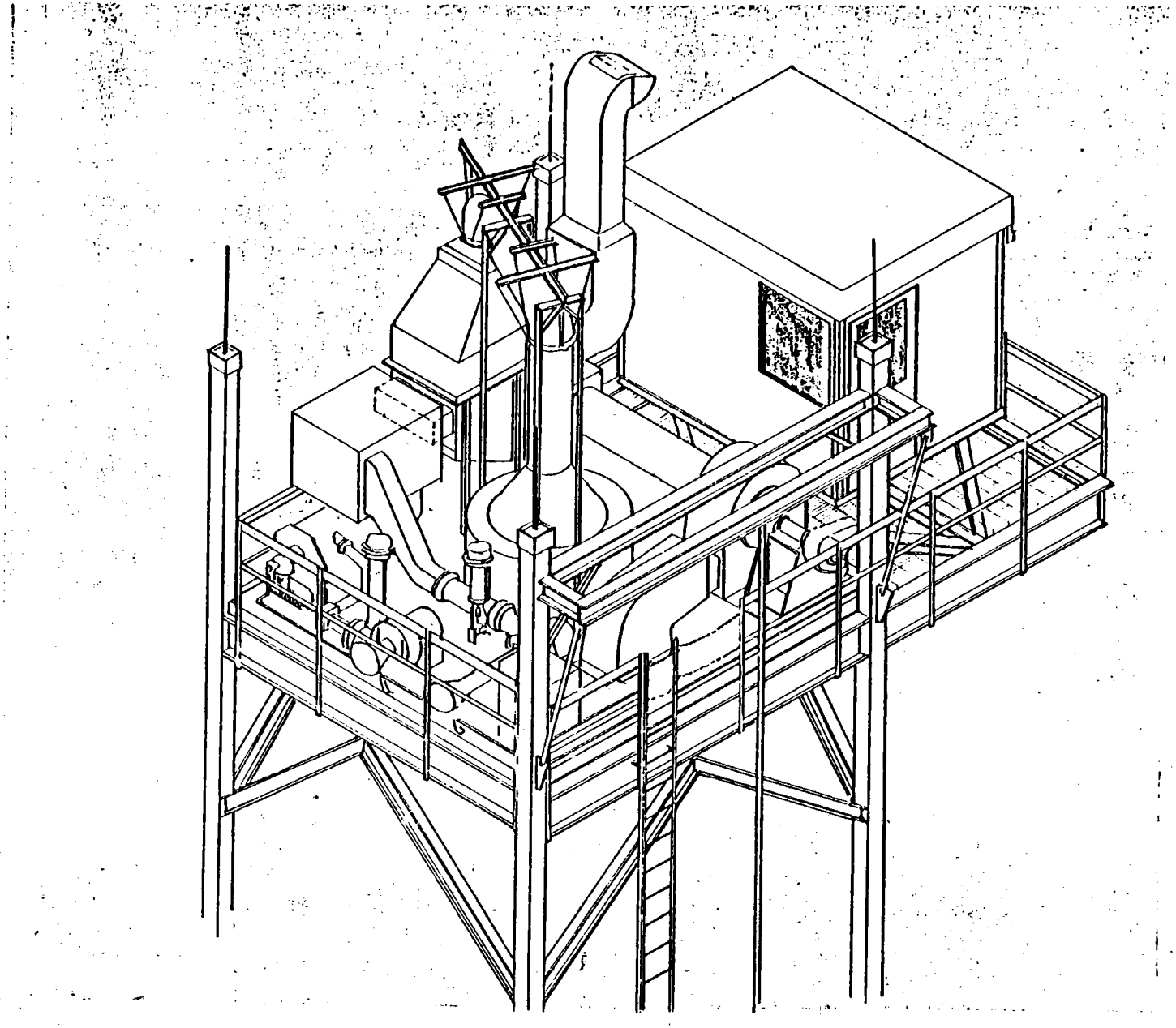

Figure 4.

The Sanders receiver was lifted into place on the tower by an 85 ton mobile crane. Access to the top side of the tower platform is provided by a man/material work hoist with a load carrying capacity of 272 kg (600 lb). A hydraulic scissors lift with a capacity of 454 kg (1000 lb) provides access to the area immediately below the work platform.

The following utilities were provided to the central work platform during the tests:

1. A potable water line with a 5.08 cm (2 in.) inside diameter with static pressure in excess of 80 psig.
2. A gravity drain line with a 10.2 cm (4 in.) inside diameter.
3. 110 VAC, single-phase, 100 amp service.
4. 208 VAC, three-phase, 150 amp service.
5. 230 VAC, three-phase, 150 amp service.
6. A conduit for instrumentation wiring with a 7.62 cm (3 in.) inside diameter.
7. Compressed air at 125 psig.
8. L.P. gas through a 2.54 cm (1 in.) line.

2.4 Data Acquisition System

During the receiver testing, data from 57 Sanders Associates transducers and 45 ACTF transducers were sampled once per second. In order to conserve computer storage space, data for each channel value that had

changed by ± 2 bits out of 4096 bits resolution from initial entry was stored. This approach precluded the repeated storage of the same value. Transducer types are listed below:

Sanders Associates	ACTF
45 thermocouples	6 thermocouples
12 pressure sensors	37 calorimeters
	1 pyrheliometer
	1 position potentiometer

At the conclusion of each test, the stored data were transmitted off-line to a magnetic tape unit. Immediate printouts of desired data were available for daily review. The magnetic tape was then transported to a Georgia Tech CDC Model 70/74 computer where it was read and reduced to produce flux contour plots, beam centroid locations, flux sums, and deviations associated with each scanning calorimeter run. In addition, one minute listings of selected channels were printed out. The tapes were then reformatted to Sanders Associates specifications (IBM Compatible) and transmitted to them for further reduction. A copy of each tape is also stored in the ACTF data archive.

An error band of ± 5 bits is associated with the outputs from thermocouples, MKS pressure sensors, pyroheliometer and scanner position potentiometer. Calorimeter error band was ± 3 bits.

During the test, several different types of real time data display were available to the Sanders Associates console operator and to the ACTF Test Director. These are listed below:

- Handcopy printout of 12 selected channels every minute (channels selected by Sanders Associates).

- Display of 70 channels on video screen, 4 of which were selected at run time. These data were updated every 6 seconds (channels jointly selected by GIT and Sanders personnel). This was the normal display mode.

- When desired as a data point, a paper copy of the video display showing the values of all 70 channels at any instant in time could be made. Run name and time of day also displayed on copy.

- Optional video display of plot of two calorimeter values versus scanner bar position, plus digital display of 20 pre-selected channels of interest during ACTF scanning calorimeter runs.

Two additional sub-programs were available for determining the solar beam centroid and integrated flux into the Sanders Associates terminal concentrator. Both routines could be summoned while the data system continued to gather, store and display data.

The first of these sub-programs printed out the beam centroid location in inches in the north-south and east-west direction derived from data from the most recent scanning calorimeter run. The second sub-program determined the total incident power in kilowatts passing through 1.42 meter (55.95 in.) diameter circle concentric with the axis of revolution of the Sanders Associates terminal concentrator and in the horizontal plane of the calorimeters (approximately 13.3 cm (5¼ in.) below the terminal concentrator inlet).

2.5 ACTF Flux Scanner

The ACTF scanning calorimeter consists of thirty-seven (37) Gardon gage type calorimeters mounted on a bar that has a travel of 1.83 m (6 ft) along stainless steel rails and measures flux levels in a horizontal plane. The calorimeters (Hy-Cal Engineering[+] Model C-1112-B) are mounted on 5.08 cm (2 in.) centers to measure the heat flux distribution in a 1.829 m (6 ft) x 1.829 m (6 ft) plane allowing the generation of a 2 inch x 2 inch flux map grid. The scanning bar can travel at speeds up to 30.5 cm/min (1 ft/min), allowing an aperture scan to be completed in approximately 6 minutes. The calorimeters are calibrated to an accuracy of $\pm$ 3 percent of full scale over a range of from 0 to 150 W/cm^2 incident flux. The scanning bar, stainless steel rails, and rail supports are water cooled.

2.6 Pyrheliometer

Direct radiation measurements during the test period were made using an Eppley Normal Incidence Pyrheliometer, Model NIP, S/N 14983E6.[*] This device is located at the southwest edge of the heliostat field and furnishes radiation information to the ACTF data system and a strip chart recorder. Radiation information from this device can be used to normalize solar flux data recorded by the flux scanning calorimeter in the evaluation of both receiver and mirror field performance.

---

[*]The EPPLEY Laboratory, Inc., Newport, R. I.

[+]Hy-Cal Engineering, Sante Fe Springs, California.

3.0 TEST PROGRAM

The test program for the Sanders receiver conducted at the ACTF involved volume flux mapping, joint ACTF and Sanders flux mapping, receiver ground pre-test, tower L.P. gas and solar testing.

Data from each phase of testing were used as an aid in periodic reviews of the detailed test program. The program included receiver pre-heat prior to solar operation as well as start-up using solar power only. The receiver was operated at a number of different cooling air flow rates and solar radiation combinations in order to evaluate the thermodynamic and structural performance of the device.

3.1 Volume Flux Mapping

In order to map the solar flux concentrated in the focal zone area, the scanning calorimeter was mounted on 4 vertical, threaded columns allowing the device to be positioned in any horizontal plane from 61 cm (2 feet) above to 62 cm (2 feet) below the top deck of the experiment platform. A series of horizontal West to East scans at 15.2 cm (6 in.) incremental levels in the vertical direction produced data for the generation of a flux map of the 1.8 x 1.8 x 1.2 m (6 x 6 x 4 ft) volume centered about the theoretical focal point.

The volume flux data were reduced using a general purpose contouring program developed by Control Data Corporation and implemented on the Georgia Tech computer system. The resulting contours (see Figures 5 through 13) were plotted with an incremental plotter.

NORM. TO 900 W/M2

DATE: 8-17-78
TIME: 13:11 TO 13:15
SCAN 1: 24 IN. ABOVE FOCAL PLANE
INSOLATION: 751-765 W/M^2

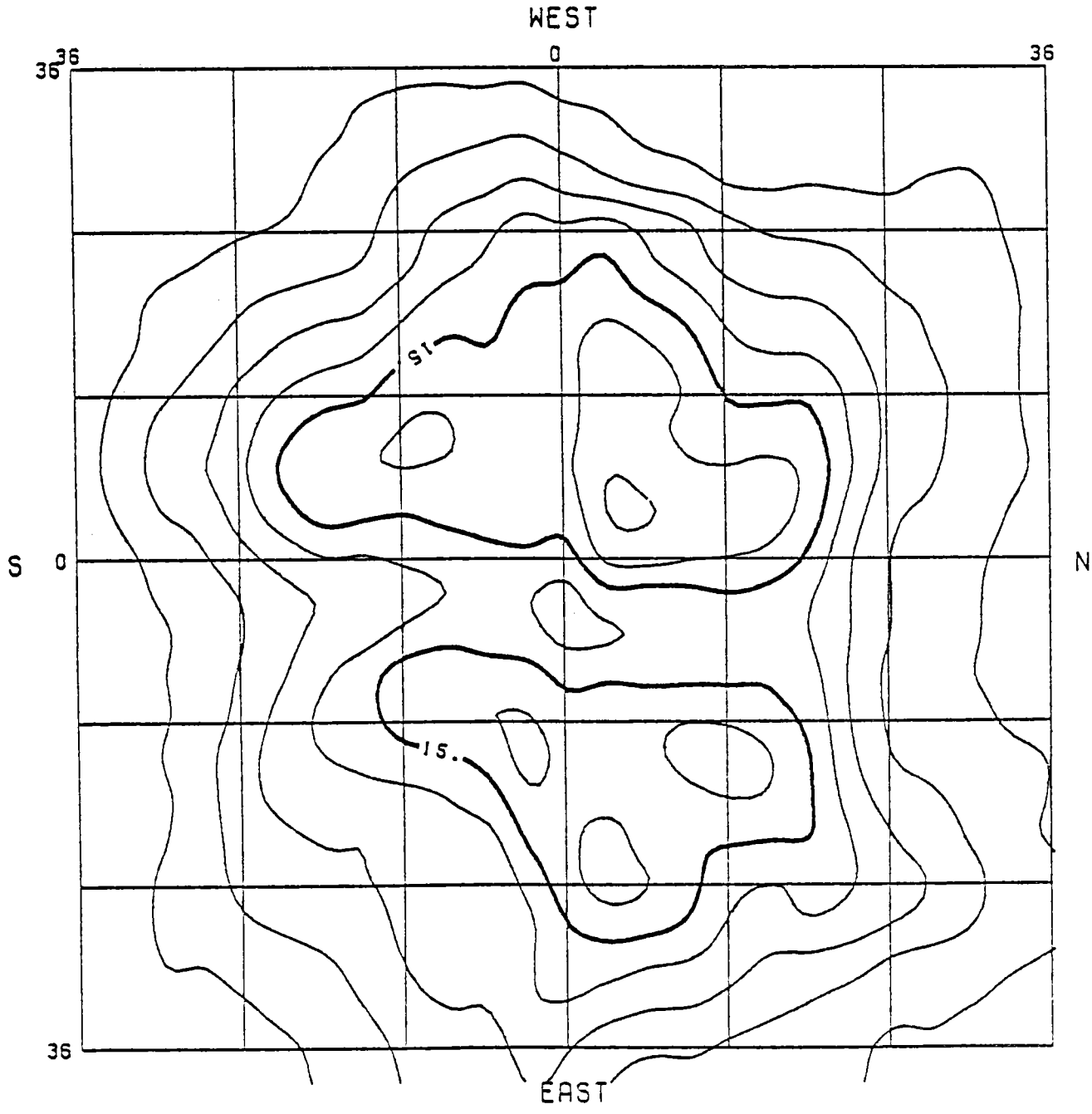

Figure 5. Flux Map - 24 Inches Above Platform.

NORM. TO 900 W/M2

DATE: 8-17-78
TIME: 13:33 TO 13:38
SCAN 2: 18 IN. ABOVE FOCAL PLANE
INSOLATION: 733-759 W/M^2

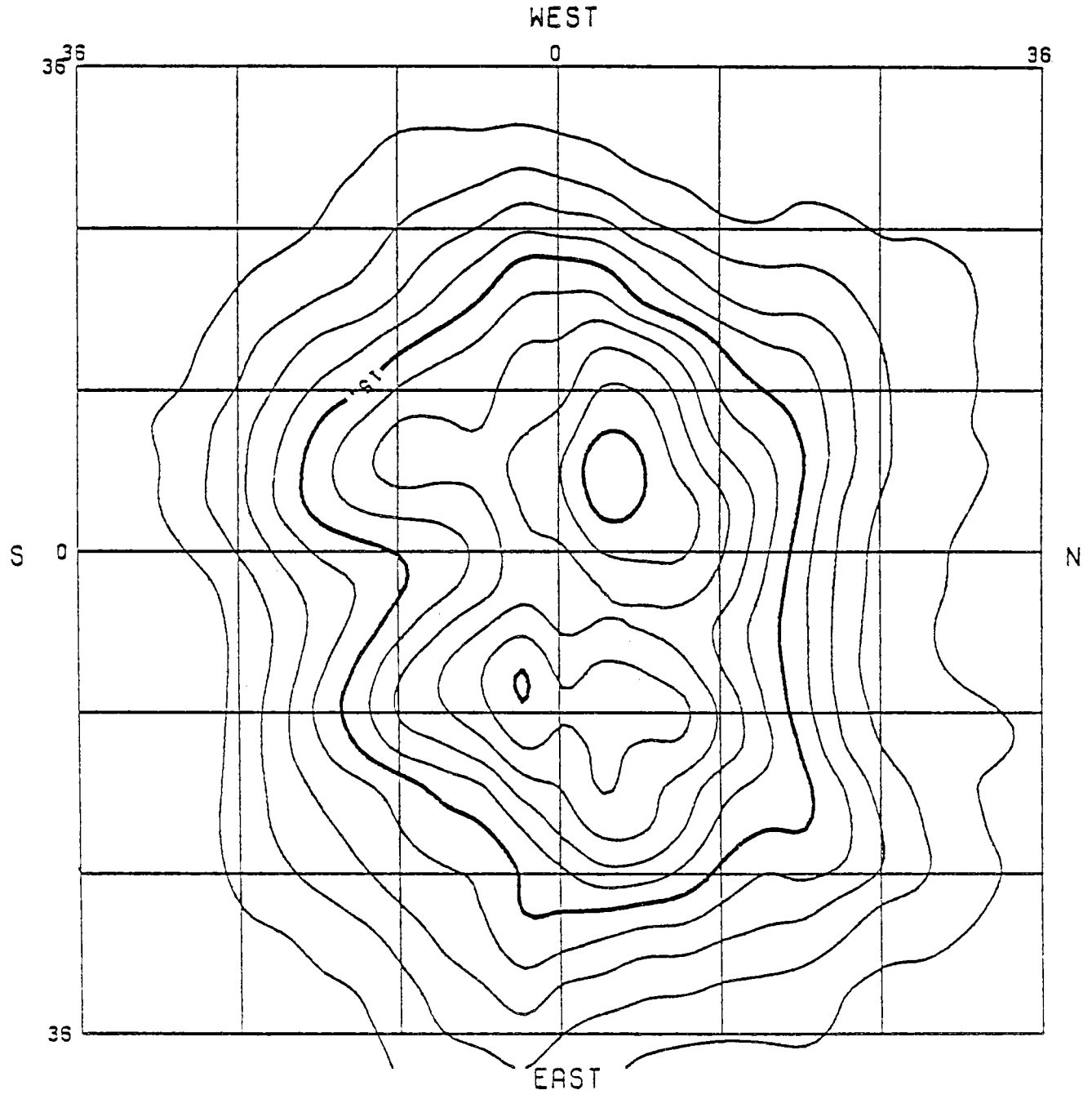

Figure 6. Flux Map - 18 Inches Above Platform.

NORM. TO 900 W/M2

DATE: 8-17-78
TIME: 13:43 TO 13:47
SCAN 3: 12 IN. ABOVE FOCAL PLANE
INSOLATION: 747-759 W/M^2

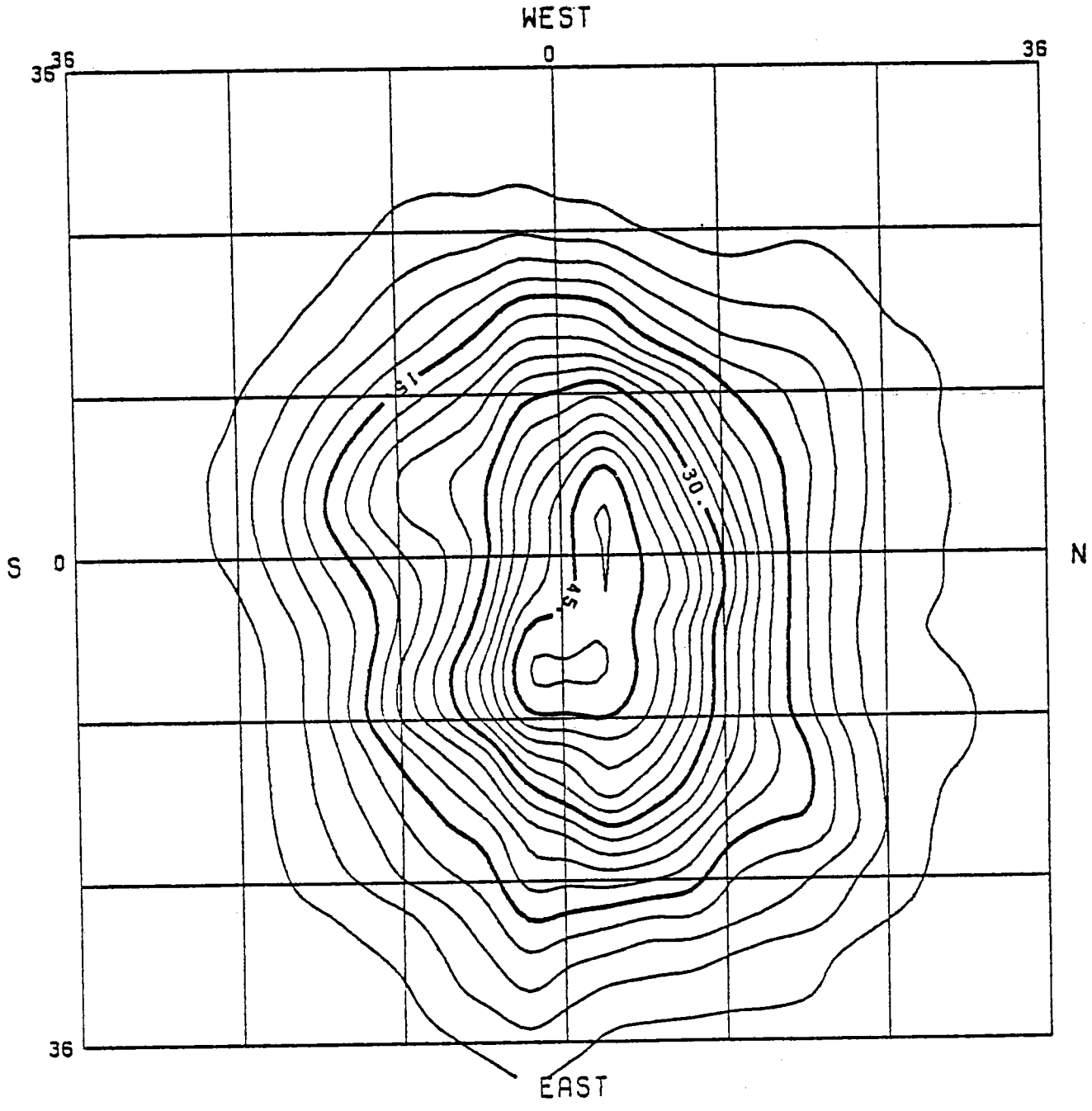

Figure 7. Flux Map - 12 Inches Above Platform.

NORM. TO 900 W/M2

DATE: 8-17-78
TIME: 13:53 TO 13:56
SCAN 4: 6 IN. ABOVE FOCAL PLANE
INSOLATION: 741-764 W/M^2

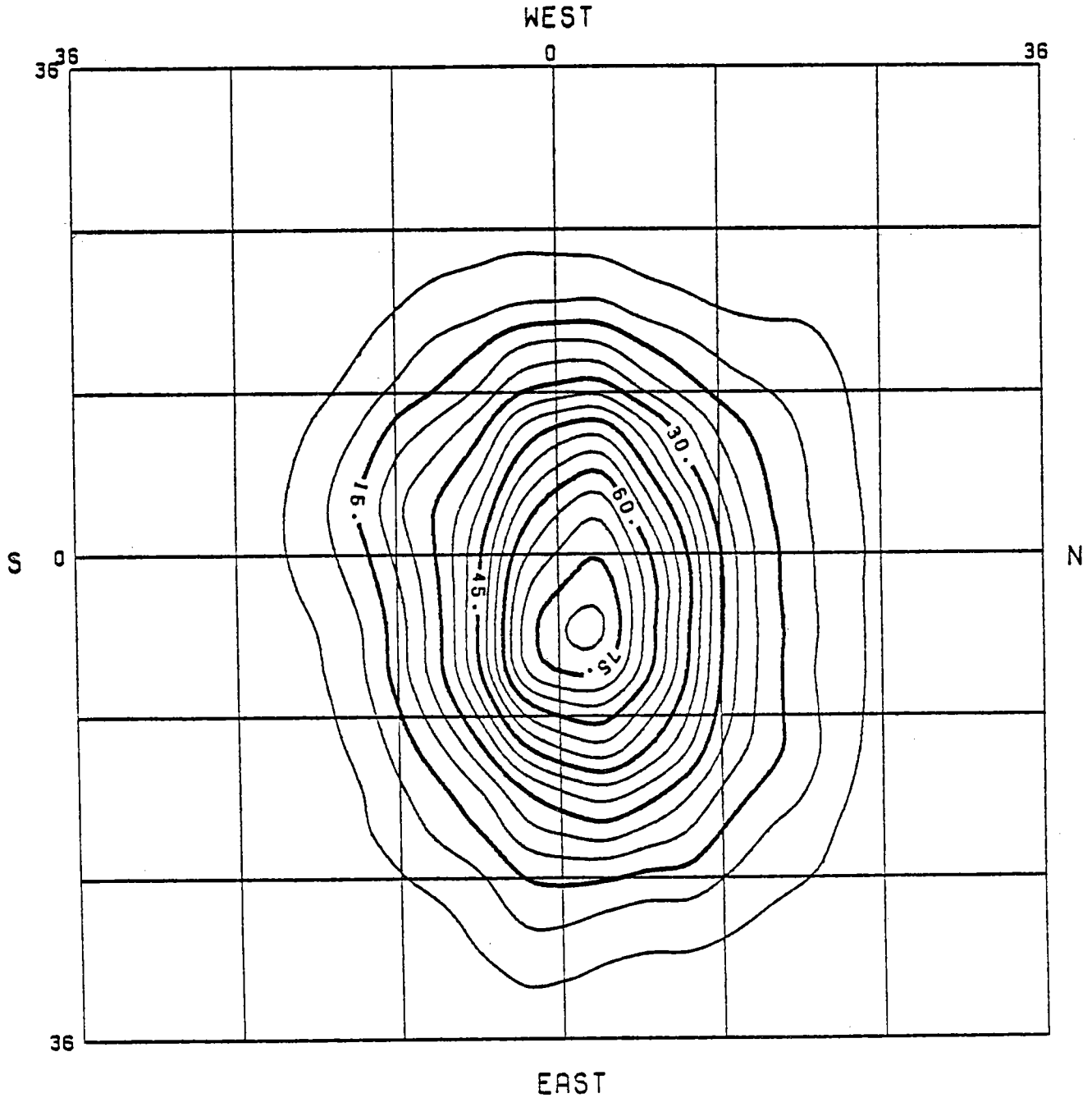

Figure 8. Flux Map - 6 Inches Above Platform.

NORM. TO 900 W/M2

DATE:	8-17-78
TIME:	14:04 to 14:09
SCAN 5:	SCAN AT FOCAL PLANE
INSOLATION:	731-755 W/M^2

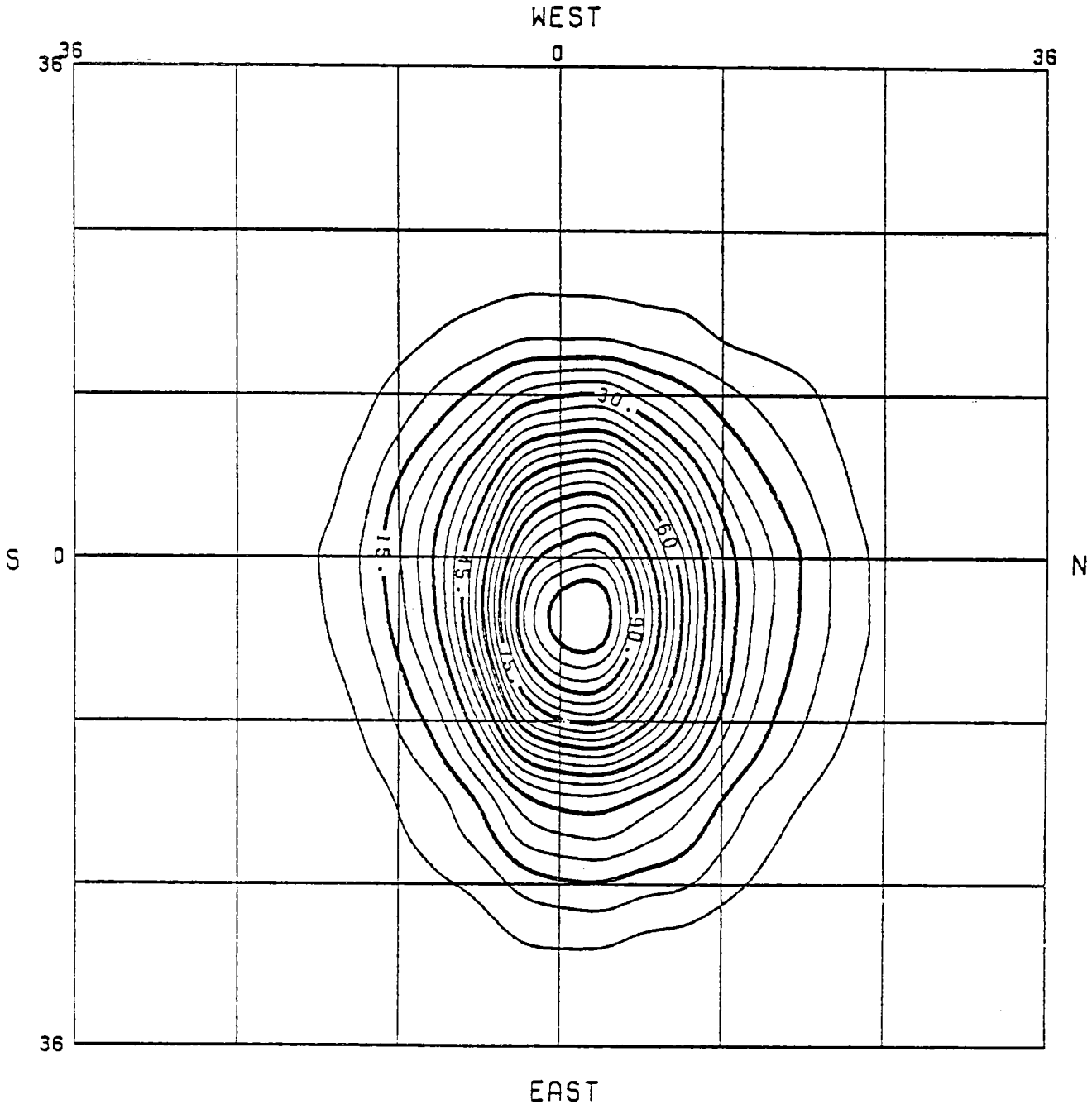

Figure 9. Flux Map - At Platform.

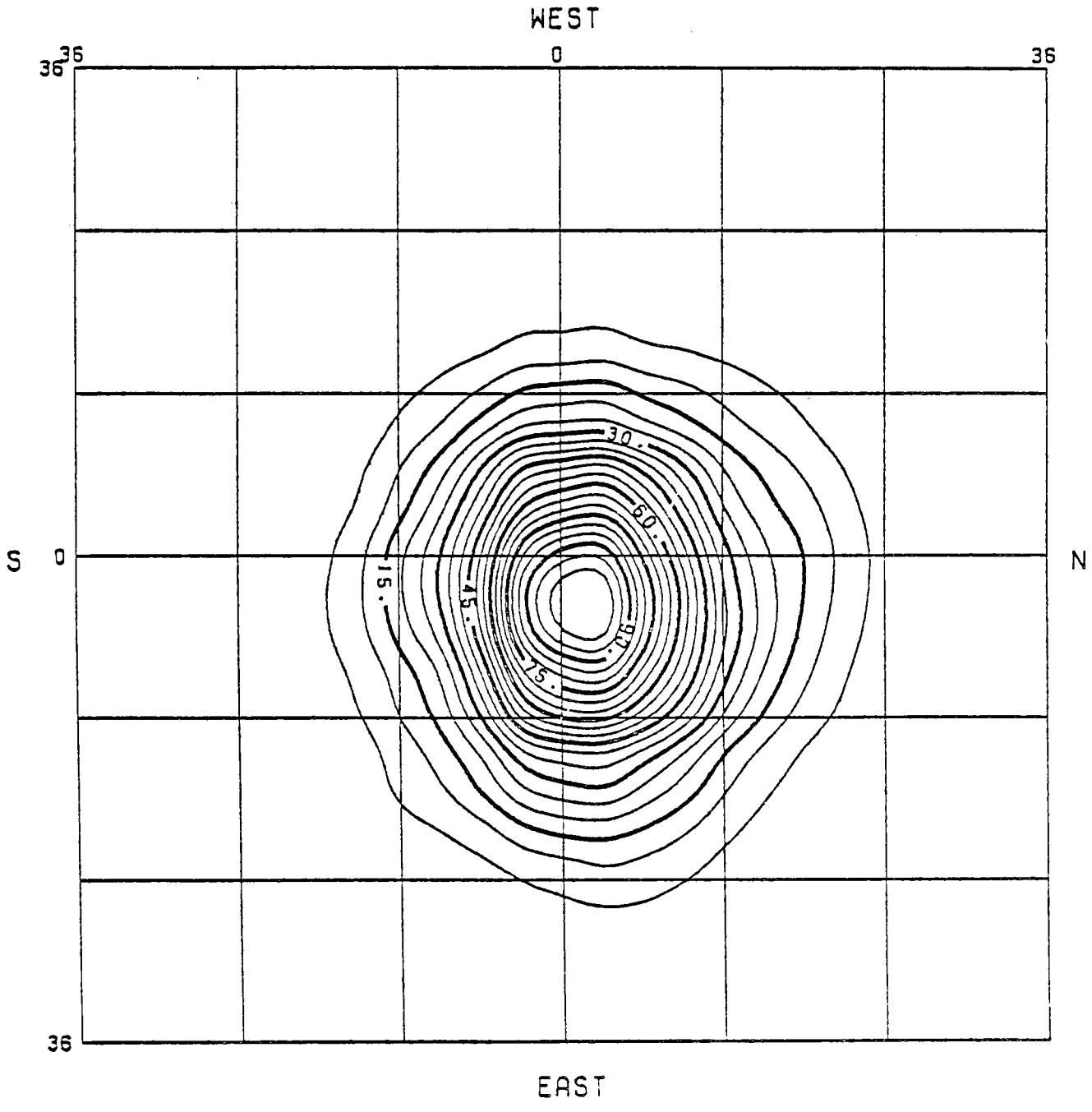

Figure 10. Flux Map - 6 Inches Below Platform.

NORM. TO 900 W/M2

DATE: 8-17-78
TIME: 14:28 TO 14:21
SCAN 7: 12 IN. BELOW FOCAL PLANE
INSOLATION: 725-747 W/M^2

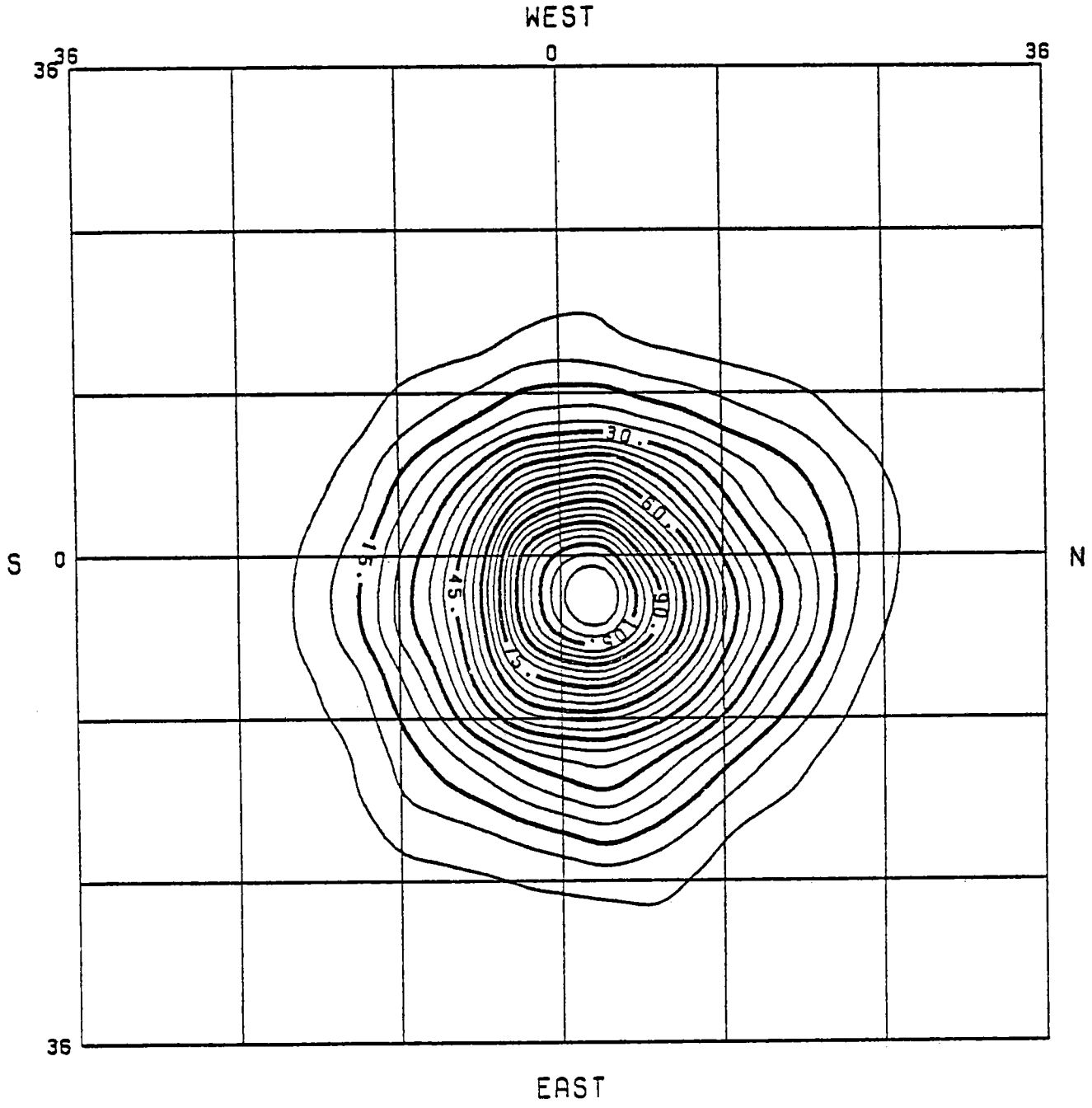

Figure 11. Flux Map - 12 Inches Below Platform.

NORM. TO 900 W/M2

DATE: 8-17-78
TIME: 14:45 TO 14:49
SCAN 8: 18 IN. BELOW FOCAL PLANE
INSOLATION: 705-740 W/M^2

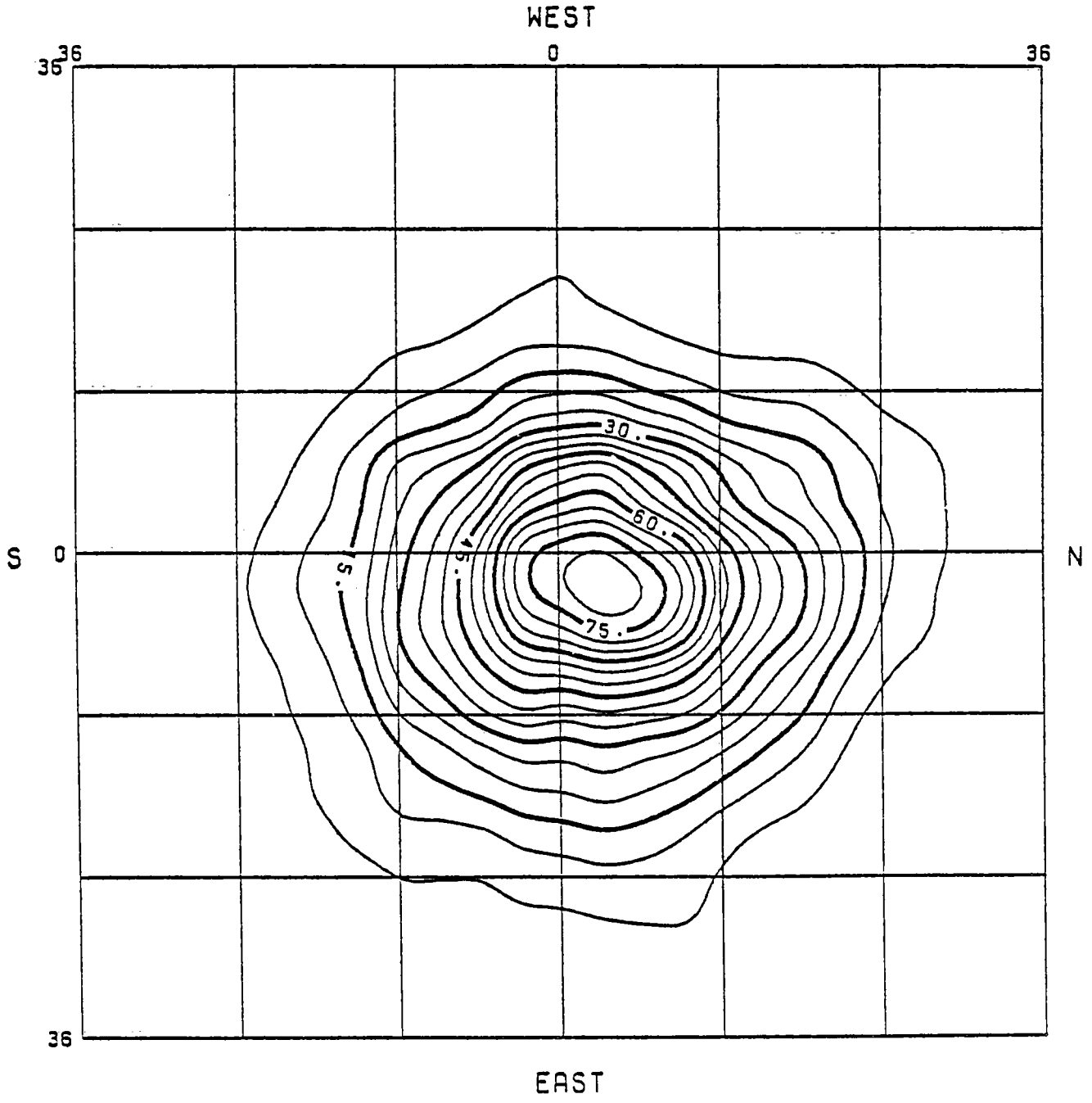

Figure 12. Flux Map - 18 Inches Below Platform.

NORM. TO 900 W/M2

DATE: 8-17-78
TIME: 14:57 TO 15:02
SCAN 9: 24 IN. BELOW FOCAL PLANE
INSOLATION: 679-722 W/M2

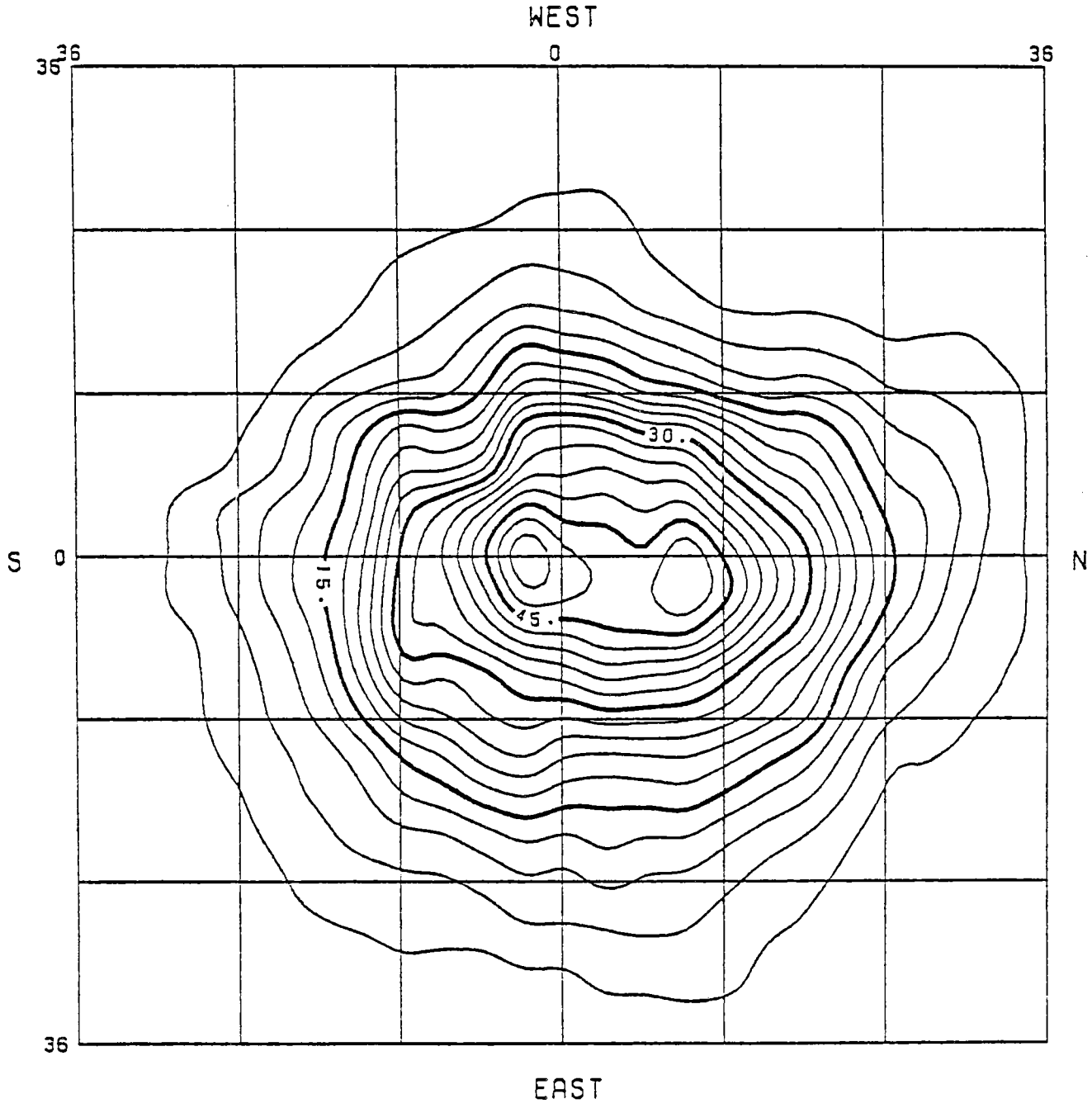

Figure 13. Flux Map - 24 Inches Below Platform.

3.2 Joint Flux Mapping

The first tests using Sanders equipment involved the Sanders flux scanning rake in conjunction with the ACTF scanning calorimeter. This effort was undertaken to correlate the ACTF scanner data taken at the Sanders aperture with radiation levels obtained inside the receiver cavity as indicated by Sanders rake data. Figure 14 illustrates the geometry and orientation of the two heat flux measuring instruments. The establishment of this relationship permitted the measurement of heat flux into the Sanders receiver by use of the ACTF scanner alone during receiver testing.

The Sanders rake consists of 25 calorimeters mounted in a bar that rotates about a vertical axis. The bar is water cooled and is arranged so that the calorimeters are rotated at various radii corresponding to the inside surfaces of the Sanders receiver cavity. The axis of rotation of the bar was centered on the Sanders terminal concentrator during this phase of the test and the ACTF scanner was located immediately beneath the concentrator inlet.

A number of scan sequences were undertaken to establish correlations with beam centroid position and time of day. Each sequence was initiated by a 360 degree clockwise scan of the Sanders rake followed immediately by a West to East ACTF scan. Data were collected from a total of 11 Sanders rake scans and 14 ACTF calorimeter scans over a three day period in order to complete this phase of the test. Figures 15 and 16 are typical flux contour maps derived from the Sanders flux rake and ACTF scanning calorimeter data.

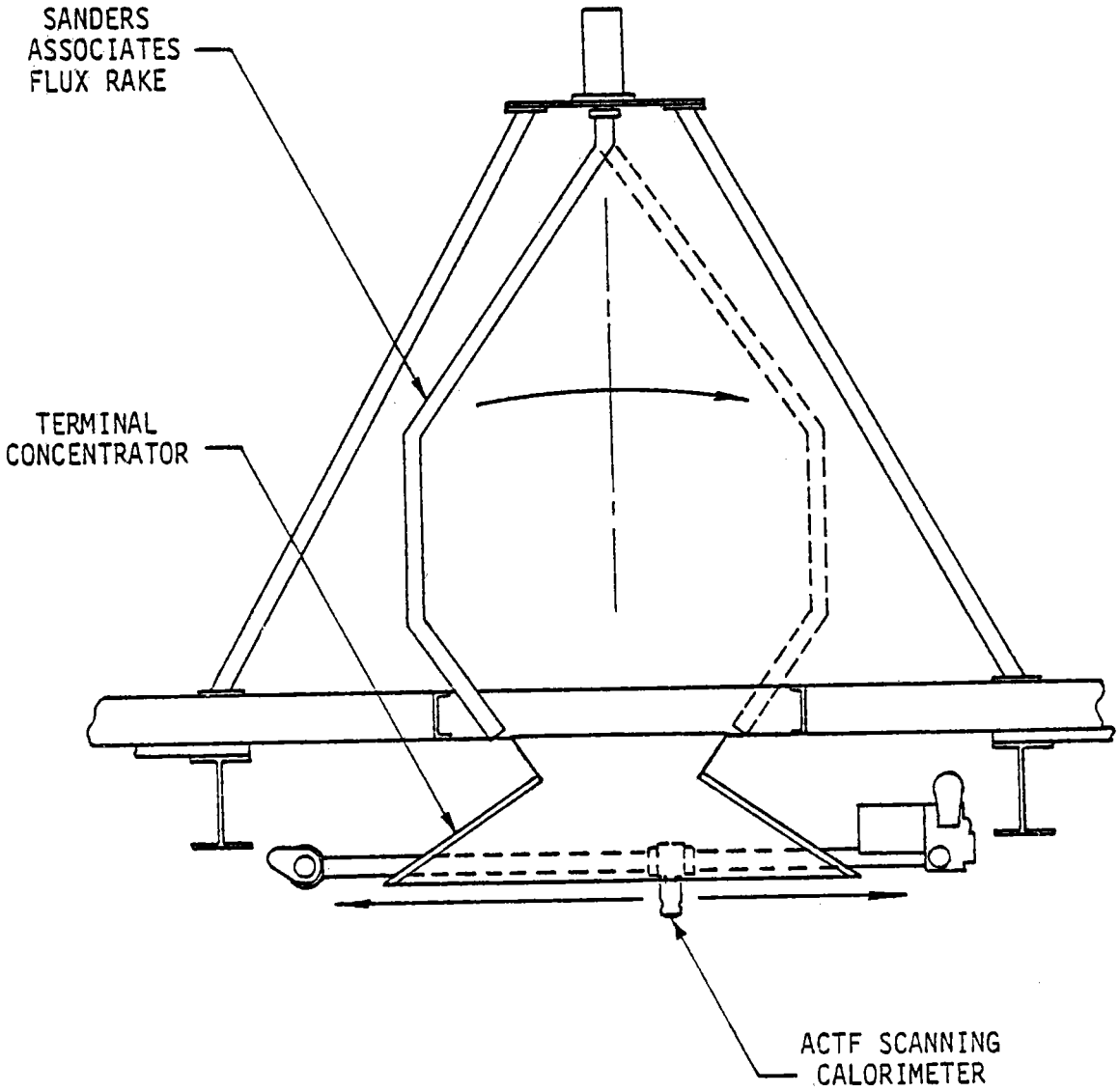

Figure 14. Arrangement of Flux Scanning Devices During Scanner Correlation Runs.

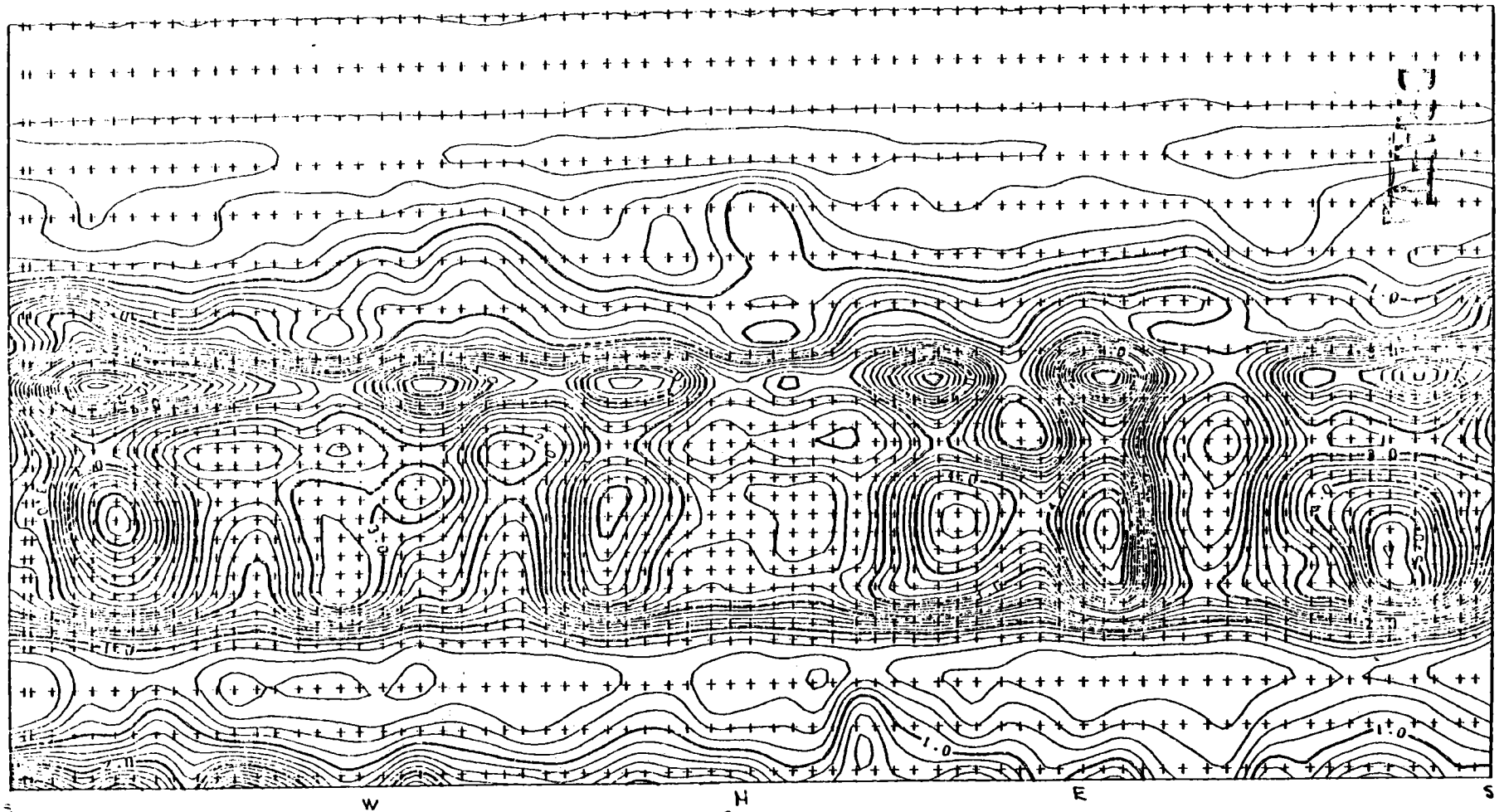

Sanders Scan 9/17/78
Normalized to 950 W/m^2

Btu/ft^2.sec.

Figure 15. Typical Sanders Rake Flux Map.

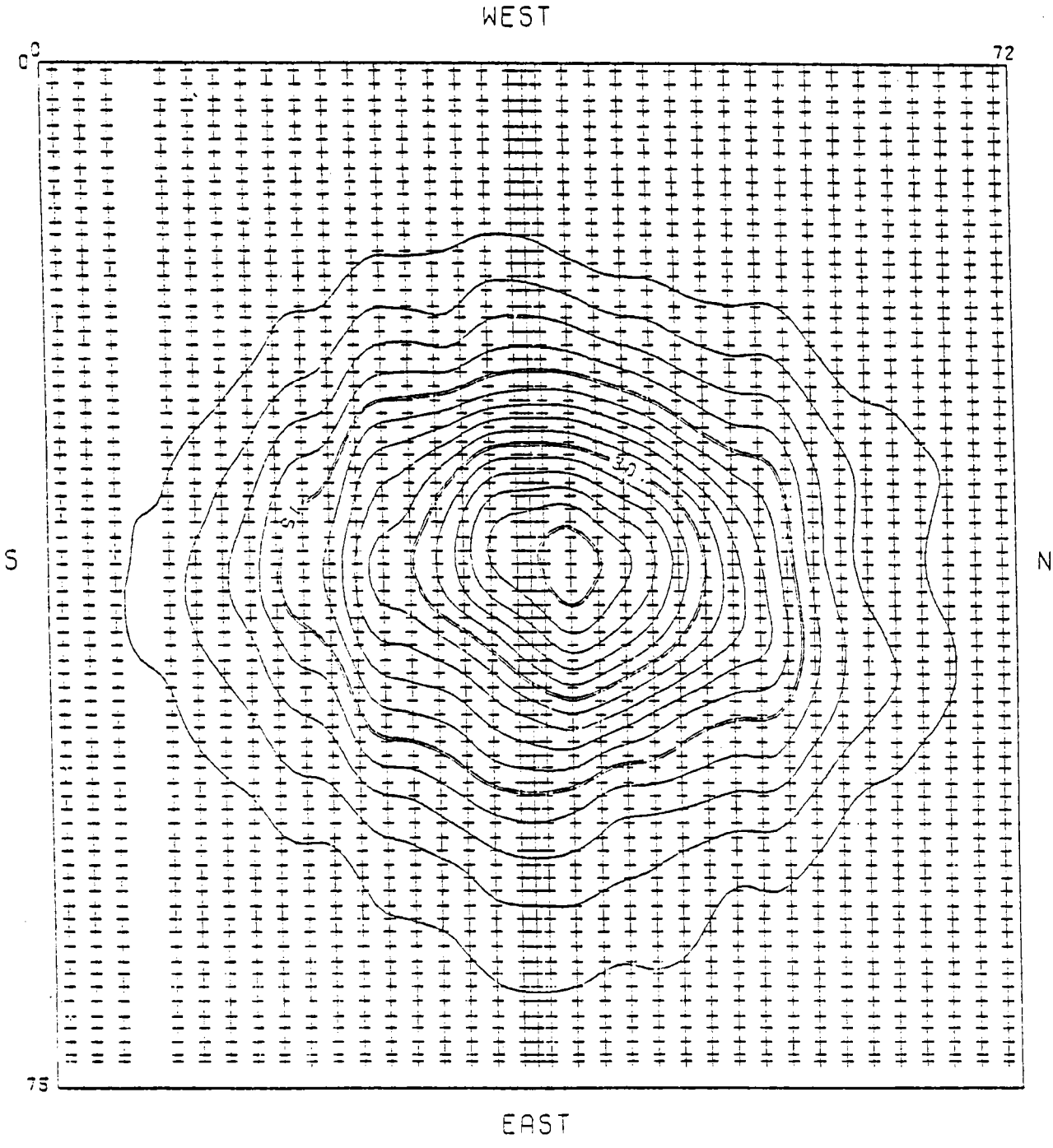

Figure 16. Typical ACTF Flux Map Taken at Aperture of Sanders Receiver.

3.3 Receiver Testing

As a parallel effort to the joint flux mapping operation, the Sanders receiver assembly was assembled at ground level and a hot checkout of the system (using L.P. gas heat) was accomplished.

On September 21, 1978, the receiver assembly was mounted on the ACTF test tower, the terminal concentrator was attached and various utilities were connected. In addition, the Sanders control panel, located in the ACTF control room was electrically connected to the receiver package and checked out.

During the following four week period, the receiver was subjected to both solar and/or L.P. gas heating cycles as called for in the test plan. Peak and integrated insolation data at the ACTF during the test period are shown in Figures 17 and 18.

4.0 DISCUSSION

During the solar phase of the Sanders test, ACTF personnel had primary responsibility for mirror field operation, flux scanner operation, data system operation, and direction of testing. Sanders personnel responsibilities included operation and monitoring of all equipment in the receiver package and coordination with the ACTF test director.

4.1 Mirror Field Operation During Testing

After completion of all system check lists and acquisition of the focal zone with the mirror field, continued image centroid management throughout the daily test period was accomplished with the aid of the ACTF calorimeter and the mirror field tracking device.

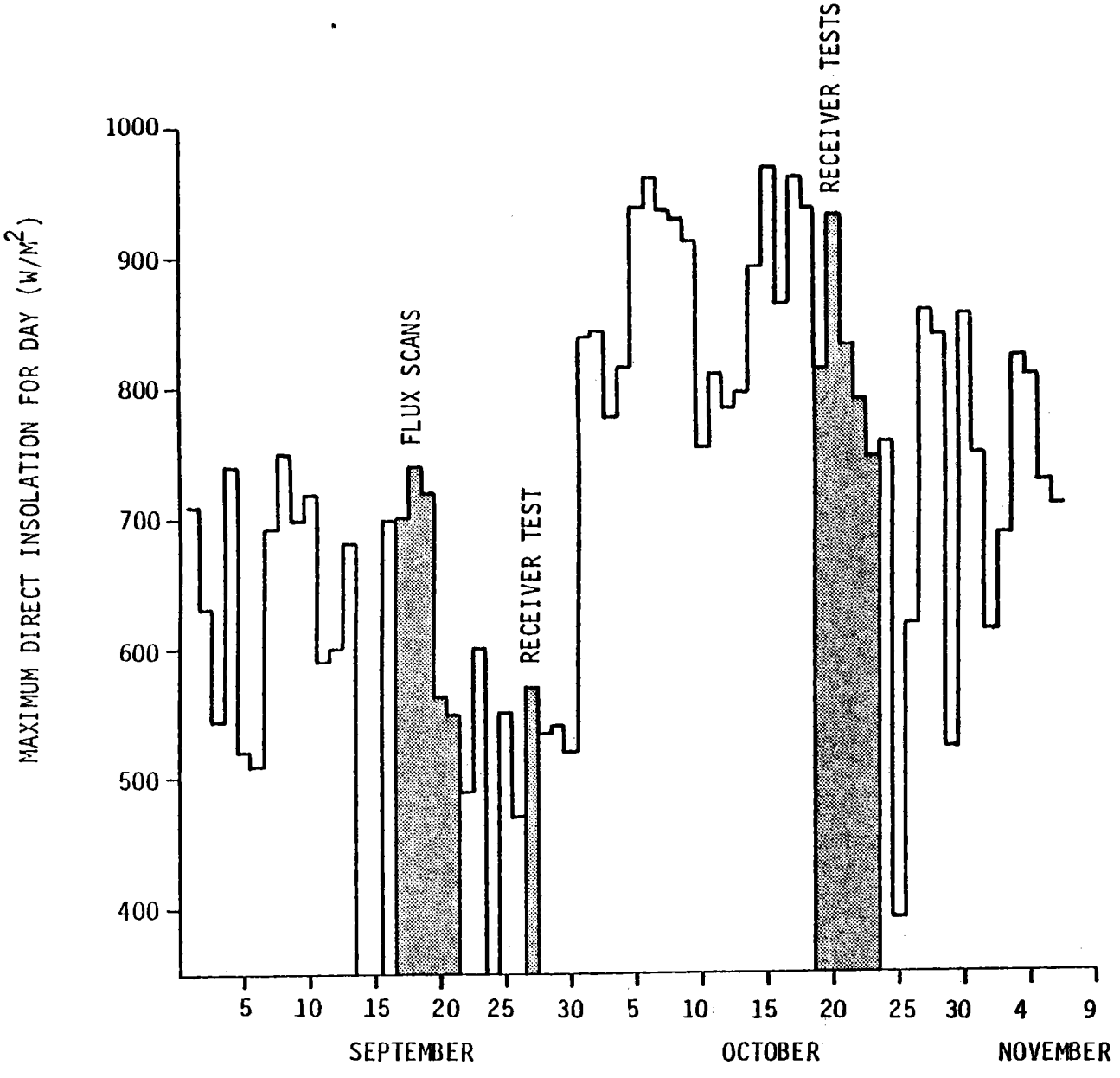

Figure 17. Maximum Insolation at ACTF By Day of Month.

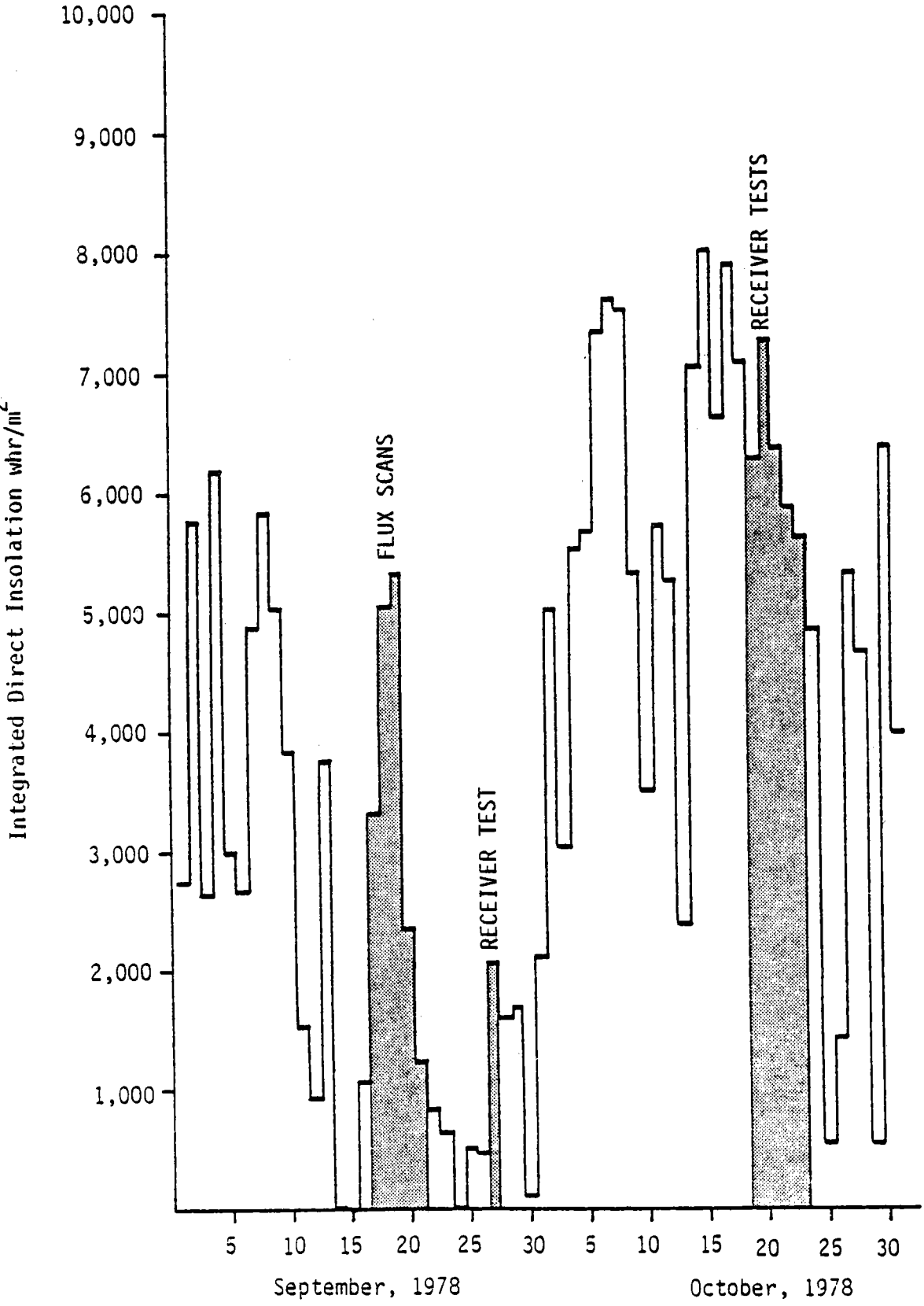

Figure 18. Integrated Insolation at ACTF By Day of Month.

Correction of normal northerly image drift resulting from seasonal solar declination changes was accomplished by manual adjustment of the kinematic motion devices. Two daily declination adjustments were required during the test period in order to maintain the image centroid in the correct north-south position. Figure 19 shows a typical flux distribution at the Sanders receiver aperture during testing. Figure 20 is a summary of receiver test data. Figures 21 through 28 show the relationship between image centroid at the Sanders receiver aperture and the centerline of the terminal concentrator during several test days.

4.2 Flux Scanning Operations

The ACTF scanning calorimeter was used as a total flux measuring device during the receiver tests as well as a beam centroid determining aid. The device, operated from the ground control console position, was used to complete some 43 west to east scans across the terminal concentrator aperture during the test period. Data from these scans in conjunction with pyrheliometer information are the basis of receiver performance calculations as well as evaluation of ACTF mirror field operations.

4.3 Post Test Activity

At the conclusion of the Sanders Associates tests the receiver assembly was removed from the tower and has been stored above grade at the ACTF site. A small electrical heat source has been positioned inside the receiver cavity to prevent moisture damage. All external parts are sealed and the entire assembly is protected with sheet plastic covering.

PEAK FLUX AND POWER DISTRIBUTION AT FOCAL PLANE OF
ACTF AT 14:20 ON 8/17/78

Insolation = 739-751 W/m^2

Radius (R)* (inches)	Flux Density At Radius (R) (W/cm^2)	Total Power Within Circle of Radius (R) Normalized to 900 W/m^2 (kW)	Percent of Total Power Within Circle of Radius (R)
0	125	0.	0
2	120-125	10.4	3.2
4	100-115	40.2	12.4
6	80-100	78.6	24.2
8	60- 80	124.9	38.5
10	40- 65	171.0	52.7
12	25- 50	211.7	65.2
14	20- 30	243.5	75.0
16	15- 20	268.2	82.6
18	10- 15	287.6	88.6
20	5- 10	301.4	92.9
22	5	309.9	95.5
24	0	315.3	97.1
36	0	324.6	100.0

*Radial distance from centroid.

Figure 19.

SUMMARY OF SOLAR FLUX DATA FROM
SANDERS ASSOCIATES RECEIVER TESTS
(Sanders aperture scans)

Scan Date	EDST Scan Time	Insolation (W/m^2) Max.	Insolation (W/m^2) Min.	Total* Flux (kW)	Flux In 1.42 m Dia. (kW)	Radial Centroid Error (cm)
10-19-78	13:12	787.6	779.2	237.1	213.5	13.9
10-19-78	14:07	757.6	739.3	218.3	200.5	0.5
10-19-78	15:42	700.1	668.8	181.5	161.5	5.6
10-20-78	10:32	832.7	822.9	212.4	184.6	12.3
10-20-78	11:01	869.9	851.0	241.7	218.9	6.1
10-20-78	11:20	890.8	859.5	250.1	227.7	6.9
10-20-78	11:58	921.5	897.4	266.4	244.9	5.5
10-20-78	12:35	920.9	890.2	266.8	247.5	2.7
10-20-78	13:14	915.7	873.2	(Incomplete Scan)		
10-21-78	10:40	759.6	752.4	192.1	172.6	6.5
10-21-78	10:52	781.1	757.6	204.8	185.4	5.9
10-21-78	11:26	799.4	787.6	226.6	207.4	4.3
10-21-78	11:55	808.5	794.8	229.1	211.6	4.1
10-21-78	12:51	826.8	812.5	244.2	225.7	6.2
10-21-78	13:35	819.0	798.1	239.5	218.6	11.5
10-21-78	14:13	801.4	748.5	226.2	206.7	6.5
10-21-78	15:34	722.3	701.4	190.9	167.5	6.7
10-21-78	15:51	705.4	684.5	176.0	154.8	3.1
10-21-78	16:25	651.8	624.4	139.7	120.5	6.2
10-22-78	13:06	785.0	764.1	238.4	221.2	5.5
10-22-78	13:39	776.5	739.3	227.3	211.0	2.3
10-22-78	14:31	764.8	741.9	223.7	205.0	0.1
10-22-78	15:23	713.2	696.2	198.3	176.7	3.5
10-22-78	16:05	677.9	655.7	166.0	145.4	3.6
10-22-78	16:44	578.0	559.1	113.8	96.6	3.0
10-23-78	10:36	672.7	633.5	164.6	146.6	10.8
10-23-78	11:18	715.8	692.3	199.2	181.6	10.8
10-23-78	11:56	725.6	693.6	208.1	191.8	5.5
10-23-78	12:40	743.2	710.6	212.0	196.2	2.9
10-23-78	14:04	713.8	680.5	204.4	186.2	2.0

*Flux over 1.8 m x 1.8 m (6 ft x 6 ft) area centered on terminal concentrator.

Figure 20.

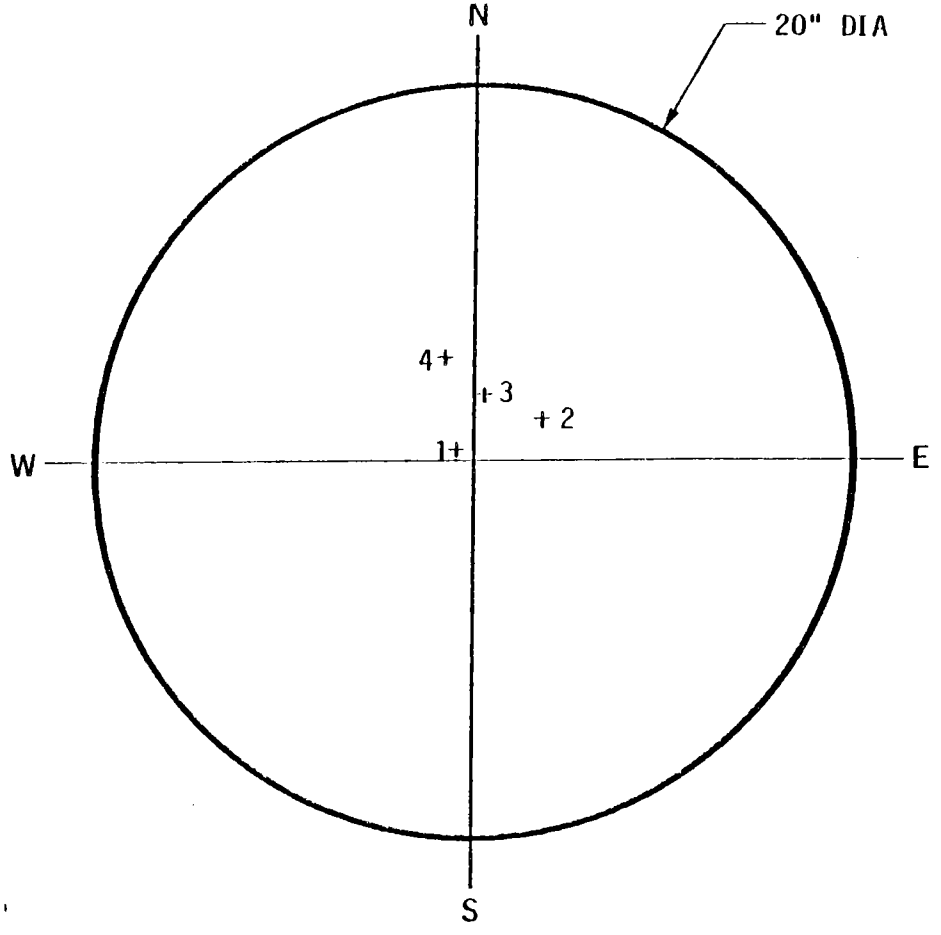

POINT		TIME	ΔR FROM TARGET ℄
1	=	10:20	1.15 in.
2	=	10:45	1.75 in.
3	=	11:17	1.95 in.
4	=	11:57	3.29 in.

Figure 21. Centroid of Solar Beam Referenced to Entrance of Sanders Terminal Concentrator-September 17, 1978.

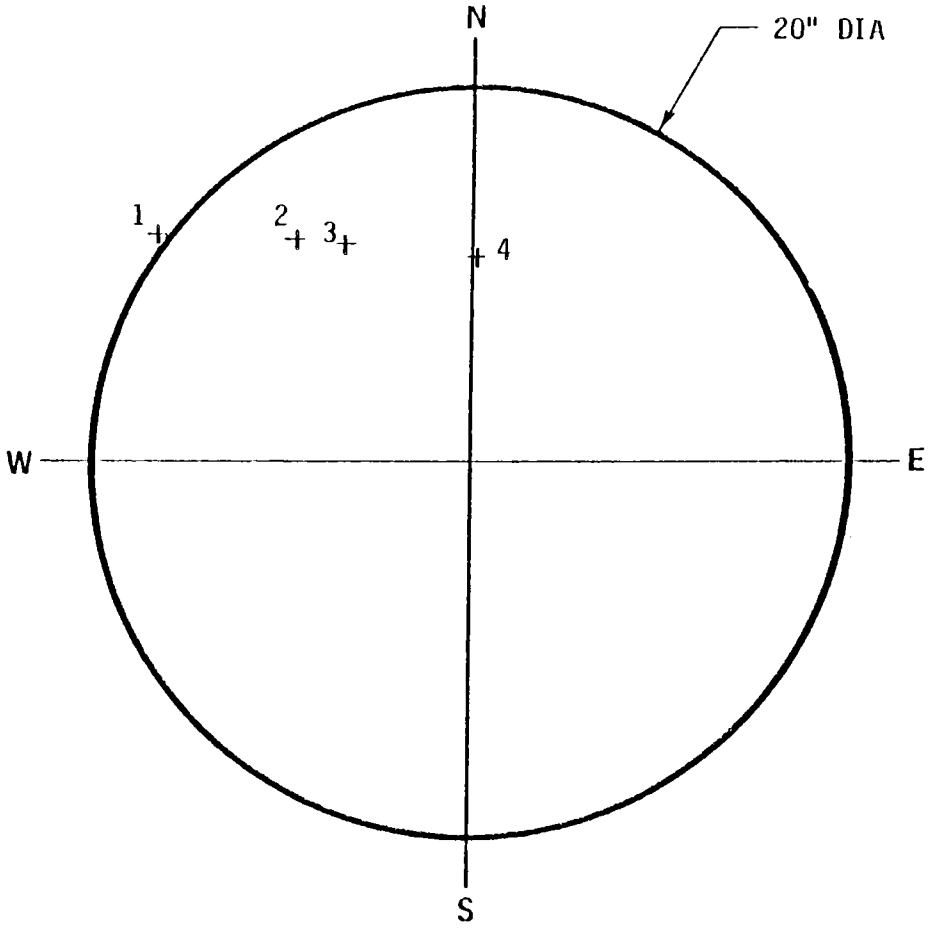

POINT		TIME	ΔR FROM TARGET ℄
1	=	14:35	10.48 in.
2	=	14:46	7.76 in.
3	=	15:30	6.95 in.
4	=	16:06	5.72 in.

Figure 22. Centroid of Solar Beam Referenced to Entrance of Sanders Terminal Concentrator - September 18, 1978.

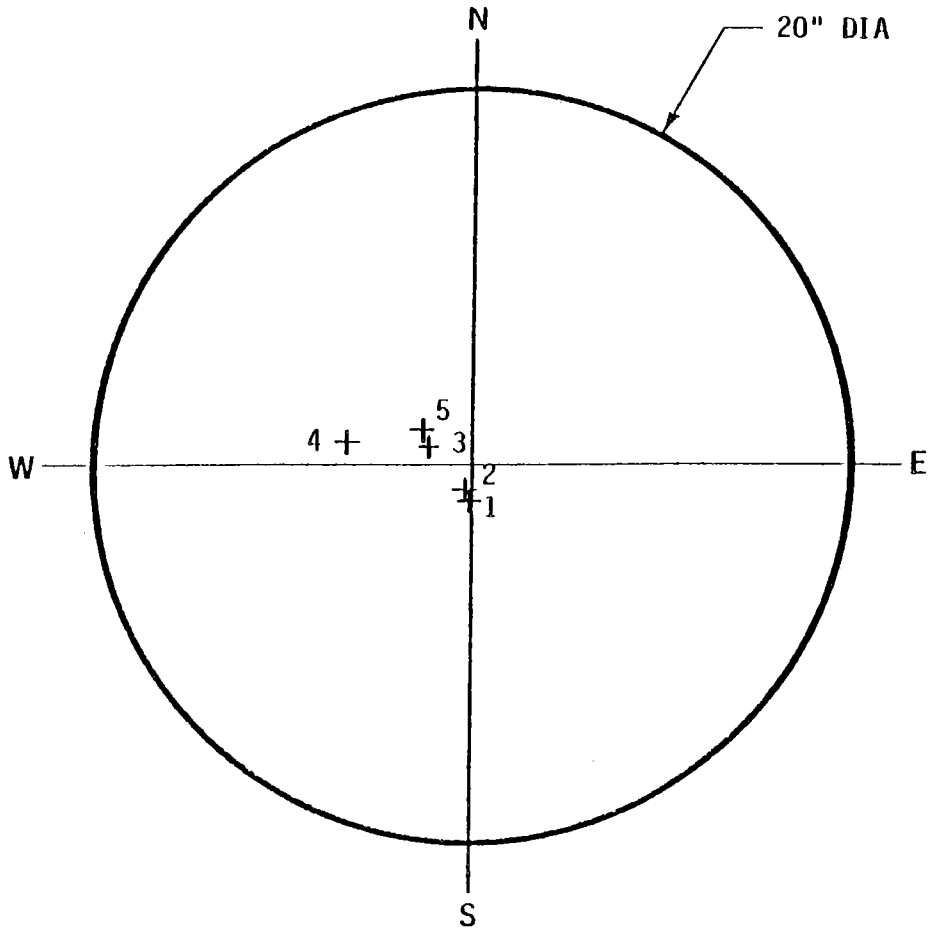

POINT		TIME	ΔR FROM TARGET ℄
1	=	10:31	1.03 in.
2	=	10:41	0.78 in.
3	=	11:23	1.72 in.
4	=	12:12	3.72 in.
5	=	13:02	2.97 in.

Figure 23. Centroid of Solar Beam Referenced to Entrance of Sanders Terminal Concentrator - September 19, 1978.

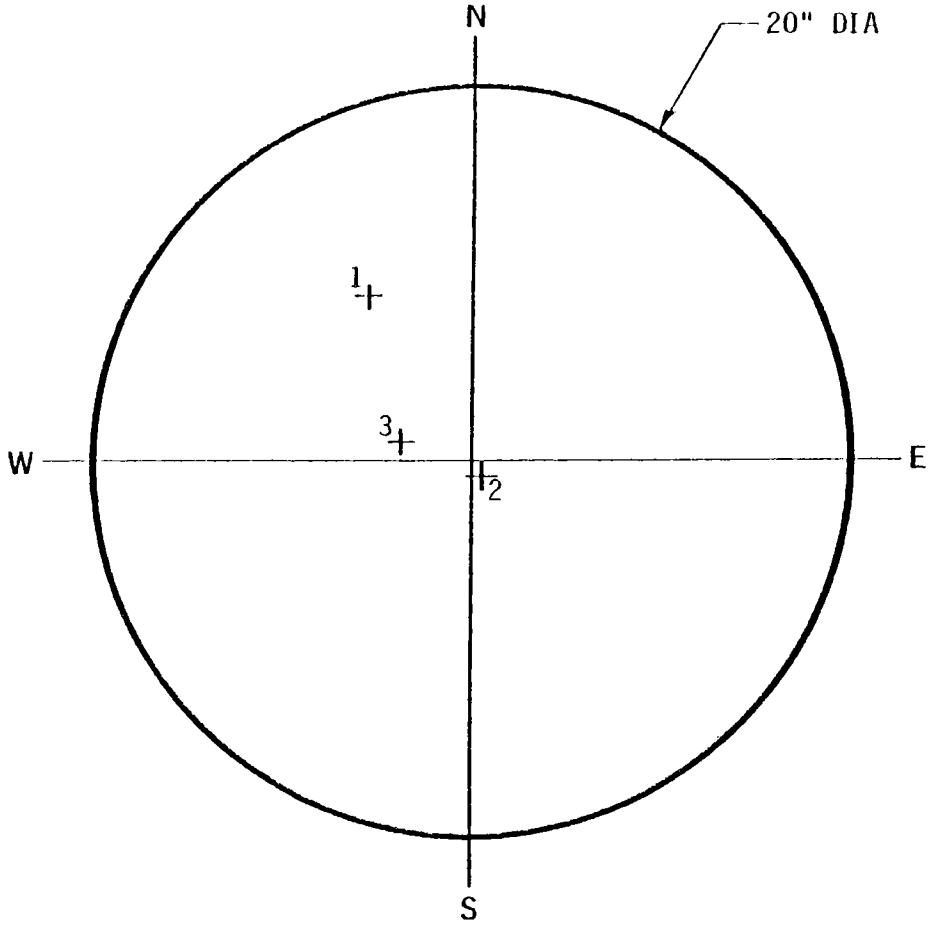

POINT		TIME	ΔR FROM TARGET ℄
1	=	13:12	5.50 in.
2	=	14:07	0.31 in.
3	=	15:41	2.29 in.

Figure 24. Centroid of Solar Beam Referenced to Entrance of Sanders Terminal Concentrator - October 19, 1978.

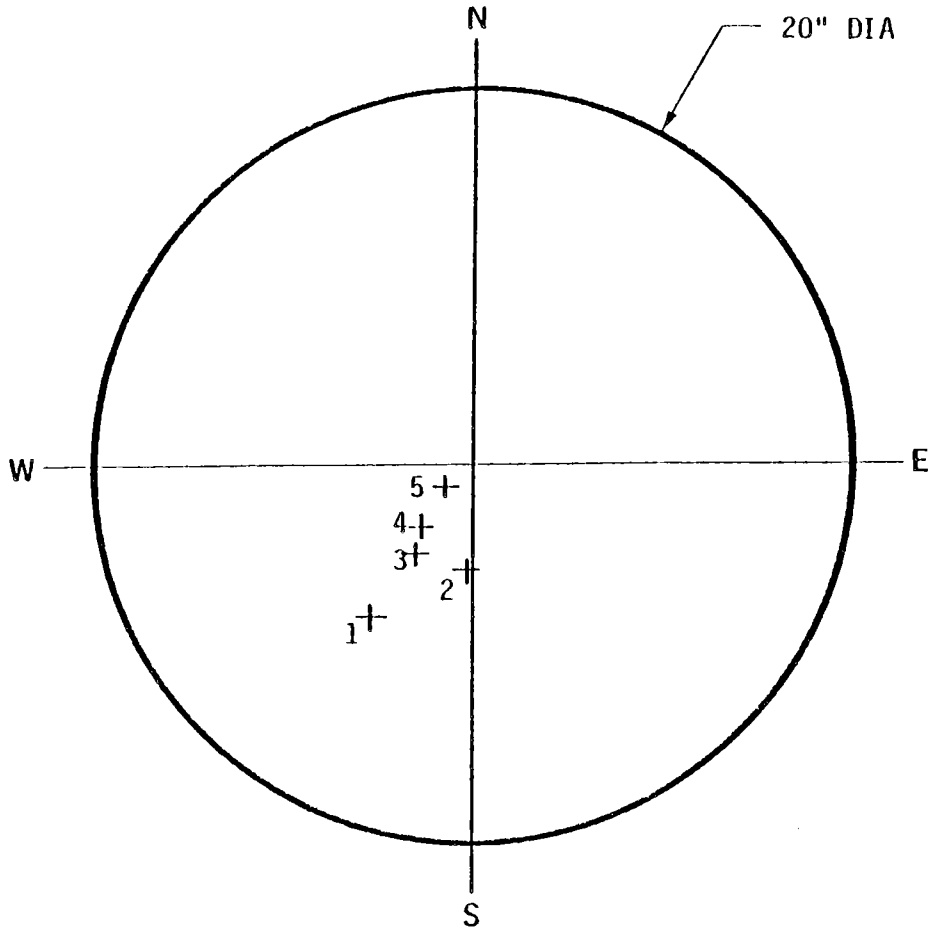

POINT		TIME	ΔR FROM TARGET ℄
1	=	10:32	4.72 in.
2	=	11:00	2.28 in.
3	=	11:19	2.64 in.
4	=	11:58	2.12 in.
5	=	12:35	1.07 in.

Figure 25. Centroid of Solar Beam Referenced to Entrance of Sanders Terminal Concentrator - October 20, 1978.

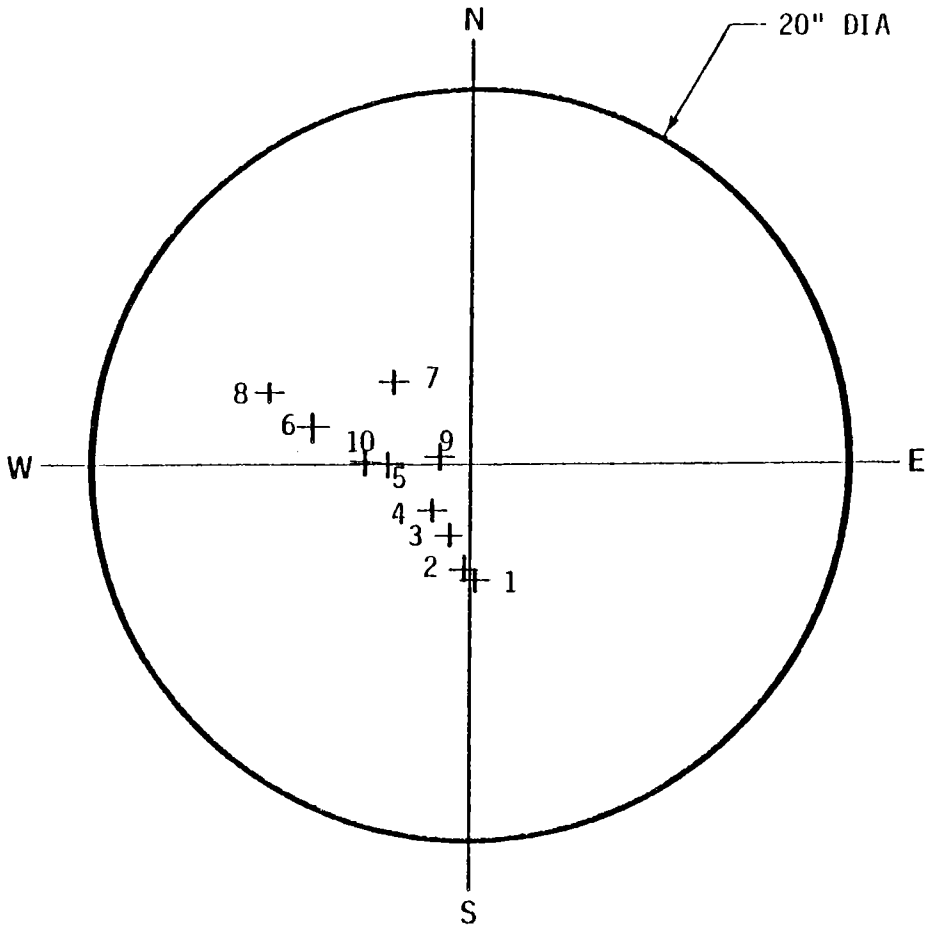

POINT		TIME	ΔR FROM TARGET ℄
1	=	10:40	2.43
2	=	10:51	2.23
3	=	11:25	1.60
4	=	11:55	1.56
5	=	12:51	2.46
6	=	13:35	4.58
7	=	14:13	2.93
8	=	15:34	5.67
9	=	15:50	1.33
10	=	16:25	2.5

Figure 26. Centroid of Solar Beam Referenced to Entrance of Sanders Terminal Concentrator - October 21, 1978.

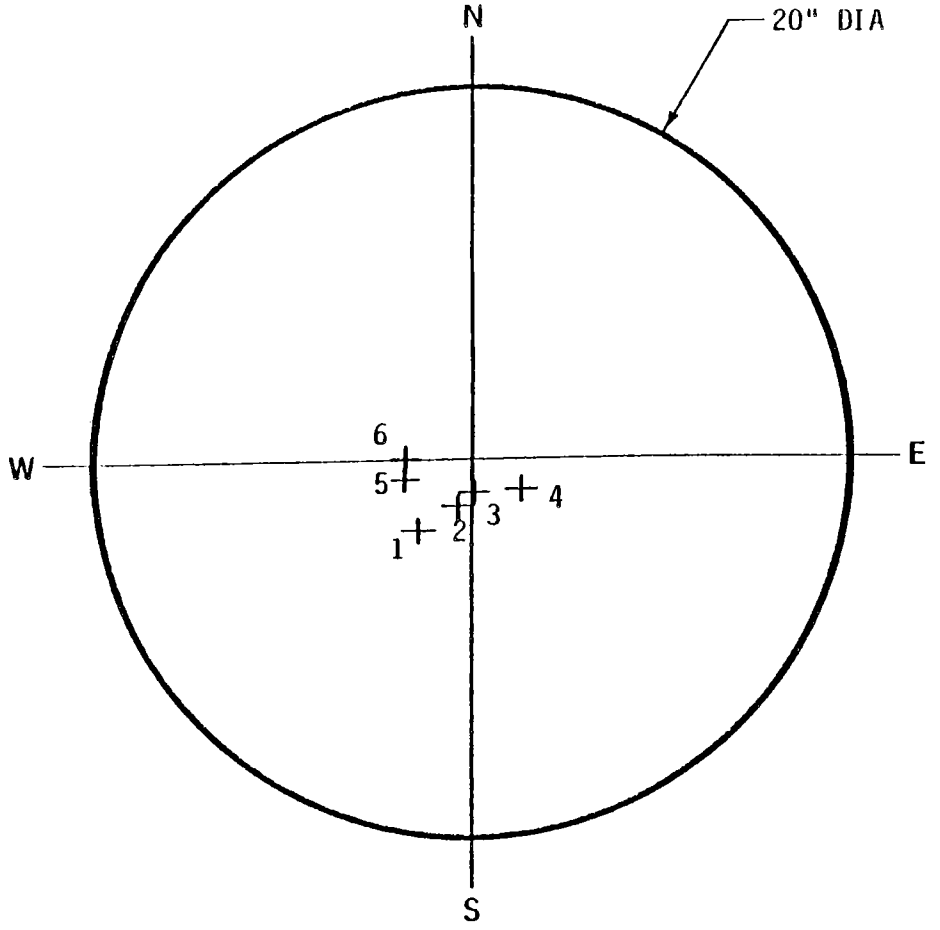

POINT		TIME	ΔR FROM TARGET ℄
1	=	13:06	2.08
2	=	13:38	0.83
3	=	14:31	0.08
4	=	15:23	1.42
5	=	16:04	1.45
6	=	16:44	1.19

Figure 27. Centroid of Solar Beam Referenced to Entrance of Sanders Terminal Concentrator - October 22, 1978.

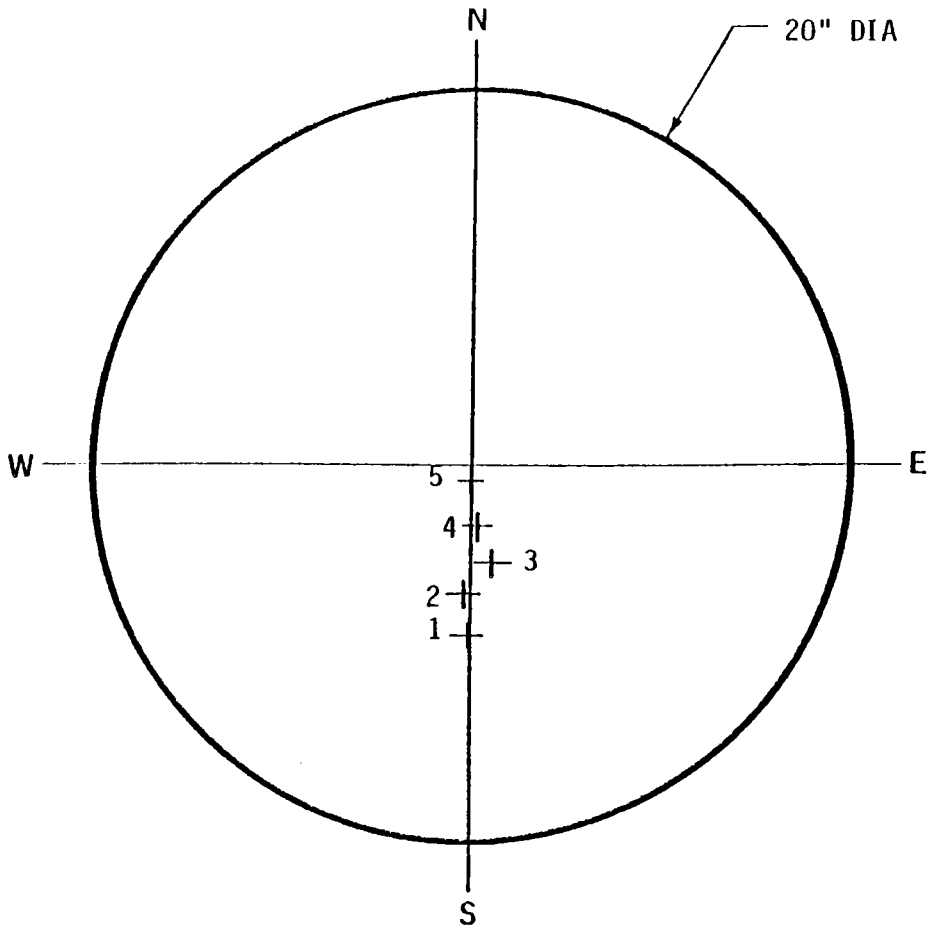

POINT		TIME	ΔR FROM TARGET ℄
1	=	10:35	4.14 in.
2	=	11:17	2.81 in.
3	=	11:55	2.05 in.
4	=	12:39	1.01 in.
5	=	14:04	0.85 in.

Figure 28. Centroid of Solar Beam Referenced to Entrance of Sanders Terminal Concentrator - October 23, 1978.

APPENDIX V
STATEMENT OF WORK

The Contractor shall provide the personnel, equipment and supplies to accomplish the following tasks.

Task 1 - Design of the 1/4 MWt Receiver

Based on the results of analyses of system configurations conducted during previous phases of Contract E(11-1)-2823, the Contractor shall design a solar thermal heat receiver of 1/4 MWt capacity and associated test equipment. The heat receiver shall use air as the working fluid (coolant). The Contractor shall design the receiver to achieve an outlet air temperature of 2000°F at an overall thermal efficiency (ratio of net heat absorbed by the receiver cooling air to the energy incident on the aperture of the receiver) of 84%. The receiver shall be configured to operate at its design point with a zero pressure difference across the aperture which will permit operation without a pressure sealing window. The receiver shall be designed to conform to the GIT field configuration, whether south-tower or central tower. Calculations shall be performed on the GIT mirror field to compare receiver performance advantages for these two field configurations.

The HELIOS computer code shall be modified by a new code to be developed by the Contractor which will trace solar rays through the terminal concentrator and the opening to the inside of the receiver cavity when multiple reflections are accounted for and flux distributions are determined.

The Contractor shall prepare a report justifying and fully detailing the design of the receiver and the analytical basis for the design. The Contractor shall submit this report to the DOE Project Manager for approval before proceeding to the construction (Task 4) of the 1/4 MWt heat receiver and associated test equipment.

Task 2 - Convective Heat Loss Experiment

Task 2A The Contractor shall design an experiment and conduct supporting analyses aimed at evaluating the magnitude of the convective losses associated with the design of the 1/4 MWt heat receiver and a commercial-scale heat receiver. The convective losses may arise from leakage of heated receiver inlet air to the ambient, leakage of ambient air into the receiver, or from other mechanisms. The Contractor shall submit the design of the experiment, test plans, supporting analyses and cost proposal for convective loss experiment and justifications to the DOE Project Manager for his approval.

Task 2B The Contractor shall construct the convective loss experiment designed in Task 2A. The experimental costs will be conducted in accordance with the test plan submitted as part of Task 2A. The Contractor shall prepare a report fully summarizing the design of the experiment, the tests conducted, the experimental results and the analysis of the data.

Task 3 - Systems Analyses

The Contractor shall perform systems analyses to assure that the 1/4 MWt heat receiver design and performance remain scalable and compatible with the best envisioned commercial application. At the time of submission of the Task 1 and Task 2 reports, the Contractor shall include the results of this Task 3 for this period. The Contractor shall include in the Final Report the details of all analyses conducted under this Task.

Task 4 - Construction of the 1/4 MWt Heat Receiver

Upon receipt of the DOE Project Manager's approval for the design of the 1/4 MWt heat receiver and the report of the Convective Heat

Transfer Loss Experiment, the Contractor shall proceed to construction of the heat receiver and associated test equipment. The Contractor shall identify critical long lead items and report these to the DOE Project Manager. The Contractor shall not make commitments to major equipment, hardware or materials expenditures prior to the initiation of Task 4 without the written approval of the DOE Project Manager.

The Contractor shall construct and assemble the heat receiver and associated test equipment incorporating mounting brackets and any other interfaces required for testing at the Georgia Institute of Technology (GIT) 400 KWt Solar Thermal Test Facility. The associated test equipment shall include: a heat exchanger to reject receiver heat and to act as a thermal load during test; heat exchanger controls to ensure constant output temperature capability for startup control; a high temperature blower to circulate the air in the receiver and heat exchanger; and, instrumentation to measure the performance and thermal efficiency of the receiver.

The Contractor shall thermally test the completed receiver and associated test equipment prior to shipping to GIT. The purposes of these tests shall be to ensure mechanical and structural integrity and adequacy of control and instrumentation. The receiver and associated test equipment shall be operated at an intermediate temperature in excess of $1000^{o}F$ for a minimum of 10 thermal cycles (ambient temperature to intermediate temperature). The Contractor shall employ a separate air heater or auxiliary burner for these thermal tests to the DOE Project Manager for his approval at least 16 working days prior to the scheduled performance of the tests.

Upon successful completion of the thermal tests, the Contractor shall deliver the 1/4 MWt heat receiver and associated test equipment to the GIT 400 KWt Solar Thermal Test Facility, Atlanta, Georgia. The Contractor shall make certain to package and transport the receiver and associated test equipment in a way that will prevent any damage in shipment.

Task 5 - Testing of the 1/4 MWt Heat Receiver

The Contractor shall prepare a plan for testing of the 1/4 MWt Heat Receiver at the GIT Facility. The Contractor shall submit the test plan to the DOE Project Manager for his approval at least 20 days prior to delivery of the receiver at the GIT Facility.

The Contractor shall as a minimum include in his plan tests that measure heat receiver thermal efficiencies and receiver air outlet temperatures as a function of insolation and energy incident on the receiver aperture. The effects of various flux distributions and inhomogeneities on the silicon carbide honeycomb and on the flow control system shall likewise be measured. Honeycomb front surface temperatures will be measured using an infrared camera to determine hot spots.

Task 6 - Liaison with Georgia Institute of Technology

The Contractor shall provide technical liaison with the Georgia Institute of Technology in the design, construction, test planning and safety aspects of the heat receiver and associated test equipment to ensure proper integration and test of the 1/4 MWt Heat Receiver in the 400 KWt Solar Thermal Test Facility. The receiver mounting design shall accommodate single aim point strategy for the GIT mirrors. The Contractor shall provide a relocatable bar for mounting the GIT flux gages for flux mapping of the receiver cavity ceiling and cylindrical wall. The Contractor shall provide all safety information requested by GIT. Copies of all documents furnished to GIT shall be sent to the DOE Project Manager.

Task 7 - Review

The Contractor shall conduct informal reviews for the DOE Technical Manager at approximately six-week intervals. These reviews shall encompass all aspects of the work conducted under this contract. In

addition, the Contractor shall make two formal presentations, one of which shall be the design of the 1/4 MWt Heat Receiver and the results of the Convective Heat Loss Experiment. The second formal presentation will be designated by the DOE Project Manager.

* U.S. GOVERNMENT PRINTING OFFICE 1933-646-069/2025